

Structure- and adatom-enriched essential properties of graphene nanoribbons

Shih-Yang Lin, Ngoc Thanh Thuy Tran, and Ming Fa-Lin*

Department of Physics, National Cheng Kung University, 701 Tainan, Taiwan

E-mail: mflin@mail.ncku.edu.tw

Abstract

A systematic study is made on geometric, electronic and magnetic properties of one-dimensional graphene nanoribbons using the first-principles calculations. The feature-rich essential properties result from the various orbital hybridizations in chemical bonds and the edge-carbon- and adatom-induced spin states. Pristine nanoribbons, with honeycomb lattices, can exhibit the planar, curving, scrolling, folding, and stacking configurations. Adatom adsorptions on surface and edge, respectively, create the buckled structures and the non-hexagonal/non-planar edges. There exist six kinds of spin-dependent electronic and magnetic properties, non-magnetic, ferromagnetic and anti-ferromagnetic metals, the non-magnetic semiconductors, and the anti-ferromagnetic semiconductors with/without the spin splitting. They are clearly illustrated by the energy gaps, the electron/hole densities, the net magnetic moment, the atom-dominated energy bands, the spatial charge distributions, the spin arrangements, and the orbital- and spin-projected density of states. The diverse essential properties are determined by the complicated relations among the finite-size confinement, edge structure, curvature effect, interlayer atomic interaction, spin configuration, and chemical adsorption. The theoretical predictions can provide the full information in potential applications, and part of them agree with the recent experimental measurements.

Keywords: Graphene; Nanoribbons

1. Introduction

2. Instruments

2.1 Theoretical calculations

2.2 Experimental instruments

3. Monolayer graphene nanoribbons

3.1 Armchair systems

3.2 Zigzag systems

4. Curved and Zipped graphene nanoribbons

4.1 Curved nanoribbons

4.2 Carbon nanotubes

5. Folded graphene nanoribbons

5.1 The rich geometric structures

5.2 The unusual electronic and magnetic properties

6. Carbon nanoscrolls

6.1 The optimal geometries

6.2 Electronic properties and magnetic configurations

6.3 Comparisons among the planar, curved/zipped, folded and scrolled systems

7. Bilayer graphene nanoribbons

7.1 stacking-enriched geometric structures and magnetic configurations

7.2 Diverse electronic properties

7.3 Differences between bilayer 1D and 2D systems

8. Edge-decorated graphene nanoribbons

8.1 Adatom edge passivations

8.2 decoration- and curvature-enriched essential properties

9. Alkali-adsorbed graphene nanoribbons

9.1 The Alkali-created conduction electrons

9.2 The edge- and adsorption-co-dominated magnetic configurations

9.3 Comparisons, measurements and applications

10. Halogen-adsorbed graphene nanoribbons

10.1 Fluorination effects

10.2 Other halogenated systems

11. Metal-adsorbed graphene nanoribbons

11.1 Al

11.2 Ti

11.3 Bi

12. Concluding remarks: covering comparisons, measurements, and applications

1. Introduction

Carbon atoms, which possess four active valence electrons, can create the dimension- and curve-related condensed-matter systems, such as, graphite,^{1,2} graphene,^{3,4} graphene nanoribbon (GNR),^{5,6} carbon nanotube,^{7,8} carbon toroid,^{9,10} and fullerene.^{11,12} The carbon-related materials, with the diverse chemical bondings (sp^3 , sp^2 and sp bondings), have attracted a lot theoretical and experimental researches since the successful syntheses of C_{60} in 1985,¹¹ multi-walled carbon nanotubes in 1991,⁷ carbon tori in 1998,⁹ and few-layer graphenes in 2004.³ They are very suitable for studying the novel physical, chemical and material phenomena, especially for the emergent low-dimensional systems. GNRs are one of the mainstream nanomaterials, because the essential properties are greatly diversified by the complex relations among honeycomb lattice, one-atom thickness, finite-size quantum confinement, edge structure, planar/non-planar geometry, stacking configuration, adatom decoration, and chemical doping. Each GNR could be regarded as a finite-width graphene or an unzipped carbon nanotube. Up to now, GNRs have been successfully synthesized by the various experimental methods under the top-down and bottom-up schemes. The direct cutting of graphene layers covers the lithographic patterning and etching,^{6,13} sonochemical breaking,^{5,14} metal-catalyzed cutting,^{15,16} and oxidization reaction.^{17,18} The unzipping of multi-walled carbon nanotubes is achieved by the chemical attack,^{19,20} laser irradiation,²¹ plasma etching,^{22,23} metal-catalyzed treatment,^{24,25} hydrogen treatment and annealing,²⁶ scanning tunneling microscope (STM) tip,²⁷ transmission electron microscopy (TEM),²⁸ intercalation and exfoliation,^{29,30} and electrochemical³¹ and sonochemical processes.^{32,33} Moreover, other strategies involve chemical vapor deposition³⁴⁻³⁶ and chemical synthesis,³⁷⁻³⁹ being able to produce macroscopic quantities of graphene nanoribbons. This systematic work is focused on the width-, layer number-, stacking-, curving-, folding-, scrolling-, decorating- and doping-dependent geometric structures, electronic properties and magnetic configurations, in which they are mainly investigated by using the first-principles calculations. Monolayer and bilayer GNRs, curved GNRs, carbon nanotubes, folded GNRs, carbon nanoscrolls, adatom-

passivated GNRs, and alkali-, halogen-, and (Al,Bi,Ti)-doped GNRs are taken into account. We propose the physical and chemical pictures to fully comprehend the rich and unique phenomena. The single- and multi-orbital hybridizations between the same or distinct atoms, and the edge- and adatom-enriched spin configurations are thoroughly analyzed from the calculation results. The detailed comparisons with the other theoretical predictions and the experimental measurements are made. The high potentials in various materials applications are also discussed.

Graphene nanoribbons, with one-dimensional quantum confinement effects, can greatly diversify the essential properties, shedding the light on potential applications in nanodevices, and thus attracting numerous theoretical studies. Monolayer graphene is a zero-gap semiconductor with zero density of states (DOS) at the Fermi level, and the other layered graphenes are semi-metals because of the interlayer atomic interactions. It should be noticed that the vanishing energy gaps have induced high barriers in certain important applications. However, electronic and magnetic properties of graphene nanoribbons are strongly affected the ribbon widths,⁴⁰ crystallographic orientations,⁴¹ and edge saturations.⁴² Energy gaps, which are created by the finite-size effects, are confirmed in both armchair and zigzag GNRs. That is, they are identified to be very sensitive to the change in edge structure. In addition to the parabolic energy bands, a pair of partially flat valence and conduction bands crossing the Fermi level is predicted to only exist in zigzag nanoribbons. The tunable electronic properties further have stirred a lot of researches on magnetic properties,^{43,44} optical excitations,^{45,46} and transport properties.^{47,48} Experimentally, the width dependent energy gaps are verified by the measurements of electrical conductance.⁶ The atomic structures, 1D parabolic energy dispersions, and low-lying asymmetric/symmetric peaks of density of states are verified by STM,⁴⁹ angle-resolved photoemission spectroscopy (ARPES),⁵⁰ and scanning tunneling spectroscopy (STS),⁵¹ respectively. On the application side, GNRs have been explored to utilized in semiconductor industry, environmental engineering, and biochemistry. GNRs with width below 10 nm can serve as field-effect transistors (FETs) at

room temperature.^{5,14} GNR arrays down to 5 nm width creates an exceptional NO_2 sensing performance.⁵² A GNR transistor integrated with solid-state nanopore becomes a sensor for DNA translocation.⁵³ How many kinds of energy gaps with/without edge passivations and their origination are the core topics of this systematic study.

The changes in geometric structures of pristine graphene nanoribbons can modify and enrich the essential properties. The curved systems are directly synthesized from the cylindrical carbon nanotubes using the physical and chemical methods.¹⁹⁻³³ The unzipping of multi-walled carbon nanotubes offers an efficient way in producing graphene nanoribbons with the controlled structure and quality. The unzipped and zipped graphene structures have been observed under the measurements of atomic force microscopy (AFM), TEM, and scanning electron microscopy (SEM). The curved surfaces and dangling bonds are an ideal chemical environment for modulating the geometric structure and electronic properties. A planar graphene nanoribbon presents a typical sp^2 bonding, being determined by the π bonding of the parallel $2p_z$ orbitals and the σ bonding of the in-plane ($2s, 2p_x, 2p_y$) orbitals. On the other hand, a perfect cylindrical surface in a carbon nanotube can create the coexistent sp^2 and sp^3 hybridizations, as verified by the theoretical calculations^{54,55} and the experimental measurements.⁵⁶ Apparently, graphene nanoribbons and carbon nanotubes sharply contrast with each other in the curvature and boundary condition, and so do the other essential properties. A cylindrical system has a periodical boundary conduction along the azimuthal direction, so that the angular momenta serve as a good quantum number in addition to the axial wave vector. The transferred longitudinal momentum and transverse angular momentum are conserved in various scattering mechanisms, e.g., optical excitations⁵⁷⁻⁵⁹ and Coulomb interactions.⁶⁰⁻⁶² However, an open boundary condition in a finite-width nanoribbon cannot create the transverse quantum number, leading to the absence of its conservation law in the excitation processes.⁶³⁻⁶⁶ These two critical factors, being responsible for the essential properties of the curved systems, are explored in detail, such as, the effects on the ground state energy, the effective interaction distance, the bond length, orbital hybridization,

the dominance of edge carbon atoms, and the semi-conducting/metallic behavior.

The folding of a honeycomb lattice may induce new and distinct properties in graphene-related systems. The folded graphene nanoribbons have been produced in experimental laboratories,^{5,67-70} being confirmed from the direct mapping of the open and closed edges using the high-resolution TEM (HRTEM). The transport measurements show that they could act as the high-performance FETs⁵ and electrode materials,⁷¹ Each unique geometric structure is composed of a chiral/non-chiral open boundary, a bilayer-like graphene, and a half carbon nanotube; that is, it consists of three distinct carbon honeycomb regions. For example, two zigzag/armchair graphene nanoribbons are connected by a fraction of armchair/zigzag carbon nanotube, in which the former are stacked in the manner of AA, AB or other configurations. The folded systems can provide the rich physical and chemical environments in term of edge structure, finite size, curvature and orbital bonding. They are predicted to exhibit the unusual phenomena, such as, the magnetic quantization of the highly-degenerate Landau levels,^{72,73} the semiconductor-metal transition under the structural transformation,⁷¹ the complex width dependences of energy gaps, and the diverse spin configurations. The multi-combined effects, which arise from the quantum confinement, the spin arrangement near the specific edges, the edge-edge interactions, the van der Waals interactions between two planes, and the mechanical bending of a curved surface, will play critical roles in the optimal geometries, electronic properties, and magnetic configurations. This is worthy of a systematic investigation by the first-principles calculations.

Carbon nanoscrolls, with the spiral cross sections, were first reported by Bacon in 1960 using the arc-discharge of graphite.⁷⁴ The distinct synthesis methods are further developed to fabricate the high-quality carbon nanoscrolls more efficiently.⁷⁵⁻⁸⁰ They present the tube-like structures under the disclosed surfaces. Each nanoscroll is an open-ended spirally wrapped graphene nanoribbon. The main features cover the inner and outer edges, the non-uniform curved surfaces, and the multi-walled structures with the tunable interlayer distances. The formation and structure stability could be simulated by the molecular dynamics method.⁸¹

As a result of the unusual structures, the essential properties are easily modulated by the chemical doings, the external fields and the mechanical strains. Carbon nanoscrolls are expected to have high potentials in applications, such as, hydrogen storages,⁸² electromechanical nanoactuators.⁸³ FETs, and microcircuit interconnect components,⁸⁰ The first-principles calculations on energy bands shows the strong dependence on edge structure and ribbon width,^{84,85} as revealed in planar systems. However, the optimal structures, the multi-orbital hybridizations and the spin arrangements need to be taken into consideration to fully understand the unusual geometric, electronic and magnetic properties, e.g., the critical configuration parameters, the diverse width dependences of energy gaps and the specific spin configurations (Chap. 6). Apparently, the structure-induced combined effects are quite different from among the scrolled, folded, curved and planar graphene nanoribbons. This means that the geometric structures will result in the diverse essential properties.

Few-layer graphene nanoribbons are frequently produced in the various experimental syntheses.^{5,13,19,22,35} The stacking symmetries of layered systems play critical roles in diversifying the essential properties, being confirmed from many theoretical⁸⁶⁻⁹¹ and experimental⁹²⁻¹⁰⁰ studies on 2D few-layer graphenes. For example, the trilayer graphenes, with AAA, ABA, ABC and AAB stackings, present the linear, parabolic, sombrero-shape and oscillatory for the first pair of energy bands measured from the Fermi level. The dramatic transitions will come to exist by modulating the stacking configurations between two layers, such as, the metal-semiconductor transition and the generation/destruction of magnetism.¹⁰¹ The shift-dependent variation of stacking symmetries could be achieved by the electrostatic manipulation of STM, as done for graphene-related systems.¹⁰²⁻¹⁰⁵ Specifically, bilayer zigzag graphene nanoribbon could serve as a model system in revealing the combined effects due to the edge-edge interactions, the stacking configurations, and the intralayer and interlayer spin arrangements. The previous theoretical calculations on typical AA and AB stackings predict the planar/non-planar profiles and the magnetic/non-magnetic configurations.¹⁰⁶⁻¹⁰⁹ More complete calculated results are required to clearly identify the stacking-induced diverse

behaviors. The shift-dependent optimal geometries, relatively stable stacking configurations, magnetic moments, spin distributions, spin degeneracies, low-lying energy dispersions, band gaps/free carrier densities, spatial charge densities near two open edges, van Hove singularities are worthy of further detailed examinations. Furthermore, the theoretical studies on the sliding bilayer graphene can fully understand the confinement-induced effects and the dimension crossover.

How to dramatically change the essential properties is one of the main-stream topics in materials science and application. The chemical functionalization is one of the most effective ways. Pristine graphene nanoribbons, without passivation, possess a honeycomb lattice and two open edges, provide a reactive chemical environment. The intrinsic dangling bonds associated with edge carbon atoms are highly unstable, so that the dopants could be applied to passivate the active boundary. The dopant-created chemical bonding will play a critical role in determining the most stable configuration and thus other essential properties. Up to now, the H-,¹¹⁰ Cl-,¹¹¹ and O-terminated¹⁹ graphene nanoribbons have been produced by chemical synthesis methods, being examined by the measurements of STM, X-ray diffraction and XPS. The first and the second adatom-decorated systems are, respectively, identified to present the planar and distorted edge structures with an open boundary. According to the theoretical calculations, the active edges tend to adsorb atoms,^{112–123} molecules^{124–126} or radical groups.^{124,125} The predicted decoration effects cover the edge reconstructions, the adatom-dominated energy bands, the greatly reduced energy gaps, and the semiconductor-metal transitions. They are closely related to the strong competitions between the edge passivation and the finite-size confinement. How many types of edge structures and width-dependent energy gaps needs to be thoroughly clarified from the detailed calculations and discussions. Specially, the adatom/molecule decorations might happen during the unzipping of carbon nanotubes through the strong chemical reactions. The edge passivation and curvature are expected to have strong effects on the geometric, electronic and magnetic properties,¹²⁷ such as, the adatom- and curvature-dominatedt planar/curved/tubular structures, the metal-

lic/semiconducting behaviors, and the anti-ferromagnetic/ferromagnetic/non-magnetic configurations.

Adatom adsorptions on honeycomb surfaces can greatly modify the essential properties of graphene nanoribbons. Alkali, halogen and metal atoms (Chaps. 9-11), which possess the unique chemical and physical features, are very suitable for exploring the adsorption-induced dramatic changes, e.g., the semiconductor-metal transition, the n- or p-type doping (the creation of free electrons or holes), and the transformation between different spin arrangements. Up to now, alkali atoms have been successfully synthesized in carbon-related systems, such as, graphite,¹²⁸ fullerene,¹²⁹ carbon nanotube,¹³⁰ and graphene.¹³¹ The alkali-doped systems are verified to present the metallic behavior, a result of the high-density conduction electrons. They have displayed highly potential applications, e.g., the Li-ion batteries based on graphene,¹³² There are a lot of theoretical studies on the n-type doping effects.^{133,134} The alkali-adsorbed graphene and graphene nanoribbon are predicted to exhibit the blue-shift Fermi level.¹³⁵ The former is confirmed by the ARPES measurements.¹³⁶ It is well known that each alkali atom has one very active s-orbital, leading to the significant chemical bonding with carbon atom. The critical orbital hybridization, which is determined from the delicate energy bands, spatial charge distribution and DOS (discussed later in Sec. 2.1), is expected to dominate the diversified electronic properties and magnetic configurations. How many conduction electrons due to the outmost s-orbitals and how to tune spin magnetism are the main focuses under systematic investigations.

Halogen atoms are very good candidates for chemical modifications, mainly owing to the rather strong electron affinities. They have five electrons in the outmost (p_x, p_y, p_z) orbitals; furthermore, the adatom-induced spin states might come to exist after chemical adsorptions. The halogenated graphene nanoribbons are expected to exhibit the complicated orbital hybridizations in chemical bonds and the adatom- and edge-C-created magnetic configurations. The diverse electronic and magnetic properties will be revealed in the variations of concentrations, distributions and edge structures. How to identify the charge- and spin-dependent

mechanisms is a critical issue and needs to be examined from the various physical quantities. Recently, there are a lot of experimental¹³⁷⁻¹³⁹ and theoretical¹⁴⁰ studies on the halogenation effects of graphene-related systems. Fluorinated,¹³⁸ chlorinated,¹³⁹ brominated¹⁴¹ and iodinated¹⁴² graphene systems have been successfully synthesized by the various chemical methods. The important differences between fluorinated and other halogenated graphene systems in the semiconducting or metallic behavior are confirmed from the transport,¹⁴³ optical,¹⁴⁴ and ARPES measurements.¹⁴⁵ However, only very few studies are conducted on 1D halogenated graphene nanoribbons. The theoretical calculations predict the very strong fluorination effects, such as, the multi-orbital hybridizations in F-C, C-C and F-F bonds, the irregular relations between energy gaps (valence hole densities) and adatom-adsorption cases, and five kinds of electronic and magnetic properties.¹⁴⁶ All the halogenation effects arising from the distinct kinds of adatoms are included in this work, especially for the adsorption conditions/mechanisms in determining the feature-rich energy bands, free carrier densities, magnetic/NM configurations, and significant differences of the F-C and (Cl,Br,I,At)-C bonds.

A thorough and systematic study is conducted on the essential properties of the structure-enriched and adatom-doped graphene nanoribbons. It covers a lot of critical mechanisms, lattice symmetries, boundary conditions, quantum confinements, edge structures, stacking-dependent interlayer interactions, curvature effects, edge-edge interactions, distributions and concentrations of adatoms, charge transfers, orbital hybridizations, magnetic environments, and adatom-created moments/spin configurations. The optimal geometric structures are related to the most/relatively stable configurations, various non-planar profiles, interlayer and edge-edge distances, stacking configurations, critical curvatures, minimum widths/inner diameters, saturated nanotube diameters, bond lengths, bond angles; positions and heights of adatoms. Energy bands are characterized by the dominances of carbon, adatom and (carbon,adatom), linear, parabolic, partial flat and oscillatory energy dispersions, symmetry or asymmetry about the Fermi level, energy gaps due to the combined effects, free electron/hole densities, state degeneracy, and spin-related splitting. The 1D critical points in

energy bands reveal as the special van Hove singularities, including plateaus, asymmetric peaks, and symmetric peaks. Specifically, the delicate atom- and orbital-projected DOSs, the atom-dominated energy bands and the spatial charge densities, provide much information about the dominating chemical bondings. They could be used to identify the orbital hybridizations in C-C, C-X and X-X bonds (X adatom). Furthermore, the magnetic configurations, the ferro-magnetic, anti-ferro-magnetic and non-magnetic ones (FM, AFM and NM) are examined from the net magnetic moment, the spin-dependent energy bands, the spatial spin distribution and the spin-decomposed DOSs. According to the rich and unique essential properties, materials functionalities and potential applications are further discussed. Also made are the consistence of theoretical calculations and experimental measurements and the required examinations.

This book is organized as follows. Chapter 2 includes the details of computational methods and experimental tools, as well as their important progresses achieved recently. The geometric, electronic and magnetic properties are studied for monolayer systems in Chap. 3, especially for the finite-size and boundary effects. Chapter 4 focuses on the zipped/unzipped variations of curved systems, in which the critical arc angles, the edge-induced chemical bondings and energy bands, and the semiconductor-metal transitions are explored thoroughly. A detailed comparison is made between curved nanoribbons and carbon nanotubes. In Chap. 5, eight typical types of high-symmetry folded graphene nanoribbons are suitable for studying the bilayer- and tube-like composite structures, the unusual low-lying energy dispersions, the semiconductor-metal transitions, the diversified width dependences of band gaps, and the distinct magnetic environments, being based on the complex combined effects. How to sustain a stable carbon nanoscroll with an optimal spiral profile is discussed in Chap. 6, especial for the sufficiently large ribbon width and inner diameter. The edge-, width-, and spin-created diverse properties are investigated. Furthermore, the important differences among the planar, curved, folded and scrolled graphene nanoribbons are fully clarified. Chapter 7 presents the dramatic transformations of the essential properties in

bilayer zigzag graphene nanoribbon by the relative displacement between two layers. Also done is for sliding bilayer graphene to illustrate the dimension-dominated behaviors. How to modify the boundary structure by the chemical edge passivation is the focus of Chap. 8. The decoration and curvature effects are examined for a lot of symmetric configurations and various adatoms to explore the diversified essential properties, especially for the types of geometric structures and the metallic/semiconducting behaviors.

The surface adatom adsorptions are investigated for graphene nanoribbons with hydrogen edge passivation. In which the critical chemical bondings and the adatom-induced spin states are proposed to explain the diversified properties. Chapter 9 explores the alkalization effects on the geometric, electronic and magnetic properties. Whether there exists a specific relation between the alkali concentration and the 1D conduction electron density is examined for any absorption configurations. Furthermore, the spin arrangements at zigzag edges are delicately tuned by changing the position and concentration of alkali adatoms. The fluorination and chlorination-related effects are investigated in Chap. 10, especially for the significant mechanisms. The focus is how to achieve the planar/buckled honeycomb structure, the high/low binding energy, the destruction/existence of the π -electronic band structure, the halogen-dependent energy bands, and the metallic or semi-conducting behavior through the multi-/single-orbital hybridizations in X-C bonds. Furthermore, the adsorption-dominated spin configuration and their strong competition with the zigzag-edge one are expected to create the different types of magnetic configurations. Chapter 11 thoroughly discusses the main features of the Al-, Ti- and Bi-adsorbed graphene nanoribbons and the significant differences among such systems. It includes the complicated orbital hybridizations arising from the distinct (s,p,d) orbitals, the metal-dominated low-lying conduction and valence bands, the adatom-induced free electron densities, and the adatom-dependent spin distributions. Finally, Chap. 12 includes concluding remarks and future studies.

2. The first-principles method and experimental instruments

The details of numerical evaluations and experimental measurements are discussed in the following two sections.

2.1 Theoretical calculations

A typical condensed-matter crystal consists of a periodic atomic arrangement, in which each atom might have several valence electrons distributed around an ionic core. Any system presents the complicated many-body effects due to the electron-electron Coulomb interactions and the electron-ion crystal potential. Apparently, it is rather difficult to accurately deal with the many-particle Schrodinger equation. The evaluation difficulties will be greatly enhanced when the unusual geometric structures and the strong chemical adsorptions need to be taken into consideration,. e.g., the folded/scrolls and adatom-doped graphene nanoribbons. Some approximation methods have been developed to obtain the reliable electronic states. Up to now, the first-principles calculations become a dominant method in getting the quantum states of periodic systems. Such numerical calculations are very efficient for studying the essential physical properties. Specifically, Vienna *ab initio* simulation package (VASP)¹⁴⁷ evaluates an approximate solution within the density functional theory by solving the Kohn-Sham equations.¹⁴⁸ Electron charge density is responsible for all the interactions of a periodic condensed-matter system; that is, it can determine the ground state energy and the essential properties. The spatial charge density will be solved by the numerical self-consistent scheme, as indicated in a flow chart of calculation (Fig. 1). Compared to this numerical method, the tight-binding model, with the atomic interaction parameters, cannot not be utilized to investigate the optimal geometric structures and the complicated orbital hybridizations in various chemical bonds. However, this model is efficient in studying the essential properties under the external fields, e.g., the quantized Landau lev-

els,^{63,149–152} magneto-optical excitations,^{153–155} magnetoplasmons,^{156,157} and Hall quantum transports.^{158,159}

The geometric structures, electronic properties and magnetic configurations are thoroughly studied for 1D GNR-related systems using VASP.¹⁴⁷ The spin-polarized density functional theory is used to realize the magnetic configurations arising from the edge structures and adatom adsorptions.¹⁶⁰ The Perdew-Burke-Ernzerhof functionals under the generalized gradient approximation can characterize the many-body Coulomb interactions, the exchange and correlation energies.¹⁶⁰ The projector-augmented wave pseudopotentials account for the electron-ion interactions.¹⁶¹ In solving the many-particle Schrodinger equation, plane waves, with an maximum energy cutoff of 400 eV, are the bases in building the Bloch wave functions. The 1D periodic boundary condition is along \hat{x} , and the vacuum spacing associated with \hat{y} and \hat{z} is larger than 15 Å to avoid the interactions between two neighboring nanoribbons. The Brillouin zone is sampled by $15 \times 1 \times 1$ and $600 \times 1 \times 1$ k point meshes within the Monkhorst-Pack scheme for geometric optimizations and further calculations on electronic structures, respectively. The convergence of energy is set to be 10^{-5} eV between two simulation steps, and the maximum Hellmann-Feynman force acting on each atom is less than 0.01 eV/Å during the ionic relaxations. Specifically, to correctly describe the significant atomic interactions between two neighboring graphene nanoribbons, the van der Waals force is included in the calculations by the semi-empirical DFT-D2 correction of Grimme.¹⁶²

For the structure-enriched and adatom-doped GNRs, the theoretical calculations cover the ground state energy, binding energy, interlayer distance, bond length, bond angle, planar/curved/buckled/scrolled/folded/stacked honeycomb lattice, hexagonal/non-hexagonal edge decoration, position and height of adatom, atom-dependent band structure, adatom-induced carrier density and energy gap, spatial charge distribution, spin arrangement, magnetic moment, and orbital- and spin-projected DOSs. The detailed analyses on the calculated results can get the concise physical and chemical pictures and thus fully comprehend the cooperative/competitive relations among the honeycomb lattice, the finite-size quantum

confinement, the edge structure, the interlayer atomic interaction, the non-planar curvature effect, and the critical orbital hybridizations in carbon-adatom bonds, and the spin configurations. Whether there exist the diverse electronic properties (semiconductors or metals) and magnetic configurations (non-magnetism, ferromagnetism or anti-ferromagnetism) is explored thoroughly. The theoretical predictions are compared with the up-to-date experimental measurements, especially for those from ARPES, STM and STS. The complete and reliable results are very useful in the development of potential applications. Moreover, the first-principles calculations are available to determine the important hopping integrals (atomic interactions; the important parameters) in the tight-binding model.¹⁶³

The critical orbitals of carbons and adatoms are fully considered in the numerical calculations. The single- or multi-orbital hybridizations in chemical bondings, which dominate the feature-rich essential properties, are clearly identified from the atom dominance of energy band, the orbital-dependent charge distribution, and the orbital-projected DOSs. For pristine graphene nanoribbons, they can comprehend the dramatic changes of chemical bondings on the non-planar surfaces, e.g., the curvature effects related to the misorientation of $2p_z$ orbitals and the sp^3 hybridization of $(2s, 2p_x, 2p_y, 2p_z)$ orbitals.¹⁶⁴ Moreover, there exist the rich and unique orbital hybridizations in the various X-C and X-X bonds. They are responsible for the optimal geometric structure, the unusual electronic properties, and even diversify the magnetic configurations. As to the edge-carbon- and/or adatom-induced spin states, they are thoroughly examined from the magnetic moment, the atom-dominated spin degeneracy, the spatial spin distribution, and the spin-decomposed DOSs, being sensitive to the edge structures, the non-planar structures, the stacking configurations, the edge decoration, the kind of adsorption atoms, the strength of X-C and X-X bonds, and the distribution and concentration of adatoms. In short, both orbital hybridizations and spin distributions will play critical roles in creating the diverse electronic properties and magnetic configurations, the FM/AFM/NM metals and semiconductors. The developed theoretical framework is very useful in the further studies on the emergent 1D and 2D materials, such as, the essential

properties of silicene-, germanene-, tinene-, and phosphorene-related systems.

2.2 Experimental instruments

Experimental measurements can directly identify the main characteristics of the essential properties; furthermore, the detailed comparisons with the theoretical predictions will provide the concise physical and chemical pictures to establish the basic concepts. Four main instruments throughout this work are TEM, STM, STS and ARPES, in which the latter three also cover the spin-polarized measurements. They are very powerful in determining lattice symmetry, bond lengths, stacking configurations, spin distribution, local nanostructures, adatom positions, van Hove singularities (special structures) in DOS, spin-split states, energy dispersions of valence bands, band-edge states, and energy gap. A brief introduction to each characterization tool and the recent experimental progress are presented as follows.

Transmission electron microscopy is a microscopy technique in which an electron beam with a uniform current density is transmitted through an ultra thin specimen to form an image, owing to the interactions between incident charges and sample. The TEM was first demonstrated by Ernst Ruska and Max Knoll in 1931. Ruska was later awarded the Nobel Prize in physics for the development of TEM. TEMs can achieve a higher resolution than light microscopes, as a result of the smaller de Broglie wavelength of electrons. A TEM instrument, as shown in Fig. 1, consists of an electron source, the first and second condenser lenses with aperture, specimen, an objective lens with aperture, intermediate and projector lenses, and a fluorescent screen. A set of condenser lenses helps to focus the beam on the sample. And then, an objective lens collects all the electrons after interactions, form image of the sample and determines the limit of structure resolution. Moreover, a set of intermediate lenses that magnifies this image and projects it on a fluorescent screen, a layer of photographic film, or a sensor. Compared to other microscopes, the main advantage of TEM measurements is to simultaneously provide accurate informations in the real space (from the imaging mode) and reciprocal space (from the diffraction mode). The de Broglie wavelength of electrons of TEM

is much smaller than atomic separations in the solids; therefore, it is achievable to observe crystal details below the atomic sizes. The resolution for TEM measurements is about 1-2 Å.¹⁶⁵

TEM is the powerful experimental technique for directly visualizing the crystal structure, locating and identifying the type of defects, and studying structural phase transitions. It has a very strong electrons' atomic scattering factor, being ~ 10000 times of that from the X-ray diffraction. This provides electron diffraction an advantage to detect even the weakest diffracted spot. However, the resolution of TEM is limited by spherical and chromatic aberrations of the lenses. More delicate techniques for improving the diffraction resolution become indispensable. By applying a monochromator and a Cs corrector into TEM, which is called high resolution TEM (HRTEM), the structural resolution can reach less than 0.5 Å.¹⁶⁶ HRTEM has been successfully and extensively used for analyzing crystal structures and lattice imperfections in various kinds of nanomaterials.^{167,168} The TEM/HRTEM measurements on graphene-related systems are very suitable in identifying the various nano-scaled geometric structures, such as the multi-walled cylindrical structures of carbon nanotubes,^{7,19} the curved,¹⁹⁻²¹ folded^{67,68} and scrolled⁷⁶⁻⁷⁸ profiles of graphene nanoribbons, as well as the stacking configurations and the interlayer distances of graphenes.^{34,169,170}

STM has become the most important experimental technique in resolving the surface structure since the first invention by Binnig and Rohrer in 1982.^{171,172} This instrument is able to image the topographies of surfaces in real space with both lateral and vertical atomic resolution, such as the nanoscale bond lengths, crystal orientations, planar/non-planar structures, step edges, local vacancies, dislocations, adsorbed adatoms/molecules, and clusters/islands. The STM instrument, as shown Fig. 2, consists of a conducting (semi-conducting) solid surface and a sharp metal tip, in which the distance of several angstroms is modulated by piezoelectric feedback devices. A weak current is built by the quantum tunneling effect in the presence of a bias voltage between surface and tip. It has a strong relation with distance, being assumed to present the exponential decay form. This current

flows from the occupied electronic states of tip into the unoccupied ones of surface under the positive bias voltage $V > 0$, or vice versa. In general, the quantum tunneling current is chosen to serve as a feedback signal. The most commonly used mode, a constant tunneling one (current and voltage), will be operated to resolve surface structure very accurately by applying a piezoelectric device. By combining a probe of metal tip and a precise scanning device, the full spectroscopic information of surface morphology is obtained at the preselected positions under the well-defined conditions. The structural response is hardly affected by the background effects, being attributes to an ultra-high vacuum environment. Up to now, the spatial resolution of STM measurements can reach 0.1 Å. In addition to STM, other experimental techniques are available in characterizing the geometric properties of low-dimensional systems, covering transmission electron microscopy (TEM),^{36,173} scanning transmission electron microscope (STEM),³⁴ atomic force microscopy (AFM)¹⁷⁴ and low-energy electron diffraction (LEED).¹⁷⁵ It should be noticed that STM is very sensitive to electron spin by using a ferromagnetic/antiferromagnetic probe tip. This spin-dependent spectroscopic mode is first proposed by Pierce in 1988 and realized by Wiesendanger et al. in 1990.^{176,177} The up-to-date spin-polarized STM (SP-STM) can provide detailed information of magnetic phenomena with atomic resolution, such as spin polarizations of individual adatoms on magnetic surfaces,¹⁷⁸ and domain structures of magnetic elements.^{179,180}

STM is a powerful experimental technique in revealing the spatially atomic distributions with the nanoscale precisions. The very accurate measurements on the carbon-related systems have confirmed the rich and unique geometric structures, illustrating the complex relations among the hexagonal lattice, the finite-size confinement, the flexible feature, and the diverse chemical bondings of carbon atoms. From the up-to-date STS observations, graphene nanoribbons present the nanoscale-width planar honeycomb lattice, accompanied with the non-chiral (armchair and zigzag) and chiral edge structures.^{50,181,182} Furthermore, they could also be formed in the curved,¹⁸¹ folded,⁵ scrolled⁷⁶ and stacked lattice structures.¹⁸³ Carbon nanotubes possess the achiral and chiral arrangements of the hexagons on

cylindrical surfaces.^{184,185} The atomic-scale measurements directly identify the AB, ABC and AAB stacking configurations of few-layer graphenes,^{170,186} the corrugated substrate and buffer graphene layer,^{187,188} the rippled structures of graphene islands,^{189–191} the adatom distributions on graphene surfaces.^{192,193} The layered graphite could exhibit the 2D networks of local defects on surface;¹⁹⁴ the pyridinic-nitrogen and graphitic-N structures.¹⁹⁵ In addition, the folded graphene nanoribbons are also confirmed by high-resolution TEM measurements.⁵

STS, as shown in Fig. 3, is an extension of STM by using more delicate operations and detailed analyses in the absence of feedback. This instrument is able to characterize the energy-dependent density of electronic states in condensed-matter systems, based on the relation between current and bias voltage. The I-V curves are obtained from a probing tip being fixed at the same height and scanning on a surface. They are closely related to the information of surface electronic states, when the tunneling current is assumed to be proportional to the constant states of a probing tip. The normalized differential conductance of the tip-surface tunneling junction is defined as $(dI/dV)/(I/V)$, being interpreted as the DOS of surface structure. For example, as to 1D graphene nanoribbon/carbon nanotube, its relation with bias voltage corresponds to the energy dependence of DOS. In the STS measurements, the normalized differential conductance, being created by a small AC modulation of dV , can be examined by using a lock-in amplifier. Furthermore, the noise involved in the measured conductance will be greatly reduced. The up-to-date experiments can achieve the highest resolution of ~ 10 pA. STS is available in the identification of the spin-split DOS, when the magnetic tips are utilized in the experimental observations. The spin-polarized STS (SP-STS) is very important in understanding the magneto-electronic properties, e.g., the metallic ferromagnetism and the semi-conducting anti-ferromagnetism.¹⁹⁶ Specially, STM and STS could be operated on the same sample to characterize the geometric and electronic properties simultaneously, such as the edge orientations and the width-dependent energy gaps of graphene nanoribbons.^{182,184,185,197–199}

The STS measurements can efficiently examine the van Hove singularities due to the

band-edge states and the semiconducting/semi-metallic/metallic behavior, since the tunneling conductance directly corresponds to DOS. They have successfully verified the diverse electronic properties in graphene nanoribbons,^{197–199} carbon nanotubes,^{184,185} few-layer graphenes,^{105,200–205} adatom-adsorbed graphenes,^{187,188,206} and graphite,^{207,208} as measured from the energy, number, intensity and form of special structures in DOSs. As for graphene nanoribbons, the width- and edge-dominated energy gaps and the asymmetric peaks of 1D parabolic bands are identified from the precisely defined crystal structures.^{182,184,185,197–199} The similar strong peaks are revealed in carbon nanotubes, in which they present the chirality- and radius-dependent band gaps and energy spacings between two neighboring subbands.^{184,185} Specifically, armchair nanotubes belong to the 1D metallic systems with a finite DOS at the Fermi level. A lot of STS measurements conducted on few-layer and adatom-doped graphenes clearly show the low-lying DOS characteristics, covering a linear E-dependence vanishing at the Dirac point in monolayer system,²⁰⁸ the asymmetry-created peak structures in bilayer graphene,^{200–202} an electric-field-induced gap in bilayer AB stacking and tri-layer ABC stacking,^{203,204} a prominent peak at E_F due to the partial flat bands in tri-layer and penta-layer ABC stacking,^{184,185} a dip structure at E_F accompanied with a pair of asymmetric peaks in tri-layer AAB stacking,¹⁸⁴ and a red shift of Dirac point arising from the metallic doping of Bi adatoms.^{187,188} The measured DOS of AB-stacked (Bernal) graphite is finite near the Fermi level characteristic of the semi-metallic property²⁰⁸ and presents the splitting π and π^* strong peaks at deeper/higher energy.²⁰⁷

ARPES is best for studying the quasi-particle energies of the occupied electronic states solids in the Brillouin zone,²⁰⁹ and such dispersion relations can directly examine the first-principles calculations. The ARPES chamber is accompanied with the instrument of sample synthesis to measure the *in – situ* band structure. When a sample is illuminated by soft X-rays (Fig. 4), the occupied valence electrons are excited to the unoccupied intermediate states after a dipole transition. Photoelectrons are stimulated by incident photons and escape outside of the material into the vacuum, and then they are counted by an angle-resolved

energy analyzer. The total momenta of photoelectrons are evaluated from the free particle model, in which the parallel and perpendicular components are determined by the polar and azimuthal angles (θ and ϕ in Fig. 4). The former are conserved during the photoemission process, while the conservation law is not suitable for the latter due to the breaking of translation symmetry along the normal direction. In general, ARPES measurements are mainly focused on two- and quasi-two-dimensional systems with the negligible energy dispersions perpendicular to surface. However, the non-conservation issue might be overcome by the important characteristic of the k_z -dependent band structure, as done for the 3D π band of layered graphite using that at $k_z = 0$.¹⁰¹ Specifically, the ARPES measurements can provide energy widths of valence states, directly reflecting the many-body de-excitation effects due to the electron-electron and electron-phonon interactions.²¹⁰ Improvements in energy and momentum have become a critical factor for the investigation of low-dimensional materials. Up to now, the highest resolutions for energy and angular distributions are, respectively, ~ 1 meV and 0.1° in the UV regime.²¹¹ Specifically, the spin-split energy bands could be examined by using the magnetic material as ARPES detector, e.g, the spin-resolved energy dispersions in topological insulators,²¹² ferromagnetic/anti-ferromagnetic materials,²¹³ and superconductors.²¹²

The high-resolution ARPES is the only experimental instrument able to directly measure the wave-vector dependence of the occupied energy bands. The measured results have verified the feature-rich band structures for the carbon-related systems, as observed under the various dimensions,^{50,93-97} layer numbers,^{93,98-100} stacking configurations,⁹² substrates,^{93,94,98} and adatom/molecule adsorptions.^{136,214,215} Graphene nanoribbons are identified to possess 1D parabolic energy subbands centered at the high-symmetry point, accompanied with an energy gap and distinct energy spacings.⁵⁰ Recently, many ARPES measurements are conducted on few-layer graphenes, in which they have confirmed the linear Dirac cone in monolayer system,⁹³⁻⁹⁵ two pairs of parabolic bands in bilayer AB stacking,^{92,93} the coexisting linear and parabolic dispersions in symmetry-broken bilayer system,⁹⁹ the linear and parabolic

bands in tri-layer ABA stacking,^{93,98} the linear, partially flat and sombrero-shaped bands in tri-layer ABC stacking,⁹⁸ the substrate-induced large energy spacing between the π and π^* bands in bilayer AB stacking,^{93,98} the substrate-created oscillatory bands in few-layer ABC stacking;⁹³ the metal-semiconductor transition and the tunable low-lying energy bands after the molecule/adatom adsorptions on graphene surface,^{136,214,215} The AB-stacked graphite exhibits the 3D band structure,^{96,97} with the bilayer- and monolayer-like energy dispersions at $k_z = 0$ and 1, respectively, (K and H points in the 3D first Brillouin zone). Furthermore, there exists the strong trigonal warping effect around the KH axis, and a weakly dispersive band near the Fermi level attributed to the stepped surface with zigzag edge.

3. Monolayer graphene nanoribbons

The edge structure play critical roles in the essential properties of GNRs. Theoretical studies of GNRs have been extensively investigated using the tight-binding (TB) method and the ab initio density-functional theory method. In 1996, TB studies have shown that GNRs with armchair edges have band gaps corresponding to the ribbon width and those with zigzag edges are metallic.²¹⁶ An ab initio calculation confirmed the metallic property of zigzag GNR using the localdensity approximation.²¹⁷ However, recent ab initio study in 2006 have shown that both ideal ZGNRs and AGNRs have band gaps, and the former one induced by edge magnetization.^{40,43} The experimental measurements of energy gaps are agree with the calculated band gaps.⁴¹

The essential properties of graphene nanoribbons with and without hydrogen termination are worth a systematic investigation. The DFT can simulate the drastic changes after the hydrogenation. The ground state energies and crucial bond lengths of armchair and zigzag systems are evaluated, especially for the edge bonding configurations and critical interaction with edge atoms. The variation of the band structure and DOS with the ribbon width is detailed discussed. The unique features of energy band, such as tunable energy gap,

weak energy dispersions, and band-edge states are clearly presented. Such features are closely related to the effects of quantum confinement. The total and orbital-projected DOSs exhibit a lot of prominent peaks. These could be further verified by the STS measurements. The feature-rich graphene nanoribbons are expected to provide future applications in nano electronic,⁵ energy materials,²¹⁸ and spintronic devices.²¹⁹

3.1 Armchair systems

The geometric and electronic properties of pristine and hydrogen-passivated armchair graphene nanoribbons (AGNRs) are investigated for various widths. The widths of AGNRs, as shown in Figs. 1(a), are characterized by the number of dimers lines N_A along \hat{y} , in which the periodical length in a unit cell along \hat{x} is $I_c = 3b$ (b is the C-C bond length). For pristine systems, since the ribbon edge is not saturated with hydrogen atoms, the geometric reconstruction takes place. The C-C bond length at the edge is shorter as a result of the dangling bonds. Such feature is hardly changed by the variation of ribbon width. The unstable dangling bonds provide suitable environment to form C-H bondings. The hydrogen-passivated AGNRs exhibit strong C-H bond with 1.13 Å bond length, which is barely affected by different widths. Their edge C-C bonds is longer than the pristine systems, which can be understood by the charge distribution (discussed later).

The electronic properties of pristine AGNRs are mainly determined by the edge structure, dangling bonds, and quantum confinement effects. The unoccupied conduction bands are asymmetric to the occupied valence bands about the Fermi level ($E_F = 0$), as shown in Fig. 2(a) for the $N_A = 8$ armchair system. Most of energy bands exhibit the strong parabolic dispersions that belong to the extended states with wide spatial distributions. There exist four energy bands (large circles) with localized carrier distributions near the ribbon edges, in which the radius of each circle represents the contribution percentage from the edge atoms. The four bands mostly come from the dangling bonds. These edge-atom dominated conduction and valence bands are doubly degenerate near $k_x = 1$, and the valence ones

possess weak energy dispersions at about -2.2 eV. The conduction ones at $k_x = 1$ and the first valence band (counted from E_F) at $k_x = 0$, respectively, correspond to the lowest unoccupied state (LUS) and the highest occupied state (HOS). As a result, a $N_A = 8$ armchair ribbon possesses an indirect energy gap of $E_g = 0.6$ eV. As for AGNRs with different ribbon width, these features remain the same, including the asymmetric conduction and valence bands, edge-atom dominated bands, and the weak dispersions ones (Fig. 2(b), 2(c), and 2(d) for $N_A = 9$, $N_A = 10$, and $N_A = 11$). However, the other low-lying conduction bands are significantly changed. Specially, for the $N_A = 9$ system, first conduction band at $k_x = 0$ becomes LUS, and thus determine the narrower direct band gap of $E_g = 0.3$ eV.

The introduction of edge hydrogen atoms largely alter the electronic structures of AGNRs, as shown in Fig. 3(a)-3(d). The edge-atom dominated conduction bands and weak dispersive valence band are absent under various ribbon widths. The strong C-H bondings and the very low bound state energy of H atom are responsible for the drastic changes in low-lying bands. The edge C and H atoms make major contribution to valence band in the range of -3 eV -5 eV. The LUS and the HOS correspond to the first conduction and the first valence band (counted from E_F) at $k_x = 0$. Hence, all the H-passivated AGNRs belong to semiconductors with direct band gap. In general, the predicted energy gaps could be examined by the experimental measurements on band structure, DOS, optical spectra and transport conductance. The energy gaps are sensitive to the ribbon width, as indicated by Fig. 4 (a) and (b). The dependence of E_g on N_A can be sorted into three groups, $N_A = 3n$, $3n + 1$, and $3n + 2$. The largest energy gap occurs for $N_A = 3n + 1$, and the smallest one for $N_A = 3n$ at the same n value. Both pristine and H-passivated AGNRs present the similar features in energy gaps.

The carrier density (ρ) and the variation of carrier density ($\Delta\rho$) can provide very useful information on the orbital bondings and energy bands. The former directly reveals the bonding strength of C-C bonds at the center or the edge of ribbons, as illustrated in Figs. 4(c) and 4(d). All the C-C bonds possess the strong covalent σ bonds and the relatively

weak π bonds simultaneously (black and grey rectangles). Such bondings are enhanced for the edge C-C bonds in pristine systems, as shown by dark red region in Fig. 4(c). This is responsible for the shorten bond lengths and the energy range of edge-atom dominated bands. As for H-terminated ones, strong C-H bondings reveal by the red region between H and C atoms, while the edge C-C bonds are weakened (Fig. 4(d)). These features reflect the variation of bond lengths, and can be further analyzed by the variation of carrier density.

The $\Delta\rho$ is very useful in understanding the electron transfer and orbital bondings, as illustrated in Figs. 4(e) and 4(f). $\Delta\rho$ is obtained by subtracting the carrier density of an isolated carbon from that of a AGNRs. Carbon atoms contribute four valence electrons to create various chemical bondings, leading to the strong σ bondings of ($2s; 2p_x; 2p_y$) orbitals. Such bondings induce the increased charge density between two atoms (red part in Fig. 4(e)). The charge increment are much more at the ribbon edge (dark red), reflecting the strength of C-C triple bond. $\Delta\rho$ in H-passivated AGNRs present clear image of charge transportation from edge carbons to hydrogens (red part near H atoms). This also accounts for the vanished edge-atom dominated energy bands.

The DOS directly reflects the main characteristics of the band structures. The low-energy DOS, as shown in Fig. 5(a) for the $N_A = 8$ armchair system, displays many peaks derived from the 1D parabolic bands. Such asymmetric peaks are in the square-root divergent forms, corresponding to the parabolic dispersion bands. Most of the peaks arise from the $k_x = 0$ state of the conduction and valence bands. Specially, edge-atom dominated valence bands exhibit one prominent peaks at about -2.5 eV. The intensity of each peak is inversely proportional to the band curvature. This can explain why the weakly k_x -dependent bands possess such strong peaks. As for the wider ribbons (Fig. 5(b)-5(d)), the peak numbers are increase, while the other features remain almost the same. On the other hand, the H-passivated GNRs present significant difference in low-energy DOS. The peaks in between plus and minus 3.0 eV are purely come from $2p_z$ orbitals of carbon, as shown by $N_A = 8$ system in Fig. 5(e). The H atom contributions appear at deeper energy (< -3.0 eV), reflecting the

very low bound state energy of hydrogen. Similar characteristics also exhibit in the wider ribbons (Fig. 5(f)-5(h)). In addition, the $2p_x$ and $2p_y$ orbitals contribute to the DOS at < -3.0 eV, which resulting from the stronger σ bonding.

3.2 Zigzag systems

Zigzag nanoribbons belong to semiconductors in the presence of edge spin configurations. Their energy bands have strong dispersion relations, as shown in Fig. 7 for various ribbon width. The occupied valence bands are asymmetric to the unoccupied conduction bands about $E_F = 0$. A pair of partially flat bands reveal within ± 1.0 eV, which mainly comes from edge carbons, as indicated by the blue circles near $k_x = 1$. The HOS and LUS come to exist at about $k_x = 2/3$, which determines the direct energy gaps for zigzag systems. Such gap become smaller when the ribbon width increase. For the wider ribbon, the number of subband is increase, and appear at deeper energy (< -2.0 eV). Specially, there exists the edge atom dominated valence and conduction bands. The former has its bond width about 1.2 eV, and the latter is weakly dispersive band at about 1.0 eV. These phenomenons are vanished after hydrogen termination, as shown in Fig. 8. The edge carbon atoms and the H atoms contribute to the energy band at much deeper energy (< -3.0 eV), being similar to that of H-passivated armchair ribbons. All the H-terminated ribbon present a smaller band gap to the pristine ribbon under the same ribbon width.

The orbital bondings and related energy bands can be understand by the carrier density (ρ) and the variation of carrier density ($\Delta\rho$). The former directly illustrates the stronger bonding strength of edge C-C bonds, as shown in Figs. 9(a). Such enhanced bondings are similar to those in armchair systems, accounting for the shorten edge C-C bonds. H-terminated system has strong C-H bondings revealed by the red region between H and C atoms, but the edge C-C bonds are slightly weakened (Fig. 9(b)). The electron transfer during the self-consistent calculations is presented by the $\Delta\rho$, as indicated by Fig. 9(c) and 9(d). Electrons in pristine system transferred to the edge zigzag chains, which shown

by the dark red region. $\Delta\rho$ in H-passivated ZGNRs exhibit significant charge transfer to hydrogens (red region near H atoms), being the main reason for the vanished edge-atom dominated energy bands. The anti-ferromagnetic moments are shown by spatial distribution of the charge difference between two spin states in Fig. 9(e) and 9(f). The smaller red and blue region reflects that the hydrogen atoms suppress the edge magnetic moments. The magnetization per edge atom is $0.67 \mu_B$ and $0.15 \mu_B$, respectively, for the pristine and H-passivated systems.

The DOS directly reflects the special features of the band structures, as shown in Fig. 10. For the $N_Z = 10$ system, the low-energy DOS displays many peaks derived from the 1D parabolic bands (Fig. 10(a)). The most prominent peak at about 1.0 eV comes from the weak dispersion conduction bands, which mostly contributed by edge carbons (brown curve). Such atoms also dominate two peaks at -0.7 eV and -1.5 eV (arrows), originating from the edge atom dominated valence bands. As for the wider ribbons (Fig. 10(b)-10(d)), these main features hardly changed, but the peak numbers are increase due to the increasing subband. On the other side, the H-passivated ZGNRs present quite difference compositions in low-energy DOS. Such peaks are only come from $2p_z$ orbitals of all carbons, as shown by $N_Z = 10$ system in Fig. 10(e). The H atoms contribute to the DOS at < -3.0 eV, resulting from the H-atom dominated bands. These characteristics are also founded in the wider ribbons (Fig. 10(f)-10(h)). In short, the edge-atom dominated prominent peak can be a distinguishable features between the pristine and H-passivated systems, and may be useful for the measurement of the tunneling conductance.

4. Curved and Zipped graphene nanoribbons

A curved graphene ribbon corresponds to an unzipped carbon nanotube. The systematic studies have been made for the latter since the successful synthesis using the arc-discharge evaporation in 1991,⁷ such as synthesis,^{9,220-223} characterization,^{184,185,224-227} property²²⁸⁻²³³

and application.^{234–238} The former could be produced from the latter by the various physical and chemical processes,^{19–33} as discussed in introduction (page 2). The previous discussions clearly show that all the planar graphene nanoribbons exhibit the semiconducting behavior. On the other hand, the cylindrical carbon nanotubes are metals or direct-gap semiconductors sensitive to the chirality and radius. Metallic nanotubes are exclusively comprised of either armchair nanotubes or very small zigzag nanotubes with radii $< \sqrt{3}b$ (b is the C-C bond length).²³⁹ The theoretical calculations^{54,55} and experimental measurements⁵⁶ have confirmed the curvature effects, the misorientations of $2p_z$ orbitals and hybridizations of carbon four ($2s, 2p_x, 2p_y, 2p_z$) orbitals, on a cylindrical surface, leading to the geometry-dependent energy gaps. Apparently, for the theoretical calculations, the essential properties are expected to present the dramatic transformation during the unzipping process. For example, the quantized quasi-Landau levels and the magneto-optical selection rule could survive in curved graphene nanoribbons, while they are almost absent in cylindrical carbon nanotubes.^{63,240,241}

The essential properties of curved graphene nanoribbons without extra termination hydrogen atoms are elaborated. The first-principles calculations can simulate their dramatic changes during the unzipping process.²⁴² The curvature- and width-dependent ground state energies and bond lengths are evaluated, especially for the critical arc angle, critical interaction distance between two-side edge atoms, zipping energy, and unzipping energy. The variation of the band structure and DOS with the curvature is investigated thoroughly. The calculated results clearly indicate the unusual features of energy band, such as energy gap, energy dispersions, band-edge states, mixing bands, band overlap, and state degeneracy. The total and local DOSs exhibit a plenty of prominent asymmetric peaks in the inverse of the square-root form. The unzipped and zipped graphene nanoribbons are quite different from each other, mainly owing to the curvature effect and the open/periodical boundary condition. These could be directly verified by the STS measurements

4.1 Curved nanoribbons

A curved graphene ribbon, as shown in Fig. 1(a), could be regarded as a part of a cylindrical carbon nanotube. Its geometric structure is described by arc angle ϕ and curvature radius $R = W/\phi \times 180^\circ/\pi$. W is the nanoribbon width proportional to the number of armchair/zigzag lines along the transverse direction. ϕ can account for the nanoribbon curvature, and $\phi = 0^\circ$ and $\phi \neq 0^\circ$ correspond to flat and curved systems, respectively. As for $\phi = 360^\circ$, a $(N_A/2,0)$ zigzag carbon nanotube [a $(N_z/2,N_z/2)$ armchair carbon nanotube; details in the next section] is a rolled-up N_A armchair nanoribbon [a N_z zigzag nanoribbon] in the cylindrical form, where N_A is an even integer. W and ϕ will be modulated in the first-principles calculations to simulate the dramatic changes of the orbital hybridizations of carbon atoms on a curved surface.

In the absence of hydrogen passivation, the geometric reconstruction takes place at the ribbon edges. The C-C bond lengths of the edge atoms are much shorter than those of the central ones. Such dangling bonds are strongly dependent on the curvature. For example, a curved armchair ribbon of $N_A = 10$ presents a bond length of $\sim 1.24 \text{ \AA}$ for the neighboring dimer atoms at the edges within the range of $0^\circ \leq \phi \leq 330^\circ$, as shown in Fig. 1(b). However, in another range of $330^\circ < \phi \leq 360^\circ$, this bond length grows rapidly with the arc angle until it reaches around 1.41 \AA in a zipped surface. The drastic changes in the edge bond lengths clearly indicate the emergences of the significant orbital interactions between the two-side carbon atoms. This range of arc angle, which corresponds to the dramatic transformation of geometric structure, will reveal the critical chemical bondings in determining the transition of electronic properties.

The dependence of the total energy per atom (E_{tot}) on the arc angle is useful in understanding the strong competition between the mechanical strain and the interactions of two-side edge atoms. E_{tot} is very sensitive to ϕ , as shown for various curved armchair ribbons in Fig. 2(a). E_{tot} grows with the increasing ϕ , reaches a maximum value at the critical angle (ϕ_c), and then declines rapidly until $\phi = 2\pi$. All the curved systems exhibit the similar

ϕ -dependence, being categorized into two thoroughly distinct regions: (I) $\phi < \phi_c$ and (II) $\phi > \phi_c$. The total energy is closely related to the bending strain and the covalent bonding. The nanoribbon changes from a flat structure into a cylindrical one during the variation of ϕ from 0° to 360° . The enhanced surface curvature leads to the strain energy and thus the increase of the total energy. For $\phi < \phi_c$, the total energy due to the extra chemical bondings is negligible because of the too large distance between two-side edge atoms, in which it is well fitted by²⁴²

$$E_{tot}(\phi; N_y) \simeq \left[1.25 \times 10^{-6} \times \exp\left(\frac{-0.13}{N_A}\right) \right] \phi^2 + \left[\frac{4.9}{N_A} - 10.1 \right] \quad (1)$$

The first term in the total energy, defined as the strain energy, is inversely proportional to the square of curvature (the dashed curve in Fig. 2(a)). The similar relation is also revealed in various carbon nanotubes.²⁴³ On the other hand, the interaction distance is sufficiently short ($d < 3.4 \text{ \AA}$) to permit carbon atoms on either side of the armchair ribbon edges to interact with one another, when the arch angle is close to ϕ_c . The very strong edge-edge atomic interactions, which largely reduce the total energy, compete with the elastic strain to determine the critical angle. The extra orbital hybridizations play a dominating role at $\phi > \phi_c$. In general, zigzag carbon nanotubes have the lower ground state energies, compared with planar armchair nanoribbons with $N_A > 8$. The chemical bondings of carbon atoms in a cylindrical surface are able to suppress the non-negligible mechanical strain.

The physical properties, which are responsible for the zipping and unzipping of a graphene nanoribbon, is worthy of a detailed examination. The critical angle, corresponding to the maximum total energy, grows with the increase of ribbon width (black circles in Fig. 2(b)). and so does the critical interaction distance (red circles). The stronger chemical bondings between the two-side edge atoms are required to overcome the higher mechanical strain in a narrow curved system, leading to the proportional relationship between d_c/ϕ_c and N_y . As for the ϕ -dependent total energy (Fig. 2(a)), it can define the zipping and unzipping

energies in the structural changes. $E_z = E_{tot}(\phi_c) - E(0^\circ)$ accounts for the transformation from a flat nanoribbon into a nanotube, The zipping energy, as shown in Fig. 2(c) (black squares), presents a monotonous decrease with the increasing N_y , directly reflecting the width-dependent strain energy (Fig. 2(a)). Moreover, the unzipping energy, being required to scissor a closed nanotube longitudinally to become an open nanoribbon, is characterized as $E_{uz} = E_{tot}(\phi_c) - E_{tot}(2\pi)$ (red squares). Except for the very narrow systems, the zipping and unzipping energies have the similar width dependence, in which the former is higher than the latter.

The curved nanographene ribbons, as shown in Figs. 3(a)-3(h), exhibit a lot of features in band structures. The important characteristics cover the asymmetry of valence and conduction bands about $E_F = 0$, diverse energy dispersions, band-edge states, state degeneracy, direct or indirect gaps, and semiconductors or metals, being sensitive to the arc angle. For a flat $N_y = 10$ armchair systems (details in Section 3.1), there are few edge-atom-dominated valence and conduction bands (EAVBs and EVCBs), with weakly dispersive relations (the dotted curves in Fig. 3(a)). An indirect gap of 1 eV is determined by the $k_x = 1$ state of EACBs and the $k_x = 0$ state of the first valence band (V_1 measured from E_F). Most of the low-lying energy bands mainly arise from the hybridizations of $2p_z$ orbitals (the π bonds at $\phi = 0^\circ$). However, the $2p_y$ orbitals (the σ bonds) make significant contributions to the third conduction band (C_3), the fourth valence band (V_4), and the EAVBs and EVCBs. It is also noted that the $2p_z$ ($2p_y/2p_x$) orbitals on a curved structure can create the π and σ bonds (σ and π bonds) simultaneously, owing to the non-parallel and non-perpendicular arrangements.^{54,55}

Band structures drastically change with the variation of curvature. The asymmetry of energy bands about E_F becomes more obvious in the increase of ϕ , e.g., $\phi = 90^\circ$ in Fig. 3(b). The energies, wave vectors, and dispersion relations of the band-edge states are strongly affected by the arc angle. When the arc angle is large than 60° , the $k_x = 0$ state of the V_2 valence band will become the HOS. Furthermore, the $k_x = 1$ state of the EACBs and

the $k_x = 0$ state of the V_2 valence band (the LUS and HOS states) approach to the Fermi level simultaneously, leading to a quick decline of an indirect energy gap. Specially, these two bands marginally overlap each other at $\phi \sim 190^\circ$ (Fig. 3(c)), so that a 1D metal, with a high DOS at E_F due to the band-edge states of parabolic bands, come to exist. The arc angle in determining the semiconductor-metal transition is relatively small for wider curved nanoribbons. The doubly degenerate states of the EACBs and EAVBs present the significant splittings. Moreover, the band-edge state energies might change the ordering of the conduction/valence bands at $k_x = 0$.

Energy bands are very different from those of the flat nanoribbon (Fig. 3(a)) for the sufficiently large arc angles, e.g., $\phi = 300^\circ$ in Fig. 3(d)). The σ bondings make more contributions on the low-lying energy bands, compared with the π bondings.^{54,55} This directly reflects the significant edge-atom interactions on two distinct boundaries by the sp^2 bonding that can create two kinds of free carriers and the significant band mixings. The V_2 valence band near $k_x = 0$ crosses E_F ; therefore, the 1D free electrons and holes coexist in the obvious band overlap. The C_4 and C_3 bands, which mainly come from the $2p_z$ and $2p_y$ orbitals, respectively, lower their energies and become very close to the Fermi level. The former lies below the latter, since it experiences a stronger curvature effect under the reduced π -bond contributions and the enhanced σ -bond ones. The double degeneracy of the EVCBs/EAVBs is largely destroyed, and the split states strongly mix with other energy bands. Specifically, the two EACBs are intermingled with the C_4 and C_3 conduction bands. The mixed four conduction bands are classified into the C_4^* , C_3^* , E_1^* and E_2^* bands, based on the predominant orbitals at the $k_x = 0$ state. They have an extra band-edge state in between $k_x = 0$ and 1.

The oscillations of energy bands become very strong, when the arc angle approaches the critical one ($\phi_c = 330^\circ$), e.g., $\phi = 320^\circ$ in Fig. 3(e). The edge-atom interactions between two different sides are greatly strengthened; therefore, they dominate the quite unstable geometric structure and the unusual band structure. The edge-atom contributions to the C_4^* and C_3^* conduction bands gradually decline. These two bands present higher energies

near $k_x = 1$, in which the degenerate states rise from zero to ~ 0.2 eV. The C_4^* conduction band moves toward E_F , while the C_3^* conduction band exhibits the opposite behavior. The former mixes with the V_2 valence band, accompanied with the creation of two extra band-edge states and an energy spacing near $k_x = 0$. Specially, the electronic states corresponding to the previous C_4^* conduction band (V_2 valence band) are dramatically changed into those of the present V_2 valence band (V_4^* conduction band).

A further increase in the arc angle beyond ϕ_c can create the rich and unique band structures, as clearly indicated for $\phi = 340^\circ$ in Fig. 3(f) and $\phi = 350^\circ$ in Fig. 3(g). The geometric structure becomes relatively stable, since the sp^2 bondings of the two-side edge atoms are initialized. The oscillations of energy bands are greatly weakened, and some band-edge states disappear. The sufficiently large curvatures lead to the hybridizations of the $2p_z$ and $2p_y/2p_x$ orbitals as a result of the shortened distances between the neighboring atoms. These hybridizations cause the C_4^* conduction band to change from an oscillating dispersion into a parabolic one. Mixing of the C_4^* and V_2 bands might be absent, and the latter deviates from E_F . As to $\phi = 340^\circ$ (Fig. 3(f)), the LUS and HOS, respectively, correspond to the C_4^* and V_1 bands, in which a small indirect $E_g=0.02$ eV represents the semiconducting behavior. A 1D metal is changed into a narrow-gap semiconductor in the range of $\phi_c < \phi < 340^\circ$. This gap will disappear as the arc angle increases to near 360° , since both C_4 and V_1 bands overlap with each other (Fig. 3(g)), i.e., the semiconductor-metal transition reoccurs. The semiconductor-metal transition happens two times during the variation of ϕ from 0° to 2π . In addition, the $k_x = 1$ degenerate states of the C_4^* and C_3^* conduction bands are considerably raised to ~ 1.5 - 2.0 eV.

A curved armchair ribbon of $\phi = 2\pi$ is a (5,0) zigzag nanotube. The two-side edge atoms bond together along the longitudinal direction to form a very stable hollow cylinder. As a result of the periodical boundary condition, each energy band, as shown in Fig. 3(h), exhibits a monotonous dispersion relation with a specific transverse quantum number.^{244,245} The band-edge states only appear at $k_x = 0$ and 1. The original edge atoms do not dominate

any energy bands (the absence of EACBs and EAVBs), and such atoms make contributions to each one. Most energy bands are doubly degenerate, as predicted by the calculations of the tight-binding model. Some bands are non-degenerate near $k_x = 0$, e.g., the V_1 , V_2 , and C_4^* bands. Both V_1 and C_4^* bands intersect at the Fermi momentum $k_F \sim 0.25$, in which the former and the latter, respectively, have the free holes and electrons. Furthermore, the V_2 band just touches the Fermi level. These can create a high DOS at E_F (discussed in Fig. 4(e)), clearly illustrating the metallic behavior of a very small (5,0) zigzag nanotube. On the other hand, the tight-binding model predicts it to be a semiconductor in the absence of curvature effects.²⁴⁶ The large curvatures induce the strong hybridizations of the ($2s, 2p_x, 2p_y, 2p_z$) orbitals (details in Section 4.2); therefore, an obvious energy decrease in the C_4^* conduction band is revealed near $k_x = 0$. The sufficiently strong sp^3 bondings are responsible for the metallic carbon nanotubes with very small radii.

The number, intensity, and energy of prominent peaks in DOS strongly depend on the geometric curvature, in which the local DOS can comprehend the contributions due to the edge and central carbon atoms. As to a flat $N_A = 10$ armchair nanoribbon, the low-lying energy bands possess a lot of asymmetric peaks, as shown for (EAVBs, V_4, V_3, V_2, V_1) (EACBs, C_1, C_2, C_3, C_4) with different symbols in Fig. 4(a). The strong peaks associated with EAVBs and EACBs (the black dots) mainly originate from the edge atoms (the dashed blue curves), while the other special structures are dominated by the non-edge ones. Before the critical curvature ($\phi < \phi_c$ in Figs. 3(b) and 3(c)), the number of asymmetric peaks grows with ϕ , since there exist the non-degenerate EAVBs and EACBs, extra mixed band-edge states and strongly oscillatory energy dispersions. For example, the non-monotonous C_4^* conduction band (the green squares in Fig. 3(d)) presents four peaks with the reduced intensities near the Fermi level at $\phi = 300^\circ$ (Fig. 4(c)). In the further increase of ϕ (high curvatures in Figs. 4(d) and 4(e)), the peak number declines as a result of the weakened oscillations of energy dispersions and the recovered degeneracy of some bands (Figs. 3(f) and 3(h)). Furthermore, it is very difficult to observe the dominating contributions from

the edge atoms; that is, the strong edge-atom bondings will suppress and even destroy the EACBs and EAVBs. A cylindrical carbon nanotube (Fig. 4(e)), with the transverse periodical boundary condition, exhibits the smallest peak number and the same contributions from all atoms except for two neighboring peaks cross $E = 0$ due to the V_1 and V_2 bands (the yellow triangle and blue circle). Specially, the peak energies near the Fermi level are responsible for the semi-conducting or metallic behavior. They are related to the V_2 band and the EACBs/ C_4^* band for $\phi < \phi_c$ (Figs. 4(b) and 4(c); $E_g = 0$), the V_1 and C_4^* bands for $\phi_c < \phi < 2\pi$ (Fig. 4(d); a narrow gap), and the V_2 , V_1 and C_4^* bands for $\phi = 2\pi$ (Fig. 4(e); zero gap), clearly illustrating the semiconductor-metal transitions during the variation of ϕ .

The theoretical predictions are worthy of the detailed experimental examinations, especially for the edge-dependent essential properties. Up to now, the curved structures of graphene nanoribbons are confirmed by TEM, SEM and ATM measurements. The delicate measurements on the curvature, the edge-atom bond length, and the hexagonal arrangement could be further done by STM, as measured for buffer graphene layer,^{187,188} graphene bubble,²⁴⁷ and carbon nanotube.^{184,185} On the other hand, the ARPES and STS measurements on electronic properties of curved systems are absent except that the latter have verified the metallic or semiconducting carbon nanotubes. They can examine the curvature-induced properties, covering the conductor-metal transitions, the oscillatory energy bands, the edge-atom-dominated energy bands with weak dispersion relations, and the reduced or recovered state degeneracy. Moreover, such measurements provide the sufficient information in identifying the effects of chemical bondings on the essential properties of curved systems.

4.2 Carbon nanotubes

Each carbon nanotube, as shown in Fig. 5(a), is formed by rolling a graphene sheet from the origin to the lattice vector $\mathbf{R}_x = m\mathbf{a}_1 + n\mathbf{a}_2$, where \mathbf{a}_1 and \mathbf{a}_2 are primitive lattice vectors of a 2D sheet. A (m, n) nanotube has a radius $r = b\sqrt{3(m^2 + mn + n^2)}/2\pi$. The chiral angle can characterize the non-chiral/chiral arrangements of carbon hexagons on a

cylindrical surface. $\theta = \tan^{-1}\sqrt{3}n/(2m+n)$, is the angle between the new x -axis (the transverse direction parallel to \mathbf{R}_x) and the original x' -axis. For all carbon nanotubes, the chiral angles are confined within $|\theta| \leq 30^\circ$. (m, m) and $(m, 0)$, respectively, represent nonchiral armchair and zigzag systems with $\theta = 30^\circ$ and 0° . It should be noticed that armchair and zigzag carbon nanotubes correspond to zigzag and armchair graphene nanoribbons, respectively. The number of carbon atoms in a primitive unit cell (a rectangle in Fig. 5(a)) is $N_u = 4\sqrt{(m^2 + mn + n^2)(p^2 + pq + q^2)}/3$, where (p, q) is determined by the primitive lattice vector ($\mathbf{R}_y = p\mathbf{a}_1 + q\mathbf{a}_2$) along the nanotube axis. The axial wave vectors in the 1D first Brillouin zone are $|k_y| \leq \pi/|\mathbf{R}_y|$.

There are a lot of theoretical calculations on the electronic properties of carbon nanotubes using the tight-binding model^{244,245} and the first-principles method since the first accurate predictions in 1992.^{248,249} By the detailed calculations and analyses, all carbon nanotubes could be classified into three types: (I) metals with a finite DOS at the Fermi level, (II) moderate-gap semiconductors with energy gaps inversely proportional to radius, and (III) narrow-gap semiconductors with $E_g \propto 1/r^2$.⁵⁴ When the curvature effects, the misorientation of $2p_z$ orbitals and the sp^3 orbital hybridization on a cylindrical surface, are not taken into account, the periodical boundary plays a critical factor in determining the metallic or semiconducting behavior. The low-energy essential properties are dominated by the π bondings of the parallel $2p_z$ orbitals. The electronic states of a 1D carbon nanotube are sampled from those of a 2D monolayer graphene. Carbon nanotubes, with $2m+n=3I$, are gapless metals, since their linear bands correspond to the Dirac-cone structure, or they can sample the Dirac point from graphene.^{244,245} Furthermore, the $2m+n \neq 3I$ carbon nanotubes are moderate-gap semiconductors. On the other hand, the full orbital hybridizations cause the non-armchair $2m+n=3I$ carbon nanotubes to become the narrow-gap semiconductors except for $r < 2.5 \text{ \AA}$, and they create the metallic nanotubes with very small radii. In short, the metallic, moderate- and narrow-gap nanotubes are, respectively, characterized by the geometric structures: (I) $m=n$ or $r < 2.5 \text{ \AA}$, (e.g., (5,0) and (6,0) nanotubes),^{250,251}

(II) $2m + n \neq 3I$; ((7,0) and (8,0) nanotubes); (III) $2m + n = 3I$ and $m \neq n$ ((9,0) and (12,0) nanotubes). Three types of energy gaps have been verified by the accurate STS measurements,^{56,184,185} The (m, m) armchair and $(m, 0)$ zigzag carbon nanotubes will be chosen for a model study to see three types of electronic structures.

All armchair nanotubes belong to 1D metals even in the presence of significant curvature effects. They have the k_y -dependent energy bands with strong dispersion relations, as shown in Fig. 6 for various armchair systems. The occupied valence bands are asymmetric to the unoccupied conduction bands about $E_F = 0$. Most of energy bands are doubly degenerate because of the cylindrical boundary condition, in agreement with the tight-binding model calculations. This clearly illustrate why the number of energy bands is much lower than that in zigzag graphene nanoribbons (e.g., (3,3) nanotube in Fig. 6(a) and $N_z = 6$ nanoribbon in Fig. ?). The band-edge states are situated at $k_y = 0$ and/or near $k_y = 2/3$ (in unit of $\pi/|\mathbf{R}_y|$). The energy dispersions relative to such critical points are in the parabolic or linear form. For larger armchair nanotubes (Figs. 6(c) and 6(d)), there are more low-lying energy band initiated from the $k_y = 2/3$ state. Specially, the first pair of valence and conduction bands, without the double degeneracy, linearly intersect at the Fermi level, indicating the 1D metallic behavior. The Fermi momentum in each armchair nanotube exhibits a red shift relative to $k_y = 2/3$, such as an obvious shift of $\sim 1/6$ revealed by a very small (3,3) nanotube (the dotted-red curved). The former approaches to the latter in the increase of nanotube radius as a result of the reduced curvature effects. Furthermore, for sufficiently large armchair nanotubes, the Fermi velocity, the slope of the linear band, is close to that of monolayer graphene ($3\gamma_0 b/2$; γ_0 the nearest-neighbor hopping integral of $2p_z$ orbitals).²⁵²

The effects of curvature on the Fermi-momentum states in armchair carbon nanotubes could also be understood from the tight-binding model. For a planar monolayer graphene, the low-lying energy bands are dominated by the π bondings of the parallel $2p_z$ orbitals (Fig. b). They present an isotropic Dirac-cone structure near the K point (the corner of the hexagonal first Brillouin zone), as shown in Fig. b, since the honeycomb lattice has three uniform

nearest-neighbor π bondings with the same hopping integral (γ_0). On the other hand, the $2p_z$ orbitals perpendicular to a cylindrical surface are not parallel to one another; furthermore, the angle between two neighboring $2p_z$ orbitals grows with the increasing curvature (or with the decrease of radius), The misorientation of $2p_z$ orbitals can reduce the π bondings and create the σ bondings (Fig. b). By the detailed calculations,^{105,253} the hopping integral on the dimer line is different from the other two, depending on the arrangement of three chemical bonds. Even with the modifications in the atomic interactions, the electronic states of armchair carbon nanotubes could sample the K point of monolayer graphene under the periodical boundary condition, being consistent with the first-principles calculations.^{248,249} However, they might induce the obvious changes in the Fermi momentum and velocity. It is also noticed that for very small armchair nanotubes, the sp^3 orbital hybridizations make significant contributions to the electronic states near E_F (discussed later in Fig. D), while they do not thoroughly alter the metallic behavior due to the linear bands.

The electron properties of carbon nanotubes are sensitive to the change in the chiral angle and radius. There are certain important differences between zigzag and armchair carbon nanotubes. All energy bands of $(m, 0)$ zigzag nanotubes, as clearly indicated in Figs. 7(a)-7(d), are initiated from the $k_y = 0$ state with the significant dispersion relations. The low-energy electronic states are doubly degenerate, especially for those in determining the metallic property and the magnitude of E_g . Specifically, the $(5, 0)$ and $(6, 0)$ nanotubes, as well as the $(4, 0)$ one,²⁵¹ present the strong overlap of the valence and conduction bands (Figs. 7(a) and 7(b)); that is, only three very small zigzag nanotubes belong to the 1D metals. This unusual metallic behavior is not dominated by the periodical boundary condition and the π bondings, while it mainly comes from the significant sp^3 orbital hybridizations on a high-curvature cylindrical surface, as confirmed by the spatial charge distributions and the orbital-projected DOS (Figs. 9 and 10). On the other hand, the $(m > 6, 0)$ zigzag nanotubes possess direct energy gaps at $k_x = 0$. The radius-dependent energy gaps could be further divided into type-II for $m = 3I + 1/3I + 2$ and type-III for $m = 3I$, in which they

are, respectively, proportional to the inverse of r and r^2 , as shown in Fig. 8 (the dashed red and blue curves).

Specially, the metal-semiconductor transitions appear, when a carbon nanotube is threaded by a uniform axial magnetic field (a magnetic flux ϕ_B). As a result of the cylindrical symmetry, the ϕ_B -dependent electronic structure exhibits the well-known periodical Aharonov-Bohm effect, with a oscillation period of flux quantum ($\phi_0 = hc/e$).²⁵⁴⁻²⁵⁷ For armchair carbon nanotubes, the linearly intersecting valence and conduction bands, with the metallic property, become the separated parabolic ones as ϕ_B grows from zero flux. Energy gap linearly reaches a maximum value at $\phi_B = \phi_0/2$ and then declines to zero at ϕ_0 . That is, the metal-semiconductor transitions occur at $\phi_B = I\phi_0$. The similar magneto-electronic properties are revealed in the type-II and type-III carbon nanotubes, in which the critical magnetic fluxes are, respectively, close to $(I \pm 1/3)\phi_0$ and $I\phi_0$. The Aharonov-Bohm effect in carbon nanotubes have been verified from the experimental measurements on the magneto-optical^{258,259} and transport properties.²⁶⁰⁻²⁶²

Armchair/zigzag carbon nanotubes are very different from zigzag/armchair graphene nanoribbons in the main features of electronic properties. The edge-atom-dominated energy bands are absent in carbon nanotubes, and each energy band is equally contributed by carbon atoms on a cylindrical surface. The metallic armchair nanotubes (Fig. T) sharply contrast with the semiconducting zigzag nanoribbons (Fig. T). The latter exhibit the anti-ferromagnetic spin configuration across the nanoribbon center, and a pair of partially flat bands with the edge-localized states in determining an energy gap. Their band gaps slowly decline with the increment of radius. The $(3I \pm 1, 0)$ and $(3I, 0)$ zigzag nanotubes (Fig. T), respectively, have moderate and narrow gaps inversely proportional to r and r^2 . However, energy gaps in armchair nanoribbons present an inverse relation with width (W), in which those of the $N_z = 3I + 2$ systems are smallest (Fig. T). The narrow gaps in zigzag nanotubes and armchair nanoribbons are induced by the non-parallel and non-uniform π bondings,^{40,54} respectively. Specifically, the metal-semiconductor transitions could be ob-

served in the magneto-electronic properties of carbon nanotubes, but not those of graphene nanoribbons.⁶³ The above-mentioned differences mainly arise from the boundary condition, the edge structure and the curvature effect. The critical roles, the geometric symmetries and the orbital hybridizations, are responsible for the essential properties.

The geometry- and orbital-dependent DOSs in carbon nanotubes, as shown in Fig. 10, can provide the useful information about the cooperative/competitive relations among the chiral angle, the periodical boundary condition, and the multi-orbital hybridizations. All armchair nanotubes possess a finite DOS in the plateau form asymmetric about the Fermi level (Figs. 10(a)-10(d)), directly reflecting the metallic behavior of the 1D linear valence and conduction bands (Fig. 6). However, the metallic zigzag nanotubes presents several prominent asymmetric peaks near E_F ((5,0) in Fig. 10(e) and (6,0) in Fig. 10(f)), being associated with the low-lying parabolic energy bands (Figs. 7(a) and 7(b)). For small carbon nanotubes, the low-energy DOSs mainly come from the $2p_z$ and $2p_x$ orbitals (perpendicular to the cylindrical surface and parallel to the tube axis, respectively; Figs. 10(a), 10(b), 10(e); 10(f) with the red and blue curves); therefore, the strong multi-orbital hybridizations can create the metallic band structures. In addition, the significant hybridization of these two orbitals also has a strong effect on the electronic properties of the highly curved nanoribbons. The contributions due to the $2p_x$ orbitals become weak in the increase of radius; that is, the decrease of curvature leads to the weakened sp^3 orbital hybridizations, or the low-energy essential properties are mainly determined by the neighboring $2p_z$ orbitals (the misorientation of $2p_z$ orbitals). The large armchair nanotubes keep the plateau structure across E_F (Figs. 10(c) and 10(d)), while the $(3I, 0)$ zigzag systems present a pair of separated asymmetric peak with a small energy gap (Figs. 10(g) and 10(h)). The chirality and the periodical boundary condition play the critical roles in the metallic/semiconducting property of large carbon nanotubes.

Whether a composite system of carbon nanotube/graphene nanoribbon can exhibit the rich and unique properties deserves a closer discussion. As a result of the rapid advance in

chemical analysis techniques, the nanoscale carbon hybrid materials have been successfully synthesized in experimental laboratories, such as, encapsulated C_{60} in single-walled carbon nanotube,²⁶³ a 1D carbon chain inside a multi-walled carbon nanotubes,²⁶⁴ graphene/carbon nanotube hybrid,²⁶⁵⁻²⁶⁷ and carbon-nanobud hybrid.²⁶⁸ A commensurate graphene nanotube-nanoribbon hybrid system is formed, when an armchair (zigzag) nanotube is adsorbed on a zigzag (armchair) nanoribbon by the weak van der Waals interactions. According to the first-principles calculations,^{269,270} the geometric, electronic and magnetic properties strongly depend on the interlayer distance, stacking configuration and spin orientation. The structural stability is examined to be dominated by the charge transfer of $2p_z$ orbitals between two sub-systems. The significant interlayer atomic interactions can greatly modify the low-lying band structures, e.g., the creation of subband spacings and band-edge states, and the destruction of spin/state degeneracy. For armchair nanotube/zigzag nanoribbon hybrids, a pair of intersecting linear bands become two separated parabolic ones with a small energy gap sensitive to the nanotube location. The antiferromagnetic configuration is steadier than the ferromagnetic one for all nanotube locations. Furthermore, the spin degeneracy is lifted when the nanotube is close to the zigzag edge. On the other hand, zigzag nanotube/armchair nanoribbon hybrids exhibit the non-magnetic configuration. The low-energy double degeneracy associated with the cylindrical symmetry is broken by the interlayer $2p_z$ -orbital interactions. The predicted essential properties of carbon nanotube-nanoribbon hybrids require further experimental examinations.

The 1D carbon nanotubes, with a unique cylindrical symmetry, are very suitable for studying the basic and applied sciences. The chirality- and radius-dependent semiconductors and metals are available in functionalized nanodevices, such as electronic and optoelectronic devices. The intrinsic 1D band structures, with the decoupled angular momenta, dominate the quantized electrical and optical properties, e.g., the geometry-dependent resistance, capacitance, inductance, and optical conductance.^{58,271,272} Up to now, the field-effect transistors (FETs) based on the semiconducting carbon nanotubes are widely developed,

mainly owing to the advantage of high carrier mobility under the low scatterings. The first FETs composed of single- or multi-walled carbon nanotubes were reported in 1998,^{235,236} which present superior electrical conductance at room temperature using the gate-voltage modulation. A very high carrier mobility ($> 10^5 \text{ cm}^2/\text{Vs}$) is identified to be related to the diffusive transport of holes under the electron-phonon scatterings.^{271,272} The nano-scaled radii allows the gate's ability to control the potential of the conducting channel in the ultimate thin FETs, while suppressing short-channel effects.^{237,238} Moreover, the semiconducting carbon nanotubes have the highly potential applications in optoelectronic devices, including electroluminescent light emitters,^{273,274} supercapacitors²⁷⁵ and photodetectors.^{276–278} The band-edge states in 1D nanotubes, with the high DOSs, can create the very prominent optical excitations.⁵⁸ The excited electrons and holes on a cylindrical surface are further driven towards each other by using an appropriate bias between source and drain of the FET. The electron-hole recombination will emit the strong electroluminescence. The highly efficient photon-emission process has been extensively utilized in light-emitting diodes (LEDs).^{279–281} The application of photodetector is based on the electric current generated by the resonant excitations. On the other hand, the metallic carbon nanotubes could be selected as candidates in future interconnect materials of integrated electronic devices.^{282,283}

5. Folded graphene nanoribbons

The folded honeycomb lattices may be more complex and intriguing, since they are expected to dramatically modify the essential properties by tuning their structures. In experiments,^{5,67–70} the folded graphene nanoribbons could be produced by the distinct methods, such as, few-layer graphene systems in a chemical solution using the powerful ultrasound,^{5,67,68} the mechanical pressing on a graphene aerogel prefabricated by freeze-drying a homogenous graphene oxide aqueous dispersion and subsequent thermal reduction,⁶⁹ and the Joule heating of suspended graphene to form the nested structures.⁷⁰ The HRTEM mea-

measurements clearly show a well-defined zigzag/armchair boundary structure, the coexistent open and closed edges, a nanotube-like curved surface, as well as the AA, AB and other stackings.^{67,68} Furthermore, the semiconducting systems could serve as field-effect transistors with on-off ratios of about 10^7 at room temperature.⁵ On the theoretical side, the tight-binding model and the first-principles method have been utilized to study the essential properties of the folded graphene nanoribbons. The former is available in understanding the unusual quantum Hall effects (the novel magnetic quantization phenomena).^{72,73,284} The latter is suitable in evaluating the folding energies, optimal geometries, band structures, energy gaps, density of states, spatial charge distributions, and spin polarizations.^{71,285–287} It should be noticed that the complex dependences on the edge structures, the nanoribbon widths, the bilayer-like stacking configurations, the van der Waals interactions, the curvatures of folded surfaces, and the spin arrangements need to be included in the calculations simultaneously. This will be explored in detail.

The folded graphene nanoribbons, with the hydrogen passivation, have the unique geometric structures composed of two close open edges, a bilayer-like flat region, and a curved surface (Fig. 1). The high-symmetry stacking configurations (AA, AA' and AB stackings) and the various ribbon widths are taken into account to reveal the rich fundamental properties, including the edge-edge distance, interlayer distance, nanotube diameter, folding energy, spatial spin density, band structure, energy gap and DOS. Among the complex geometric structures, we systematically classify four types of armchair and zigzag systems, according to the edge structure, folding energy, number of armchair/zigzag lines, and stacking configuration. Furthermore, the width-dependent energy gaps of the former are further divided into six categories on the basis of the stacking configurations. These eight types of folded systems are predicted to exhibit the diverse essential properties, such as the lower folding energy in the AA' or AB stackings, the saturated geometric parameters for sufficiently large widths, the metallic linear bands or the separated parabolic bands nearest to E_F , the complex width dependences of energy gaps, the creation or destruction of magnetism, and the spin-split

energy bands and van Hove singularities. Such features are closely related to the combined effects of quantum confinement, open-edge interaction, van der Waals interaction, curvature, and spin arrangement. The feature-rich folded graphene nanoribbons are expected to provide potential applications in energy materials,²¹⁸ as well as electronic⁵ and spintronic devices.²¹⁹

5.1 The rich geometric structures

The folded graphene nanoribbons, with the achiral boundaries passivated by the hydrogenated atoms, are chosen for a model investigation. They possess the rich geometric structures. A single flat graphene nanoribbon could be bent into a folded system, in which the latter consists of two flat ribbons connected by a fractional nanotube in the position to generate the curved surface. Figures 1(a) and 1(b), respectively, correspond to folded armchair and zigzag nanoribbons, accompanied with the hydrogen passivation along the longitudinal x -direction (white balls). Each folded nanoribbon, as shown in Figs. 1(c) and 1(d), is characterized by the interlayer distance (I_z), nanotube diameter (D_n), edge distance (d_{edge}), edge structure, stacking configuration, and width. The stable geometric structures are identified from the high-symmetry stacking configurations and the number of armchair/zigzag lines along the transverse direction. There exist three kinds of typical stacking configurations, AA, AB and AA' ones (Fig. 1(e)). Specifically, the AA' stacking is an intermediate configuration between AA and AB ones, where the C-C dimer of one layer is projected at the hexagonal center of another layer. According to the number of armchair lines, the stable geometric structures could be classified into four types: an even N_A with (I) AA' (even-aAA') and (II) AA (even-aAA) stackings (Figs. 2(a)-2(b)); an odd N_A with (III) AA (odd-aAA) and (IV) AA' (odd-aAA') ones (Figs. 2(c)-2(d)). The similar configurations for zigzag systems cover an even N_Z with (I) AA (even-zAA) and (II) AB (even-zAB) stackings (Figs. 2(e)-2(f)); an odd N_Z with (III) AA' (odd-zAA') and (IV) AB (odd-zAB) ones (Figs. 2(g) and 2(h)). The even-aAA and odd-aAA' can be, respectively, realized by shifting the upper layers of the even-aAA' and odd-aAA along the y -direction with the distance of $\sqrt{3}b/2$. A similar

relation exists between the even-zAB and even-zAA stackings (the odd-zAB and odd-zAA' ones), but with a shift of b ($b/2$). Specifically, for the even-aAA', odd-zAA', odd-aAA and even-zAA stackings (Figs. 2(a), 2(g), 2(c); 2(e)), the edge of the upper layer lines up with that of the lower layer, indicating the same y positions for all the edge atoms. Furthermore, the former two only present the C_2 rotation symmetry about the y -axis, while the others have the $z = 0$ -plane mirror symmetry.

The optimal folded structures are achieved under the accurate relaxation simulation. Each stacking configuration exhibits the unique behavior in terms of nanotube diameter, interlayer distance and folding energy. D_n and I_z , respectively, reflect the curvature and stacking effects. They, as clearly indicated in Figs. 3(a) and 3(b), are very sensitive to the changes of nanoribbon width and stacking configuration. As for folded armchair nanoribbons, the dependence of D_n on width is weak except that the even-aAA stacking exhibits the decreasing behavior in the increase of N_A and reveals a saturation value at $N_A \geq 40$ (the red circles in the upper part of Fig. 3(a)). The minimum nanotube diameters of the even-aAA, even-aAA', odd-aAA, and odd-aAA' stackings are, respectively, 7.1 Å, 7.0 Å, 7.0 Å, and 7.2 Å. They are close to that (7.05 Å) of a perfect (9,0) zigzag nanotube. The dependence of interlayer distance on width is negligible. Furthermore, I_z of the AA stackings (the red circles and triangles in the lower part of Fig. 3(a)) is larger than that of the AA' ones (the green squares and blue triangles), regardless of the even or odd dimer lines. The perceivable I_z 's of the former and the latter are 3.5 Å and 3.3 Å, respectively. On the other side, D_n 's of folded zigzag nanoribbon initially grow with an increase of N_Z and then reaches a saturation value at $N_Z \geq 40$ (Fig. 3(b)). The maximum nanotube diameters of the even-zAA, even-zAB, odd-zAA' and odd-zAB stackings, respectively, reach 9.2 Å, 9.3 Å, 8.7 Å and 8.5 Å. They correspond to (7,7) and (6,6) armchair carbon nanotubes, consistent with the experiment measurements.⁶⁷ The interlayer distances weakly depend on the ribbon width, in which the saturated I_z 's at $N_Z \geq 38$, respectively, correspond to 3.5 Å, 3.2 Å, 3.3 Å and 3.2 Å following the same sequence as for D_n 's. The above-mentioned results show that both D_n and

I_z are almost constant for the enough large widths. The nanotubes diameters of the folded armchair nanoribbons are smaller than those of the zigzag systems, reflecting the larger deformation (the softer mechanical property) in the former. The similar mechanical-strain response is presented in the deformed carbon nanotubes.²⁸⁸ The interlayer distances are mainly determined by the stacking effect. The AB and AA' stackings have the smaller I_z 's, compared with the AA stacking. This is consistent with those revealed in bilayer graphene nanoribbons¹⁰¹ and bilayer graphenes.^{170,186,289–291}

The folding energy, which is required to form a folded graphene nanoribbon from a flat one, is the total energy difference of the former and the latter. E_{fold} consists of the van der Waals energy ($E_{vdW} < 0$), the edge-induced energy ($E_{edge} < 0$) and the bending energy ($E_{bend} > 0$), being contributed by the flat two-layer interaction, edge-edge interaction and mechanical strain, respectively. E_{fold} is greater than zero, since E_{bend} is always larger than $|E_{vdW}| + |E_{edge}|$. E_{vdW} is dependent on the range of the flat region, interlayer distance, and stacking configuration and length of the flat region. This attractive energy is enhanced by the increasing overlap region or the decreasing interlayer distance. Moreover, the magnitude of E_{edge} grows as the distance between two edges declines. As a result, E_{fold} decreases with the increment of width (Figs. 4(a) and 4(b)), mainly owing to the almost constant E_{edge} and E_{bend} (for a specific edge structure and a saturated D_n), and the reduced E_{vdW} (for a widened overlap area). The folded armchair nanoribbons exhibit the stacking-dependent behavior, as clearly shown in Fig. 4(a). E_{fold} is smaller in the AA' stacking, compared with the AA one. The former is more stable, regardless of the even or odd dimer lines. The edge-edge interactions do not play an important role in the even and odd stackings because of the nearly same inter-edge distance (3.6 Å). On the other side, for the sufficiently wide zigzag systems with $N_z \geq 38$ (Fig. 4(b)), the folding energies of four types of stackings present the specific descending order: even-zAA > odd-zAA' > odd-zAB > even-zAB. This indicates the higher stability in the AB stacking configurations. Furthermore, the even-zAB stacking has a lower E_{fold} than the odd-zAB one, since the shorter inter-edge distance in the former

(3.1 Å and 3.6 Å in the even and odd systems, respectively) lead to the stronger edge-edge interaction. In addition, the bending energy might account for the difference between zigzag and armchair systems.

5.2 The unusual electronic and magnetic properties

The main features of energy bands strongly depend on the quantum confinements, the edge structure, the surface curvature, the stacking configuration and the magnetic configuration. The folded armchair nanoribbons, as shown in Figs. 5(a)-5(h), present a lot of asymmetric valence and conduction bands about E_F . The parabolic dispersions are initiated from the $k_x = 0$ state. Some of the band-edge states are doubly degenerate due to the stacking effect. The low-lying bands mainly from the intralayer and the interlayer interactions of $2p_z$ orbitals. The edge-localized energy bands are absent, as observed in planar armchair systems (Fig. ?). The top of valence band and the bottom of conduction one are located at $k_x = 0$; that is, all the folded armchair systems belong to the direct-gap semiconductors. Apparently, energy gaps change with ribbon width, in which there exists an oscillational relation between N_A and E_g for the AA or AA' stacking.²⁸⁵ The similar dependence is revealed in the flat armchair nanoribbons (Fig.). However, the oscillation period of energy gap is, respectively, characterized by six N_A 's and three N_A 's for the folded (Fig. 6) and planar armchair systems.⁴⁰ For the $N_A=34$ and $N_A=37$ systems, they possess larger energy gaps, and the AA' stacking is higher (Figs. 5(a) and 5(d)), compared with the AA stacking (Figs. 5(e) and 5(h)).

The folded armchair nanoribbons are different from the planar systems in the width dependences of energy gaps. Based on the AA or AA' stacking, E_g 's of the former could be classified into six categories: $6I$, $6I + 1$, $6I + 2$, $6I + 3$, $6I + 4$; $6I + 5$. Each category, as shown in Figs. 6(a) and 6(b), exhibits the declining behavior in the increase of ribbon width, reflecting the quantum-confinement effect. The magnitude of energy gap could be further understood from the even or zigzag dimer lines, as identified from the three N_A -relations.

For the even-aAA stacking, it has the largest and smallest energy gaps for $N_A = 6I + 4$ and $6I$, respectively (red and purple squares in Fig. 6(a)). Furthermore, the odd-aAA stacking owns a smaller gap in $N_A = 6I + 5$ (purple crosses), but the largest energy gap lies in the $N_A = 6I + 3$ (black crosses) or $6I + 1$ category (green crosses). Similarly, three categories of width-dependent energy gaps are revealed in the even-aAA'/odd-aAA' stacking. The even-aAA' stacking, with $N_A = 6I + 4$ (red squares in Fig. 6(b)), exhibits the largest energy gap among all the armchair systems. The smallest energy gap corresponds to the $6I + 2$ category (blue squares). The odd-aAA' stacking for the $6I + 1$ ($6I + 3$) category [green (blue) crosses] has a larger (smaller) energy gap. The above-mentioned complex width-dependences are attributed to the combined confinement, stacking and curvature effects in this unique folding structure. Specially, for the flat armchair nanoribbons, the smallest energy gap is the $3I + 2$ category (Chap. 3), in great contrast with the case for the folded systems. Instead, another category associated with the smallest energy gap here is $3I$ corresponding to the even-aAA and odd-aAA' stackings.

The electronic structure is closely related to the magnetic configuration. The magnetism of folded graphene nanoribbons is determined by the edge structure and the edge-edge distance. The armchair systems prefer the non-magnetic behavior, as observed in planar monolayer ones.⁴⁰ Specially, the spin arrangements in the zigzag systems could be modified by the geometric structure. The odd-zAA' and odd-zAB stackings, like planar zigzag nanoribbons, present the anti-ferromagnetic configuration at the open edges, as clearly illustrated in the spin charge densities (Figs. 7(a) and 7(b)). Each carbon atom in zigzag edge possesses a magnetic moment of $\sim 0.14 \mu_B$. On the other hand, the magnetic configuration is absent in the even-zAA, even-zAB stackings. Whether the magnetism could survive is dependent on the edge-edge interactions. The strong interactions will effectively suppress the magnetic moments at a sufficiently short distance. The edge-edge distances of the even-zAA, even-zAB, odd-zAA' and odd-zAB stackings are, respectively, 2.9, 3.1, 3.5, and 3.6 Å's, being responsible for the existence of magnetism. The similar magnetic suppression could also be

found in bilayer graphene nanoribbons (discussed latter in Chap. 7).

The magnetism and curvature effect will greatly enrich the electronic properties of the folded zigzag nanoribbons, compared with those of the armchair systems (Fig. 5) or the planar zigzag ones (Fig. ?). Most of the energy bands, as shown in Figs. 7(c)-7(f), present parabolic dispersions. Each subband might have several band-edge states, in which they are situated at $k_x = 0, 1$ and in between them. For the higher/deeper electronic states, there are many anti-crossing subbands with the band-edge states near the zone boundary, mainly owing to the significant interlayer atomic interactions and the enhanced hybridizations of the $(2s, 2p_x, 2p_y, 2p_z)$ orbitals on the curved surface. Specially, the valence and conduction energy bands, which are closest to E_F , exhibit the partially flat and parabolic dispersions at $2/3 < k_x \leq 1$ and $0 \leq k_x \leq 2/3$, respectively. The weak energy dispersions mainly come from the local edge atoms (the circle radii representing the edge-atom contributions). The edge-localized energy bands quite differ among four types of folded zigzag nanoribbons in terms of the existence of energy dispersion, band gap and spin splitting.

Both even-zAA and even-zAB stackings exhibit the non-magnetic energy bands, as shown in Fig. 7(c) and 7(d). The former are the only 1D metals, with the linearly intersecting valence and conduction bands at the Fermi level. The metallic behavior is induced by the very strong edge-edge interactions. The Fermi momentum of $k_x \sim 2/3$ is similar to the Dirac point of an armchair carbon nanotube (Fig. ?), since each folded zigzag nanoribbon has an armchair cylindrical surface characterized by D_n . The quasi-Dirac-cone structure is also shown in the AA-stacked bilayer graphenes,^{292,293} bilayer zigzag nanoribbons (Fig. ?) and collapsed carbon nanotubes,^{294,295} as a result of the mirror symmetry. On the other hand, the latter belong to the narrow-gap semiconductors. A pair of linearly crossing bands become two anti-crossing parabolic bands with a small direct gap. The breaking of mirror symmetry, which comes from the variation of stacking configuration, is responsible for the metal-semiconductor transition, as observed in bilayer zigzag nanoribbons (Fig. ?) and collapsed carbon nanotubes.²⁹⁴ As to the antiferromagnetic odd-zAA' and odd-zAB stackings

(Figs. 7(e) and 7(f)), they are semiconductors without a gapless or separated Dirac-cone structure. Specially, the double degeneracy of spin degree of freedom is present in odd-zAA' stacking, but absent in the odd-zAB system. Whether the spin-dependent degeneracy is broken depend on the spatial spin arrangements. The y -coordinates of the edge atoms on the upper and lower layers are different for the odd-zAB stacking (Fig. 7(b)), so that the spin-up and spin-down states experience the distinct magnetic environments (red and blue dots). However, the opposite is true for the odd-zAA' stacking.

The width dependences of energy gaps in the folded zigzag nanoribbons are mainly determined by the curvature effect, the quantum confinement, and the magnetic configuration. E_g 's of the even-zAB stacking are insensitive to nanoribbon width (~ 60 meV in Fig. 8 by the purple circles). This reflects the almost constant nanotube diameters (Fig. 3(b)) and the comparable curvature effect on the separated Dirac-cone structure. In a sharp contrast, band gaps of the odd-zAA' (green circles) and odd-zAB stackings (red and blue triangles) monotonously decline in the increment of width, clearly indicating the finite-size effect. The former are higher than the latter as a result of the absence of spin splitting. For narrow systems ($N_z \leq 32$), the stacking-dependent order of energy gap is odd-zAA' > odd-zAB with spin down > odd-zAB with spin up > even-zAB. However, the odd-zAB stacking has the smaller gaps for sufficiently wide widths, compared with the even-zAB one. Apparently, the folding structure leads to the diverse N_z -dependent energy gaps, compared with the planar zigzag system (Fig. ?).

The geometric structures and magnetic configurations play important roles in the form, energy, number, and height of van Hove singularities in DOS. All the folded armchair nanoribbons, as shown in Figs. 9(a)-9(d), present a lot asymmetric peaks in the square-root form. Most of them correspond to the $k_x = 0$ state of the parabolic bands (Figs. 5(a)-5(h)). The two adjacent peaks across E_F can determine the width-dependent energy gaps. The main features of DOS is dramatically changed by the edge structure. For folded zigzag nanoribbons, the even-zAA stacking exhibits two prominent peaks on either side of E_F (solid and

hollow squares in Fig. 9(e)), a plateau across E_F , and many square-root asymmetric peaks, respectively, arising from the partially flat, linearly crossing and parabolic bands (Fig. 7(c)). The strong peaks are principally contributed by the local edge atoms. The low-lying constant plateau represents the 1D metal, as observed in armchair carbon nanotubes (Fig. ?).^{245,248,249} However, the even-zAB stacking only has two separate asymmetric peaks near E_F in determining a narrow energy gap (red solid and hollow circles in Fig. 9(e)). Specially, the anti-ferromagnetic odd-zAA' and odd-zAB stackings possess the spin-up- and spin-down-dependent DOS's (red and blue curves in Figs. 9(f) and 9(g)). The two-component contributions are not distinguishable for the former, but distinct for the latter. That is, the odd-zAB stacking has double low-lying, prominent and square-root peaks. Moreover, regardless of the spin states, the energy spacing of two prominent peaks is smaller in the odd-zAA' and odd-zAB stackings than in the even-zAB one.

The STS/SP-STs measurements could be utilized to identify the types of folded graphene nanoribbons from the various features in DOS's. The zigzag systems possess a pair of strong valence and conduction peaks, a characteristic absent in the armchair ones. The energy and number of the spin-dependent special structures are useful in examining the even or odd zigzag lines. Only the even-zAA stacking has a plateau at E_F . The energy spacing of two prominent peaks is smaller for the odd-zAA' and odd-zAB stackings; furthermore, the spin-split double peaks exist in the latter. On the other hand, it is relatively difficult to confirm four types of armchair systems, since the odd-aAA, even-aAA', even-aAA, and odd-aAA' stacking present the similar DOS's. However, energy gaps in DOS are a critical property in identifying the width-dependent six categories. The previous experimental measurements have verified the curvature effect in carbon nanotubes²²⁰ and rippled graphenes,^{189,191} and the stacking effect in few-layer graphenes.²⁰³ These two combined effects in folded armchair systems could be further examined by the STS measurements.

6. Carbon nanoscrolls

Carbon nanoscrolls and carbon nanotubes could be regarded as the rolled-up graphitic sheets, while they, respectively, possess the open and closed surfaces. Both of them might be produced simultaneously in some experimental syntheses. The scrolled honeycomb structures have been successfully fabricated by the different physical and chemical methods, including the arc discharge,⁷⁴ high-energy ball milling of graphite,⁷⁵ chemical route related to intercalation and sonication,^{76–78} gas atom absorption on graphene nanoribbons,⁷⁹ and monolayer graphene predefined with substrates in a chemical solution.⁸⁰ The spiral profiles are identified from the HRTEM measurements. The high-quality carbon nanoscrolls could serve as FETs, and they are demonstrated to sustain a high current up to 10^7 A/cm².⁸⁰ The open edges and the curved surfaces can provide the available environments in the chemical modifications. Such systems are suitable for both fundamental and applied research. Theoretical calculations were first performed by employing the continuum elasticity theory to analyze the structure and stability of carbon nanoscrolls.^{296,297} However, this approach cannot characterize the atomic-level structural features. The molecular dynamics simulations are available in studying the formation and stability of nanoscrolls.^{81,82} The first-principles calculations predict the high-capacity hydrogen storage after the alkali doping⁸² and the strong electromechanical response under the charge injection.⁸³ The electronic properties show the strong dependence on edge structures and ribbon widths.^{84,85} The roles of quantum confinement, multi-orbital hybridizations, interlayer interactions and magnetic environments need to be clarified in the further calculations. Clearly, carbon nanoscrolls possess the flexible interlayer spaces to intercalate or to be susceptible to doping, indicating the high application potentials in electronic devices, energy storages, Li-batteries, and mechanical devices.

How to form carbon nanoscrolls with the non-uniform curvatures is worthy of a detailed investigation. The first-principles method is suitable in studying the combined effects due to the finite-size confinement, the edge-dependent interactions, the interlayer atomic interactions, the mechanical strains, and the magnetic configurations. The complex mechanisms

can induce the unusual essential properties, e.g., the optimal structures, magnetisms, band gaps and energy dispersions. To reach a stable spiral profile, the requirements on the critical nanoribbon width and overlapping length will be thoroughly explored by evaluating the W -dependent scrolling energies. A comparison of formation energy between armchair and zigzag nanoscrolls is useful in understanding the experimental characterizations. The spin-up and spin-down distributions near the zigzag edges are examined for their magnetic environments. This accounts for the conservation or destruction of spin degeneracy. The various curved surfaces on a relaxed nanoscroll will create the complicated multi-orbital hybridizations, so that the low-lying energy dispersions and energy gaps are expected to be very sensitive to ribbon width, especially for those of armchair systems. Finally, the planar, curved, folded, scrolled graphene nanoribbons are compared with one another to illustrate the geometry-induced diversity.

6.1 The optimal geometries

A carbon nanoscroll is a rolled-up graphene nanoribbon in the open form. It presents a spiral structure in the transverse cross section (the top view of the $y - z$ plane in Fig. 1), as well as a periodic arrangement along the longitudinal direction (the side view). Its geometry is characterized by two specific edges, an open and curved surface, and a overlapping region with an internal length. The initial and final edges are assumed to be passivated by hydrogen atoms (green balls) in the current calculations. For typical achiral systems, the number of armchair/zigzag lines on the scrolled surface can represent the total and internal lengths (red balls). (N_A, N_{in}) and (N_Z, N_{in}) , respectively, correspond to armchair and zigzag carbon nanoscrolls. The initial ideal structure, as shown in Figs. 1(a) and 2(b), is a perfect arch shape with a specific inter-layer distance. The optimal structures of carbon nanoscrolls are dependent on the initial conditions including ribbon widths and internal lengths (or inner diameters).

After the self-consistent constraint is imposed, an ideal arch structure is gradually changed

into an irregular shape. The relaxed scroll geometry, as clearly indicated in Figs. 1(b)-1(d) and Figs. 2(b)-2(d), is sustained by the layer-layer interactions and simultaneously counterbalanced by the strain forces. The reduced overlapping region caused by the insufficient width will hinder the formation of a carbon nanoscroll. The critical length is closely related to the inner length. Disregarding the periodic edge shape, all the interlayer distances are between 3.22 Å and 3.35 Å, and the average distance is about 3.34 Å. A deeper understanding shows that all the interlayer configurations in carbon nanoscrolls are similar/close to that of the bilayer AB-stacked graphene,²⁸⁹⁻²⁹¹ mainly owing to the higher cohesive energy in the AB stacking. Perceivably, a carbon nanoscroll can be presented as a stable structure, being determined by the sufficiently large width and overlapping length.

The formation of a carbon nanoscroll lies in two geometric parameters: the inner length and the scroll width. To hold the structure as a scroll, the required formation energy, the energy difference between the total energy of a carbon nanoscroll and that of a flat graphene nanoribbon, is defined as $E_{scr} = E_{int} + E_{bend}$. E_{int} is the energy arising from the interlayer atomic interactions in the overlapping region; meanwhile, E_{bend} is that due to the restoring force of the mechanic strain. It is obvious that the bending energy is larger than the interlayer interaction energy ($|E_{int}|$), i.e., $E_{scr} > 0$. Roughly, the former is inversely proportional to the square of the effective diameter, as obtained from the various curved nanoribbons (Eq. (1)) and carbon nanotubes.²⁴³ In addition, the significant edge-edge interactions in folded graphene nanoribbons (Sec. 5.1) are absent in carbon nanoscrolls.

The critical widths and internal lengths rely on the edge structure. Among armchair carbon nanoscrolls, the minimum/threshold width, being examined by the detailed calculations, is associated with the (34,7) system with the critical internal length $N_{in} = 7$. In general, with the increasing nanoscroll width, the overlapping region and the effective diameter grow simultaneously, leading to the enhanced inter-layer atomic interactions and the reduced bending energy. This is responsible for the declining behavior of the scrolling energy, as clearly indicated in Fig. 3(a). Within the width range of $N_A = 34 - 36$ (blue

diamonds), the interlayer distances are relatively large near the end of the overlapping region. The weaker interlayer interactions are reflected in a smaller and smoother variation of the scrolling energy. Concerning $N_A = 37 - 40$, a more stable AB stacking is reached in the optimal structure. Specially, the carbon atoms close to the final edge start to move towards the adjacent layer, so that the scrolling energy decreases more dramatically. In the further increase from $N_A = 41$, the scrolling energy begins with a slow change, but then evolves into a quick decline under the simultaneous cooperation of the interlayer interactions and bending energies. When the critical inner length grows, a wider critical width is required to form a stable nanoscroll. $N_{in} = 9$ and 11 (brown squares and green triangles), respectively, correspond to the minimum widths of $N_A = 43$ and 47. The enhancement of the interlayer interactions cannot effectively compensate that of the mechanical strain. The only way is to reduce the nanocroll curvature by the increment of the threshold width. In considering different inner lengths, it is concluded that all the scrolling energies have a similar dependence on width and a longer inner length corresponds to a lower energy. These results further illustrate the fact that a larger inner diameter results in a smaller bending energy, as discussed earlier.

The zigzag nanoscrolls are similar to the armchair ones in the width-dependent scrolling energy. Specifically, the smallest zigzag system is, as shown in Fig. 4(b), is (18,4) when the minimum inner length is $N_{in} = 4$ (blue diamonds). The scrolling energy exhibits the wave-like width dependence with the downward trend, mainly owing to the complex competition between the interlayer interactions and the mechanical strains. This indicates that both zigzag and armchair systems share a common dependence during the geometric variation. As for $N_{in} = 6$ and 8 (brown squares and green triangles), the threshold widths are $N_Z = 20$ and 22, respectively. Specially, the scrolling energies of zigzag nanoscrolls are much lower than those of armchair systems, mainly owing to the obvious differences in the overlapping region and curvature. This means that the former are relatively easily to be formed and become more stable in the experimental syntheses.

There exist important differences between carbon nanoscrolls and folded graphene nanoribbons in terms of the geometric structures and combined interactions. The former only present the stable AB stacking in the overlapping region, while the latter could reveal the AA, AB and other stackings. The inner diameters grow with the increase of nanoscroll width. However, they reach a saturated value for the wide folded nanoribbons. Such differences are closely related to the combined effects in the unique structures. Carbon nanoscrolls do not have the edge-edge interactions and the distinct magnetic configurations between two zigzag edges. On the other hand, the folding structures possess more complicated interactions. Their width-dependent formation energies exhibit the monotonously declining behaviors (Fig. ?), when they are characterized by the stacking configuration and the even or odd number of armchair/zigzag lines. That is, the diverse width dependences could be observed in folded graphene nanoribbons.

6.2 Electronic properties and magnetic configurations

Band structures are sensitive to edge structure and width, as displayed in Figs. 4 and 5. For armchair nanoscrolls (Fig. 4), the low-lying energy bands present three distinct types, based on the $N_A = 3I + 2$, $3I + 1$ and $3I$ widths. There are a lot of 1D parabolic bands with the asymmetric valence and conduction energy spectra. They are initiated from the $k_x = 0$ and/or 1 band-edge states. Furthermore, many band-edge states associated with the band mixings are situated at other k_x 's, revealing the complex interlayer atomic interactions and curvature effects. Specifically, the $N_A = 3I + 2$ armchair nanoscrolls have a pair of non-monotonous energy bands nearest to the Fermi level, e.g., the (38,7) system in Fig. 4(a). The highest occupied valence state and the lowest unoccupied conduction state occur at the same wave vector of $k_x = 0.1$, which, thus, leads to a direct energy gap, The similar energy dispersions are revealed in the $N_A = 3I + 1$ armchair nanoscrolls, such as the (40,7) system in Fig. 4(c). However, such systems have the smaller energy gaps (discussed later in Fig. ?), compared with the $N_A = 3I + 2$ ones. As for the $N_A = 3I$ armchair systems, they exhibit

a pair of weakly dispersive energy bands with the distinct extreme points near $k_x = 0$, e.g., the (39,7) system in Fig. 4(b). They belong to the indirect-gap semiconductors. It should be noticed that the unusual energy dispersions in determining the direct/indirect gaps are absent in the planar graphene nanoribbons (Figs. 4(d)-4(f)).

Electronic structures of zigzag carbon nanoscrolls are enriched by the magnetic configuration. The anti-ferromagnetic spin arrangements is clearly revealed at the initial and final zigzag edges, as shown in Fig. 5(a) for the (36,4) system. For the distinct spin states, the H-passivated carbon atoms at two open ends experience the different interactions with the surrounding atoms. This is responsible for the four spin-split energy bands nearest to the Fermi level, e.g., the spin-up and spin-down states represented by the red and blue curves in Fig. 5(b), respectively. Such bands, with the weak energy dispersions, belong to the edge-localized states, as observed in planar zigzag ribbons (Fig. 5(c)). They will determine two kinds of spin-dependent direct energy gaps. For example, the spin-up and spin-down energy gaps are 0.18 eV and 0.23 eV, respectively. The other energy bands remain the double spin degeneracy, indicating that the distinct magnetic environments only affect the low-lying electronic states. In comparison, the flat systems, with the antiferromagnetic configuration across two zigzag edges (Fig. ?), present the spin-degenerate energy bands under the equivalent magnetic environment.

The low-lying energy bands are closely related to the orbital bondings on the curved and planar surfaces. Armchair and zigzag carbon nanoscrolls will present the similar and distinct charge distributions (Figs. 6(a) and 6(b)), and so do the orbital hybridizations. The spatial charge density is very sensitive to the surface profile. As for the planar region of the armchair (38,7) nanoscroll, resembling a flat nanoribbon as enclosed by the rectangle in Fig. 6(a), the $(2s, 2p_x, 2p_y)$ orbitals of a carbon atom interact with those of the nearby ones to form the σ bonds ((I) in orange shades).

6.3 Comparisons among the planar, curved/zipped, folded and scrolled systems

The flexible carbon honeycomb lattice can be presented in the various forms under a very strong σ bonding. Such structures create the diverse essential properties and thus induce the important differences among the planar, curved, folded, and scrolled graphene nanoribbons. For armchair nanoribbons, only part of the curved systems exhibit the 1D metallic property, mainly owing to the very edge-edge interactions. The similar behavior is revealed in the even-zAA stacking of the folded zigzag systems. The valence and conduction bands, which determines the metallic or semiconducting property, are very sensitive to the geometric structure. All the planar and folded armchair systems have the parabolic bands with direct energy gaps at $k_x = 0$. However, the curved and scrolled ones might possess the non-monotonous energy dispersions with direct or indirect energy gaps. Those of zigzag systems belong to the partially flat edge-localized bands at $k_x > 2/3$. An obvious spin splitting appears near the Fermi level when the magnetic environments are different for spin-up and spin-down states near the open edges, e.g., the folded odd-zAB and scrolled zigzag nanoribbons. Specially, only the folded even-zAB stacking presents a pair of linearly intersecting energy band at $k_x \sim 2/3$, as observed in armchair carbon nanotubes.

The width dependences of energy gaps are greatly enriched by the geometric structures. There are three categories in the planar and scrolled armchair nanoribbons, but six categories in the folded systems. In addition to $N_A = 3I$, $3I + 1$ and $3I + 2$, the last ones also depend on the odd/even number of dimer lines. For $N_A = 3I + 2$, the planar systems have the smallest energy gaps because of the finite-size confinement. However, the opposite is true for the scrolled systems under the combined effects. In comparisons among the various pristine systems, the highest energy gaps are revealed in the even-aAA' folded armchair nanoribbons of $N_A = 6I + 4$. As to zigzag nanoribbons, only the scrolled and odd-zAB folded systems present the spin-split energy gaps. The width-dependent declining behavior is obvious except for the folded even-zAB stacking systems with the strong edge-edge interactions.

Furthermore, the wave-like fluctuation comes to exist in the scrolled systems.

7. Bilayer graphene nanoribbons

Few-layer graphene nanoribbons have been synthesized by cutting graphene,^{5,13} unzipping multi-walled carbon nanotubes,^{19,22} and chemical vapor deposition.³⁵ They will present quite different essential properties compared with monolayer systems, mainly owing to the number of layers, the various stacking configurations, and the distinct interlayer spin distributions. Specially, the variation of stacking configuration could be initiated by the STM tip to overcome the Van der Waals interactions. Up to now, the electrostatic-manipulation STM is successfully performed on a highly oriented pyrolytic graphite surface,¹⁰² graphene/graphite flakes,^{103,104} and trilayer graphene,¹⁰⁵ clearly indicating the transformation of stacking configuration. The sliding bilayer graphene nanoribbon is expected to be achieved by this method. As for the previous theoretical studies, most of them are focused on bilayer graphene nanoribbons, especially for the typical AA and AB stackings.¹⁰⁶⁻¹⁰⁹ The calculated results show that stacking configurations play important roles in essential properties. However, the theoretical predictions are not consistent with one another with regard to the existence of magnetism and the planar/non-planar geometry. The controversies might lie in the calculations of the optimal geometric structures. In this work, a thorough study is conducted on bilayer zigzag graphene nanoribbon by varying the stacking and spin arrangements.

Modulating stacking configuration is one of the efficient ways to diversify the essential properties of the layered graphene-related systems. The bilayer zigzag graphene nanoribbons are suitable in understanding the combined effects due to the stacking configuration, edge-edge interaction, finite-size confinement, intralayer and interlayer spin arrangements. The relative shift of the upper and lower layers is predicted to create the dramatic transformations in stacking symmetries and electronic properties.¹⁰¹ The shift-enriched geometric profiles, edge-edge distances, interlayer distances, energy dispersions, band gaps/band overlaps, band-

edge state energies, van Hove singular structures in DOS, magnetic moments, magnetic configurations, and spin-split electronic states are explored in detail. The relatively/most stable configuration, the width-dependent asymptotic behavior, the existence of magnetism, and the metal-semiconductor transition are considered in the delicate calculations. A detailed comparison between bilayer 1D graphene nanoribbon and 2D graphene is also made for illustrating the dimension-dominated diverse properties.

7.1 Stacking-enriched geometric structures and magnetic configurations

Bilayer zigzag graphene nanoribbons, with hydrogen passivation (red balls), are chosen to investigate the effects due to the stacking configurations, the van der Waals interactions, and the spin distributions. The various shift-dependent stackings are considered in the calculations. The upper and lower layers, respectively, correspond to green and brown circles, as shown in Fig. 1(a). Each nanoribbon has two sublattices A and B, indicated by solid and hollow circles, respectively. The four high-symmetry stacking configurations cover AA, AB_α , AA' , and AB_β (Figs. 1(b)-1(e)). The similar geometric structures could also be observed in folded graphene nanoribbons (Sec. 5.1). As a result of the 1D finite-width confinement, the AB-stacked systems present two edge-related configurations, AB_α and AB_β (Figs. 1(d) and 1(e)). The hydrogen atoms in the AA and AB_α stackings are projected on the same line; however, those in the AA' and AB_β ones are staggered on the distinct lines

After the detailed self-consistent calculations, bilayer zigzag systems exhibit the rich geometric properties, as clearly shown in Fig. 2. Both AA and AB_α stackings have the arch-shaped structures in the side view (the $N_Z = 10$ systems in Figs. 2(a) and 2(b)). The upper and lower nanoribbons of the former bend in the opposite directions with a convex profile. However, a wave-like profile, with the same bending manner, is revealed in the latter. The interlayer distances are shorter near two open edges involving twelve carbon atoms, compared with those in the central region. Specially, the degree of bending in terms of the scope

is insensitive to the nanoribbon width. The edge-edge atomic interactions are thus expected to play important roles in certain essential properties. On the other side, the AA' and AB_β stackings possess the nearly flat profiles, as observed in monolayer systems. The interlayer distances almost remain uniform from the edge to the central region. Apparently, the arched structures strongly correlate to the interlayer distances. As for (AA,AB_α,AA',AB_β) stackings, the interlayer distances are, respectively, (3.00, 3.10, 3.72; 3.76 Å) and (3.70, 3.43, 3.71; 3.75 Å) at the boundary and central regions.

The magnetic properties are diversified by the bilayer stacking configurations. The AA and AB_α stackings do not have any magnetic moments on the open zigzag edges, while the opposite is true for the AA' and AB_β ones. Furthermore, the magnetic moments hardly depend on the relative displacement between the former two or the latter two (Path I or II discussed later). This stacking-induced difference could be comprehended from the dependence of magnetic moment on the edge-edge distance, as clearly indicated in Fig. 3. The former two exhibit a similar d_{edge} -dependence (open circles and squares for AA and AB_α, respectively). Magnetic moments vanish for $d_{edge} < 3.2$ Å, but appear with a strength of $0.15 \mu_B$ for $d_{edge} > 3.9$ Å. Contrarily, those of the latter two keep a saturated value of $\sim 0.15 \mu_B$ (solid diamonds and triangles), as a result of the large initial edge-edge distance (> 3.7 Å). Moreover, the d_{edge} -dependent magnetic moments behave similarly for the four types of spin arrangements in AA' and AB_β stackings. The typical intralayer and interlayer spin arrangements are characterized by (I) AFM-AFM (antiferromagnetic and antiferromagnetic configurations, respectively in Fig. 3(b)), (II) FM-AFM, (III) AFM-FM, and (IV) FM-FM. Both AFM-AFM and AFM-FM bilayer zigzag nanoribbons, like an AFM monolayer system, are suitable for a model investigation because of the lower ground state energies.

The cohesive energy, the energy difference between the total energy of bilayer graphene nanoribbons and that of two decoupled subsystems, can identify the relatively stable stacking configuration. E_{coh} strongly depend on the relative displacement (d_y) between the upper and lower layers, in which two typical paths along the armchair direction (Fig. 1(a)) are

(I) $AA \rightarrow AB_\alpha$ and (II) $AA' \rightarrow AB_\beta$. Along Path I in the absence of magnetism, the d_y -dependent cohesive energy presents the non-monotonous behavior, being classified into two regions by the critical displacement ($d_{edge} < d_c$ and $d_{edge} > d_c$), as shown in Fig. 4(a) for the $N_Z = 10$ systems (open circles). d_c (1.06 Å) is smaller than the C-C bond length ($b=1.42$ Å). The bilayer AA stacking, with $d_y = 0$, possesses the largest edge-edge interaction and the smallest stacking effect. With the increasing displacement, the edge-edge interaction and the stacking effect, respectively, declines and grows until $d_y = b$ (AB_α). Their strong competition determines the relative stable configuration beyond the AB_α one in the sense that the latter is not the only dominating mechanism. This configuration exists in between the AA and AB_α stackings, but closer to AB_α . In another region, the cohesive energy increases with the displacement until $d_y = 3b/2$. The edge-edge interaction is largely reduced and thus the stacking effect makes the major contribution.

Along Path II under the same magnetism, the shift-dependent cohesive energy mainly arises from the composite stacking, edge and spin effects. With the increasing d_y , E_{coh} quickly declines until $d_y = b/2$ (AB_β), and then gradually reaches a minimum at $d_y = 0.84$ Å (Fig. 4(a)). Furthermore, it starts to rebound and present a local maximum at $d_y = 3b/2$ (AA). The relatively stable configuration is slightly away from the AB_β stacking, owing to the smaller energy difference due to the interlayer interactions near the central and boundary regions, and the spin arrangements. Specially, there exists two stable spin configurations, AFM-AFM and AFM-FM, being distinguished by the interlayer spin arrangements. The former has the lower ground state energy at $d_y < b/2$ (open diamonds), in which their energy difference is not significant. The latter becomes more stable in a further increase of shift (open squares). That is to say, a variation of stacking configuration can create a transformation of interlayer spin arrangement.

The combined effects are responsible for the shift process of bilayer zigzag graphene nanoribbon. The relative stable configuration is determined by the strong competition among the stacking configurations, the edge-edge interactions and the spin arrangements. The crit-

ical shift (d_{yc}), corresponding to this configuration, presents an obvious change when ribbon width grows from $N_Z = 4$, as shown in Fig. 4(b). Along Paths I and II, d_{yc} 's, respectively, approach to b and $b/2$ at sufficiently large widths (open circles and squares/diamonds). This clearly indicates that with an increased width, the configuration of bilayer nanoribbon will change into the AB stacking, as observed in 2D graphene system. The width-dependent asymptotic behavior lies in the enhanced stacking effect, while it hardly depends on the inter-edge interactions and the magnetic configurations. That is, it directly reflects the reduced quantum confinement effect. Specially, for any ribbon widths, the most stable configuration exists between AA and AB_α stackings in Path I, according to the lowest cohesive energy.

7.2 Diverse electronic properties

The combined effects can create the rich and unique electronic properties. The band structures near the Fermi level are dominated by the $2p_z$ -orbital hybridizations. For the $N_Z = 10$ AA-stacked bilayer nanoribbon, the higher/deeper parabolic bands exhibit the anti-crossing behavior with extra band-edge states as a result of the interlayer atomic interactions. Such interactions also result in two pairs of low-lying conduction and valence bands across E_F . Specially, there exist the fourfold-degenerate states (including two spins) near the zone boundary for $E^c = 0.51$ eV and $E^v = -0.85$ eV. These bands are partially flat and mostly contributed by the local edge atoms (open circles), as observed in monolayer nanoribbon. One pair of energy bands linearly intersects at the Fermi momentum, indicating the metallic property with a finite DOS at E_F . They behave as those in even-zAA stacking of folded zigzag system (Fig. ?). Electronic states near K_F are dominated by all carbon atoms, in sharp contrast to the edge-localized states near the zone boundary. The Fermi-momentum states mainly come from the largely enhanced edge-edge interactions under the arc-shaped edge structures (Fig. 2(a)). This is clearly identified from the loop-like charge density in Fig. 5(e), especially for the continuous evidences around two boundaries. The significant chemical bonding between

two arc-shaped zigzag edges causes the Fermi-momentum states to be similar to the Dirac points in an armchair carbon nanotube (Fig. ?).

A relative shift between two layers strongly changes the edge-edge interaction, leading to the dramatic transformation of band structure. Two linearly intersecting energy bands become a pair of anti-crossing parabolic bands for various shifts along Path I, as clearly shown in Figs. 5(b)-5(d). Such bands have a direct energy gap between the highest valence state and the lowest conduction state near $k_x = 2/3$. Obviously, the metal-semiconductor transition appears during the modulation of stacking configuration, as observed between the even-zAA and even-zAB stackings in folded zigzag nanoribbons (Fig. ?). This directly reflects the weakened inter-edge chemical bonding under a larger distance (Fig. 5(f)?). However, the fourfold degeneracy of the low-lying bands near the zone boundary keeps the same. The higher/deeper energy bands are slightly affected by shift, since they are closely related to the intralayer and interlayer atomic interactions.

The distinct magnetic configurations can diversify the electronic structures in terms of band gap and spin degeneracy. The low-lying energy bands in Path II, being composed of parabolic and partially flat dispersions, strongly depend on the interlayer spin arrangements. For the AA' stacking with AFM-AFM, they are doubly degenerate except for the fourfold-degenerate states near the zone boundary. An indirect-gap semiconductor arises from two anti-crossing bands nearest to E_F , as shown in Fig. 6(a) for $N_Z = 10$ with $E_g^i = 0.2$ eV. Specially, the double and fourfold degeneracies would be broken under the relative displacement, since the environment of the spin-up distribution gradually deviates from that of the spin-down one in the increase of d_y from zero (e.g., Fig. 3(b)). The AB_β stacking (Fig. 6(b)) exhibits the spin-split energy bands, as observed in odd-zAB folded zigzag nanoribbons (Fig. ?) and zigzag nanoscrolls (Fig. ?). The spin-up and spin-down energy gaps are opened up by modulating the stacking configurations. On the other hand, the energy bands of AA' stacking (Fig. 6(c)), with AFM-FM, are mostly doubly degenerate and occasionally fourfold degenerate near the zone boundary. The stacking variation does not break the spin degen-

eracy, reflecting the same magnetic environment of the spin-up and spin-down states under the various shifts along Path II (Fig. 3(b)). However, the fourfold degeneracy is separated into two doubly degeneracies, and an indirect energy gap might become a direct one.

The band-edge states in bilayer systems appear as the van Hove singularities diversified by the stacking configurations. For the AA stacking, the low-energy DOS, as shown in Fig. 7(a), presents a plateau structure across E_F , two prominent peaks on either side of E_F (solid and hollow squares), and some square-root asymmetric peaks (diamonds and triangles). Such special structures are, respectively, associated with the linear, partially flat bands and parabolic bands (Fig. 5(a)). A constant DOS at E_F clearly indicates the metallic behavior, as observed in armchair carbon nanotubes (Fig. ?) and even-zAA folded zigzag nanoribbons (Fig. ?). However, the AB_α stacking has a narrow direct gap determined by two separate peaks across E_F (solid and hollow circles in Fig. 7(b)). The similar structures are revealed in the AA' stacking with AFM-AFM (Fig. 7(c)). During the shift from AA' to AB_β stackings, the destruction of spin degeneracy leads to the spin-up and spin-down peaks (red and blue marks in Fig. 7(d)). The interlayer spin arrangement only has a weak effect on the number and energy of peak structures in the AA' -stacked systems. The AFM-FM and AFM-AFM configurations both exhibit the similar DOSs (Figs. 7(e) and (c)). With the increase of shift, the number of prominent peaks is drastically changed, e.g., two conduction and two valence peaks in the AB_β stacking with AFM-FM (squares in Fig. 7(f)).

The band-edge states, with the relatively high DOSs, can create the strong perturbation responses and thus dominate the measured physical quantities, such as, tunneling currents in STS, Coulomb excitations, optical absorptions, and electrical conductivities. Their energies ($E_{be}^{c,v}$), as clearly shown in Figs. 8(a)-8(c), rely on the various stacking configurations. They are characterized by circles, diamonds, squares and triangles, based on how close to the Fermi level. The former three arise from the composite bands with parabolic and partially flat dispersions, in which the third ones are due to the edge-localized states near the zone boundary. Furthermore, the conduction and valence states are identified by the hollow and

solid symbols, respectively. The energy difference between E_{be}^c and E_{be}^v , both being nearest to E_F (hollow and solid circles), is energy gap. As for Path I, E_g increases with d_y , then reaches a maximum value at $d_y \sim 1.1 \text{ \AA}$, and finally decreases in the range of $1.1 \text{ \AA} < d_y < 1.7 \text{ \AA}$ (black circles in Fig. 8(d)). Specially, the spin-up and spin-down state energies are distinguishable in Path II with AFM-AFM (Fig. 8(b)), e.g., those with the prominent peaks in DOS (red and blue squares in Fig. 7(d)). The spin-up energy gap (red circles in Fig. 8(d)) grows with shift until $d_y \sim 0.9 \text{ \AA}$, and declines in the further increase of d_y . However, the spin-down one present the opposite dependence (blue circles in Fig. 8(d)). The spin splitting is absent in Path II with AFM-FM (Fig. 8(c)), while the degenerate edge-localized state energy might be split under the variation of d_y (black squares). The energy gap exhibits the strongest d_y -dependence (green circles in Fig. 8(d)); that is, E_g possesses the largest value at $d_y \sim b/2$, and is sensitive to a change in the stacking configuration.

7.3 Differences between bilayer 1D and 2D systems

The distinct dimensions can greatly diversify the essential properties, being illustrated by the significant differences between bilayer 2D graphene and 1D graphene nanoribbon. When bilayer graphene, as shown in Fig. 9(a), shifts from the AA stacking along the armchair direction, it gradually approaches to the AB stacking at $d_y = b$, and then it reaches the AA' until $d_y = 3b/2$. Apparently, layered graphene, with a uniform interlayer distance, presents a planar structure, but not an arc-shaped profile. With the shift of AA→AB→AA', I_z varies as $3.53 \text{ \AA} \rightarrow 3.35 \text{ \AA} \rightarrow 3.45 \text{ \AA}$ (solid triangles in Fig. 9(b)). The highest and the lowest total ground state energies (hollow circles), respectively, correspond to the AA and AB stackings; therefore, the latter is the most stable configuration. They are fully dominated by the interlayer van der Waals interactions, and the edge- and spin-dependent interactions are absent in 2D systems.

Band structures of bilayer graphene are dramatically changed during the variation of stacking configuration. The AA stacking, as clearly displayed in Fig. 10(a), has two pairs of

valence and conduction Dirac cones intersecting at the same K point (the corner of the first Brillouin zone). It is a semimetal with the strong band overlap; that is, there are free holes and electrons, respectively, arising from the valence cone of the first pair and the conduction cone of the second pair. It should be noticed that the free carrier density in bilayer graphene ($\sim 10^{12} - 10^{13} \text{ e/cm}^2$) is low, compared with that of a 2D metal ($\sim 10^{14} \text{ e/cm}^2$). The 2D free carrier density, being purely induced by the interlayer atomic interactions of the $2p_z$ orbitals,^{290,298} is highest in the AA stacking among all the bilayer systems. With an increased shift, the vertical Dirac-cone structures become distorted, and an arc-shaped stateless region appears near the Fermi level, as shown in Fig. 10(b) at $d_y = b/8$. This region grows rapidly, and the gapless Dirac points start to separate at $d_y = 4b/8$ (Fig. 10(c)). After this drastic change, two pairs of well-behaved parabolic bands are formed in the AB stacking ($d_y = b$ in Fig. 10(d)). The similar effects, the strong mixings of energy bands and the arc-shaped region, are revealed in the further increase of d_y ($d_y = 11b/8$ in Fig. 10(e)). Furthermore, the Dirac-cone structures are gradually recovered. Finally, two pairs of isotropic cone structures are presented in the AA' stacking ($d_y = 3b/2$ in Fig. 10(f)), in which they have the tilted axes with the non-vertical Dirac points. They contrast sharply with the vertical Dirac-cone structures in the AA stacking (Fig. 10(a)).

The special structures of the van Hove singularities in DOS are determined by the dimensions. The low-energy DOS, as clearly indicated in Figs. 11(a)-11(f), is finite at $E_F = 0$ for all the stacking configurations, further illustrating the semi-metallic behavior of bilayer graphene. It is largest in the AA stacking with the strongest band overlap. The bilayer 2D graphene can exhibit the V-shape structures, the broadening shoulders, and the symmetric peaks, respectively, corresponding to the isotropic Dirac cones; the extreme points and the saddle ones in the energy-wave-vector space (the band-edge states of parabolic bands).^{290,298,299} Specially, both AA and AA' stackings present the coexistent plateau and cusp (Figs. 11(a) and 11(f)), since they are the superposition of two V-shape structures with the different Dirac-point energies (the distinct initiated energies). A composite structure and

a pair of shoulders are revealed in the $11b/8$ stacking (Fig. 11(e)), reflecting the complicated low-lying bands. The latter also appears in the AB stacking (Fig. 11(d)). Specially, the symmetric peaks, being associated with the highly distorted energy bands, could be observed in the $b/8$ and $4b/8$ stackings (Figs. 11(b) and 11(c)).

There are a lot of significant differences between bilayer graphene and graphene nanoribbon. The finite-size confinement, edge structure and spin distribution are absent in the former, and so do the non-planar structure, edge-dependent chemical bonding, partially flat edge-localized bands, spin-split electronic states, energy gap, and magnetic moment. The most stable configuration of the former is the AB stacking, while that of the latter deviates from it. The former and the latter belong to semimetals and semiconductors/metals, respectively. Most of 1D nanoribbons present the direct or indirect energy gaps. Specifically, the linear bands in 2D and 1D systems, respectively, create the semi-metallic and metallic behaviors as a result of dimension-dominated carrier density. Graphene nanoribbons might have the intralayer and interlayer spin arrangements near the zigzag edges, leading to the magnetism-enriched band structures and DOSs. The special structures in 2D and 1D DOSs, respectively, appear as a composite plateau and cusp/ shoulders/symmetric peaks and a plateau/asymmetric peaks/prominent peaks, being induced by the critical points in the energy-wave-vector spaces.

8. Edge-decorated graphene nanoribbons

The open edges of graphene nanoribbons, with the dangling bonds, are available in modulating the essential properties by the adatom decorations. The strong chemical bondings between adatoms and carbons might reconstruct the edge structures and thus dramatically change the electronic properties. During the chemical synthesis of graphene nanoribbons, the monoatomic molecules could be attached to the edge carbon atoms, e.g., H^{110} and O .¹⁹ Furthermore, the edge chlorination of graphene systems has been achieved under the specific

chemical methods.¹¹¹ The H-decorated $N_A = 7$ armchair nanoribbon, with planar and open edges, is identified from the STM measurements and simulations. The oxygen passivation appears in the unzipping of carbon nanotube using $\text{KMnO}_4/\text{H}_2\text{SO}_4$, in which the O-C bonds are examined by the XPS measurements. The open and distorted edge structures, with the stacking configurations, in the chlorinated graphene nanoribbons and nanographenes are confirmed by the X-ray single-crystal diffractions. Furthermore, the XPS analyses present the strong evidences of the Cl-C bonds. In addition to the well-known H adatoms, some elements are predicted to be stable in the edge passivation, such as, K,¹¹² F^{113,114} O,^{115,116} B,¹¹⁷ Mg,¹¹⁷ Ru,¹¹⁸ Te,¹¹⁹ and transition metal.¹²⁰ Such studies are mainly focused on the modulation of electronic properties under specific planar configurations. These edge-decorated systems may be 1D metals or semiconductors. There also exist a few investigations done for the most stable configurations of the edge-decorated systems.^{121–123} When the curved and flat graphene nanoribbons are successfully produced through chemical methods by unzipping carbon nanotubes,^{19,20,29–31} the adatom decorations might occur simultaneously during the strong reaction processes. The curved structures and dangling bonds provide a very suitable environment for modulating the geometric structures and electronic properties. The previous calculations show that the combined effects arising from the curvature and adatom passivation play critical roles in the diversified essential properties,¹²⁷ especially in the tubular/curved/flat structures and the metallic/semiconducting behaviors. Apparently, a systematic study is indispensable in understanding the chemical functionalization of nanomaterials.

How to diversify geometric structures and electronic properties by the edge passivation could be thoroughly investigated using the first-principles calculations (Sec. 8.1). The decoration adatoms, with atomic numbers lower than twenty in the periodic table, are chosen to make a systematic study, since they tend to form the most stable configurations. Many symmetric configurations of adatom-decorated armchair nanoribbons are examined to achieve the most stable one. The X-C and X-X bond lengths, planar or nonplanar structures, ad-

sorption energies, charge transfers, energy gaps, band structures, and density of states are evaluated in detail. How many types of geometric structures are obtained from the various adatom decorations. The edge-carbon- and adatom-dominated energy bands, the adatom- and C-orbital-decomposed DOSs, and the edge charge distributions are useful in understanding the decoration effects due to the significant C-C, X-C and X-X bondings, e.g., the drastic changes in the width dependences of energy gaps and the special structures of DOS.

The adatom decoration during the unzipping of carbon nanotube can present the edge-passivation and curvature effects and thus the rich essential properties (Sec. 8.2). Armchair carbon nanotubes and highly curved/planar zigzag graphene nanoribbons are suitable for a model study. Decorating adatoms, which have atomic number of lower than 30 and are capable of bonding with edge carbon atoms, are used to systematically investigate the optimal geometric structures, depending on the X-C distances, X-X distances, charge transfers, and edge-atom interactions. The magnetic configurations in zigzag edges and ten transition metal elements are taken into consideration. The bending strains induced by the curvature increase the total energy, while the edge-edge interactions reduce or enhance the total energy. The competitive or cooperative relationship between these two effects that decides the resulting decorated structure will be explored in detail by the simulation model. The curvature effect and the decorating atoms will give rise to the feature-rich electronic properties, especial for the low-lying energy band and the metallic/semiconducting behaviors. The DOSs at the Fermi level are compared with those of metallic carbon nanotubes, and they might be potentially important in various applications.

8.1 Adatom edge passivations

The $N_A = 8$ armchair graphene nanoribbon is chosen as a representative system, in which an unit cell contains 4 adatoms and 16 carbon atoms. The armchair boundaries are relatively easy in creating the edge reconstruction, compared with the zigzag ones. Elements, with an atomic number of less than 20, can serve as the edge-passivated adatoms to fully

illustrate the decoration effects. An obvious charge transfer, being induced by the significant chemical bondings between the edge carbon atoms and the adatoms, is evaluated from the Bader analysis method. Moreover, the adsorption energy, the reduced total energy due to the adatoms bonding with the edge carbons, is characterized as the total energy difference between an edge-decorated graphene nanoribbon and two independent sub-systems (pristine nanoribbon and isolated adatoms). Specially, the former might have part of the total energy arising from a mechanical strain. In addition, the delicate calculations on the various total energies are done for the same unit cell.

With the detailed relaxation calculations, a lot of symmetric configurations have been examined for distinct passivation atoms. The most stable structure, as clearly illustrated in Figs. 1(a)-1(c), corresponds to each adsorbed element in the state of the lowest total energy. According to the planar distortions/reconstructions and the edge-atom arrangements, the optimal geometric structures could be classified into three types: type I, type II, and type III. The main features, the geometric profiles, charge distributions and charge transfers, are discussed as follows.

Adatoms, which can create the planar edge-decorated systems, cover H, N, Be, and B (Fig. 1(a)). The H-decorated nanoribbon has a regular honeycomb lattice with the H-C bond length of 1.08 Å. A tiny electric charge of ~ 0.02 e is transferred from H towards the outermost C atom (Table 1), revealing a covalent H-C bond. Furthermore, this bond only appears as a protruding edge structure, but not one part of a polygon. That is to say, the H adatoms cannot bridge the strong interactions of carbon atoms on the neighboring edge dimers. Apparently, the 1s orbital is not sufficient in creating the multi-chemical bondings. On the other hand, the unusual bridging effects are clearly revealed in the other type-I systems as the distinct closed profiles (the different polygons).

The N-decorated graphene nanoribbon presents a periodic heptagon-pentagon edge structure, accompanied with the regular hexagons (Fig. 1(a)). A significant reconstruction occurs after edge absorption, in which this composite profile has the non-uniform chemical bonds.

The N-C bond lengths in the heptagons and pentagons are, respectively, 1.30 Å and 1.28 Å (Table 1). However, the C-C bond length near the ribbon center agrees well with that of pristine graphene (~ 1.42 Å). N has the higher electronegativity, compared with C. More electrons are distributed closer to the adatoms, as clearly illustrated by a strong covalent bonding in Fig. 2(a) (red region). Each N adatom is estimated to gain extra 3.13 e and 2.77 e in heptagonal and pentagonal regions, respectively. Specially, the Be adatoms can bond with the C atoms at the same and neighboring dimers simultaneously, so that a closed triangle-pentagon edge structure is formed at each edge. The original honeycomb lattice almost keeps the same. The Be-C bond lengths are 1.73 Å and 1.85 Å in the triangular and pentagonal parts, respectively. Each Be adatom contributes two outmost valence electrons to the bonding carbon atoms (2 e in Table 1). The full charge transfer indicates the highly ionic behavior of adatom. As for the B-decorated system, the non-uniform pentagons, with B-C and C-C bonds, appear at the edges. The B-B bonds, with a length of 2.00 Å, play a critical role in creating the closed edge structures. Each B adatom transfers ~ 1.48 e to the neighboring C atom, indicating a significant covalent bonding. As for the type-I systems, the unusual adatom-dependent edge morphologies are closely related to the atomic radii and the number of valence electrons.

Type-II systems present the open and distorted edge structures, as predicted in an oxygen-decorated system.^{121,123} Their total ground state energies are mainly determined from the competition of the edge bonding and the mechanical distortion. According to the lowered total energies (Table 1), the former can effectively suppress the latter. There exist two stable configurations, namely, X_{same} - and X_{opp} -decorated armchair nanoribbons (Fig. 1(b)), compared to the higher-energy planar configuration. X represents a certain kind of adatom. The X-C bonds exhibit the opposite distortions in the periodic form along the edges. As to the corresponding X-C bonds placed across the nanoribbon center, they are located at the same z -position for the former, while the opposite is true for the latter. Specially, these two configurations only have a small total energy difference of a few meVs. The

lower-energy X_{same} -decorated systems, without magnetism, are suitable for a model study.

The neighboring X-C bonds, as shown by the O- and S-decorated systems, possess the opposite distortions along the armchair edges. For the F and Cl adatoms, the first two attached with a carbon dimer lie above the ribbon plane while the following two are situated at the opposite position, and so on. Among these four kinds of adatoms, only the O-decorated system presents a higher-energy planar structure, with two closed heptagon-pentagon edges, as observed in the N-decorated system (Fig. 1(a)). Specially, the type-II oxygen passivation creates a short O-C bond length of 1.22 Å, with a high charge distribution by a strong covalent bonding. The bond lengths grow with the atomic number for the same group in the periodical table, such as, S-C > O-C and Cl-C > F-C (Table 1). With higher electronegativities, O and F can attract 1.73 e and 0.78 e from the neighboring carbon atom, respectively. Moreover, the cross section of the charge distribution, as shown in Fig. 2(b), illustrates the covalent bondings in sulfur dimers and S-C bonds. In addition, it might have certain chemical bonding between two S adatoms associated with the neighboring dimers (green color).

The type-III systems, which consist of much bigger adatoms ($X = \text{Li, Na, K, Ca, Mg, Al, Si, and P}$), are characterized by the distorted and closed edge structures, as shown in Fig. 1(c). The adatoms symmetrically stack up in the distorted pentagons, accompanied with the uniform carbon hexagons. All of them could transfer part of valence electrons to the bonding carbon atoms (Table 1), especially for Li, Na and K. Alkali adatoms have the lower electronegativity ($\sim 3/5$), compared with carbon atom. For example, the atomic interactions in the Li-C bonds are highly ionic, since most of valence charges are distributed closer to the edge C atoms (Fig. 2(c)). The attractive interactions in the X-C bonds compete with the repulsive ones in the stacked adatoms; therefore, their competition determines the optimal X-C and X-X bond lengths. Among type-III systems, the P-decorated system has the shortest X-C and X-X bonds, indicating the significant atomic interactions (Fig. 2(d)). This directly reflects more valence charges in the P adatoms.

In general, the geometric structures of the edge-passivated graphene nanoribbons are

dominated the complicated cooperation/competition of the atomic interactions among the C-C, X-C and X-X bonds. Whether the edge decorations could be achieved in the experimental growth strongly depend on adsorption energies. E_{ads} 's are respectively, -5.881 eV, -5.776 eV, -5.500 eV, and -4.795 eV in the N-, O-, B-, and F-decorated systems, in which they are lower than that (-4.359 eV) of the H-decorated system frequently utilized in the experimental measurements. According to the detailed theoretical predictions, the first one exhibits the lowest adsorption energy among all the systems. On the other side, it might be difficult to synthesize the Na- and Ca-decorated systems with the higher adsorption energies of -0.732 eV and -0.819 eV, respectively. Up to now, some adatoms, which are as stable as a diatomic gas, have been applied to passivate the nanoribbon edge in a monatomic form, such as H,¹¹⁰ O,¹⁹ and Cl.¹¹¹ The open and distorted edge structures are confirmed by using the STM measurements and the X-ray single-crystal analyses. The experimental syntheses on the other adatom-decorated systems are useful in identifying the diverse geometric structures, covering the triangle-pentagon, pentagon-heptagon, and hexagon edges in planar profiles, and the edge-buckled and adatom-stacked-up configurations.

The strong orbital hybridizations in various chemical bonds, combined with the finite-size effects, can greatly diversify the electronic properties. A pristine $N_A = 8$ armchair nanoribbon, as shown in Fig. 3(a), exhibits an indirect band gap of $E_g^i = 0.473$ eV. The highest occupied state and the lowest unoccupied state are situated at $k_x = 0$ and 1, respectively. The former and the latter are, respectively, dominated by the non-edge and edge carbon atoms (distinguished by the black circles. 3(a)). Moreover, the dangling bonds at the edges are responsible for two pairs of valence and conduction bands (discussed earlier in Fig. ?). The main features of band structures, atom dominance, energy dispersion and band gap, are dramatically changed after the significant edge passivation, as clearly indicated in Figs. 3(b)-3(c). Apparently, the edge-carbon-dominated energy bands disappear in the presence of X-C bonds, i.e., the absence of dangling bonds will thoroughly modify the electronic structures.

The low-lying energy bands depend on the kinds of adatoms. The N-decorated system presents the linear and non-monotonous energy dispersions near the Fermi level, being associated with carbon atom and adatoms (inset in Fig. 3(b)). Their band edge states at $k_x = 0$ determine a narrow direct gap of $E_g^d = 0.04$ eV. Specially, the N adatoms make much contribution to four valence bands in the range of $-1.6 \text{ eV} \leq E^{c,v} \leq -0.9 \text{ eV}$, in which they are almost doubly degenerate and have weak energy dispersions (blue circles). As for the S-decorated system, there exists a pair of energy bands with parabolic dispersions close to $k_x = 0$ (Fig. 3(c)). The smallest energy spacing is a middle direct gap of $E_g^d = 0.395$ eV. The S adatoms dominate the shallowest two valence bands (large yellow circles) except for the electronic states near the highest occupied one. Moreover, they contribute to some valence and conduction bands. Unusually, the Li adatoms could create the semiconductor-metal transitions; that is, the Li-decorated system might become a 1D metal (Fig. 3(d)). The lowest conduction band overlaps with the two highest valence bands; the latter are associated with the Li adatoms (green circles). Some free electrons and holes, respectively, occupy the lowest conduction band and the highest valence one. Such a band overlap is also revealed in Na-, K-, Ca-, Mg-, and Be-passivated systems. This indicates that the quantum confinement is effectively suppressed by the charge redistributions due to the edge X-C and X-X bonds.

The distinct adatom decorations could dramatically alter the width dependence of energy gap, since the band-edge states near E_F are sensitive to the edge passivation. For $N_A \geq 6$ pristine armchair nanoribbons, E_g declines in the increase of width according to the $N_A = 3I$, $3I + 1$ and $3I + 2$ categories (Fig. 4(a), as discussed earlier in Fig. ?). A linearly inverse relationship is absent, reflecting the strong competition between the edge dangling bond and the finite-size effect. Among three categories, energy gaps present a simple ordering: $E_g(3I + 1) > E_g(3I + 2) > E_g(3I)$ (red squares, blue dots and green triangles). After the edge decoration, the X-C bonds and the quantum confinement account for energy gaps and might thoroughly change the specific behaviors. Three types of X-decorated systems, as shown in Figs. 4(b)-4(d), have certain important differences in energy gaps, such as the

irregular width dependence, the greatly reduced magnitudes, and the semiconductor-metal transition. Both N- and Li-decorated systems possess much smaller gaps (Figs. 4(b) and 4(d)), compared with pristine ones. The former exhibit a non-monotonous N_A -dependence, and a severe fluctuation for the $N_A = 3I$ category (red squares in Fig. 4(b)). The main reason is that N adatoms and C atoms co-dominate the energy dispersions nearest to E_F . Moreover, the significant Li-C bonding make the conduction and valence bands approach to E_F for the $N_A = 3I$ and $3I + 1$ categories, or overlap for the $N_A = 3I + 2$ systems. The narrow gaps in the former two become vanishing when the widths are sufficiently large [$N_A \geq 15$ (red squares in Fig. 4(d)) and $N_A \geq 22$ (blue dots)]. Apparently, the weakened finite-size effect leads to the semiconductor-metal transition. On the contrary, the S-decorated systems behave similar to pristine ones (Fig. 4(c)), since the adatoms are almost independent of the highest occupied state and the lowest unoccupied state (Fig. 3(c)). The adatom-enriched energy gaps could be examined by the STS experiments. The tunable energy gaps and free carrier densities are very useful for potential applications, e.g., FETs and light-emitting diodes.

The atom- and orbital-decomposed DOSs, as illustrated in Figs. 5(a)-5(d), can comprehend the decoration effects related to the C-C, X-C and X-X bondings. There are a lot of asymmetric peaks and part of symmetric peaks (red circles) arising from the parabolic and weakly dispersive bands, respectively. The $N_A = 8$ pristine armchair nanoribbon presents a pair of asymmetric peaks across the Fermi level at $E = \pm 0.24$ eV, in which the valence and conduction band-edge states are exclusively contributed by the $2p_z$ orbitals (red curves in Fig. 5(a)) and the $(2s, 2p_x, 2p_y)$ orbitals (blue and green curves), respectively. The $2p_z$ orbitals (the π bondings) make important contributions in the range of $-3 \text{ eV} \leq E \leq 3 \text{ eV}$, while the other orbitals (the σ bondings) dominate those of $E \leq -2.2 \text{ eV}$ and $0.2 \text{ eV} \leq E \leq 1.7 \text{ eV}$. The σ -orbital contribution to the low-lying conduction states mainly arises from the edge dangling bonds. This is fully replaced by the $2p_z$ -orbital contribution in the presence of edge passivation (red curves in Figs. 5(b)-5(d)). Furthermore, the $2s$ -orbital DOS is largely reduced at $E \geq -3 \text{ eV}$.

The adatoms have drastically changed the energy, number, height of the special structure in DOS. Their DOS corresponds to the difference between the total DOS and that of carbon atoms. Specifically, the N-decorated system exhibits the adatom-dominated shoulder structure near E_F and six prominent peaks in the range of $-1.6 \text{ eV} \leq E \leq -0.9 \text{ eV}$ (Fig. 5(b)). Such peaks are combined with the significant $(2p_x, 2p_y)$ contributions, indicating the strong interactions among the N adatoms and the dominant carbon orbitals in a planar structure. Specially, the S-enriched peaks appear in the wide ranges of $E \leq -0.65 \text{ eV}$ and $E \geq 1.3 \text{ eV}$, being accompanied with the $2p_z$ -orbital ones. The large energy width clearly confirms the existence of S-S bonds in the distorted edges. The merged peaks arise from the non-planar S-C bonds covering valence charges of adatoms and carbon $2p_z$ orbitals. As to the Li-decorated system, the one valence electron in each adatom only makes a partial contribution to DOS, especially for the range of $-1.5 \text{ eV} \leq E \leq 0 \text{ eV}$. A finite DOS is revealed at E_F , in which the metallic property is ascribed to the critical chemical bonding between Li adatom and carbon atom.

8.2 decoration- and curvature-enriched essential properties

The edge passivation in the unzipping process of carbon nanotube, as shown in Figs. 6(a) and 6(b), is investigated by the first-principles method. The zigzag lines along the nanotube axis are relatively easily to be separated, compared with the armchair ones. Furthermore, their decorations can create more types of geometric structures and thus diversify essential properties. The adatoms, with an atomic number less than 30, are included in the investigations. An armchair carbon nanotube, corresponding to a zigzag graphene nanoribbon, is chosen for a model study. When it is being cut longitudinally, the odd- and even- N_Z zigzag nanoribbons result. An odd-width nanoribbon is more stable, so this work is focused on its decoration effects. By the detailed calculations, the optimal geometric structures cover three types: (I) a zipper-line decorated carbon nanotube (Fig. 6(c)), (II) an edge-decorated curved nanoribbon (Fig. 6(d)) and (III) a flat nanoribbon with edge passivation (Fig. 6(e)).

The formation of each geometric structure is first discussed through a detailed analysis of its total energy. The different electronic configurations of decorating adatoms bring about various types of edge-carbon-adatom interactions. These are categorized into three types, being identified from the charge transfer, C-C bond length, etc. Moreover, the adatom distribution is very useful for further understanding the electronic properties.

The arc angle in range of $0^\circ \leq \phi \leq 360^\circ$, as defined in Sec. 4.1, can characterize a curved/planar nanoribbon, and a unzipped/zipped nanotube. In order to determine an optimal geometric structure, the θ -dependent total energy (ΔE_{tot}), being measured from that of a flat nanoribbon, is calculated for each type of decoration configuration. ΔE_{tot} , as shown in Fig. 2(a), presents three types of adatom-dominated arc angle dependences. The critical arc angle, corresponding to the local maximum of ΔE_{tot} , plays a critical role in determining a stable configuration. When ϕ_c is larger than the initial arc angle, the zipper-line-decorated nanotube (type I; red circles) and highly curved ribbon (type II; blue squares) are formed. On the contrary, the resulting structure is a planar nanoribbon with edge passivation. Moreover, all type-III structures are planar in the absence of ϕ_c (green triangles). The ϕ dependence of ΔE_{tot} is mainly attributed to the mechanical strain and the edge-edge atomic interactions. These two effects cooperate in deciding the resulting decorated structures for type III. However, they become a strong competition for type I and type II. Specially, the ϕ -dependent energies in type-II systems are well fitted as¹²⁷

$$\Delta E_t \simeq [3.762 \times 10^{-6} \times \exp(\frac{13.336}{N_y})]\theta^2 + 2 \sum_{\alpha=1}^2 \frac{1}{4\pi\epsilon_0} \frac{(\vec{p}_{l,\alpha} \cdot \vec{p}_{r,\alpha}) - 3(\vec{p}_{l,\alpha} \cdot \hat{n})(\vec{p}_{r,\alpha} \cdot \hat{n})}{r_\alpha^2}, \quad (2)$$

The first term in Eq. (2) is the mechanical strain energy inversely proportional to ϕ (radius), as discussed earlier in Sec. 4.1. Furthermore, the second term represents the dipole-dipole interactions from the edge-dependent electric dipole moments.³⁰⁰ ϵ_0 is the free-space dielectric constant, $\vec{p}_{l,\alpha}$ ($\vec{p}_{r,\alpha}$) the dipole moment on the left-hand (right-hand) side, \hat{n} the unit vector along two moments, and r_α the distance between them. $\alpha=1$ and 2, respectively, represent

the nearest and next-nearest neighbors. The factor of 2 indicates a dipole interacting with one dipole on each side. The detailed discussions will be provided later.

Different decorating adatoms (e.g., B, Be, H, and C) lead to the dramatic changes of the total energies and thus decide the optimal geometric structures. According to the arc angle dependence, ΔE_{tot} could be divided into two zones: (I) $\phi < \phi_c$ and (II) $\phi > \phi_c$. This is clearly shown in Fig. 7(a) for the $N_Z = 7$ system. In zone I, it is almost identical for all types of edge-decorated curved systems, in which the ϕ -square dependence agrees with the first term of Eq. (2), as revealed in carbon nanotubes.²⁴³ The increase of the total energy directly reflects the enhanced mechanical strain. Zone II refers to a region at sufficiently large ϕ 's. Specially, the adatom-dependent total energies start to behave differently and diverge from one another. The edge-edge interactions need to be taken into account when the inter-edge distance is getting smaller. In general, various edge adatoms result in three different types of edge interactions: strong covalent bonds, significant dipole-dipole interactions, and dominant repulsive forces. For type-I boron decoration, its energy declines quickly as the arc angle exceeds the critical one. The slopes in the cases of boron (red circles) and carbon (black crosses) atoms are similar, clearly indicating that the resulting configuration is ascribed to the very strong sp^2 covalent bonds. The bonding energy could be fitted by the linear superposition of $1/d$ and $1/d^2$, where d is the distance between two edges. Concerning type-II structure, the quasi-stable configuration in beryllium case (blue squares in Fig. 7(a)) is an open curved nanoribbon with large charge transfers between Be adatoms and C atoms (discussed later), being characterized by the dipole interaction model. The nearest and next-nearest dipole-dipole interactions in Eq. (2) match the non-monotonous ϕ -dependence of ΔE_{tot} well. In comparison with the boron and the carbon cases, the decrease in total energy happens at a smaller critical angle, mainly owing to the longer interactive distance of non-bonding forces. The hydrogen-decorated nanoribbon belongs to type III, which is very different from types I and II. As the arc angle gradually grows, the repulsive interactions become strong and thus enhance the total energy (green triangles in Fig. 7(a)). The edge

adatoms are in saturated states so that no chemical bonding forms between two edges, and the charge transfer between H and C atoms is too small in creating the effective dipole-dipole interactions. As a result, the quasi-stable structures are absent; that is, only a flat nanoribbon is allowed.

The formation of type-II structures could be understood from the energy variation in zone II (blue squares). With the increasing arc angle, the reduction in the total energy is attributed to the shorter distance and the approximately anti-parallel arrangement for the two-side dipoles (most contributions from the first part of the second term in Eq. (2)). The enhanced attractive interactions lead to a local minimum energy at a specific arc angle. Furthermore, the energy difference between the curved nanoribbon (the dashed black curve) and the Be-decorated system represents that created by the dipole interactions. For Be and Mg adatom decorations, such energy differences are, respectively 1.9 eV and 1.1 eV in the first-principles calculations, being comparable to 2.1 eV and 1.2 eV by calculating the second term of Eq. (2). This further illustrates that the dipole interaction model can account for the optimal type-II configurations. The type-II decorating adatoms exhibit the similar behavior in the highly curved nanoribbons, while various electric dipole moments result in different curvatures of the quasi-stable structures. In addition, the total energy will grow in the further increase of ϕ , e.g., the extra repulsive interaction energy at $\phi = 2\pi$.

For type-I and type-II configurations, the critical interaction distance and the energy barrier (E_b) in preventing the production of flat structures strongly depend on the ribbon width, as indicated in Figs. 7(b) and 7(c), respectively. Because of the reduced mechanical strains, the wider ribbons only require the relatively weak edge-atom interactions to prevent flat ribbons from occurring. This is responsible for the straightforward increasing relationship between N_Z and d_c (red solid circles in Fig. 7(b) and blue solid squares in Fig. 7(c)). E_b , the total energy difference between the stable (quasi-stable) structure and the critical one, for boron (beryllium) will gradually rise in the increase of N_Z . Furthermore, the tendency of E_b and d_c levels off for $N_Z \geq 15$. These are mainly determined by the competition between

the bending energy and the attractive edge-atom interactions. According to Figs. 7(a) and 7(b), the type-I and type-II configurations, with sufficiently large widths, could form spontaneously when the interaction distance is less than 7 Å.

The zipped/curved/planar adatom-decorated zigzag nanoribbons present very rich characteristics, such as charge transfers, X-X and X-C bond lengths, magnetic moments and metallic/semiconducting behaviors listed in Table 2. For boron and nitrogen adatoms, classified as type I, the strong covalent bonds are created in X-X and X-C bonds. To create type-I structures, it is essential that the number of occupied valence electrons, X-X distance, X-C distance and electronegativity are all close to those of carbon. A boron atom possesses three valence electrons. Two of them are assumed to form the two B-B single bonds and thus make a zigzag adatom chain, while the third one causes the B-C single bond to zip the curved ribbon into a cylindrical nanotube. However, a nitrogen adatom can generate two N-N single bonds and one N-C single bond, in which two unshared electrons are left for making up a full octet. This bonding configuration induces a serious deformation of a zipped nanotube. The zigzag nitrogen atoms, which protrude from the non-uniform cylindrical surface, are responsible for the anti-ferromagnetism of the edge carbon atoms ($\sim 0.13 \mu_B$), as revealed in deformed boron nitride nanotubes.³⁰¹ Except for B and N, other non-metal elements, e.g., O, S, F, Cl, Si and P, can bond only with carbon atoms, but not form a tubular structure in the absence of the three above-mentioned essential conditions. As a result, these elements exhibit the edge passivation in flat zigzag nanoribbons.

It is well known that transition metals play critical catalysts in synthesizing carbon nanotubes.^{8,220,302} According to the theoretical predictions, seven of the transition metals in the fourth row of the periodic table can exhibit type-I nanotube structures (Table 1). Such elements have many $3d$ orbitals and provide occupied/unoccupied states, leading to the X-X single bond. While the X-X bond lengths in transition metals are larger than those of boron and nitrogen, they still remain stable under the moderate deformations of tubular structures. Specifically, transition metals can give rise to magnetic moments on the edge carbon atoms

except that non-ferrous metal copper possesses a nearly zero magnetic moment. The highly curved type-II structure is only revealed in Ti adatoms, directly reflecting that they have only two occupied valence electrons, the high charge transfer and the long X-X bond (also sees next paragraph). Concerning Zn and Sc, electrons fully occupy the $3d$ orbitals of the former and one $3d$ electron appears in the valence state of the latter. These two kinds of adatoms could bond with carbon atoms, but it is impossible to hybridize with each other. Furthermore, their charge transfers are too low to create any dipole moments. As a result, the Zn- and Sc-decorated zigzag nanoribbons present the type-III planar structures.

For a zigzag nanoribbon decorated with metal elements, the high charge transfer between adatoms and carbons could create the significant electric dipoles on the edges and thus stabilize the type-II curved structures. The self-consistent calculations reveal the much longer X-X distances, compared with those in type I. The metal-decorated systems do not present the deformed/non-uniform cylindrical structures, since the long interatomic distances make it impossible for the metal atoms to share electrons in single bonds. Both Be- and Mg-decorated type-II structures mainly come from the appropriate X-X distance and the relatively high electron transfer. Such essential conditions cause the electronic dipole effects to become dominant. An Al-decorated structure is regarded as a special case, in which the relatively low charge transfer could induce sufficient dipole moments to achieve the highly curved structure. The Al adatoms have three valence electrons, while the very large differences among the X-X, X-C and C-C bond lengths could prevent the formation of type-I nanotube structures. The Ti adatoms, which possess the highest electron transfer among the transition metals, show the similar behavior. They give rise to ferromagnetic moments of edge carbon atoms, being absent in other type-II structures. On the other side, the only one valence electron in alkali metal adatoms cannot provide enough charge transfer for generating type-II systems. The decoration by other metal elements such as Ca does not result in type-II structures when the X-C bond length is too long. This could be attributed to the lengthy bond that behaves as electric monopoles, leading to a repulsive force between two-side edges.

Li, Na, K and Ca, for instance, form stable structures of flat adatom-decorated nanoribbons.

The electronic properties of nanoribbon-related systems are greatly diversified by the adatom decorations and the curvature variations. As for pristine systems, an armchair nanotube has two linear bands intersecting at the Fermi level ((4,4) in Fig. 8(a)), while a flat zigzag nanoribbon has a pair of partial flat bands with an indirect gap (Fig. ? in Chap. 4). These two kinds of energy bands are, respectively dominated by all carbons and edge ones. The low-energy features dramatically change with the various adatoms. A B-decorated cylindrical nanotube, as clearly indicated in Fig. 3(b), exhibits two unique features: three energy bands crossing the Fermi level, and a pair of partial flat bands below it. The first linear energy band intersecting with E_F near $k_x = 1/2$ mainly originates from the B-B bond in the adatom zigzag chain, with the dominance represented by the radius of circle. The other two nonlinear bands are closely related to B-C bonds and most C-C bonds. The carrier transport along the edge B-B and B-C bonds is deduced to be quite important. On the other hand, a pair of partial flat bands attributed to the edge C-C bonds has no energy spacing at the zone boundary, reflecting the absence of anti-ferromagnetism at both edges (different from Fig. 8(d)). Specifically, the partial flat bands and one linear band are absent in other nanotube-related systems where boron atoms are uniformly distributed, e.g., BC_3 ³⁰³ and BC_2N nanotubes.³⁰⁴ This difference further illustrates the geometry-enriched electronic properties. In addition, a N-decorated nanotube, with a protruding surface, is a direct-gap semiconductor of $E_g = 0.2$ eV (?) (Table 2).

The low-lying energy bands of a highly curved nanoribbon present the composite features related to a H-terminated flat nanoribbon (Fig. 3(d)) and a carbon nanotube (Fig. 3(a)). The Be-decorated curved nanoribbon, as shown in Fig. 3(c), has a pair of partially flat bands below E_F mainly arising from the edge atoms, and two linear bands intersecting at E_F . These clearly indicate that the Be-decorated nanoribbon is a 1D metal, whereas the H-terminated one is a semiconductor with two separated flat bands. One of the linear bands is dominated by all the carbon atoms, and the other is partially contributed by the Be-C bonds

(green circles). As a result, electrons can be transported either through uniformly through the carbon atoms or specifically through the decorating adatoms. These characteristics are also revealed in larger-width systems. Other type-II systems, such as Mg- and Al-decorated ones, exhibit the similar low-energy behaviors. Although the origins of linear bands might be somewhat different, the type-II systems possess the almost same peculiar feature as the armchair carbon nanotubes: the metal-like electrical conductivity required for use as 1D nanowires, being a promising feature to apply in future nanoelectronics.

The low-energy DOSs in edge-decorated curved zigzag nanoribbons, as shown in Figs. 9(a)-9(d), could exhibit a plateau across E_F , two prominent peaks, and several asymmetric peaks in the square-root form. The plateau DOS (Figs. 9(a) and 9(c)) is due to a pair of linearly intersecting bands in an armchair nanotube (Fig. 8(a)) and a Be-decorated nanoribbon (Fig. 8(c)). The negligible E -dependence is absent in the metallic B-decorated nanotubes (Fig. 9(b)) because of the two nonlinear energy bands (Fig. 8(b)). This system might have the highest DOS at E_F among the 1D nanostructures, so it is expected to present a very high electrical conductivity. The two prominent peaks exist in the adatom-decorated systems (red triangles in Figs. 9(b)-9(d)), clearly indicating the important contributions of edge carbon atoms (red curves). They are located separately above and below E_F for the H-terminated flat nanoribbon, while the B- and Be-decorated curved/tubular systems show two neighboring structures beneath E_F . Specifically, both B- and H-decorated systems possess an extra peak (the blue circle in Figs. 9(b) and 9(d)) near the prominent peaks. This special structure, respectively, arises from the $k_x = 0$ state of the B -dependent nonlinear band (blue curve; Fig. 8(b)) in the former and the $k_x \sim 3/4$ state of the partial flat band in the latter (Fig. 8(d)).

The metallic/semiconducting behavior of an adatom-decorated zigzag depends on the magnitude of DOS at E_F , as listed in Table 1. Most decorating atoms could provide free carriers and thus enhance $\text{DOS}(E_F)$, i.e., such decorated systems are conductors.. Compared to metallic armchair carbon nanotube, they possess a much higher $\text{DOS}(E_F)$ except

for Be- and Mg-decorated systems with a comparable value. When the anti-ferromagnetic configuration induced by zigzag edges comes to exist, the partial flat bands near E_F become splitting and create a vanishing $\text{DOS}(E_F)$. For example, the H-, Li-, and F-terminated zigzag nanoribbons belong to semiconductors. However, the Si-decorated system is a metal even if it owns an AFM configuration. The main reason is that the Si adatoms, with more valence electrons, can dominate the the valence electrons across E_F . As to the transition-metal-related systems, they tend to maintain the intrinsic properties of the decorating atoms, and hence are conductors. The only exception is a tiny-gap Cr-decorated system. This gap might disappear in wider systems The feature-rich DOSs near E_F could be examined by the STS measurements to identify the decoration and curvature effects, such as the adatom-dependent $\text{DOS}(E_F)$ and peaks, and the edge-C-dominated peak energies,

9. Alkali-adsorbed graphene nanoribbons

In addition to zipping, folding, stacking, scrolling and edge decoration, the surface adsorption is a very efficient method in diversifying the essential properties of graphene nanoribbons. Alkali adatoms are very suitable for a model study, since only the outmost s-orbital plays a critical role in the active chemical environment. The single-orbital hybridization of the X-C bond is relatively easy in understanding the alkali-induced dramatic changes. The alkali-created chemical modifications on the carbon-related systems with sp^2 bondings have been extensively studied both experimentally and theoretically, such as, graphite,¹²⁸ fullerenes,¹²⁹ carbon nanotubes,¹³⁰ few-layer graphenes,¹³¹ and graphene nanoribbons.³⁰⁵ Such systems after alkali intercalation/adsorption, such systems can present very high conduction electron densities and thus electrical conductivities. The n-type superconductivities are observed in graphite intercalation compounds; alkali-doped C_{60} fullerenes³⁰⁶ and carbon nanotube bundles.³⁰⁷ Specially, Li-based graphene compounds could serve as anode of high-performance batteries, in which they are very durable within the frequent charging processes. Lithium

is smallest among all the alkalis, so Li-adsorbed graphene nanoribbons are expected to be most stable and present high concentrations in experimental syntheses. They are chosen to illustrate the alkalization effects.

The chemical modifications on the essential properties of graphene nanoribbons could be easily achieved by the alkali surface adsorptions under the active environment, especially for the adatom-induced free carrier density and the diversified spin arrangements. The significant orbital hybridizations in X-C, C-C and X-X bonds need to be examined in detail from the atom-dominated energy bands, the spatial charge distributions, and the atom- and orbital-projected DOSs. The geometric features of alkali-adsorbed graphene nanoribbons, the binding energy, optimal position, C-C & C-X bond lengths, and adatom height, are included in the first-principles calculations. The effects of alkali adatoms on conduction and valence bands are investigated for various adsorption configurations, covering the variations in the kind of adatom, concentration, relative position, single or double sides, edge structure and width. The systematic calculations and analyses are available in determining the specific/simple relation between the linear free carrier density and the adatom concentration. Specially, the position and concentration of alkali adatoms on zigzag nanoribbon will be tuned to explore the dramatic changes in the partially flat bands and the spatial spin density, such as the spin-split edge-localized bands and the transformation from anti-ferromagnetism to non-magnetism/ferromagnetism.

9.1 The Alkali-created conduction electrons

Graphene nanoribbons, with open edges passivated by hydrogen atoms, are adsorbed by alkali atoms on surfaces. The geometric, electronic and magnetic properties are investigated under the different alkali adatoms, concentrations, distributions, widths, and edge structures. Both armchair and zigzag systems behave similarly except for magnetic configurations, so the former are suitable for a model study in the alkali-induced free carriers. The optimal adatom position, as shown in Fig. 1(a) for $N_A = 10$ armchair nanoribbon, is the hollow site, but not

the bridge and top sites. The similar position in 2D graphene has been confirmed by the low-energy electron microscopy.³⁰⁸ The binding energy of each adatom, the reduced energy arising from alkali adsorption, is defined as $E_b = [E_{sys} - E_{gra} - nE_A]/n$, where n is the number of adatoms; E_{sys} , E_{gra} and E_A are, respectively, the total energies of the alkali-adsorbed system, graphene nanoribbon, and isolated alkali atoms. Li and Na adatoms, respectively, possess the highest and lowest binding energies (-1.14 eV and -0.55 eV in Table 3(a)). It is relatively easy to produce Li adsorption in experimental syntheses among all alkali adatoms. As to the adatom height (the A-C bond length), it varies from 1.80 Å to 3.03 Å (2.31 Å to 3.35 Å) as Li→Cs. Graphene nanoribbon remains the planar structure after alkalization for any concentrations and distributions. This clearly indicates that the σ bonding due to $(2s, 2p_x, 2p_y)$ orbitals of carbon atoms is almost unchanged by alkali adsorption. However, the C-C bond lengths are sensitive to the positions of carbon atoms, but not those of alkali adatoms. In addition, the total ground state energy only exhibits a slight variation (about several meV's) for the distinct adatom positions.

The alkali-atom adsorption can dramatically alter band structures of graphene nanoribbons, especially for the blue shift of the Fermi level (the creation of free electrons in conduction bands). We first discuss the single-side adsorption with one alkali adatom $[(1)_s]$ situated at the center of edge hexagon (Fig. 1(a)). An energy spacing (~ 1.18 eV) between the valence and conduction bands almost keeps the same after the alkali adsorption, as indicated from those in pristine (Fig. 2(a)) and alkali-doped systems (Figs. 2(b)-2(f)). Furthermore, the valence bands are dominated by carbon atoms and hardly depend on alkali adatoms (very small red blue circles). further illustrating the unchanged σ bonding and the slightly distorted π bonding. On the other hand, the asymmetry of energy bands about E_F becomes more obvious after alkali adsorption. Specially, some conduction bands are fully/partially dominated by alkali adatoms, e.g., the first/second/third conduction band measured from E_F . They might have unimportant differences among the various alkali systems. These clearly indicate that the significant interactions between the neighboring alkali adatoms is

able to generate energy bands. Most important of all, the Fermi level presents a blue shift; that is, it shifts from the middle of energy gap to the conduction bands. E_F is determined by the alkali-induced conduction electrons. The Fermi momentum (k_F) can characterize the 1D free carrier density (λ_e) by a simple formula: $\lambda_e = 2k_F/\pi$. The dependence of λ_e on the kind, distribution and concentration of alkali adatoms will be fully clarified in Table 3(b). In addition, energy bands are hardly affected by the various positions under the single-adatom adsorption.

Band structures of alkali-adsorbed systems strongly depend on the concentrations, relative positions, single- and double-side adsorptions, and edge structures (Sec. 9.2). The number of the alkali-dependent conduction bands is greatly enhanced in the increase of adatom concentration, as clearly indicated in Figs. 3(a)-3(f) for various Li adsorptions (the blue circles). More conduction bands become occupied, indicating the rapid generation of free carriers during the alkalization process. Specially, each conduction band is closely related to the alkali adatoms under the full surface adsorption [(1-8)_s in Fig. 3(d) and (1-16)_d in Fig. 3(f)]. In general, the dependence of valence bands on adatom concentrations is weak. The low-lying conduction bands near E_F are sensitive to the relative positions, e.g., (4 Li)_s and (4, Li)_s in Figs. 3(b) and 3(c), respectively. Also, they are drastically changed by the single- and double-side adsorptions [(8 Li)_s in Fig. 3(d) and (8 Li)_d in Fig. 3(e)]. By the detailed examinations, even although the Fermi momenta in the occupied conduction bands present obvious changes, their sum keeps the same under a specific Li concentration. This is irrespective of the kind of alkali adatoms.

After systematic calculation and analysis, the total conduction electron density below E_F is linearly proportional to the alkali concentration, as clearly revealed in Table 3(b). λ_e hardly depends on the adatom kind, relative position, single- or double-side adsorption, ribbon width, and edge structure; that is, the ratio between the free carrier density and the adatom concentration is very close to one under various adsorption configurations. This means that each alkali adatom contributes the outmost s-orbital electron as conduction car-

rier through the significant X-C, C-C (π bonding) and X-X bondings (ρ in Fig. ?). As to $N_A = 10$ alkali-adsorbed systems, λ_e is $\sim 2.34 \times 10^7$ e/cm for a single-atom adsorption, and it could reach $\sim 3.18 \times 10^8$ e/cm in the double-side full adsorption. It is relatively easy to generate the higher carrier densities in the wider nanoribbons because of more available adsorption positions. The alkali-induced n-type dopings have been observed in carbon-related systems, such as, graphite,^{309,310} fullerene,^{306,311} carbon nanotube,^{312,313} and graphene.^{92,314} The electrical conductance is expected to be greatly enhanced in the increase of alkali concentration. The alkali-adsorbed graphene nanoribbons might have high potentials in nano-electronic devices.³⁰⁵

The spatial charge distributions, which create the rich electronic properties, present the orbital hybridizations in chemical bonds. They are characterized by charge density (ρ) and the variation of charge density after adsorption ($\Delta\rho$), in which the latter is the density difference between adatom-adsorbed and pristine systems. A pristine graphene nanoribbon has the π and the σ bondings arising from the parallel $2p_z$ orbitals and the planar ($2s; 2p_x; 2p_y$) orbitals, respectively, as clearly indicated by the dashed and the solid rectangles in Fig. 4(a). The m orbital hybridizations, with rather high charge density between two carbon atoms, belong to very strong covalent bonds in all the alkali-adsorbed systems (Figs. 4(b)-4(f)). They remain almost the same under the alkali adsorptions, corresponding to slight variation of charge density ($\Delta\rho$ in Figs. 4(g)-4(k)). However, the modified π bondings could survive in a planar graphene nanoribbon for various configurations, concentrations and edge structures. The changes on the π bondings are observable through the charge variations between carbon and alkali atoms (the heavy dashed rectangles), and they are relatively easily identified at high concentrations (Figs. 4(i)-4(k)). These clearly indicate the single-orbital $s - 2p_z$ hybridization in the X-C bond. They could account for the absence of the alkali-dominated valence bands (Figs. 2 and 3). At sufficient high concentrations, there exist obvious charge variations on x-y plane between two neighboring alkali atoms (the solid rectangles in Figs. 4(i) and 4(k)), illustrating the significant $s - s$ orbital hybridization in A-A bonds.

The special structures in the orbital- and atom-decomposed DOSs are very useful in the further identifications of the critical orbital hybridizations in X-C and X-X bonds. Alkali adatoms can induce obvious changes in DOSs, especially for those at $E \geq 0$. An energy gap in pristine nanoribbon, being characterized by one pair of opposite-side anti-symmetric peaks (Fig. 5(a)), become an energy spacing below the Fermi level ~ 1 eV after alkali adsorption (the blue-shift E_F). There are minor modifications on the prominent valence-state peaks due to the $2p_z$ (red curves) and $2p_x + 2p_y$ (blue curves) orbitals, as shown in Figs. 5(b)-5(f). Furthermore, such asymmetric peaks are almost independent of alkali adatoms. However, the opposite is true for the strong conduction-state peaks. Their number, energy and intensity are very sensitive to alkali concentration and distribution. Some of asymmetric peaks above $E \geq -1$ eV are dominated by/related to alkali adatoms (green curves). They are merged with those of the $2p_z$ orbital (red curves), clearly illustrating the s - $2p_z$ hybridizations in X-C bonds. The alkali-dependent prominent peaks appear in the overall conduction-state range, when adatom concentrations are sufficiently highly, e.g., Figs. 5(d)-5(f). A very wide continuous distribution directly reveals the s - s orbital hybridization in X-X bonds. The alkali-induced structure variations in DOS and charge density differences could provide the consistent pictures in orbital hybridizations.

9.2 The edge- and adsorption-co-dominated magnetic configurations

The edge-dependent band structures and magnetisms in zigzag graphene nanoribbons could be greatly diversified by alkali surface adsorptions. The low-lying energy bands exhibit the dramatic changes even for single-adatom adsorptions, as shown in Figs. 6(a)-6(e). When one Li adatom is situated at the center of edge hexagon [$(1)_s$ in Fig. 6(b)], the main features of the edge-localized partially flat bands are thoroughly changed, covering the splitting of spin-up and spin-down electronic states, and the intersecting with the Fermi level. The \uparrow - and \downarrow -dominated energy bands clearly indicate that the spin distribution in pristine zigzag

nanoribbon (discussed later in Fig. 7(a)), the anti-ferromagnetic ordering across the nanoribbon and the ferromagnetic configuration at each zigzag edge, is dramatically transformed by the significant orbital hybridization in X-C bond. The optimal spin configuration is determined by the competitions between the alkali-induced chemical bondings and the spin-dependent on-site Coulomb interactions.¹³⁵ The occupied free electron densities are different in the spin-split conduction bands (blue triangles), corresponding to the ferromagnetic spin configuration (Fig. 7(b)). Another pair, which belongs to valence bands, are fully occupied, irrespective of magnetism. The spin splitting declines rapidly as Li gradually approaches to the nanoribbon center [(3)_s and (5)_s in Figs. 6(b) and 6(c)]. A 1D metallic zigzag nanoribbon, with spin degeneracy, appears under the central adsorption [(9)_s in Fig. 6(d)]. Its spin configuration is similar to that of a pristine system (Fig. 7(e)). The energy spacings/dispersions of the partially flat conduction and valence bands are affected by alkali adsorption; furthermore, part of electronic states in the former becomes occupied. Specially, these two edge-localized bands are merged together and possess four-fold degeneracy in the range of $k_x \leq 0.5$ for two adatoms at distinct edges, e.g., (1,18)_s in Fig. 7(f). The energy spacings, being created by the edge spin configurations, vanish mean the absence of magnetism. The destruction of spin distributions could be driven by the edge surface adsorptions. It should be noticed that the dramatic changes in the low-lying conduction bands do not alter the summation of the Fermi momenta/the total free carrier density under the same alkali concentration. By the detailed calculations and examinations, the alkali-induced conduction electron density is deduced to be independent of edge structure and magnetic configuration (Table 3(b)).

The spatial spin densities can present the diverse magnetic configurations in alkali-doped zigzag graphene nanoribbons. For a pristine system, the spin-up and spin-down configurations, respectively, appear in the A and B sublattices, as illustrated in Fig. 7(a) by the red and blue balls. Their densities decrease quickly from zigzag edge to ribbon center, in which the former/the latter dominates the upper/lower edge spin distribution. They, respectively,

create the anti-ferromagnetic and ferromagnetic configurations along the longitudinal and transverse directions. As a result, there exist the separated edge-localized conduction and valence bands with spin-degenerate states (Fig. 6(a)). The lower-edge spin distribution is fully destroyed by one alkali adatom there $[(1)_s$ in Fig. 7(b)], so that only the spin-up-dominated distribution survives in the upper edge. This is responsible for the spin-split free electrons in conduction bands (Fig. 6(b)). The spin-down-dependent distribution gradually recovers as adatom leaves from edge $[(3)_s$ and $(5)_s$ in Figs. 7(c) and 7(d)]. The central adsorption is similar to the pristine case in terms of magnetic configuration $[(9)_s$ in Fig. 7(e)]. However, the s - $2p_z$ hybridization in X-C bond changes the semiconducting into the metallic behavior (Fig. 6(e)). Specially, spin configuration becomes absent for two adatoms at the upper and lower edges (not shown). The non-magnetic 1D metals are expected to be relatively easily observed in the high-concentration alkali-adsorbed zigzag graphene nanoribbons.

The alkali-enriched magnetic configurations are directly reflected in the low-energy DOS structures, as clearly indicated in Figs. 8(a)-8(f). These are the main differences between the zigzag and armchair systems. The former can present the delta-function-like symmetric peaks due to the edge-localized energy bands, strongly depending on the spin configurations. The ferromagnetic, anti-ferromagnetic and non-magnetic alkali-adsorbed zigzag graphene nanoribbons, respectively, exhibit three peaks (blue triangles in Figs. 8(b)-8(d)), a pair of symmetric peaks below the Fermi level (Fig. 8(e)), and a merged peak (Fig. 8(f)). The peak intensities are, respectively, and enhanced in the spin-split and merged energy bands (Figs. 6(b)-6(d) and Fig. 6(f)). It might have some weaker peaks between them (red circles), since the edge-localized energy bands possess an extra band-edge state at larger k_x . Apparently, the number, energy and intensity of the low-energy symmetric peaks are mainly determined by the magnetic configurations. The STS measurements on the main features of DOS could be utilized to identify the zigzag-edge spin distributions under the alkali surface adsorptions.

Up to now, there are no experimental examinations for the unusual energy bands and the diverse magnetic configurations in alkali-adsorbed graphene nanoribbons. The ARPES/spin-

resolved ARPES measurements are required to verify the occupied valence and conduction bands below the Fermi level, including the smallest energy spacing between them, the alkali-dominated conduction bands, the carbon-related conduction and valence bands, and the spin-split/spin-degenerate edge-localized energy bands in zigzag nanoribbons. They are available in identifying the π and σ bondings in C-C bond, the s - $2p_z$ hybridization in X-C bond, and the s - s hybridization in X-X bond. Specifically, the experimental verifications on the finite/vanishing energy spacing and spin splitting/degeneracy in zigzag systems are associated with the ferromagnetic/anti-ferromagnetic/non-magnetic configurations. The critical orbital hybridizations and the diverse spin distributions could also be identified from the STS/spin-polarized STS measurements on the special structures of DOS, covering the main features of asymmetric peaks and delta-function-like symmetric peaks in the overall energy range. Among three kinds of magnetic configurations, the ferromagnetic energy bands can create the spin-split absorption spectra in magneto-optical Kerr measurements^{315,316} and the spin-polarized currents in transport measurements. The latter might have potential applications in spintronic devices.^{317,318}

10. Halogen-adsorbed graphene nanoribbons

Halogens are quite different from alkalis in the valence electrons of the outmost orbitals, and so do the adsorption effects on the essential properties. The halogenated graphenes are verified/predicted to exhibit the rich and unique electronic and magnetic properties, especially for the fluorinated systems. The full fluorination of graphene can destroy the Dirac-cone band structure and create a direct energy larger than 3 eV.^{140,319} Furthermore, the metallic behavior might appear at certain low-concentration distributions.³¹⁹ These clearly show the strong competitions between the π and F-C bondings. The tunable electronic properties have been identified to have the high potential in various applications, such as, lithium batteries,³²⁰ supercapacitors,³²¹ molecule detectors,³²² and biosensors.³²³ However,

the (Cl,Br,I,At)-adsorbed graphenes belong to the p-type metals with the modified conducting π bondings.^{citehalogen2017,chu2012charge} In addition to the NM configuration, the FM spin distributions are also revealed under specific distributions and concentrations.³¹⁹ All the halogen adatoms might induce the spin states after the chemical adsorptions. Based on the extra quantum-confinement and edge-structure effects, the halogenation effects of graphene nanoribbons are expected to become more complicated. Electronic structures and magnetic configurations are relatively easily diversified in the variations of adsorption cases; That is, the 1D halogenated systems will present more kinds of essential properties. Specifically, the relation between hole density and adatom concentration could be exactly evaluated from 1D energy bands.

The various halogenation effects on graphene nanoribbons could be understood from five electrons in the outmost orbitals using the first-principles calculations. The critical orbital hybridizations in X-C, C-C and X-X bonds and the diverse spin configurations due to halogen adatoms and zigzag-edge carbons are explored thoroughly. Specifically, the latter are identified from the magnetic moment, the spin-split energy bands associated with adatoms and/or carbons, the spatial spin distribution, and the spin-up- and spin-down-decomposed DOSs. The X-C bonding strength, which determines the relations between the chemical adsorptions and the electronic properties, is reflected in the bond length, the binding energy, the change of the π -electronic band structure, the (X,C)-co-dominated energy bands, the variation of the spatial charge density, and the merged prominent peaks in DOSs. The X-C bonds and the X-induced spin states will be utilized to distinguish the fluorination and chlorination-related effects, such as, the semiconducting or metallic behavior, the existence of a simple relation between the free hole density and adatom concentration, and the dependence of FM/AFM/FM configurations on concentrations, distributions. and edge structures. How many kinds of electronic and magnetic properties are, respectively, revealed in fluorinated and other halogenated systems is the main focus.

10.1 Fluorination effects

The fluorination effects induce the unusual geometric properties clearly illustrated in Table 4. The top site is the optimal F-adatom position, regardless of adsorption cases, edge structures and ribbon widths. In general, the double-side/higher-concentration adsorptions have the larger binding energies, compared with the single-side/lower-concentration ones. With F adsorptions, the passivated carbon atoms deviate from the GNR plane, being sensitive to distributions and concentrations. Their heights vary from 0.320 Å to 0.542 Å, leading to the buckled honeycomb structure. The deviation becomes more obvious at high concentrations, e.g., $\sim 0.21 - 0.22$ Å in the fully fluorinated systems. F adatoms are very close to carbon atoms, in which the shortest and longest F-C bond lengths, 1.384 Å and 1.563 Å, respectively, correspond to the highest and lowest concentrations. Moreover, the nearest C-C bonds are lengthened in the range of 0.056–0.135 Å, as measured from those of pristine systems. These indicate that the strong F-C bondings are responsible for the featured geometric structures and are deduced to modify the π and σ bondings. The F-C bonds will play critical roles in other essential properties. In short, the fluorine- and alkali-adsorbed systems sharply contrast with each other in the binding energy, the planar/non-planar structure, the optimal position; the X-C and C-C bond lengths.

The fluorine adsorptions dramatically change the main features of electronic structures (Fig. 2): band gap, free carrier density, energy dispersion, subband spacing, atom dominance, and spin degeneracy. Concerning the single-adatom case, all the F-adsorbed armchair graphene nanoribbons exhibit the metallic energy bands, as shown in Figs. 2(b) and 2(c) (also in Table 4). The Fermi level is shifted to the C-dominated valence states (Figs. 2(a) and 2(b)), i.e., E_F exhibits a red shift. There exist free holes in the unoccupied valence states between two Fermi momenta, since electrons are transferred from carbon atoms to fluorine adatoms. The low-lying energy bands mainly originate from the conducting π bondings of carbon atoms, being almost independent of adatom positions. Their energy dispersions and spacings are drastically changed after fluorination. Moreover, the (F,C)-co-dominated en-

ergy bands, accompanied with the modified σ bands, come to exist at $E^v \leq -2.5$ eV. They possess the weak energy dispersions and the narrow band widths. The feature-rich energy bands clearly illustrate that the critical F-C bondings induce the significant modifications on π and σ bands (π and σ bondings). Specifically, the spin-split band structures might appear under certain distributions, e.g., $(1)_s$ adsorption in Fig. 2(c). The low-lying energy bands across the Fermi level determine the magnetic moment/FM configuration (Table 4 & Fig. 4(a)), in which they are dominated by carbon atoms. The F-adatom adsorption is deduced to induce the spin distribution of the neighboring carbons. This will diversify the spatial spin distributions or create the diverse magnetic configurations.

Band structures are greatly enriched by the concentration, relative position, and edge structure, but not single- or double-side adsorptions. With the gradual increment of concentration, the two-F systems could belong to the 1D p-type metals, as shown in Figs. 2(d)-2(g). The total free hole density, the summation of the Fermi momenta in partially unoccupied π -electronic valence bands, becomes higher [$(6,13)_s$ in Fig. 2(d) and $(6,13)_d$ in Fig. 2(e); Table 4] or keeps the same [$(1,20)_d$ in Fig. 2(f)], compared with that of the single-F case (Figs. 2(b) and 2(c)). On the other hand, the metallic band structure might be thoroughly transformed into the semiconducting one for two close adatoms, e.g., an indirect gap of 0.96 eV under the $(1,6)_d$ adsorption (Fig. 2(g)). This suggests the termination/serious distortion of the extended π bonding in the honeycomb lattice. The semiconducting behavior appears more frequently in the further increase of F-concentration, mainly owing to the great enhancement of the F-C bonding effects ($(4F)_d$ -case in Fig. 2(h) and $(8F)_d$ -case in Fig. 2(j)). The critical concentration in which all the F-doped AGNRs belong to gap-semiconducting systems is estimated to be over 40% (F:C=8:20). Specifically, the high-concentration semiconductors do not present the spin-split energy bands (Figs. 2(j)-2(l)) and belong to the NM systems (Table 4). This reveals the magnetic suppression closely related to the strong F-F bonds (discussed later). Such systems might have large direct/indirect energy gaps, e.g., $E_g^d = 3.2$ eV under the full fluorination. Such gaps are mainly determined by the σ -orbital

hybridizations of C-C bonds, and the multi-orbital hybridizations in F-C and F-F bonds, since the conducting π bonding is absent. In addition, the single- and double-side adsorptions present the almost identical low-lying energy bands (e.g., Figs. 2(d) and 2(e)) under the specific (x,y) projection and concentration.

The strong competition/cooperation between fluorination and zigzag edge further diversifies the essential properties. The drastic changes on electronic structures cover the spin degeneracy, number, energy gap and hole density of the partially flat bands (Figs. 3(a)-3(f)). When one F adatom is situated at the zigzag edge, the number of edge-localized energy bands becomes half in the presence of spin splitting, as revealed under the $(3)_s$ adsorption in Fig. 3(b). Such bands intersect with the Fermi level and possess free holes (Table 4), in which the number of occupied states is different in the spin-up and spin-down components. This system, with magnetic moment, belongs to a 1D FM metal. Specifically, the partially flat bands disappear under two adatoms near distinct zigzag edges [e.g., $(3,38)_d$ in Fig. 3(d)]; furthermore, a direct energy gap appears in the absence of spin splitting and magnetism (a NM semiconductor with $E_g^d = 0.27$ eV). The strong F-C bands could destroy localization behavior and spin configuration due to the edge carbons. But for the central two-F adsorption, the partially flat bands, with spin splitting, become double [$(19,22)_d$ in Fig. 3(e)], in which half of them correspond to the edge- or center-localized electronic states. An indirect narrow gap ($E_g^i = 0.17$ eV) is accompanied with the vanishing magnetic moment, indicating a AFM semiconductor. On the other side, the number of low-lying flat bands remain unchanged, when two adatoms are, respectively, close to edge and center [$(3,19)_d$ in Fig. 3(f)]. The spin splitting means a 1D FM metal.

The fluorinated graphene nanoribbons possess four kinds of spin-dependent electronic and magnetic properties. The spin-split energy bands strongly depend on fluorine adsorption and edge structure. The pristine armchair systems belong to the confinement-induced semiconductors without spin splitting in band structure and magnetism. The NM semiconductors are frequently revealed in fluorinated systems especially for the higher-concentration cases

(the first kind in Figs. 2(i)-2(l) and Table 4). As to the metallic systems, they present the spin-degenerate energy bands in the absence of magnetism (the second kind in Figs. 2(d) and 2(e)), or the spin splitting under the FM configuration (the third kind in Figs. 2(c), 2(f) and 2(g); discussed later in Fig. 4(a)-4(c)). In addition to NM semiconductors and FM metals, the fluorinated zigzag systems are the AFM semiconductors with spin splitting (the fourth kind in Figs. 3(e) and Fig. 4(f)). However, the spin splitting is absent in the AFM pristine systems (the fifth kind in Fig. 3(a)). The ARPES and spin-resolved ARPES are available in examining the predicted five kinds of electronic structures and magnetic configurations. That is to say, the complicated relations among the finite-size effects, the edge structures, the spin configurations, and the multi-orbital hybridizations could be veri-

ed from such measurements.

The p-type doping in NM and FM metals deserves a closer investigation. A simple relation between the fluorination-induced hole density and adatom concentration is absent except for one-F case, according to various calculations and detailed analyses. A single F in a unit cell can create one free hole for distinct adsorption positions (Table 4). One electron is transferred from the bonded carbon atom to the adatom under a rather strong fluorine affinity. The metallic 2-, 4-, 6-, and 8-adatom adsorptions can present one or two free holes in a unit cell, depending on the spin-degenerate and spin-split energy bands in Fig. 2 (FM and NM configurations in Table 4). Furthermore, only the lower-carrier case is revealed in zigzag systems (Figs. 3(b) and 3(f); Table 4). The fluorination and alkalization effects quite differ from each other in the metallic behavior. The latter belongs to the n-type doping even for the 100 regardless of adatom distributions. This will lead to very high conduction electron density. However, the strong F-C bonds could destroy/seriously distort the conducting π bonding, leading to the great reduce of hole density and even creating the semiconducting behavior.

The spatial spin densities and magnetic moments could provide more information about magnetic properties. They can characterize the FM configuration and the AFM ones without

and with spin-split energy bands. The spin arrangements are sensitive to the distribution and edge structure, as revealed in Figs. 4(a)-4(f). Furthermore, the competition between the spin-up and spin-down components determines the net magnetic moment in a unit cell (Table 4). The spin densities are mostly distributed near the edge structures except for the last kind (Fig. 4(f)). When one F is situated at the armchair edge, it creates the spinup and spin-down distributions of the neighboring carbons (the red and blue colors in Fig. 4(a)). The former dominates the FM configuration and their contribution leads to a net magnetic moment of $0.47 \mu\text{B}$ ((1)_s in Table 4). The ferromagnetism is greatly enhanced for two adatoms near distinct boundaries, e.g., $(1,20)_d$ and $(1,6,13,20)_d$ ($2 \mu\text{B}$ in Fig. 4(b) and $2 \mu\text{B}$ in Fig. 4(c)). As to the zigzag structure, the edge-F adatom could suppress the intrinsic carbon-spin states, but induce the dominating spin-down configuration at another edge. For example, the $(3)_s$ adsorption present the FM configuration with magnetic moment $-0.77 \mu\text{B}$ (Fig. 4(d)). There is no magnetism for two adatoms at the upper and lower zigzag edges. Specifically, the AFM configuration in a pristine system (Fig. 4(e)) becomes more complex, under the central two-F adsorption (Fig. 4(f)). The coexistence of the edge- and center-initiated spin distributions indicates an unusual AFM configuration without magnetic moment.

The charge density, charge density difference, and partial charge density (ρ_p) can directly identify the multi-orbital hybridizations in F-C, C-C & F-F bonds and the semiconducting/metallic behavior. There exist much charge density between fluorine and carbon, as indicated from pristine and fluorinated systems (Figs. 5(a), 5(b) and 5(d)). Furthermore, fluorination leads to an obvious change in the π bonding and an observable decline in the σ bonding. The strong fluorination effects also induce the drastic density variations, especially for Δ_ρ near F adatoms on $(x; z)$ and $(y; z)$ planes (Figs. 5(c) and 5(e)). These clearly indicate the complicated $(2p_x; 2p_y; 2p_z) - (2p_x; 2p_y; 2p_z)$ hybridizations in F-C bonds. As to F-F bonds, the significant $(2p_x; 2p_y)$ hybridizations appear for two neighboring fluorine adatoms, as illustrated in Figs. 5(c) and 5(e) (red rectangles on $(x; z)$ and $(y; z)$ planes).

The partial charge density, which corresponds to electronic states very close to the Fermi level, might exhibit the distorted and terminated π bondings. The former and the latter, as shown in Figs. 5(f) & 5(h) and Figs. 5(g) & 5(i), are responsible for the metallic and metallic properties.

The diverse band structures with/without spin splitting are directly reflected in the orbital- and spin-projected DOSs (Fig. 6), further illustrating the orbital hybridizations and magnetic configurations. A lot of asymmetric and symmetric peaks are, respectively, associated the parabolic and partially flat bands. When the F-concentration is below 40 % (Figs. 6(a)-6(b) & 6(e)-6(j)), the low-energy DOS is dominated by the distorted π bonding of C- $2p_z$ orbitals (red curves). Such bonding also makes significant contributions to the deeper-energy DOS. The peak structures due to the σ bonding of C- $(2p_x, 2p_x)$ orbitals appear at $E \approx -2.5$ eV (green curves). The similar structures are induced by the $(2p_x, 2p_y)$ and $2p_z$ orbitals of the F adatoms (dashed blue and pink curves). The former present a sufficiently wide energy width of ≈ 2 eV; that is, there exist the significant $(2p_x, 2p_y)$ orbital hybridizations in F-F bonds. Specifically, all the orbitals contribute to the merged peak structures at deeper energy, being attributed to the $(2p_x, 2p_y, 2p_z)$ - $(2p_x, 2p_y, 2p_z)$ multi-orbital hybridizations in F-C bonds. As for high-concentration DOSs, the energy width of the F-induced bands might be more than 5 eV (Figs. 6(c)-6(d)); furthermore, the corresponding peaks are stronger than those of the σ bands. The occupied valence states in the range of $E \geq -5$ eV mainly arise from the $(2p_x, 2p_y)$ orbitals of F and C. This indicates the serious destruction of the π bonding.

Five kinds of electronic and magnetic properties in fluorinated and pristine systems are characterized by the low-energy DOS peak structures. A pair of antisymmetric peaks across the Fermi level, being divergent in the opposite direction, is characteristic of energy gap in the absence of spin splitting (the first kind), as shown in Figs. 6(a)-6(d). As to NM metals (the second kind), a similar pair presents a blue shift of $\approx 0.5 - 1.0$ eV about $E = 0$ (Figs. 6(e) and 6(f)), in which DOS is finite at the Fermi level. The spin-polarized peak

structures are revealed in FM metals (the third kind in Figs. 6(g) and 6(h)). They are quite different for spin-up and spin-down configurations (black arrows); furthermore, the former predominates the occupied states of $E \leq 0$. Specifically, the partially flat bands in fluorinated zigzag systems could create more pairs of symmetric peaks centered about $E = 0$ in the presence of spin splitting, as indicated in Fig. 6(i) by blue triangles. The fourth kind of peak structures originates from AFM narrow-gap semiconductors. A pristine zigzag system only induces a pair of symmetric peaks (Fig. 6(i)), accompanied with an energy gap and one peak due to an extra band-edge state (Fig. 3(a)). This represents an AFM semiconductor without spin degeneracy (the fifth kind). The above-mentioned five kinds of low-lying DOSs could be examined by the STS and SP-STS measurements on energy gap, a finite value at E_F ; the spin-polarized and edge-localized peaks.

10.2 Chlorination-related systems

The Cl-, Br-, I- and At-adsorbed graphene nanoribbons quite differ from the fluorinated systems in essential properties. The former remain the planar structures (Tables 4(a) and 4(b)); furthermore, they are much higher than the latter ($\sim 3.5 \text{ \AA}$ versus $\sim 1.5 \text{ \AA}$). These clearly indicate the weak but significant orbital hybridizations in non-fluorinated X-C bonds. The F-C bonds create the highest binding energy, e.g., the variation of E_b from $\sim -3.02 \text{ eV}$ to $\sim -0.25 \text{ eV}$ for single adatom in $N_A = 10$ armchair system as $\text{F} \rightarrow \text{At}$. The nearest C-C bond length gradually grows in the increase of halogen concentration. The STM and TEM measurements could be utilized to examine the predicted geometric properties, covering the planar/buckled structure, the height and position of halogen adatom, and the nearest C-C bond length. The single- or multi-orbital hybridization and coupling strength in chemical bonds will determine the diversified electronic properties and magnetic configurations.

The other halogen adatoms exhibit the similar electronic properties and can dramatically alter the low-lying energy bands. We first discuss single adatom adsorption (dilute concentration). The original valence and conduction bands due to carbon honeycomb lat-

tice almost keep the same after surface adsorptions, as revealed from a direct comparison between Fig. 1(a) and Figs. 1(b)-1(e). Specially, the Cl-related adatoms create four spin-split energy subbands (the green circled curves), in which most of them present very weak dispersion relations. Energy dispersions might become strong in the increment of atomic number. The Fermi level has a blue shift of ~ 0.8 eV; furthermore, it intersects with one carbon-dominated valence band and the spin-down energy bands (Cl and Br in Figs. 1(b) and 1(c)) or the spin-split energy bands (I and At in Figs. 1(d) and 1(e)). The crossing behaviors depend on the kind of halogen adatoms, while the summation of the spin-up and spin-down Fermi momenta (the linear hole density) is identical for various adatoms. For example, the different hole densities in the unoccupied spin-up and spin-down states (red and black curves) represent the ferromagnetic spin configuration (discussed later in Fig. ?). Apparently, the important differences between the Cl-related and fluorinated systems (Figs. 1(b)-1(f)) lie in the drastic changes of the low-lying spin-split energy bands or the valence bands.

The halogenation effects on energy bands of armchair systems are very sensitive to adatom concentrations, but not distributions (?). For two adatom adsorption (Fig. 2(a)), more valence states become unoccupied and change into free holes, including two carbon-dominated valence bands and two spin-down Cl-related energy bands. The total hole density is double that of single-adatom adsorption, and so does the ferromagnetism (magnetic moment in Table 4). With the increase of Cl concentration (Figs. 2(b)-2(d)), there are more spin-split Cl-related energy bands, accompanied with a wider distribution range. Specifically, the spin splitting disappears under concentration

All the Cl-related halogenation systems belong to 1D *p*-type metals for different concentrations, distributions and edge structures, as clearly indicated in Tables 4 and 5. For the concentration lower than 50 %, one halogen adatom in a unit cell can provide one free hole. However, the free carrier density is reduced to half under the high concentration. This simple relationship is also suitable for odd-adatom configurations, e.g., three/ten holes

for three/nineteen adatoms. It is absent in fluorinated systems, since most of them are semiconductors. Halogenation is comparable to alkalization in creating free carriers (Table 3). The metallic systems might be ferromagnetic or non-magnetic, depending on adatom concentration. The magnetic moment is in the range of $\sim 0.43 - 1.09 \mu_B$ for adatom concentration lower than 50 %; otherwise, it is vanishing. Non-magnetism indicates that the spin-dependent on-site Coulomb interactions are fully suppressed by the strong X-X bondings at high concentration.

The Cl-induced spin configurations can create the diverse magnetic properties, namely ferromagnetism & non-magnetism in armchair systems, and ferromagnetism, non-magnetism & anti-ferromagnetism in zigzag systems. Armchair edges do not have the C-dependent spin configurations, so that only halogen adatoms dominate the spatial spin distributions. At concentrations $< 50\%$, the spin-up configurations are induced by Cl adatoms, as shown in Figs. 2(a)-2(f). Their densities grow with the increasing concentration, corresponding to the enhanced magnetic moment (Table 4). However, the strong Cl-Cl bondings under high concentrations are responsible for the vanishing magnetic configurations. On the other side, the C-dependent spin distributions at zigzag edges present the cooperative/competitive relation with Cl-induced spin configurations. When a single Cl exists at the top site of edge carbon (Fig. 2(g)), it generates the spin-up configuration and largely suppresses the spin-up and spin-down distributions due to the neighboring carbons (Fig. 2(f)). Furthermore, this adatom also leads to the spin-up-dominated configuration at the lower edge. This ferromagnetic configuration is recovered to the anti-ferromagnetic one for two adatoms at the upper and lower edges (Fig. 2(h)), since Cl- and C-induced spin configurations are identical. Apparently, the net magnetic moment is vanishing for two-edge absorption (Table 5). Such carbon-related edge spin configurations are hardly affected by the central adatom (Fig. 2(i)). However, an extra spin-up configuration appears there, leading to a new spin arrangement. Another spin distribution comes to exist, when two adatoms are, respectively, situated at edge and center (Fig. 2(j)). The Cl-induced spin-up states dominate spin distribution, while

the C-related edge spin distributions are thorough destroyed, or are largely suppressed.

In general, the fluorination and chlorination-related effects sharply contrast with each other in the essential properties, being attributed to the strength of orbital hybridizations in the X-C bonds and the halogen-induced spin configurations. All the halogen adatoms are situated at the top-site positions. However, the F-adatom adsorptions create the buckled structures, the shortest F-C bond length with the $(2p_x, 2p_y, 2p_z)$ multi-orbital hybridizations ($\sim 1.5 \text{ \AA}$), the largest binding energy ($\sim -4.269 \text{ eV}$ for single-F adsorption), the (F,C)-co-dominated deeper valence bands clearly shown at various adsorptions, the p-type metals only under certain low-concentration distributions, the high charge difference between F and C. and five kinds of electronic and magnetic properties. The very strong F-C bondings destroy/seriously distort the π bondings, so that there is no simple relation between free hole densities and F concentrations. Furthermore, they greatly modify the $(2p_x, 2p_y)$ -dependent C-C and F-F bonds, leading to the merged van Hove singularities in DOSs associated with three kinds of chemical bonds. The F-adsorbed graphene nanoribbons belong to FM & NM metals, NM semiconductors, and AFM semiconductors with/without spin splitting. Whether the F adatoms could generate the spin states of the neighboring carbons is very sensitive to distributions and concentrations. It is relatively difficult to observe the adatom-induced spin configurations, compared with other halogenated systems. On the other hand, the Cl-related systems present a planar honeycomb structure, the long X-C bond due to the weak single-orbital hybridization by their p_z orbitals ($\sim .3.3 - 3.8 \text{ \AA}$), the smaller binding energy ($\sim -? \text{ eV}$ for single-Cl adsorption), the adatom-dominated energy bands with observable spin-split dispersions near the Fermi level at concentrations lower than 50 %, the metallic behavior under any concentrations and distributions, three kinds of electronic and magnetic properties, and the concentration- and edge-dependent magnetic configurations. Two/one adatoms could provide one hole in a unit cell for concentrations above/below 50%. Such systems are FM, NM and AFM metals, in which the third kind only exhibits the spin-split behavior. The NM configuration concentrations come to exist at high concentrations, mainly

owing to the full suppression of the rather strong X-X bond on the magnetic configuration. Moreover, the X-induced spin states and their serious competitions with the edge-C ones lead to the complicated spin distributions and thus diversify the spin-dependent energy bands and DOSs. In addition, there are also important differences between halogen- and alkali-adsorbed graphene nanoribbons, covering the top-site/hollow-site adatom position, the p-type/n-type doping, and the existence/absence of magnetic configurations in armchair systems. That the alkali adatoms present the simple s-2p_z hybridizations in X-C bonds and have no spin configurations is responsible for such differences.

13. Concluding remarks: covering comparisons, measurements, and applications

This systematic work is conducted on the geometric strictures, electronic properties and magnetic configurations of the 1D graphene nanoribbons. They are thoroughly investigated by the first-principles calculations. The rich and unique essential properties arise from the various geometries, adatom dopings and spin arrangements. There exist the planar, folded, curved, zipped, stacked, edge-passivated, and adatom-adsorbed nanoribbon structures. The responsible mechanisms covers the sp^2 and sp^3 bondings in the angle-dependent C-C bonds, the significant orbital hybridizations in adatom-adatom bonds, and the single- or multi-orbital hybridizations in C-adatom bonds. Electronic structures exhibit the semiconducting and metallic behaviors, accompanied with the non-magnetism, anti-ferromagnetism and ferromagnetism. A lot of factors, the hexagonal/non-hexagonal lattice, non-uniform bond lengths, finite-size confinement, edge structure, non-planar structure, stacking configuration, layer number, boundary condition, distribution and concentration of adatoms, Van der Waals interactions, and spin-dependent many-body effects, are taken into consideration to get the concise physical and chemical pictures. These will be very helpful in investigating materials science and applications The calculated results are compared with

those from the previous theoretical predictions. Part of them have been confirmed by the experimental measurements. Specially, a theoretical framework is developed by means of the first-principles calculations. The critical orbital hybridizations in various chemical bonds, which diversify the essential properties, are obtained from the detailed analyses on the atom dominance of energy bands, the spatial charge distributions & density differences, and the orbital-projected DOSs. Furthermore, the edge-carbon- and adatom-dependent magnetic configurations are identified from the net magnetic moment, the spin-split energy bands, the spin density distributions, and the spin-decomposed DOSs. This method could be further improved and generalized to explore the chemically modified materials.

The curvature, width/radius, edge structure/chiral angle, and boundary condition can create the diverse essential properties in curved graphene nanoribbons and carbon nanotubes. During the zipping process of a graphene nanoribbon, the edge-atom bond length and the ground state energy dramatically vary with the arc angle. The critical zipping and unzipping energies, arc angle, and interaction distance are sensitive to the width and edge structure. They depend on the very strong competition between the mechanical strain and the chemical bonding of the two-side edge atoms. Apparently, the increasing curvatures induce the drastic changes of electronic properties, such as energy gaps, weak or strong energy dispersions, band-edge states, band mixing, band overlap, state degeneracy, complex orbital hybridizations, and van Hove singularities in DOS. The semiconductor-metal transitions occur near the critical arc angle, directly reflecting the contribution of the edge atoms, the competition between π and σ bondings, and the hybridization of the $2p_z$ and $2p_y$ orbitals. The predicted geometric structures and electronic properties could be examined by the STM, STS and ARPES measurements. As a result of the geometric symmetries and the boundary conditions, there exist important differences between armchair/zigzag nanotubes and zigzag/armchair nanoribbons in the main features of electronic properties. They cover the existence of the transverse quantum number, the contributions of the edge and non-edge carbon atoms to each energy band, the metallic or semiconducting behavior, and the anti-

ferromagnetic or non-magnetic spin configuration. Three types of carbon nanotubes are: (I) metallic armchair and $(m \leq 6, 0)$ zigzag systems: (II) moderate-gap $(m = 3I \pm 1, 0)$ and (III) narrow-gap $(3I, 0)$ zigzag ones (inversely proportional to r and r^2). The significant sp^3 orbital hybridization and the $2p_z$ -orbital misorientation, respectively, lead to the metallic and narrow-gap zigzag nanotubes. All armchair nanotubes, with a specific hexagonal arrangement on a cylindrical surface, are 1D metals arising from the linearly intersecting valence and conduction bands at the Fermi level. However, the semiconducting zigzag nanoribbons present a pair of separated edge-localized energy bands because of the anti-ferromagnetic spin arrangement at the two-side zigzag edges. Both $(m > 6, 0)$ zigzag nanotubes and armchair nanoribbons exhibit the semiconducting property, in which a simple inverse relation between energy gap and radius/width appears for $m = 3I \pm 1$ and any N_A 's. Specifically, the small energy gaps in $N_A = 3I + 2$ nanoribbons are closely related to the non-uniform π bondings at the distinct carbon positions.

The folded graphene nanoribbons, with the flat and curved structures, exhibits the rich geometric, electronic and magnetic properties, mainly owing to the combined confinement, edge, stacking and curvature effects. There are eight typical types of geometric structures, according to the achiral edge, the number of armchair/zigzag lines and the AA/AA'/AB stacking. The armchair AA' stacking or the even-zAB stacking is the most stable configuration. The edge-edge distance, the interlayer distance and the nanotube diameter are sensitive to the stacking configuration and ribbon width. Only the even-zAA stacking, with the mirror symmetry, exhibit a pair of metallic liner bands under the strong edge-edge interactions. The other stacking systems belong to the direct-gap semiconductors. In general, band gap declines with the increasing width because of the weakened finite-size effect. However, it almost keeps the same for any even-zAB stacking, being attributed to the breaking of mirror symmetry, and the saturated edge-edge distance and nanotube diameter. Six categories of width-dependent energy gaps are revealed in folded armchair nanoribbons, in a sharp contrast with three categories in planar systems. Specially, the $N_A + 6I = 4$ even-aAA'

stacking has the highest energy gaps, compared with the various pristine graphene nanoribbons. The magnetic configurations depend on the edge structure, the edge-edge interaction, and the stacking symmetry. As to the main structures of DOS, they cover a plateau across E_F , strong peaks, and asymmetric peaks, respectively, arising from the linear, partially flat and parabolic bands. The non-magnetic behavior occur in all armchair systems and (even-zAA,even-zAA) stackings with the dominating edge-edge interactions. Both odd-zAA' and odd-zAB stackings present the anti-ferromagnetic spin distribution across two parallel open edges. For the latter, the different spin-up and spin-down environments lead to the spin splitting and decreasing energy gaps. The spin-polarized STS and ARPES are available in the identifications of the spin-dependent van Hove singularities and valence bands. Apparently, the folded structures have greatly diversified the lattice symmetries, the semiconducting and metallic properties, and the spin configurations, compared with the planar ones.

Carbon nanoscrolls, with the non-uniform curved surfaces, are formed under the strong competitions between the interlayer atomic interactions and the mechanical strains. Each optimal structure possesses a spiral profile after the self-consistent relaxations. The scrolling energy exhibits the declining and fluctuating behaviors in the increase of width because of the complex curvature variations. It is higher in armchair nanoscrolls, compared with zigzag systems. The latter are predicted to be relatively easily produced in experimental syntheses. The similar difference could also be observed in folded armchair and zigzag systems. To sustain a stable nanoscroll, it needs to have the sufficiently large ribbon width and inner diameter. Two critical geometric parameters depend on the edge structure. For armchair (zigzag) nanoscrolls, the minimum widths are $N_A = 34, 43; 47$ ($N_Z = 18, 20; 22$), respectively, corresponding to the critical diameters of $N_{in} = 7, 9; 11$ (4, 6; 8). The bilayer-like configuration is close/similar to the AB stacking, as revealed in the most stable bilayer graphene. Armchair systems have the significant orbital hybridizations related to the inner open edge and the curved surface, leading to the unusual low-lying energy dispersions and band gaps. These exist three categories of energy gaps according to $N_A = 3I, 3I + 1; 3I + 2$,

in which their values are quite different from those of the planar armchair nanoribbons. On the other hand, both edge structure and quantum confinement also dominate the partially flat bands of zigzag systems. The spin-split edge-localized bands, with narrow energy gaps, come to exist when the spin-up and spin-down distributions experience the distinct magnetic environments. The various combined effects can induce the important differences among the planar, curved/zipped, folded and scrolled graphene nanoribbons, such as, the existence of the critical/saturated internal diameter and the stable stacking configurations, the categories of the width-dependent energy gaps, the parabolic/linear/oscillatory bands nearest to E_F , the semiconductor-metal transitions, and the breaking or conservation of spin degeneracy. This clearly illustrates that the boundary condition, the edge-dependent interactions, the single- or multi-orbital hybridizations and the magnetic configurations are responsible for the diversified essential properties.

The essential properties of bilayer zigzag graphene nanoribbons are greatly enriched by the relative shift between the upper and lower layers. They rely on the stacking configurations, interlayer edge-edge interactions, spin distributions, and ribbon widths. The AA and AB_α stackings exhibit the arc-shaped structure with the convex and wave-like profiles, respectively, in which the shorter edge-edge distances lead to the strong interactions and thus the destruction of magnetism. The most stable configuration in all the bilayer systems lies between them, mainly owing to the strong competition of the combined effects. The low-lying energy bands are composed of parabolic/linear and partially flat dispersions. The significant loop-like charge distribution in the AA stacking can create a pair of linear bands intersecting at E_F . The 1D metal becomes a direct semiconductor during the variation of stacking configuration, while the four-fold degeneracy near the zone boundary keeps the same. The metal-semiconductor transition also appears in folded zigzag nanoribbons. On the other side, the AA' and AB_β stackings have the nearly flat structures, as observed in monolayer system. There are two relatively stable magnetic configurations: AFM-AFM and AFM-FM. Most of the magnetic bilayer systems have indirect gaps and fourfold degeneracy

near $k_x = 1$. As to the interlayer AFM configuration, energy bands are split into the spin-up and spin-down ones under the distinct magnetic environments except for those of the AA' stacking. The 1D and 2D bilayer systems quite differ from each other in terms of the most stable configuration, spatial charge distribution, low-lying energy dispersions, van Hove singularities, band overlap/band gap, magnetism, and spin degeneracy, further illustrating the critical roles of the combined effects.

The edge passivation and the curvature effect could thoroughly change geometric structures and electronic properties of armchair graphene nanoribbons. For the edge-terminated armchair nanoribbons, the former has a very strong effect on adatom arrangements, bond lengths, charge distributions, and energy dispersions. Elements, with an atomic number of less than 20, are classified into three types depending on the optimal geometric structures: (I) the planar structures with the open edges, or the heptagon-pentagon/triangle-pentagon/hexagon edges, (II) the open and edge-buckled profiles and (III) the closed and adatom-stacked-up configurations. Especially, the nitrogen-decorated system is the most stable one with a heptagon-pentagon structure at the edges. The non-monotonous energy dispersions and the adatom-dominated bands come to exist after the adatom decoration, while the weakly dispersive bands due to the edge carbon atoms disappear. The dependence of energy gap on ribbon width might become more complicated, e.g., the absence of a linearly inverse relationship, and the existence of the semiconductor-metal transition. The atom- and carbon-orbital-projected DOSs are available in identifying the significant C-C, X-C and X-X bondings. On the other side, during the unzipping of an armchair nanotube, three stable geometric structures are revealed in the edge decorations for the elements with an atomic number less than 30. The first type is a regular/deformed zipper-like nanotube formed by the covalent bonds of decorating (B,N,V,Cr,Mn,Fe,Co,Ni,Cu) adatoms. The second one consists of the highly curved zigzag nanoribbons created by the dipole-dipole interactions between two open edges when decorated with Be, Mg, Al and Ti adatoms. The final structure is a flat nanoribbon produced due to the repulsive forces between two edges, and

most decorated structures belong to this type. Various decorating adatoms, different curvature angles, and the zigzag edge structure are reflected in the electronic properties, magnetic properties, and bonding configurations. Most of the resulting structures are conductors with relatively high free carrier densities, compared with metallic armchair nanotubes. However, few are semiconductors due to the zigzag-edge-induced anti-ferromagnetism.

The alkali-adsorbed graphene nanoribbons exhibit the feature-rich geometric, electronic and magnetic properties, being dominated by the finite-size confinement, the critical orbital hybridizations in C-C, X-C and X-X bonds, and the spin arrangements at two edges. The optimal position of adatom is situated at the hollow site of a planar graphene, in which its height grows with the atomic number. The predicted structure could be verified by the STM measurements. The well-extended π bonding in graphene is somewhat affected by alkali adsorption; furthermore, there exist charge variations between alkali and carbon/alkali atoms. The former is responsible for the modifications on the carbon-dominated valence bands. The latter arises from the s - $2p_z$ and s - s orbital hybridizations so that the alkali- and carbon-dependent conduction bands depend on the kind, distribution, and concentration of adatoms. Specially, a linear relation between free electron density and adatom concentration is thoroughly examined from various surface adsorptions. That is, each alkali atom contributes the outmost s orbital to become a conduction electron under any adatom configurations. The creation of very high carrier density indicates that the 1D n -type alkali-adsorbed graphene nanoribbons might have potential applications in nano-electronic devices. The metallic alkali-adsorbed zigzag nanoribbons can present three types of spin configurations: the anti-ferromagnetic ordering across two edges, ferromagnetic ordering along one edge and non-magnetism. These are reflected in the edge-localized energy bands and the low-energy prominent peaks of DOS. That the single-edge adatom adsorption leads to the spin-split metallic energy bands could be considered as promising materials for future applications in spintronic devices.²¹⁹ There exist important differences between the alkali- and halogen-adsorbed systems in terms of the optimal hollow/top site, the planar/buckled structure, the

single-/multi-orbital hybridizations in X-C bonds, the semiconducting/metallic/behavior, and the magnetic/non-magnetic spin configuration. In addition to graphene, the emergent layered materials include silicene, germanene, tinene, phosphorene, MoS₂ and so on. Whether the alkali adsorptions on these semiconducting nanoribbon systems could create the high free carrier density is worthy of a thorough and systematic study.

The essential properties of halogenated graphene nanoribbons strongly depend on the fluorination and chlorination-related effects. All the systems exhibit the top-site adsorptions, regardless of the kind of halogen adatoms. The critical F-C bonds in fluorinated systems can create the buckled honeycomb structure, the short bond length, the high binding energy, the multi-orbital hybridizations of $(2p_x, 2p_y, 2p_z)$, the F-C-co-dominated valence bands at deeper energy, the destruction/the serious modification of the π -electronic energy bands, the p-type doping or the semiconducting behavior, the correlation effects on the C-C and F-F bonds, and the spin configurations under certain low-concentration distributions. Most of F-adsorbed graphene nanoribbons belong to NM and AFM semiconductors. The FM and NM metals are revealed only at certain low-concentration distributions; that is, they provide the low-density free holes. The F-, C- and (F,C)-dominated energy might come to exist simultaneously, being directly reflected in the merged peaks of the orbital-projected DOSs. The magnetic configurations are very sensitive to the edge structures, concentrations and distributions. The AFM configuration is mainly determined by the carbon-induced spin arrangement near the zigzag edges. while the FM one arise from the F-induced spin distributions of the neighboring carbons or its competition with that of the zigzag-edge carbons. As to other halogenated systems, the weaker (Cl,Br,I,At)-C bonds, with the single- p_z hybridization, are responsible for the planar structure, the long bond length, the small binding energy, the slight distortion of the conducting π bonding, the high free hole densities, the low-lying halogen-created energy bands with/without spin splitting, the negligible effects on the σ -orbital hybridizations in C-C and X-X bonds, and the various spin distributions except for > 50 concentrations. There exists a specific relation: two/one free holes in a unit cell for

concentrations higher/lower than 50 %. The low-energy van Hove singularities are due to the π -electronic and the adatom-dependent states. The prominent DOS peaks, which come from the (p_x, p_y) orbitals of carbons and halogens, could be clearly separated at low concentrations. It is relatively easy to observe the Cl-induced spin distributions, compared with the F-adsorption cases. Halogen adatoms and zigzag-edge carbons co-determine the FM, AFM and NM configurations, in which the third type appears at high concentrations because of the full suppression from the strong X-X bonds. Based on the significant differences between fluorinated and other halogenated graphene nanoribbons, the latter might be more suitable in the applications of electronic and spintronic devices.²¹⁹

This review work could serve as a first step toward a full understanding of other layered condensed-matter systems characterized by the nano-scaled thickness and width, the specific lattice symmetries, and the different stacking configurations. In addition to graphene/graphene nanoribbon, the emergent layered materials have been successfully synthesized by the various experimental methods. For example, the 1D silicene, germanene, stanene, phosphorene, and MoS₂ nanoribbons are, respectively, grown Ag(111)/Ir(111)/ZrB₂ surfaces.³²⁴⁻³²⁸ They are expected to be suitable for exploring the novel physical, chemical and material properties and have high potentials in near-future applications. Such main-stream materials possess the unique geometric structures and the rich intrinsic interactions, covering the atom-dependent lattice symmetries, the planar/buckled/puckered/curved structures, the achiral/chiral edge structures, the diversified stacking configurations, the equivalent/inequivalent sublattices, the intra- and inter-layer atomic interactions, the single- and multi-orbital chemical bondings, the atom- and orbital-induced site energies, two kinds of spin-orbital couplings, and the atom- and edge-dependent spin configurations. The composite effects will be directly revealed in the various Hamiltonians. Up to now, there are some theoretical calculations on the essential properties using the first-principles method^{329,330} and the tight-binding model,^{331,332} illustrating the unusual geometric structures, electronic properties and magnetic configurations. According to the current theoretical framework, the former could provide very thor-

ough and systematic investigations on the edge-, buckling-, folding-, curving-, scrolling-, layer-, stacking-, edge-decoration-, and adatom-absorption-created diverse phenomena. The diversities among the similar/distinct layered materials are one of the studying focuses, being distinguished from the critical characteristics of the orbital bondings and spin configurations. As to the quantization phenomena arising from the external magnetic field, the latter is available in exploring the main features of Landau levels, and the magneto-optical selection rules.

Part of theoretical calculations are consistent with the experimental measurements. The STM/TEM/AFM/SEM/XPS/x-ray diffraction measurements are utilized to confirm the feature-rich geometric structures in various pristine graphene nanoribbons, covering the arm-chair/zigzag/chiral open boundaries,³³³ the curved surfaces (the unzipped nanotubes),¹⁹ the bilayer-like folded structures (the composite nanoribbon and nanotube structures),⁵ the spiral nanoscrolls,⁷⁶ the AB/AA stackings,¹⁰⁹ and the H-/Cl/O decorations with the planar or distorted edge structures.³³⁴ They are available in examining the optimal geometries of adatom-adsorbed systems, such as, the adsorption positions, the X-C and X-X bond lengths, and the planar/buckled honeycomb lattices. As to electronic structures of planar graphene nanoribbons, the ARPES measurements have confirmed the 1D parabolic energy dispersions near the Γ point, accompanied with as an energy gap and distinct energy spacings.⁵⁰ The structure- and adatom-induced drastic changes in energy bands, especially for the metallic/semiconducting behaviors, the dominance of carbons and adatoms, and the spin splitting/degeneracy, are worthy of detailed experimental investigations. The width- and edge-dependent energy gaps and the 1D asymmetric peaks in DOSs have been verified for graphene nanoribbons using the STS measurements.⁴⁹ The further STS/SP-STs examinations are required to observe the diverse electronic and magnetic properties, the FM/AFM/NM semiconductors and metals due to geometric symmetries, passivation/decoration, and adsorption. The rich and unique essential properties will be further revealed in transport and optical properties. The transport experiments could test the semiconducting or metallic behavior,

the n- or p-type doping, the relation between the conduction electron/valence hole density and the adatom concentration, and the spin-polarized currents, such as the Hall and Seebeck effects.³³⁵ Moreover, the optical/magneto-optical experiments are useful in identifying the main features of the spin-split band structure, e.g., the Kerr effects.^{315,316}

The diverse essential properties clearly indicate that the structure- and adatom-enriched graphene nanoribbons are highly potential materials in the near-future applications. The pristine graphene nanoribbons, with planar/layered structures and semiconducting characteristics, could serve as FETs,¹⁴ chemical/biochemical sensors,³³⁶ and lithium-ion battery anode,³³⁷ The folded graphene nanoribbons are suitable for FETs⁵ and high-performance flexible electrode materials.⁶⁹ Carbon nanoscrolls possess the hollow spiral structure, the unusual electronic properties, and the special mechanical strains, so that they could be utilized for hydrogen storages,⁸² microcircuit interconnect components,⁸⁰ and electromechanical nanoactuators.⁸³ Specifically, the tunable metallic and semiconducting behaviors of fluorinated graphene nanoribbons, as identified from 2D systems, are expected to have various applications, e.g., lithium batteries,³³⁸ supercapacitors,³³⁹ molecule detectors,³⁴⁰ and biosensors.³²³ Moreover, the alkali-, Cl- and metal-adsorbed graphene nanoribbons, which could generate very high-density free carriers in the presence/absence of magnetism, are promising candidates in developing the next-generation electronic/spintronic devices,³⁴¹ high-capacity batteries³⁴² and energy storages.³⁴³

Table 1: The edge passivation of $N_A = 8$ armchair graphene nanoribbon using adatoms with an atomic number less than 20, in which the boundary reconstructions present the various characteristics: type-I, type-I or type-III edge structures, X-C bond length, X-X bond lengths, absorption energies, charge transfers, and semiconducting or metallic behaviors.

Type	Adatom	X-C bond (Å)	X-X bond (Å)	ΔE (eV)	Charge transfer (e) [*]	Metal / Semiconductor
I	H	1.08	1.83	-4.359	0.02	S
	N	1.30 / 1.28	2.12	-5.881	3.13 / 2.77	S
	Be	1.85 / 1.73	2.15	-3.707	2.00	M
	B	1.57	2.23	-5.500	1.48	S
II	O	1.22	3.03	-5.776	-1.73	S
	S	1.75	2.03	-4.274	0.09	S
	F	1.34	2.58	-4.795	-0.78	S
	Cl	1.71	3.21	-3.276	-0.16	S
III	Li	2.01	2.38	-2.216	0.83	M
	Na	2.49	3.06	-0.732	0.59	M
	K	2.81	3.86	-1.413	0.51	M
	Ca	2.39	3.38	-0.819	0.90	M
	Mg	2.25	2.78	-2.011	1.05	M
	Al	2.14	2.78	-3.558	1.60	S
	Si	2.15	2.23	-3.483	1.16	S
	P	1.83	2.23	-3.732	0.50	S

*The plus or minus signs respectively denotes that electrons are gained or lost.

Table 2: The $N_Z = 7$ zigzag graphene nanoribbon decorated by adatoms with an atomic number less than 30, revealing the type-I, type-II or type-III structures (the tubular, highly curved, or flat structures), charge transfers, X-C bond lengths, X-X bond lengths, magnetic moments, spin configurations, and semiconducting/conducting behaviors.

Type	Atom	Charge Transfer* (e)	Atom-Carbon distance (\AA)	Atom-Atom distance (\AA)	(μ_B) Carbon/Atom	AFM/FM	(Semi-) conductor
I	B	0.62	1.514	1.695	0.00/0.00		M
	C	0.00	1.424	1.424	0.00/0.00		M
	N	-0.18	1.427	1.522	0.13/0.01	AFM	S
II	Be	1.30	1.823	2.899	0.00/0.00		M
	Mg	1.10	2.146	3.124	0.00/0.00		M
	Al	0.55	2.058	2.899	0.00/0.00		M
III	H	0.41	1.092		0.15/0.00	AFM	S
	Li	0.81	1.911		0.14/0.00	AFM	S
	Na	0.49	2.385		0.00/0.00		M
	K	0.35	2.656		0.00/0.00		M
	Ca	0.71	2.290		0.00/0.00		M
	Si	0.92	1.880		0.12/0.02	AFM	M
	P	0.58	1.761		0.00/0.00		M
	O	0.59	1.255		0.00/0.00		M
	S	0.12	1.719		0.00/0.00		M
	F	-0.43	1.349		0.14/0.03	AFM	S
Cl	-0.42	1.734		0.00/0.00		M	
I	V	0.52	2.119	2.422	0.03/0.70	AFM	M
	Cr	0.54	2.110	2.542	0.14/2.98	AFM	S
	Mn	0.46	2.094	2.557	0.12/3.21	FM	M
	Fe	0.25	1.895	2.447	0.16/2.32	FM	M
	Co	0.23	1.841	2.299	0.00/0.51	AFM	M
	Ni	0.18	1.844	2.428	0.00/0.25	FM	M
	Cu	0.18	1.934	2.520	0.00/0.00		M
II	Ti	0.58	2.107	2.848	0.13/0.15	FM	M
III	Sc	0.45	2.213		0.08/0.73	FM	M
	Zn	0.52	2.267		0.19/0.03	AFM	M

*The plus and minus signs respectively denote attracting and repelling electrons.

Table 3: (a) Binding energies, C-C & C-X bond lengths, alkali heights, and free electron densities of $N_A = 10$ alkali-adsorbed graphene nanoribbons with one adatom in a unit cell; (b) free electron densities for various distributions and concentrations of adatoms in $N_A = 12$ and $N_z = 8$ Li-adsorbed graphene nanoribbons.

(a)					
$N_A = 10$	E_b (eV)	C-C (Å)	C-X (Å)	heights (Å)	λ /adatom (e)
Li	-1.14	1.381	2.24	1.76	0.997
Na	-0.55	1.372	2.29	1.83	1.015
K	-0.87	1.369	3.22	2.91	0.995
Rb	-0.75	1.370	3.34	3.05	1.011
Cs	-0.72	1.368	3.38	3.09	0.995

(b)				
graphene nanoribbon	configurations	λ ($10^7 e/cm$)	λ /adatom concentration (e)	Bader charge transfer (e)
Armchair $N_A = 12$	(1) <i>single</i> ; Li	2.31	0.995	0.75
	(1) <i>single</i> ; K	2.31	0.995	0.45
	(1) <i>single</i> ; Cs	2.31	0.995	0.54
	(3,7) <i>single</i> ; Li	4.67	1.008	0.69
	(3,7) <i>double</i>	4.62	0.989	0.75
	(1,10) <i>single</i>	4.68	1.008	0.74
	(1,10) <i>double</i>	4.67	1.008	0.74
	(1,4,7,10) <i>double</i>	9.24	0.994	0.71
	(1,2,5,6,9,10) <i>double</i>	13.96	1.007	0.70
	(1,3,5,7,9,2,4,6,8,10) <i>double</i>	23.03	0.988	0.68
(1 \rightarrow 10,1 \rightarrow 10) <i>double</i>	46.36	0.995	0.68	
Zigzag $N_z = 8$	(1) <i>single</i>	2.02	1.001	0.88
	(7) <i>single</i>	2.03	1.009	0.89
	(1,13) <i>single</i>	4.10	1.015	0.88
	(1,13) <i>double</i>	4.02	1.001	0.88
	(1,7,13) <i>single</i>	6.13	1.011	0.87
	(1,7,13) <i>double</i>	6.08	1.002	0.88

Table 4: Binding energy, magnetic moment/magnetism, metal/energy gap, free hole density, F-C bond length, deviation height of C and the first C-C bond length for fluorinated $N_A = 10$ armchair and $N_Z = 10$ zigzag graphene nanoribbons under various distributions and concentrations. NM, FM and AFM correspond to non-magnetism, ferro-magnetism and anti-ferro-magnetism, respectively.

GNRs	Systems	E_b (eV)	M_{tot} (μ B) /magnetism	E_g (eV) /metal	# of holes	F-C (\AA)	C deviation (\AA)	Nearest C-C (\AA)
AGNR	Pristine	-	0/NM	1.1	0	-	0	1.428
	(6) _s	-2.5414	0/NM	M	1	1.562	0.423	1.484
	(1) _s	-3.3139	0.91/FM	M	1	1.472	0.472	1.491
	(6,13) _s	-2.9268	0/NM	M	2	1.507	0.542	1.492
	(6,13) _d	-2.9324	0/NM	M	2	1.508	0.428	1.495
	(1,20) _s	-3.5401	2.00/FM	0.214	0	1.462	0.471	1.491
	(1,20) _d	-3.5456	2.00/FM	0.214	0	1.463	0.450	1.491
	(1,6) _d	-3.9783	0/NM	0.956	0	1.485	0.440	1.495
	(1,6,13,20) _d	-3.5811	1.00/FM	M	1	1.477	0.343	1.494
	(1,2,5,6) _d	-4.5844	0/NM	0	1	1.450	0.338	1.536
	(6,9,14,18) _d	-3.2003	0/NM	1.562	0	1.507	0.359	1.499
	(6F) _d	-3.2155	1.196/FM	M	1	1.474	0.501	1.481
	(6F) _d	-4.6830	0/NM	1.548	0	1.419	0.452	1.541
	(8F) _d	-3.3430	3.129/FM	M	1	1.449	0.519	1.547
	(8F) _d	-4.6047	0/NM	1.01	0	1.429	0.409	1.501
	(10F) _d	-4.5445	0/NM	0.479	0	1.418	0.530	1.553
(20F) _d	-4.5813	0/NM	3.4	0	1.396	0.459	1.556	
ZGNR	Pristine	-	0/AFM	0.374	0	-	0	1.428
	(3) _s	-4.2690	-0.768/FM	M	1	1.476	0.428	1.492
	(19) _s	-2.2481	-0.670/FM	M	1	1.563	0.320	1.485
	(3,19) _d	-3.5647	-0.888/NM	M	1	1.546	0.321	1.481
	(19,22) _d	-2.8859	0/AFM	0.169	0	1.499	0.324	1.493
	(3,38) _d	-4.7638	0/NM	0.272	0	1.455	0.427	1.493
	(40F) _d	-4.1984	0/AFM	2.969	0	1.384	0.397	1.563

Table 5: Similar quantities in Table 4, but shown for Cl-related graphene nanoribbons.

Figure captions

Chap. 2

Figure 1: The TEM instrument in measuring electron diffraction pattern.

Figure 2: The schematic illustration of STM in observing surface configuration by controlling the tip height under a specific tunneling current.

Figure 3: The schematic diagram of taking the current-dependent normalized conductance spectrum by using STS.

Figure 4: The photo-electronic spectrum of ARPES in determining the momentum-dependent valence state energies.

Chap. 3

Figure 1: Geometric structures of $N_A = 10$ armchair nanoribbon.

Figure 2: Energy bands of pristine (a) $N_A = 8$, (b) $N_A = 9$, (c) $N_A = 10$, and (d) $N_A = 11$ armchair nanoribbons, in which the contributions from the edge carbon atoms are denoted by the blue circles.

Figure 3: Energy bands of H-passivated (a) $N_A = 8$, (b) $N_A = 9$, (c) $N_A = 10$, and (d) $N_A = 11$ armchair nanoribbons, in which the contributions from the edge hydrogen atoms are denoted by the blue circles.

Figure 4: Width dependent energy gaps for (a) pristine and (b) H-passivated armchair graphene nanoribbon. The spatial charge distributions for (c) pristine and (d) H-passivated armchair nanoribbon. (e) and (f) are the charge differences for pristine and H-passivated armchair nanoribbon, respectively.

Figure 5: The total and orbital-projected DOSs for pristine (a) $N_A = 8$, (b) $N_A = 9$, (c) $N_A = 10$, and (d) $N_A = 11$ armchair nanoribbons and H-passivated (e) $N_A = 8$, (f) $N_A = 9$, (g) $N_A = 10$, and (h) $N_A = 11$ armchair nanoribbons.

Figure 6: Geometric structures of zigzag nanoribbon.

Figure 7: Energy bands of pristine (a) $N_Z = 10$, (b) $N_Z = 11$, (c) $N_Z = 12$, and (d) $N_Z = 13$ zigzag nanoribbons, in which the contributions from the edge carbon atoms are

denoted by the blue circles.

Figure 8: Energy bands of H-passivated (a) $N_Z = 10$, (b) $N_Z = 11$, (c) $N_Z = 12$, and (d) $N_Z = 13$ zigzag nanoribbons, in which the contributions from the edge hydrogen atoms are denoted by the blue circles.

Figure 9: The spatial charge distributions for $N_Z = 10$ (a) pristine and (b) H-passivated zigzag nanoribbon. (c) and (d) are the charge differences for pristine and H-passivated zigzag nanoribbon, respectively. The difference between two spin states for (e) pristine and (f) H-passivated zigzag nanoribbon.

Figure 10: The total and orbital-projected DOSs for pristine (a) $N_Z = 10$, (b) $N_Z = 11$, (c) $N_Z = 12$, and (d) $N_Z = 13$ zigzag nanoribbons and H-passivated (e) $N_Z = 10$, (f) $N_Z = 11$, (g) $N_Z = 12$, and (h) $N_Z = 13$ zigzag nanoribbons.

Chap 4.

Figure 1: (a) Geometric structure of an $N_A = 10$ curved armchair graphene nanoribbon with radius and arc angle, and (b) the dependence of the edge-C-C bond length on ϕ .

Figure 2: (a) The ϕ -dependent ground state energy per atom for armchair nanoribbons with distinct widths, (b) the critical arc angles and interaction distances; (c) the zipping and unzipping energies. Also shown in (a) are the strain energies fitted by the dashed curves.

Figure 3: Band structures of the $N_A = 10$ curved armchair nanoribbon under (a) $\phi = 0^\circ$, (b) 90° , (c) 190° , (d) 300° , (e) 320° , (f) 340° , (g) 350° and (h) 360° . The radii of open circles represent the contributions due to edge atoms.

Figure 4: DOSs arising from the total atoms, edge atoms and center atoms for the $N_A = 10$ curved armchair nanoribbon under (a) $\phi = 0^\circ$, (b) 190° , (c) 320° , (d) 340° , and (e) 360° .

Figure 5: (a) A carbon nanotube, a rolled-up graphene sheet in the cylindrical structure from the origin to the vector $\mathbf{R}_x = m\mathbf{a}_1 + n\mathbf{a}_2$, (b) a (5,5) armchair nanotube and (c) a (9,0) zigzag nanotube.

Figure 6: Energy bands of armchair nanotubes: (a) (3,3), (b) (5,5), (c) (10,10) and (d) (20,20).

Figure 7: Electronic structures for zigzag nanotubes: (a) (5,0), (b) (6,0), (c) (7,0) and (d) (9,0).

Figure 8: Energy gaps of zigzag carbon nanotubes including $(3I, 0)$, $(3I + 1, 0)$ and $(3I + 2, 0)$.

Figure 9: The spatial charge distributions for (a) (3,3) & (20,20) armchair nanotubes, and (b) (5,0) & (9,0) zigzag systems.

Figure 10: The total and orbital-projected DOSs for (a) (3,3), (b) (5,5), (c) (10,10), (d) (20,20). (e) (5,0), (f) (6,0), (g) (7,0) and (h) (9,0) nanotubes.

Chap. 5

Figure 1: The side view of a folded graphene nanoribbon passivated by hydrogen atoms (white balls): (a) armchair and (b) zigzag systems with (c) & (d) nanotube diameter (D_n), interlayer distance (I_z) and edge distance (d_{edge}). (e) shows the top views for the AA, AB and AA' stackings

Figure 2: The four types of top views for armchair folded graphene nanoribbons: (I) even-aAA', (II) even-aAA, (III) odd-aAA; (IV) odd-aAA' stackings, and the similar configurations for zigzag systems: (I) even-zAA, (II) even-zAB, (III) odd-zAA'; (IV) odd-zAB stackings.

Figure 3: The width-dependent nanotube diameters and interlayer distances of four types of folded (a) armchair and (b) zigzag graphene nanoribbons.

Figure 4: The dependence of folding energy on nanoribbon width for four types of folded (a) armchair and (b) zigzag systems.

Figure 5: The 1D band structures of the folded armchair graphene nanoribbons for (a) (even-zAA, $N_A=34$), (b) (odd-zAA, $N_A=35$), (c) (even-zAA, $N_A=36$), (d) (odd-zAA, $N_A=37$), (e) (even-zAA', $N_A=34$), (f) (odd-zAA', $N_A=35$), (g) (even-zAA', $N_A=36$); (h) (odd-zAA', $N_A=37$).

Figure 6: Six categories of width-dependent energy gaps for folded armchair nanoribbons with (a) AA and (b) AA' stacking configurations.

Figure 7: The spatial spin densities of the (a) odd-zAA' and (b) odd-zAB stackings, and the band structures for (c) (even-zAA, $N_Z=32$), (d) (even-zAB, $N_Z=32$), (e) (odd-zAA',

$N_Z=33$) and (b) (odd-zAB, $N_Z=33$).

Figure 8: The width-dependent energy gaps of the folded zigzag nanoribbons for the even-zAB, odd-zAA' and odd-zAB stackings.

Figure 9: The 1D density of states of the folded graphene nanoribbons for (a) (even-aAA, $N_A=34$) & (even-AA', $N_A=34$), (b) (odd-aAA, $N_A=35$) & (odd-AA', $N_A=35$), (c) (even-aAA, $N_A=36$) & (even-aAA', $N_A=36$), (d) (odd-AA, $N_A=37$) & (odd-AA', $N_A=37$), (e) (even-zAA, $N_Z=32$) & (even-zAB, $N_Z=32$), (e) (odd-zAA', $N_Z=33$) with spin-up and spin-down components; (f) (odd-zAB, $N_Z=33$) with separate spin contributions.

Chap 6.

Figure 1: For armchair carbon nanoscrolls, the ideal structure of (a) (34,7) and the optimal structures of (b) (34,7), (c) (43,9); (d) (47,11) under the (y, z)-plane top view. Also shown in (f) is the side view for the relaxed (34,7) system.

Figure 2: For zigzag carbon nanoscrolls, the ideal structure of (a) (18,4) and the optimal structures of (b) (18,4), (c) (27,4); (d) (36,4).

Figure 3: The width-dependent scrolling energies for (a) armchair and (b) zigzag carbon nanoscrolls with the distinct internal lengths.

Figure 4: Band structures of (a) (38,7), (b), (39,7) and (c) (40,7) armchair carbon nanoscrolls, and those of (d) $N_A=38$, (e) 39 and (f) 40 armchair nanoribbons.

Figure 5: (a) The spatial spin-up and spin-down density distributions in the (36,4) zigzag carbon nanoscroll, indicated by red and blue regions, respectively. Band structures are shown for (b) the (36,4) zigzag carbon nanoscroll and (c) the $N_Z = 36$ zigzag nanoribbon.

Figure 6: The width-dependent energy gaps for (a) armchair carbon nanoscrolls with $N_{in} = 7$ and (b) zigzag systems with $N_{in} = 4$.

Figure 7: The spatial charge distribution and the density difference for (a) the (38,7) armchair nanoscroll and (b) the (36,4) zigzag one.

Figure 8: Density of states for the (a) (38,7), (b) (39,7) and (c) (40,7) armchair nanoscrolls; for the (36,4) zigzag one.

Chap. 7.

Figure 1: Geometric structures of bilayer zigzag graphene nanoribbons: (a) the relative displacement between the upper and lower layers along the armchair direction, (b) AA, (c) AB_α , (d) AA' and (e) AB_β stackings.

Figure 2: Optimal structures of bilayer zigzag graphene nanoribbons in the side view for (a) AA, (b) AB_α , (c) AA' and (d) AB_β stackings with width of $N_Z = 10$.

Figure 3: Dependence of the magnetic moment on the inter-edge distance for AA, AB_α , AA' and AB_β stackings with width of $N_Z = 10$.

Figure 4: (a) The shift-dependent cohesive energy for the $N_Z = 10$ bilayer zigzag system along $AA \rightarrow AB_\alpha$ and $AA' \rightarrow AB_\beta$, and (b) the dependence of the critical shift on the nanoribbon width.

Figure 5: Band structures of $N_Z = 10$ bilayer zigzag nanoribbons under the shifts along Path I: (a) $d_y = 0$, (b) $b/4$, (c) $b/2$ and (d) b . Also shown are the spatial charge densities for (e) $d_y = 0$ and (f) b (?). Band structures of $N_y = 10$ for (a) AA: AFM-AFM, (b)

Figure 6: Same plot as Fig. 5, but shown for (a) AA' stacking with AFM-AFM, (b) AB_β stacking with AFM-AFM, (c) AA' stacking with AFM-FM; (d) AB_β stacking with AFM-FM. The spin-up and spin-down states are indicated by the red dashed and blue solid curves, respectively.

Figure 7: The stacking-dependent DOSs of the $N_Z = 10$ bilayer zigzag nanoribbons for (a) AA, (b) AB_α , (c) AA' with AFM-AFM, (d) AB with AFM-AFM, (e) AA' with AFM-FM; (f) AB_β with AFM-FM (colors of squares should be black in Carbon).

Figure 8: The shift-dependent band-edge state energies of the $N_Z = 10$ bilayer zigzag nanoribbons along (a) Path I, (b) Path II with AFM-AFM, and (c) Path II with AFM-FM. Also shown in (d) are the shift-enriched energy gaps.

Figure 9: (a) Geometric structures of bilayer graphene shifting along the armchair direction, and (b) their ground state energies and interlayer distances.

Figure 10: The shift-dependent band structures for bilayer graphenes with (a) $d_y = 0$,

(b) $b/8$, (c) $4b/8$, (d) b , (e) $11b/8$, and (f) $3b/2$.

Figure 11: The shift-dependent DOSs for bilayer graphenes with (a) $d_y = 0$, (b) $b/8$, (c) $4b/8$, (d) $8b/8$, (e) $11b/8$, and (f) $12b/8$.

Chap. 8

Figure 1: Geometric structures of (a) type-I, (b) type-II and (c) type-III edge-decorated graphene nanoribbons.

Figure 2: The spatial charge densities for (a) N-, (b) S-, (c) Li- and P-decorated $N_A = 8$ armchair nanoribbons.

Figure 3: Energy bands of (a) pristine, (b) N-, (c) S-, and (d) Li-decorated $N_A = 8$ armchair nanoribbons, in which the contributions from the nonpassivated edge carbon atoms or the adatoms are denoted by the open circles.

Figure 4: The width-dependent energy gaps for the (a) pristine, (b) N-, (c) S- and (d) Li-decorated armchair nanoribbons.

Figure 5: DOSs of the (a) pristine, (b) N-, (c) S- and Li-decorated $N_A = 8$ armchair nanoribbons. Also shown are the orbital-projected components due to the carbon atoms. The symmetric peaks are denoted by the red circles.

Figure 6: Geometric structures: (a) A single-walled armchair carbon nanotube as a starting material, (b) an unzipped nanotube in an environment of decorating adatoms, (c) type-I, (d) type-II, and (e) type-III adatom-decorated nanotube/nanoribbon-related systems.

Figure 7: (a) The arc-angle-dependent total energies, measured from those at $\phi = 0^\circ$, for the B-, Be- and H-decorated $N_Z = 7$ armchair nanoribbons, as well as an unzipped carbon nanotube. The width dependence of the critical interaction distance and the energy barrier in (b) type-I and (c) type-II adatom-decorated systems.

Figure 8: Band structures for (a) (4,4) armchair nanotube, (b) B-, (c) Be- and H-decorated $N_Z = 7$ systems, in which the adatom contributions are represented by the circle radii.

Figure 9: DOSs and local DOSs due to adatoms and edge carbons for (a) (4,4) armchair

carbon nanotube, (b) B-, (c) Be- and (d) H-decorated $N_Z = 7$ zigzag nanoribbons.

Chap. 9.

Figure 1: Geometric structures of alkali-adsorbed graphene nanoribbons: (a) $N_A = 10$ armchair and (b) $N_Z = 10$ zigzag systems with unit cells enclosed by the dashed rectangles. The grey, white and purple balls, respectively, represent carbon, hydrogen and alkali atoms.

Figure 2. Band structures of $N_A = 10$ armchair graphene nanoribbons with hydrogen passivation for (a) pristine system and (b) Li-, (c) Na-, (d) K-, (e) Rb- and (f) Cs-adsorbed ones. Only one adatom is situated at $(1)_s$.

Figure 3. Energy bands of Li-adsorbed $N_A = 10$ armchair graphene nanoribbons under various distributions and concentrations: (a) $(2 \text{ Li})_s$, (b) $(4 \text{ Li})_s$, (c) $(4 \text{ Li})_s$ (d) $(8 \text{ Li})_s$, (e) $(8 \text{ Li})_d$, and (f) $(16 \text{ Li})_d$.

Figure 4: The spatial charge densities of Li-adsorbed $N_A = 10$ armchair nanoribbons under various adatom configurations: (a) pristine, (b) $(1, \text{Li})_s$, (c) $(4, \text{Li})_s$, (d) $(8, \text{Li})_s$; (e) $(8, \text{Li})_d$. The charge density differences, corresponding to (b)-(e), are shown in (g)-(j), respectively. (f) and (k) are those of $N_z = 10$ zigzag system under single adatom adsorption.

Figure 5: The atom- and orbital-projected DOSs of Li-adsorbed $N_A = 10$ armchair systems under various adatom configurations: (a) pristine, (b) $(1 \text{ Li})_s$, (c) $(2 \text{ Li})_s$, (d) $(4 \text{ Li})_s$, (e) $(8 \text{ Li})_s$; (f) $(16 \text{ Li})_d$.

Figure 6: Band structures of $N_z = 10$ Li-adsorbed zigzag graphene nanoribbons for various adatom configurations: (a) pristine, (b) $(1)_s$, (c) $(3)_s$, (d) $(5)_s$, (e) $(9)_s$, and (f) $(1, 18)_s$.

Figure 7: The spatial spin distributions for $N_z = 10$ Li-adsorbed zigzag graphene nanoribbons under various adatom configurations: (a) pristine, (b) $(1)_s$, (c) $(3)_s$, (d) $(5)_s$, (e) $(9)_s$, and (f) $(1, 18)_s$.

Figure 8: The atom- and orbital-projected DOSs of Li-adsorbed $N_z = 10$ zigzag systems for various adatom configurations: (a) pristine, (b) $(1)_s$, (c) $(3)_s$, (d) $(5)_s$, (e) $(9)_s$, and (f) $(1, 18)_s$.

Chap. 10

Figure 1: Geometric structures of F-adsorbed graphene nanoribbons for (a) $N_A = 10$ armchair structure and (b) $N_Z = 10$ zigzag one.

Figure 2: Band structures of $N_A = 10$ armchair graphene nanoribbon for (a) pristine, (b) $(13)_s$, (c) $(1)_1$, (d) $(6,21)_s$, (e) $(6,21)_d$, (f) $(1,23)_s$, (g) $(1,23)_d$, (h) $(6,21)_s$, (i) $(6F)_d$, (j) $(8F)_d$, (k) $(16F)_d$, & (l) $(20F)_d$. Blue circles represent the contribution of F adatoms. The red and black curves denote the spin-split energy bands. **change the distributions and concentrations.

Figure 3: Band structures of $N_z = 8$ zigzag graphene nanoribbon for (a) pristine, (b) $(3)_s$, (c) $(13)_s$, (d) $(3,30)_d$, (e) $(11,14)_d$ and (f) $(3,14)_d$ cases.

Figure 4: The spatial spin density of $N_A = 10$ fluorinated armchair graphene nanoribbon under (a) $(1)_s$, (b) $(1,23)_s$; (c) $(1,23)_d$ cases. Similar plots for $N_Z = 10$ zigzag system under (d) $(3)_s$, (e) pristine, and (f) $(11,14)_d$ cases. [Check $(3,14)$ with FM in zigzag case; Has another spin distribution in armchair cases?]

Figure 5: The spatial charge density of $N_A = 10$ armchair graphene nanoribbon for (a) Pristine, (b) $(13)_s$, & (d) $(24F)_d$ cases; the charge density difference for (c) $(13)_s$, (e) $(24F)_d$ cases. The partial charge density is shown for (f) armchair- $(6,21)_d$, (g) zigzag- $(3,14)_d$, (h) armchair- $(1,6)_d$, and (i) zigzag- $(11,14)_d$.

Figure 6: Orbital- and spin-projected DOSs for (a) pristine, (b) $(10F)_d^-$, (c) $(20F)_d^-$, (d) $(24F)_d^-$, (e) $(13)_s^-$, (f) $(6,21)_d^-$, (g) $(1,23)_d^-$ -adsorbed $N_A = 10$ armchair systems; (h) $(3,14)_d^-$ & (i) $(11,14)_d^-$ -adsorbed and (j) pristine $N_Z = 10$ zigzag systems. Blue triangles arise from the partially flat bands. [spin-up and spin-down in (h) is wrong]

Figure 7: The spatial spin densities of Cl-adsorbed $N_A = 10$ armchair nanoribbons under various configurations: (a) $(1 \text{ Cl})_s$, (b) $(2 \text{ Cl})_d$, (c) $(4 \text{ Cl})_d$, (d) $(8 \text{ Cl})_d$, and (e) $(9 \text{ Cl})_d$. Similar plots for $N_z = 10$ zigzag systems: (f) (pristine), (g) (one edge), (h) (two edges) $_d$, (i) one center, and (j) (one center, one edge) $_d$.

References

- (1) Bernal, J. The structure of graphite. *Proceedings of the Royal Society of London. Series A, Containing Papers of a Mathematical and Physical Character* **1924**, *106*, 749–773.
- (2) Tuinstra, F.; Koenig, J. L. Raman spectrum of graphite. *The Journal of Chemical Physics* **1970**, *53*, 1126–1130.
- (3) Novoselov, K. S.; Geim, A. K.; Morozov, S. V.; Jiang, D.; Zhang, Y.; Dubonos, S. V.; Grigorieva, I. V.; Firsov, A. A. Electric field effect in atomically thin carbon films. *science* **2004**, *306*, 666–669.
- (4) Geim, A. K.; Novoselov, K. S. The rise of graphene. *Nature materials* **2007**, *6*, 183–191.
- (5) Li, X.; Wang, X.; Zhang, L.; Lee, S.; Dai, H. Chemically derived, ultrasmooth graphene nanoribbon semiconductors. *Science* **2008**, *319*, 1229–1232.
- (6) Han, M. Y.; Özyilmaz, B.; Zhang, Y.; Kim, P. Energy band-gap engineering of graphene nanoribbons. *Physical review letters* **2007**, *98*, 206805.
- (7) Iijima, S. Helical microtubules of graphitic carbon. *nature* **1991**, *354*, 56.
- (8) Iijima, S.; Ichihashi, T. Single-shell carbon nanotubes of 1-nm diameter. *Nature* **1993**, *363*, 603–605.
- (9) Liu, J.; Dai, H.; Hafner, J. H.; Colbert, D. T. Fullerene ‘crop circles’. *Nature* **1997**, *385*, 780.
- (10) Sano, M.; Kamino, A.; Okamura, J.; Shinkai, S. Ring closure of carbon nanotubes. *Science* **2001**, *293*, 1299–1301.
- (11) Kroto, H. W.; Heath, J. R.; O’Brien, S. C.; Curl, R. F.; Smalley, R. E. C 60: buckminsterfullerene. *Nature* **1985**, *318*, 162–163.

- (12) Kroto, H. W. C 60 buckminsterfullerene. *MRS Online Proceedings Library Archive* **1990**, *206*.
- (13) Bai, J.; Duan, X.; Huang, Y. Rational fabrication of graphene nanoribbons using a nanowire etch mask. *Nano letters* **2009**, *9*, 2083–2087.
- (14) Wang, X.; Ouyang, Y.; Li, X.; Wang, H.; Guo, J.; Dai, H. Room-temperature all-semiconducting sub-10-nm graphene nanoribbon field-effect transistors. *Physical review letters* **2008**, *100*, 206803.
- (15) Datta, S. S.; Strachan, D. R.; Khamis, S. M.; Johnson, A. C. Crystallographic etching of few-layer graphene. *Nano letters* **2008**, *8*, 1912–1915.
- (16) Ci, L.; Xu, Z.; Wang, L.; Gao, W.; Ding, F.; Kelly, K. F.; Yakobson, B. I.; Ajayan, P. M. Controlled nanocutting of graphene. *Nano Research* **2008**, *1*, 116–122.
- (17) McAllister, M. J.; Li, J.-L.; Adamson, D. H.; Schniepp, H. C.; Abdala, A. A.; Liu, J.; Herrera-Alonso, M.; Milius, D. L.; Car, R.; Prud'homme, R. K. Single sheet functionalized graphene by oxidation and thermal expansion of graphite. *Chemistry of materials* **2007**, *19*, 4396–4404.
- (18) Fujii, S.; Enoki, T. Cutting of oxidized graphene into nanosized pieces. *Journal of the American Chemical Society* **2010**, *132*, 10034–10041.
- (19) Kosynkin, D. V.; Higginbotham, A. L.; Sinitskii, A.; Lomeda, J. R.; Dimiev, A.; Price, B. K.; Tour, J. M. Longitudinal unzipping of carbon nanotubes to form graphene nanoribbons. *Nature* **2009**, *458*, 872–876.
- (20) Cataldo, F.; Compagnini, G.; Patané, G.; Ursini, O.; Angelini, G.; Ribic, P. R.; Margaritondo, G.; Cricenti, A.; Palleschi, G.; Valentini, F. Graphene nanoribbons produced by the oxidative unzipping of single-wall carbon nanotubes. *Carbon* **2010**, *48*, 2596–2602.

- (21) Kumar, P.; Panchakarla, L.; Rao, C. Laser-induced unzipping of carbon nanotubes to yield graphene nanoribbons. *Nanoscale* **2011**, *3*, 2127–2129.
- (22) Jiao, L.; Zhang, L.; Wang, X.; Diankov, G.; Dai, H. Narrow graphene nanoribbons from carbon nanotubes. *Nature* **2009**, *458*, 877–880.
- (23) Jiao, L.; Zhang, L.; Ding, L.; Liu, J.; Dai, H. Aligned graphene nanoribbons and crossbars from unzipped carbon nanotubes. *Nano Research* **2010**, *3*, 387–394.
- (24) Elías, A. L.; Botello-Méndez, A. R.; Meneses-Rodríguez, D.; Jehová González, V.; Ramírez-González, D.; Ci, L.; Muñoz-Sandoval, E.; Ajayan, P. M.; Terrones, H.; Terrones, M. Longitudinal cutting of pure and doped carbon nanotubes to form graphitic nanoribbons using metal clusters as nanoscalpels. *Nano letters* **2009**, *10*, 366–372.
- (25) Parashar, U. K.; Bhandari, S.; Srivastava, R. K.; Jariwala, D.; Srivastava, A. Single step synthesis of graphene nanoribbons by catalyst particle size dependent cutting of multiwalled carbon nanotubes. *Nanoscale* **2011**, *3*, 3876–3882.
- (26) Talyzin, A. V.; Luzan, S.; Anoshkin, I. V.; Nasibulin, A. G.; Jiang, H.; Kauppinen, E. I.; Mikoushkin, V. M.; Shnitov, V. V.; Marchenko, D. E.; Noreus, D. Hydrogenation, purification, and unzipping of carbon nanotubes by reaction with molecular hydrogen: road to graphene nanoribbons. *ACS nano* **2011**, *5*, 5132–5140.
- (27) Paiva, M. C.; Xu, W.; Fernanda Proença, M.; Novais, R. M.; Lægsgaard, E.; Besenbacher, F. Unzipping of functionalized multiwall carbon nanotubes induced by STM. *Nano letters* **2010**, *10*, 1764–1768.
- (28) Kim, K.; Sussman, A.; Zettl, A. Graphene nanoribbons obtained by electrically unwrapping carbon nanotubes. *Acs Nano* **2010**, *4*, 1362–1366.
- (29) Cano-Márquez, A. G.; Rodríguez-Macías, F. J.; Campos-Delgado, J.; Espinosa-González, C. G.; Tristán-López, F.; Ramírez-González, D.; Cullen, D. A.; Smith, D. J.;

- Terrones, M.; Vega-Cantú, Y. I. Ex-MWNTs: graphene sheets and ribbons produced by lithium intercalation and exfoliation of carbon nanotubes. *Nano letters* **2009**, *9*, 1527–1533.
- (30) Kosynkin, D. V.; Lu, W.; Sinitiskii, A.; Pera, G.; Sun, Z.; Tour, J. M. Highly conductive graphene nanoribbons by longitudinal splitting of carbon nanotubes using potassium vapor. *Acs Nano* **2011**, *5*, 968–974.
- (31) Shinde, D. B.; Debgupta, J.; Kushwaha, A.; Aslam, M.; Pillai, V. K. Electrochemical unzipping of multi-walled carbon nanotubes for facile synthesis of high-quality graphene nanoribbons. *Journal of the American Chemical Society* **2011**, *133*, 4168–4171.
- (32) Jiao, L.; Wang, X.; Diankov, G.; Wang, H.; Dai, H. Facile synthesis of high-quality graphene nanoribbons. *Nature nanotechnology* **2010**, *5*, 321–325.
- (33) Xie, L.; Wang, H.; Jin, C.; Wang, X.; Jiao, L.; Suenaga, K.; Dai, H. Graphene nanoribbons from unzipped carbon nanotubes: atomic structures, Raman spectroscopy, and electrical properties. *Journal of the American Chemical Society* **2011**, *133*, 10394–10397.
- (34) Campos-Delgado, J.; Romo-Herrera, J. M.; Jia, X.; Cullen, D. A.; Muramatsu, H.; Kim, Y. A.; Hayashi, T.; Ren, Z.; Smith, D. J.; Okuno, Y. Bulk production of a new form of sp^2 carbon: crystalline graphene nanoribbons. *Nano letters* **2008**, *8*, 2773–2778.
- (35) Wei, D.; Liu, Y.; Zhang, H.; Huang, L.; Wu, B.; Chen, J.; Yu, G. Scalable synthesis of few-layer graphene ribbons with controlled morphologies by a template method and their applications in nanoelectromechanical switches. *Journal of the American Chemical Society* **2009**, *131*, 11147–11154.

- (36) Sprinkle, M.; Ruan, M.; Hu, Y.; Hankinson, J.; Rubio-Roy, M.; Zhang, B.; Wu, X.; Berger, C.; De Heer, W. A. Scalable templated growth of graphene nanoribbons on SiC. *Nature nanotechnology* **2010**, *5*, 727–731.
- (37) Yang, X.; Dou, X.; Rouhanipour, A.; Zhi, L.; Räder, H. J.; Müllen, K. Two-dimensional graphene nanoribbons. *Journal of the American Chemical Society* **2008**, *130*, 4216–4217.
- (38) Cai, J.; Ruffieux, P.; Jaafar, R.; Bieri, M.; Braun, T.; Blankenburg, S.; Muoth, M.; Seitsonen, A. P.; Saleh, M.; Feng, X. Atomically precise bottom-up fabrication of graphene nanoribbons. *Nature* **2010**, *466*, 470–473.
- (39) Blankenburg, S.; Cai, J.; Ruffieux, P.; Jaafar, R.; Passerone, D.; Feng, X.; Müllen, K.; Fasel, R.; Pignedoli, C. A. Intraribbon heterojunction formation in ultranarrow graphene nanoribbons. *Acs Nano* **2012**, *6*, 2020–2025.
- (40) Son, Y.-W.; Cohen, M. L.; Louie, S. G. Energy gaps in graphene nanoribbons. *Physical review letters* **2006**, *97*, 216803.
- (41) Barone, V.; Hod, O.; Scuseria, G. E. Electronic structure and stability of semiconducting graphene nanoribbons. *Nano letters* **2006**, *6*, 2748–2754.
- (42) Lee, G.; Cho, K. Electronic structures of zigzag graphene nanoribbons with edge hydrogenation and oxidation. *Physical Review B* **2009**, *79*, 165440.
- (43) Son, Y.-W.; Cohen, M. L.; Louie, S. G. Half-metallic graphene nanoribbons. *Nature* **2006**, *444*, 347–349.
- (44) Dutta, S.; Manna, A. K.; Pati, S. K. Intrinsic half-metallicity in modified graphene nanoribbons. *Physical review letters* **2009**, *102*, 096601.
- (45) Yang, L.; Cohen, M. L.; Louie, S. G. Excitonic effects in the optical spectra of graphene nanoribbons. *Nano letters* **2007**, *7*, 3112–3115.

- (46) Huang, Y.; Chang, C.; Lin, M.-F. Magnetic and quantum confinement effects on electronic and optical properties of graphene ribbons. *Nanotechnology* **2007**, *18*, 495401.
- (47) Li, Z.; Qian, H.; Wu, J.; Gu, B.-L.; Duan, W. Role of symmetry in the transport properties of graphene nanoribbons under bias. *Physical review letters* **2008**, *100*, 206802.
- (48) Wakabayashi, K.; Takane, Y.; Yamamoto, M.; Sigrist, M. Electronic transport properties of graphene nanoribbons. *New Journal of Physics* **2009**, *11*, 095016.
- (49) Tapasztó, L.; Dobrik, G.; Lambin, P.; Biró, L. P. Tailoring the atomic structure of graphene nanoribbons by scanning tunnelling microscope lithography. *Nature nanotechnology* **2008**, *3*, 397–401.
- (50) others,, et al. Electronic structure of atomically precise graphene nanoribbons. *Acs Nano* **2012**, *6*, 6930–6935.
- (51) Kobayashi, Y.; Fukui, K.-i.; Enoki, T.; Kusakabe, K.; Kaburagi, Y. Observation of zigzag and armchair edges of graphite using scanning tunneling microscopy and spectroscopy. *Physical Review B* **2005**, *71*, 193406.
- (52) Abbas, A. N.; Liu, G.; Liu, B.; Zhang, L.; Liu, H.; Ohlberg, D.; Wu, W.; Zhou, C. Patterning, characterization, and chemical sensing applications of graphene nanoribbon arrays down to 5 nm using helium ion beam lithography. *ACS nano* **2014**, *8*, 1538–1546.
- (53) Traversi, F.; Raillon, C.; Benameur, S.; Liu, K.; Khlybov, S.; Tosun, M.; Krasnozhan, D.; Kis, A.; Radenovic, A. Detecting the translocation of DNA through a nanopore using graphene nanoribbons. *Nature nanotechnology* **2013**, *8*, 939–945.
- (54) Kane, C. L.; Mele, E. Size, shape, and low energy electronic structure of carbon nanotubes. *Physical Review Letters* **1997**, *78*, 1932.

- (55) Shyu, F.-L.; Lin, M. F. Electronic and optical properties of narrow-gap carbon nanotubes. *Journal of the Physical Society of Japan* **2002**, *71*, 1820–1823.
- (56) Ouyang, M.; Huang, J.-L.; Cheung, C. L.; Lieber, C. M. Energy gaps in” metallic” single-walled carbon nanotubes. *Science* **2001**, *292*, 702–705.
- (57) Ajiki, H.; Ando, T. Aharonov-Bohm effect in carbon nanotubes. *Physica B: Condensed Matter* **1994**, *201*, 349–352.
- (58) Lin, M. F.; Shung, K. W.-K. Plasmons and optical properties of carbon nanotubes. *Physical Review B* **1994**, *50*, 17744.
- (59) Shyu, F.-L.; Chang, C.-P.; Chen, R.-B.; Chiu, C.-W.; Lin, M. F. Magnetoelectronic and optical properties of carbon nanotubes. *Physical Review B* **2003**, *67*, 045405.
- (60) Longe, P.; Bose, S. Collective excitations in metallic graphene tubules. *Physical Review B* **1993**, *48*, 18239.
- (61) Lin, M. F.; Shung, K. W.-K. Elementary excitations in cylindrical tubules. *Physical Review B* **1993**, *47*, 6617.
- (62) Lin, M. F.; Chuu, D.-S.; Huang, C.-S.; Lin, Y.-K.; Shung, K. W.-K. Collective excitations in a single-layer carbon nanotube. *Physical Review B* **1996**, *53*, 15493.
- (63) Chung, H.-C.; Chang, C.-P.; Lin, C.-Y.; Lin, M. F. Electronic and optical properties of graphene nanoribbons in external fields. *Physical Chemistry Chemical Physics* **2016**, *18*, 7573–7616.
- (64) Saroka, V.; Shuba, M.; Portnoi, M. Optical selection rules of zigzag graphene nanoribbons. *Physical Review B* **2017**, *95*, 155438.
- (65) Sasaki, K.-i.; Kato, K.; Tokura, Y.; Oguri, K.; Sogawa, T. Theory of optical transitions in graphene nanoribbons. *Physical Review B* **2011**, *84*, 085458.

- (66) Brey, L.; Fertig, H. Elementary electronic excitations in graphene nanoribbons. *Physical Review B* **2007**, *75*, 125434.
- (67) Liu, Z.; Suenaga, K.; Harris, P. J.; Iijima, S. Open and closed edges of graphene layers. *Physical review letters* **2009**, *102*, 015501.
- (68) Zhang, J.; Xiao, J.; Meng, X.; Monroe, C.; Huang, Y.; Zuo, J.-M. Free folding of suspended graphene sheets by random mechanical stimulation. *Physical review letters* **2010**, *104*, 166805.
- (69) Liu, F.; Song, S.; Xue, D.; Zhang, H. Folded structured graphene paper for high performance electrode materials. *Advanced Materials* **2012**, *24*, 1089–1094.
- (70) Huang, J. Y.; Qi, L.; Li, J. In situ imaging of layer-by-layer sublimation of suspended graphene. *Nano Research* **2010**, *3*, 43–50.
- (71) Chang, S.-L.; Wu, B.-R.; Yang, P.-H.; Lin, M. F. Geometric, magnetic and electronic properties of folded graphene nanoribbons. *RSC Advances* **2016**, *6*, 64852–64860.
- (72) Prada, E.; San-Jose, P.; Brey, L. Zero Landau level in folded graphene nanoribbons. *Physical review letters* **2010**, *105*, 106802.
- (73) Feng, J.; Qi, L.; Huang, J. Y.; Li, J. Geometric and electronic structure of graphene bilayer edges. *Physical Review B* **2009**, *80*, 165407.
- (74) Bacon, R. Growth, structure, and properties of graphite whiskers. *Journal of Applied Physics* **1960**, *31*, 283–290.
- (75) Li, J.; Peng, Q.; Bai, G.; Jiang, W. Carbon scrolls produced by high energy ball milling of graphite. *Carbon* **2005**, *43*, 2817–2833.
- (76) Viculis, L. M.; Mack, J. J.; Kaner, R. B. A chemical route to carbon nanoscrolls. *Science* **2003**, *299*, 1361–1361.

- (77) Savoskin, M. V.; Mochalin, V. N.; Yaroshenko, A. P.; Lazareva, N. I.; Konstantinova, T. E.; Barsukov, I. V.; Prokofiev, I. G. Carbon nanoscrolls produced from acceptor-type graphite intercalation compounds. *Carbon* **2007**, *45*, 2797–2800.
- (78) Shioyama, H.; Akita, T. A new route to carbon nanotubes. *Carbon* **2003**, *41*, 179–181.
- (79) Sidorov, A.; Mudd, D.; Sumanasekera, G.; Ouseph, P.; Jayanthi, C.; Wu, S.-Y. Electrostatic deposition of graphene in a gaseous environment: a deterministic route for synthesizing rolled graphenes? *Nanotechnology* **2009**, *20*, 055611.
- (80) Xie, X.; Ju, L.; Feng, X.; Sun, Y.; Zhou, R.; Liu, K.; Fan, S.; Li, Q.; Jiang, K. Controlled fabrication of high-quality carbon nanoscrolls from monolayer graphene. *Nano letters* **2009**, *9*, 2565–2570.
- (81) Braga, S. F.; Coluci, V. R.; Legoas, S. B.; Giro, R.; Galvão, D. S.; Baughman, R. H. Structure and dynamics of carbon nanoscrolls. *Nano letters* **2004**, *4*, 881–884.
- (82) Mpourmpakis, G.; Tylianakis, E.; Froudakis, G. E. Carbon nanoscrolls: a promising material for hydrogen storage. *Nano letters* **2007**, *7*, 1893–1897.
- (83) Rurali, R.; Coluci, V.; Galvao, D. Prediction of giant electroactuation for papyruslike carbon nanoscroll structures: first-principles calculations. *Physical Review B* **2006**, *74*, 085414.
- (84) Chen, Y.; Lu, J.; Gao, Z. Structural and electronic study of nanoscrolls rolled up by a single graphene sheet. *The Journal of Physical Chemistry C* **2007**, *111*, 1625–1630.
- (85) Lai, L.; Lu, J.; Wang, L.; Luo, G.; Zhou, J.; Qin, R.; Chen, Y.; Li, H.; Gao, Z.; Li, G. Magnetism in carbon nanoscrolls: Quasi-half-metals and half-metals in pristine hydrocarbons. *Nano Research* **2009**, *2*, 844–850.
- (86) Lin, C. Y.; Do, T. N.; Huang, Y. K.; Lin, M. F. Optical properties of graphene in magnetic and electric fields. IOP Publishing, e-book. 2017.

- (87) Tran, N. T. T.; Lin, S. Y.; Lin, C. Y.; Lin, M. F. Geometric and electronic properties of graphene-related systems: Chemical bondings. CRC Press, book. 2017.
- (88) Wang, Y.; Ni, Z.; Liu, L.; Liu, Y.; Cong, C.; Yu, T.; Wang, X.; Shen, D.; Shen, Z. Stacking-dependent optical conductivity of bilayer graphene. *ACS nano* **2010**, *4*, 4074–4080.
- (89) Chen, Z.; Wang, X.-Q. Stacking-dependent optical spectra and many-electron effects in bilayer graphene. *Physical Review B* **2011**, *83*, 081405.
- (90) Koshino, M. Stacking-dependent optical absorption in multilayer graphene. *New Journal of Physics* **2013**, *15*, 015010.
- (91) Park, C.; Ryou, J.; Hong, S.; Sumpter, B. G.; Kim, G.; Yoon, M. Electronic properties of bilayer graphene strongly coupled to interlayer stacking and an external electric field. *Physical review letters* **2015**, *115*, 015502.
- (92) Ohta, T.; Bostwick, A.; Seyller, T.; Horn, K.; Rotenberg, E. Controlling the electronic structure of bilayer graphene. *Science* **2006**, *313*, 951–954.
- (93) Ohta, T.; Bostwick, A.; McChesney, J. L.; Seyller, T.; Horn, K.; Rotenberg, E. Interlayer interaction and electronic screening in multilayer graphene investigated with angle-resolved photoemission spectroscopy. *Physical Review Letters* **2007**, *98*, 206802.
- (94) Siegel, D. A.; Regan, W.; Fedorov, A. V.; Zettl, A.; Lanzara, A. Charge-carrier screening in single-layer graphene. *Physical review letters* **2013**, *110*, 146802.
- (95) Bostwick, A.; Ohta, T.; Seyller, T.; Horn, K.; Rotenberg, E. Quasiparticle dynamics in graphene. *Nature physics* **2007**, *3*, 36–40.
- (96) Sugawara, K.; Sato, T.; Souma, S.; Takahashi, T.; Suematsu, H. Fermi surface and edge-localized states in graphite studied by high-resolution angle-resolved photoemission spectroscopy. *Physical Review B* **2006**, *73*, 045124.

- (97) Grüneis, A.; Attaccalite, C.; Pichler, T.; Zabolotnyy, V.; Shiozawa, H.; Molodtsov, S.; Inosov, D.; Koitzsch, A.; Knupfer, M.; Schiessling, J. Electron-electron correlation in graphite: a combined angle-resolved photoemission and first-principles study. *Physical review letters* **2008**, *100*, 037601.
- (98) Coletti, C.; Forti, S.; Principi, A.; Emtsev, K. V.; Zakharov, A. A.; Daniels, K. M.; Daas, B. K.; Chandrashekar, M.; Ouisse, T.; Chaussende, D. Revealing the electronic band structure of trilayer graphene on SiC: An angle-resolved photoemission study. *Physical Review B* **2013**, *88*, 155439.
- (99) Bostwick, A. Coexisting massive and massless Dirac fermions in symmetry-broken bilayer graphene. *Bulletin of the American Physical Society* **2014**, *59*.
- (100) Sutter, P.; Hybertsen, M.; Sadowski, J.; Sutter, E. Electronic structure of few-layer epitaxial graphene on Ru (0001). *Nano letters* **2009**, *9*, 2654–2660.
- (101) Chang, S.-L.; Wu, B.-R.; Wong, J.-H.; Lin, M.-F. Configuration-dependent geometric and electronic properties of bilayer graphene nanoribbons. *Carbon* **2014**, *77*, 1031–1039.
- (102) Xu, P.; Yang, Y.; Qi, D.; Barber, S.; Schoelz, J.; Ackerman, M.; Bellaiche, L.; Thibado, P. Electronic transition from graphite to graphene via controlled movement of the top layer with scanning tunneling microscopy. *Physical Review B* **2012**, *86*, 085428.
- (103) Feng, X.; Kwon, S.; Park, J. Y.; Salmeron, M. Superlubric sliding of graphene nanoflakes on graphene. *ACS nano* **2013**, *7*, 1718–1724.
- (104) Liu, Z.; Yang, J.; Grey, F.; Liu, J. Z.; Liu, Y.; Wang, Y.; Yang, Y.; Cheng, Y.; Zheng, Q. Observation of microscale superlubricity in graphite. *Physical review letters* **2012**, *108*, 205503.

- (105) Que, Y.; Xiao, W.; Chen, H.; Wang, D.; Du, S.; Gao, H.-J. Stacking-dependent electronic property of trilayer graphene epitaxially grown on Ru (0001). *Applied Physics Letters* **2015**, *107*, 263101.
- (106) Guo, Y.; Guo, W.; Chen, C. Semiconducting to half-metallic to metallic transition on spin-resolved zigzag bilayer graphene nanoribbons. *The Journal of Physical Chemistry C* **2010**, *114*, 13098–13105.
- (107) Santos, H.; Ayuela, A.; Chico, L.; Artacho, E. van der Waals interaction in magnetic bilayer graphene nanoribbons. *Physical Review B* **2012**, *85*, 245430.
- (108) Lima, M. P.; Fazzio, A.; da Silva, A. J. Edge effects in bilayer graphene nanoribbons: Ab initio total-energy density functional theory calculations. *Physical Review B* **2009**, *79*, 153401.
- (109) Paulla, K. K.; Farajian, A. A. Stacking stability, emergence of magnetization and electromechanical nanosensing in bilayer graphene nanoribbons. *Journal of Physics: Condensed Matter* **2013**, *25*, 115303.
- (110) Talirz, L.; Söde, H.; Cai, J.; Ruffieux, P.; Blankenburg, S.; Jafaar, R.; Berger, R.; Feng, X.; Müllen, K.; Passerone, D. Termini of bottom-up fabricated graphene nanoribbons. *Journal of the American Chemical Society* **2013**, *135*, 2060–2063.
- (111) Tan, Y.-Z.; Yang, B.; Parvez, K.; Narita, A.; Osella, S.; Beljonne, D.; Feng, X.; Müllen, K. Atomically precise edge chlorination of nanographenes and its application in graphene nanoribbons. *Nature communications* *4*, 2646.
- (112) Mao, Y.; Hao, W.; Wei, X.; Yuan, J.; Zhong, J. Edge-adsorption of potassium adatoms on graphene nanoribbon: A first principle study. *Applied Surface Science* **2013**, *280*, 698–704.

- (113) Huang, H.; Li, Z.; Kreuzer, H.; Wang, W. Disintegration of graphene nanoribbons in large electrostatic fields. *Physical Chemistry Chemical Physics* **2014**, *16*, 15927–15933.
- (114) Lu, D.-b.; Song, Y.-l.; Yang, Z.-x.; Li, G.-q. Energy gap modulation of graphene nanoribbons by F termination. *Applied Surface Science* **2011**, *257*, 6440–6444.
- (115) Hu, X.; Tian, H.; Zheng, W.; Yu, S.; Qiao, L.; Qu, C.; Jiang, Q. Metallic-semiconducting phase transition of the edge-oxygenated armchair graphene nanoribbons. *Chemical Physics Letters* **2010**, *501*, 64–67.
- (116) Peng, X.; Velasquez, S. Strain modulated band gap of edge passivated armchair graphene nanoribbons. *Applied Physics Letters* **2011**, *98*, 023112.
- (117) Gorjizadeh, N.; Farajian, A. A.; Esfarjani, K.; Kawazoe, Y. Spin and band-gap engineering in doped graphene nanoribbons. *Physical Review B* **2008**, *78*, 155427.
- (118) Sarikavak-Lisesivdin, B.; Lisesivdin, S.; Ozbay, E. Ab initio study of Ru-terminated and Ru-doped armchair graphene nanoribbons. *Molecular Physics* **2012**, *110*, 2295–2300.
- (119) Autès, G.; Yazyev, O. V. Engineering quantum spin Hall effect in graphene nanoribbons via edge functionalization. *Physical Review B* **2013**, *87*, 241404.
- (120) Wang, Y.; Cao, C.; Cheng, H.-P. Metal-terminated graphene nanoribbons. *Physical Review B* **2010**, *82*, 205429.
- (121) Simbeck, A. J.; Gu, D.; Kharche, N.; Satyam, P. V.; Avouris, P.; Nayak, S. K. Electronic structure of oxygen-functionalized armchair graphene nanoribbons. *Physical Review B* **2013**, *88*, 035413.
- (122) Wagner, P.; Ewels, C. P.; Adjizian, J.-J.; Magaud, L.; Pochet, P.; Roche, S.; Lopez-Bezanilla, A.; Ivanovskaya, V. V.; Yaya, A.; Rayson, M. Band gap engineering via

- edge-functionalization of graphene nanoribbons. *The Journal of Physical Chemistry C* **2013**, *117*, 26790–26796.
- (123) Lin, Y.-T.; Chung, H.-C.; Yang, P.-H.; Lin, S.-Y.; Lin, M. F. Adatom bond-induced geometric and electronic properties of passivated armchair graphene nanoribbons. *Physical Chemistry Chemical Physics* **2015**, *17*, 16545–16552.
- (124) Cervantes-Sodi, F.; Csanyi, G.; Piscanec, S.; Ferrari, A. Edge-functionalized and substitutionally doped graphene nanoribbons: Electronic and spin properties. *Physical Review B* **2008**, *77*, 165427.
- (125) Seitsonen, A. P.; Saitta, A. M.; Wassmann, T.; Lazzeri, M.; Mauri, F. Structure and stability of graphene nanoribbons in oxygen, carbon dioxide, water, and ammonia. *Physical Review B* **2010**, *82*, 115425.
- (126) da Rocha, C. G.; Clayborne, P. A.; Koskinen, P.; Häkkinen, H. Optical and electronic properties of graphene nanoribbons upon adsorption of ligand-protected aluminum clusters. *Physical Chemistry Chemical Physics* **2014**, *16*, 3558–3565.
- (127) Chang, S.-L.; Lin, S.-Y.; Lin, S.-K.; Lee, C.-H.; Lin, M.-F. Geometric and electronic properties of edge-decorated graphene nanoribbons. *Scientific reports* **2014**, *4*, 6038.
- (128) Watanabe, K.; Kondow, T.; Soma, M.; Onishi, T.; Tamaru, K. Molecular-sieve type sorption on alkali graphite intercalation compounds. *Proceedings of the Royal Society of London A: Mathematical, Physical and Engineering Sciences*. 1973; pp 51–67.
- (129) Pekker, S.; Janossy, A.; Mihaly, L.; Chauvet, O.; Carrard, M.; Forró, L. Single-crystalline (KC60)_n: a conducting linear alkali fulleride polymer. *Science* **1994**, *265*, 1077–1078.
- (130) Bower, C.; Suzuki, S.; Tanigaki, K.; Zhou, O. Synthesis and structure of pristine and

- alkali-metal-intercalated single-walled carbon nanotubes. *Applied Physics A: Materials Science & Processing* **1998**, *67*, 47–52.
- (131) Howard, C.; Dean, M.; Withers, F. Phonons in potassium-doped graphene: the effects of electron-phonon interactions, dimensionality, and adatom ordering. *Physical Review B* **2011**, *84*, 241404.
- (132) Li, N.; Chen, Z.; Ren, W.; Li, F.; Cheng, H.-M. Flexible graphene-based lithium ion batteries with ultrafast charge and discharge rates. *Proceedings of the National Academy of Sciences* **2012**, *109*, 17360–17365.
- (133) Giovannetti, G.; Khomyakov, P.; Brocks, G.; Karpan, V. v.; Van den Brink, J.; Kelly, P. J. Doping graphene with metal contacts. *Physical review letters* **2008**, *101*, 026803.
- (134) Pi, K.; McCreary, K.; Bao, W.; Han, W.; Chiang, Y.; Li, Y.; Tsai, S.-W.; Lau, C.; Kawakami, R. Electronic doping and scattering by transition metals on graphene. *Physical Review B* **2009**, *80*, 075406.
- (135) Lin, Y.-T.; Lin, S.-Y.; Chiu, Y.-H.; Lin, M.-F. Alkali-created rich properties in grapheme nanoribbons: Chemical bondings. *Scientific Reports* **2017**, *7*.
- (136) Zhou, S.; Siegel, D.; Fedorov, A.; Lanzara, A. Metal to insulator transition in epitaxial graphene induced by molecular doping. *Physical review letters* **2008**, *101*, 086402.
- (137) Poh, H. L.; Šimek, P.; Sofer, Z.; Pumera, M. Halogenation of graphene with chlorine, bromine, or iodine by exfoliation in a halogen atmosphere. *Chemistry-A European Journal* **2013**, *19*, 2655–2662.
- (138) others., et al. Properties of fluorinated graphene films. *Nano letters* **2010**, *10*, 3001–3005.

- (139) Li, B.; Zhou, L.; Wu, D.; Peng, H.; Yan, K.; Zhou, Y.; Liu, Z. Photochemical chlorination of graphene. *Acs Nano* **2011**, *5*, 5957–5961.
- (140) Medeiros, P. V.; Mascarenhas, A. J.; de Brito Mota, F.; de Castilho, C. M. C. A DFT study of halogen atoms adsorbed on graphene layers. *Nanotech.* **2010**, *21*, 485701.
- (141) Li, Y.; Chen, H.; Voo, L. Y.; Ji, J.; Zhang, G.; Zhang, G.; Zhang, F.; Fan, X. Synthesis of partially hydrogenated graphene and brominated graphene. *Journal of Materials Chemistry* **2012**, *22*, 15021–15024.
- (142) Zhang, X.; Lu, G. The spin-orbit coupling induced spin flip and its role in the enhancement of the photocatalytic hydrogen evolution over iodinated graphene oxide. *Carbon* **2016**, *108*, 215–224.
- (143) Withers, F.; Russo, S.; Dubois, M.; Craciun, M. F. Tuning the electronic transport properties of graphene through functionalisation with fluorine. *Nanoscale research letters* **2011**, *6*, 526.
- (144) Chantharasupawong, P.; Philip, R.; Narayanan, N. T.; Sudeep, P. M.; Mathkar, A.; Ajayan, P. M.; Thomas, J. Optical power limiting in fluorinated graphene oxide: an insight into the nonlinear optical properties. *The Journal of Physical Chemistry C* **2012**, *116*, 25955–25961.
- (145) others., et al. Highly p-doped epitaxial graphene obtained by fluorine intercalation. *Applied Physics Letters* **2011**, *98*, 184102.
- (146) Nguyen, D. K.; Lin, Y.-T.; Lin, S.-Y.; Chiu, Y.-H.; Tran, N. T. T.; Fa-Lin, M. Fluorination-Enriched Electronic and Magnetic Properties in Graphene Nanoribbons. *Physical Chemistry Chemical Physics* **2017**, *19*, 20667–20676.
- (147) Kresse, G.; Furthmüller, J. Efficient iterative schemes for ab initio total-energy calculations using a plane-wave basis set. *Physical review B* **1996**, *54*, 11169.

- (148) Kohn, W.; Sham, L. J. Self-consistent equations including exchange and correlation effects. *Physical review* **1965**, *140*, A1133.
- (149) Guinea, F.; Neto, A. C.; Peres, N. Electronic states and Landau levels in graphene stacks. *Physical Review B* **2006**, *73*, 245426.
- (150) Lukose, V.; Shankar, R.; Baskaran, G. Novel electric field effects on Landau levels in graphene. *Physical review letters* **2007**, *98*, 116802.
- (151) Lai, Y.; Ho, J.; Chang, C.; Lin, M. F. Magnetoelectronic properties of bilayer Bernal graphene. *Physical Review B* **2008**, *77*, 085426.
- (152) Lin, C.-Y.; Wu, J.-Y.; Ou, Y.-J.; Chiu, Y.-H.; Lin, M. F. Magneto-electronic properties of multilayer graphenes. *Physical Chemistry Chemical Physics* **2015**, *17*, 26008–26035.
- (153) Gusynin, V.; Sharapov, S.; Carbotte, J. Magneto-optical conductivity in graphene. *Journal of Physics: Condensed Matter* **2006**, *19*, 026222.
- (154) Gusynin, V.; Sharapov, S.; Carbotte, J. AC conductivity of graphene: from tight-binding model to 2+ 1-dimensional quantum electrodynamics. *International Journal of Modern Physics B* **2007**, *21*, 4611–4658.
- (155) Ho, Y.-H.; Chiu, Y.-H.; Lin, D.-H.; Chang, C.-P.; Lin, M. F. Magneto-optical selection rules in bilayer Bernal graphene. *ACS nano* **2010**, *4*, 1465–1472.
- (156) Berman, O. L.; Gumbs, G.; Lozovik, Y. E. Magnetoplasmons in layered graphene structures. *Physical Review B* **2008**, *78*, 085401.
- (157) Yuan, S.; Roldán, R.; Katsnelson, M. I. Excitation spectrum and high-energy plasmons in single-layer and multilayer graphene. *Physical Review B* **2011**, *84*, 035439.
- (158) Kane, C. L.; Mele, E. J. Quantum spin Hall effect in graphene. *Physical review letters* **2005**, *95*, 226801.

- (159) Wu, J.-Y.; Chen, S.-C.; Roslyak, O.; Gumbs, G.; Lin, M. F. Plasma excitations in graphene: Their spectral intensity and temperature dependence in magnetic field. *ACS nano* **2011**, *5*, 1026–1032.
- (160) Perdew, J. P.; Burke, K.; Ernzerhof, M. Generalized gradient approximation made simple. *Physical review letters* **1996**, *77*, 3865.
- (161) Blöchl, P. E. Projector augmented-wave method. *Physical Review B* **1994**, *50*, 17953.
- (162) Grimme, S. Semiempirical GGA-type density functional constructed with a long-range dispersion correction. *Journal of computational chemistry* **2006**, *27*, 1787–1799.
- (163) Amara, H.; Latil, S.; Meunier, V.; Lambin, P.; Charlier, J.-C. Scanning tunneling microscopy fingerprints of point defects in graphene: A theoretical prediction. *Physical Review B* **2007**, *76*, 115423.
- (164) Lin, S.-Y.; Chang, S.-L.; Shyu, F.-L.; Lu, J.-M.; Lin, M.-F. Feature-rich electronic properties in graphene ripples. *Carbon* **2015**, *86*, 207–216.
- (165) Lentzen, M. Progress in aberration-corrected high-resolution transmission electron microscopy using hardware aberration correction. *Microscopy and Microanalysis* **2006**, *12*, 191–205.
- (166) Kisielowski, C.; Freitag, B.; Bischoff, M.; Van Lin, H.; Lazar, S.; Knippels, G.; Tiemeijer, P.; van der Stam, M.; von Harrach, S.; Stekelenburg, M. Detection of single atoms and buried defects in three dimensions by aberration-corrected electron microscope with 0.5-Å information limit. *Microscopy and Microanalysis* **2008**, *14*, 469–477.
- (167) Ray, M.; Basu, T. S.; Bandyopadhyay, N. R.; Klie, R. F.; Ghosh, S.; Raja, S. O.; Dasgupta, A. K. Highly lattice-mismatched semiconductor–metal hybrid nanostructures: gold nanoparticle encapsulated luminescent silicon quantum dots. *Nanoscale* **2014**, *6*, 2201–2210.

- (168) Ophus, C.; Rasool, H. I.; Linck, M.; Zettl, A.; Ciston, J. Automatic software correction of residual aberrations in reconstructed HRTEM exit waves of crystalline samples. *Advanced structural and chemical imaging* **2017**, *2*, 15.
- (169) Warner, J. H.; Rümmeli, M. H.; Gemming, T.; Büchner, B.; Briggs, G. A. D. Direct imaging of rotational stacking faults in few layer graphene. *Nano letters* **2008**, *9*, 102–106.
- (170) Lee, J.-K.; Lee, S.-C.; Ahn, J.-P.; Kim, S.-C.; Wilson, J. I.; John, P. The growth of AA graphite on (111) diamond. *The Journal of chemical physics* **2008**, *129*, 234709.
- (171) Binnig, G.; Rohrer, H. Scanning tunnel microscope. *Helvetica Physica Acta*. 1982; pp 726–735.
- (172) Binnig, G.; Rohrer, H. Scanning tunneling microscopyXfrom birth to adolescence. *reviews of modern physics* **1987**, *59*, 615.
- (173) Liu, X. H.; Wang, J. W.; Liu, Y.; Zheng, H.; Kushima, A.; Huang, S.; Zhu, T.; Mao, S. X.; Li, J.; Zhang, S. In situ transmission electron microscopy of electrochemical lithiation, delithiation and deformation of individual graphene nanoribbons. *Carbon* **2012**, *50*, 3836–3844.
- (174) Masubuchi, S.; Ono, M.; Yoshida, K.; Hirakawa, K.; Machida, T. Fabrication of graphene nanoribbon by local anodic oxidation lithography using atomic force microscope. *Applied Physics Letters* **2009**, *94*, 082107.
- (175) De Padova, P.; Quaresima, C.; Ottaviani, C.; Sheverdyaeva, P. M.; Moras, P.; Carbone, C.; Topwal, D.; Olivieri, B.; Kara, A.; Oughaddou, H. Evidence of graphene-like electronic signature in silicene nanoribbons. *Applied Physics Letters* **2010**, *96*, 261905.
- (176) Pierce, D. T. Spin-polarized electron microscopy. *Physica Scripta* **1988**, *38*, 291.

- (177) Wiesendanger, R.; Güntherodt, H.-J.; Güntherodt, G.; Gambino, R.; Ruf, R. Observation of vacuum tunneling of spin-polarized electrons with the scanning tunneling microscope. *Physical Review Letters* **1990**, *65*, 247.
- (178) Yayon, Y.; Brar, V.; Senapati, L.; Erwin, S.; Crommie, M. Observing spin polarization of individual magnetic adatoms. *Physical review letters* **2007**, *99*, 067202.
- (179) Pietzsch, O.; Kubetzka, A.; Bode, M.; Wiesendanger, R. Spin-polarized scanning tunneling spectroscopy of nanoscale cobalt islands on Cu (111). *Physical review letters* **2004**, *92*, 057202.
- (180) Rusponi, S.; Weiss, N.; Cren, T.; Epple, M.; Brune, H. High tunnel magnetoresistance in spin-polarized scanning tunneling microscopy of Co nanoparticles on Pt (111). *Applied Physics Letters* **2005**, *87*, 162514.
- (181) Tao, C.; Jiao, L.; Yazyev, O. V.; Chen, Y.-C.; Feng, J.; Zhang, X.; Capaz, R. B.; Tour, J. M.; Zettl, A.; Louie, S. G. Spatially resolving edge states of chiral graphene nanoribbons. *Nature Physics* **2011**, *7*, 616–620.
- (182) Magda, G. Z.; Jin, X.; Hagymási, I.; Vancsó, P.; Osváth, Z.; Nemes-Incze, P.; Hwang, C.; Biro, L. P.; Tapasztó, L. Room-temperature magnetic order on zigzag edges of narrow graphene nanoribbons. *Nature* **2014**, *514*, 608–611.
- (183) Johnson, J. L.; Behnam, A.; Pearton, S.; Ural, A. Hydrogen Sensing Using Pd-Functionalized Multi-Layer Graphene Nanoribbon Networks. *Advanced Materials* **2010**, *22*, 4877–4880.
- (184) Wilder, J. W.; Venema, L. C.; Rinzler, A. G.; Smalley, R. E.; Dekker, C. Electronic structure of atomically resolved carbon nanotubes. *Nature* **1998**, *391*, 59–62.
- (185) Odom, T. W.; Huang, J.-L.; Kim, P.; Lieber, C. M. Atomic structure and electronic properties of single-walled carbon nanotubes. *Nature* **1998**, *391*, 62–64.

- (186) Rong, Z. Y.; Kuiper, P. Electronic effects in scanning tunneling microscopy: Moiré pattern on a graphite surface. *Physical Review B* **1993**, *48*, 17427.
- (187) Chen, H.-H.; Su, S.; Chang, S.-L.; Cheng, B.-Y.; Chong, C.-W.; Huang, J.; Lin, M. F. Long-range interactions of bismuth growth on monolayer epitaxial graphene at room temperature. *Carbon* **2015**, *93*, 180–186.
- (188) Chen, H.-H.; Su, S.; Chang, S.-L.; Cheng, B.-Y.; Chen, S.; Chen, H.-Y.; Lin, M. F.; Huang, J. Tailoring low-dimensional structures of bismuth on monolayer epitaxial graphene. *Scientific reports* **2015**, *5*.
- (189) Meng, L.; He, W.-Y.; Zheng, H.; Liu, M.; Yan, H.; Yan, W.; Chu, Z.-D.; Bai, K.; Dou, R.-F.; Zhang, Y. Strain-induced one-dimensional Landau level quantization in corrugated graphene. *Physical Review B* **2013**, *87*, 205405.
- (190) Bai, K.-K.; Zhou, Y.; Zheng, H.; Meng, L.; Peng, H.; Liu, Z.; Nie, J.-C.; He, L. Creating one-dimensional nanoscale periodic ripples in a continuous mosaic graphene monolayer. *Physical review letters* **2014**, *113*, 086102.
- (191) De Parga, A. V.; Calleja, F.; Borca, B.; Passeggi Jr, M.; Hinarejos, J.; Guinea, F.; Miranda, R. Periodically rippled graphene: growth and spatially resolved electronic structure. *Physical review letters* **2008**, *100*, 056807.
- (192) Pandey, D.; Reifengerger, R.; Piner, R. Scanning probe microscopy study of exfoliated oxidized graphene sheets. *Surface Science* **2008**, *602*, 1607–1613.
- (193) Balog, R.; Jørgensen, B.; Nilsson, L.; Andersen, M.; Rienks, E.; Bianchi, M.; Fanetti, M.; Lægsgaard, E.; Baraldi, A.; Lizzit, S. Bandgap opening in graphene induced by patterned hydrogen adsorption. *Nature materials* **2010**, *9*, 315–319.
- (194) Červenka, J.; Katsnelson, M.; Flipse, C. Room-temperature ferromagnetism in

- graphite driven by two-dimensional networks of point defects. *Nature Physics* **2009**, *5*, 840–844.
- (195) Kondo, T.; Casolo, S.; Suzuki, T.; Shikano, T.; Sakurai, M.; Harada, Y.; Saito, M.; Oshima, M.; Trioni, M. I.; Tantardini, G. F. Atomic-scale characterization of nitrogen-doped graphite: Effects of dopant nitrogen on the local electronic structure of the surrounding carbon atoms. *Physical review B* **2012**, *86*, 035436.
- (196) Pietzsch, O.; Kubetzka, A.; Bode, M.; Wiesendanger, R. Real-space observation of dipolar antiferromagnetism in magnetic nanowires by spin-polarized scanning tunneling spectroscopy. *Physical Review Letters* **2000**, *84*, 5212.
- (197) Huang, H.; Wei, D.; Sun, J.; Wong, S. L.; Feng, Y. P.; Neto, A. C.; Wee, A. T. S. Spatially resolved electronic structures of atomically precise armchair graphene nanoribbons. *Scientific reports* **2012**, *2*, 983.
- (198) Söde, H.; Talirz, L.; Gröning, O.; Pignedoli, C. A.; Berger, R.; Feng, X.; Müllen, K.; Fasel, R.; Ruffieux, P. Electronic band dispersion of graphene nanoribbons via Fourier-transformed scanning tunneling spectroscopy. *Physical Review B* **2015**, *91*, 045429.
- (199) Chen, Y.-C.; De Oteyza, D. G.; Pedramrazi, Z.; Chen, C.; Fischer, F. R.; Crommie, M. F. Tuning the band gap of graphene nanoribbons synthesized from molecular precursors. *ACS nano* **2013**, *7*, 6123–6128.
- (200) Luican, A.; Li, G.; Reina, A.; Kong, J.; Nair, R.; Novoselov, K. S.; Geim, A. K.; Andrei, E. Single-layer behavior and its breakdown in twisted graphene layers. *Physical review letters* **2011**, *106*, 126802.
- (201) Li, G.; Luican, A.; Dos Santos, J. L.; Neto, A. C.; Reina, A.; Kong, J.; Andrei, E. Observation of Van Hove singularities in twisted graphene layers. *Nature Physics* **2010**, *6*, 109–113.

- (202) Cherkez, V.; de Laissardière, G. T.; Mallet, P.; Veuillen, J.-Y. Van Hove singularities in doped twisted graphene bilayers studied by scanning tunneling spectroscopy. *Physical Review B* **2015**, *91*, 155428.
- (203) Lauffer, P.; Emtsev, K.; Graupner, R.; Seyller, T.; Ley, L.; Reshanov, S.; Weber, H. Atomic and electronic structure of few-layer graphene on SiC (0001) studied with scanning tunneling microscopy and spectroscopy. *Physical Review B* **2008**, *77*, 155426.
- (204) Yankowitz, M.; Wang, F.; Lau, C. N.; LeRoy, B. J. Local spectroscopy of the electrically tunable band gap in trilayer graphene. *Physical Review B* **2013**, *87*, 165102.
- (205) Pierucci, D.; Sediri, H.; Hajlaoui, M.; Girard, J.-C.; Brumme, T.; Calandra, M.; Velez-Fort, E.; Patriarche, G.; Silly, M. G.; Ferro, G. Evidence for flat bands near the Fermi level in epitaxial rhombohedral multilayer graphene. *ACS nano* **2015**, *9*, 5432–5439.
- (206) Gyamfi, M.; Eelbo, T.; Waśniowska, M.; Wiesendanger, R. Fe adatoms on graphene/Ru (0001): Adsorption site and local electronic properties. *Physical Review B* **2011**, *84*, 113403.
- (207) Klusek, Z. Investigations of splitting of the π bands in graphite by scanning tunneling spectroscopy. *Applied surface science* **1999**, *151*, 251–261.
- (208) Li, G.; Luican, A.; Andrei, E. Y. Scanning tunneling spectroscopy of graphene on graphite. *Physical Review Letters* **2009**, *102*, 176804.
- (209) Hüfner, S. *Photoelectron spectroscopy: principles and applications*; Springer Science & Business Media, 2013.
- (210) Cuk, T.; Lu, D.; Zhou, X.; Shen, Z.-X.; Devereaux, T.; Nagaosa, N. A review of electron–phonon coupling seen in the high- T_c superconductors by angle-resolved photoemission studies (ARPES). *physica status solidi (b)* **2005**, *242*, 11–29.

- (211) Levy, G.; Nettke, W.; Ludbrook, B.; Veenstra, C.; Damascelli, A. Deconstruction of resolution effects in angle-resolved photoemission. *Physical Review B* **2014**, *90*, 045150.
- (212) Qi, X.-L.; Zhang, S.-C. Topological insulators and superconductors. *Reviews of Modern Physics* **2011**, *83*, 1057.
- (213) others., et al. Droplet-like Fermi surfaces in the anti-ferromagnetic phase of EuFe₂As₂, an Fe-pnictide superconductor parent compound. *EPL (Europhysics Letters)* **2010**, *89*, 27007.
- (214) Papagno, M.; Rusponi, S.; Sheverdyeva, P. M.; Vlaic, S.; Etzkorn, M.; Pacilé, D.; Moras, P.; Carbone, C.; Brune, H. Large band gap opening between graphene Dirac cones induced by Na adsorption onto an Ir superlattice. *Acs Nano* **2011**, *6*, 199–204.
- (215) Grüneis, A.; Vyalikh, D. V. Tunable hybridization between electronic states of graphene and a metal surface. *Physical Review B* **2008**, *77*, 193401.
- (216) Nakada, K.; Fujita, M.; Dresselhaus, G.; Dresselhaus, M. S. Edge state in graphene ribbons: Nanometer size effect and edge shape dependence. *Physical Review B* **1996**, *54*, 17954.
- (217) Miyamoto, Y.; Nakada, K.; Fujita, M. First-principles study of edge states of H-terminated graphitic ribbons. *Physical Review B* **1999**, *59*, 9858.
- (218) Bhardwaj, T.; Antic, A.; Pavan, B.; Barone, V.; Fahlman, B. D. Enhanced electrochemical lithium storage by graphene nanoribbons. *Journal of the American Chemical Society* **2010**, *132*, 12556–12558.
- (219) Yazyev, O. V.; Katsnelson, M. Magnetic correlations at graphene edges: basis for novel spintronics devices. *Physical Review Letters* **2008**, *100*, 047209.

- (220) Thess, A.; Lee, R.; Nikolaev, P.; Dai, H.; Petit, P.; Robert, J.; Xu, C.; Lee, Y. H.; Kim, S. G.; Rinzler, A. G. Crystalline ropes of metallic carbon nanotubes. *Science* **1996**, 483–487.
- (221) de Heer, W. A.; Bacsá, W.; Chatelain, A.; Gerfin, T.; Humphrey-Baker, R. Aligned carbon nanotube films: production and optical and electronic properties. *Science* **1995**, 268, 845.
- (222) Ren, Z.; Huang, Z.; Xu, J.; Wang, J.; Bush, P.; Siegal, M.; Provencio, P. Synthesis of large arrays of well-aligned carbon nanotubes on glass. *Science* **1998**, 282, 1105–1107.
- (223) Fan, S.; Chapline, M. G.; Franklin, N. R.; Tomblér, T. W.; Cassell, A. M.; Dai, H. Self-oriented regular arrays of carbon nanotubes and their field emission properties. *Science* **1999**, 283, 512–514.
- (224) Bandow, S.; Asaka, S.; Saito, Y.; Rao, A.; Grigorian, L.; Richter, E.; Eklund, P. Effect of the growth temperature on the diameter distribution and chirality of single-wall carbon nanotubes. *Physical Review Letters* **1998**, 80, 3779.
- (225) Rao, A.; Richter, E.; Bandow, S.; Chase, B.; Eklund, P.; Williams, K.; Fang, S.; Subbaswamy, K.; Menon, M.; Thess, A. Diameter-selective Raman scattering from vibrational modes in carbon nanotubes. *Science* **1997**, 275, 187–191.
- (226) Bernaerts, D.; Zettl, A.; Chopra, N. G.; Thess, A.; Smalley, R. Electron diffraction study of single-wall carbon nanotubes. *Solid state communications* **1998**, 105, 145–149.
- (227) Cowley, J.; Nikolaev, P.; Thess, A.; Smalley, R. E. Electron nano-diffraction study of carbon single-walled nanotube ropes. *Chemical Physics Letters* **1997**, 265, 379–384.
- (228) Kataura, H.; Kumazawa, Y.; Maniwa, Y.; Umezú, I.; Suzuki, S.; Ohtsuka, Y.;

- Achiba, Y. Optical properties of single-wall carbon nanotubes. *Synthetic metals* **1999**, *103*, 2555–2558.
- (229) Jost, O.; Gorbunov, A.; Pompe, W.; Pichler, T.; Friedlein, R.; Knupfer, M.; Reibold, M.; Bauer, H.-D.; Dunsch, L.; Golden, M. Diameter grouping in bulk samples of single-walled carbon nanotubes from optical absorption spectroscopy. *Applied physics letters* **1999**, *75*, 2217–2219.
- (230) Bursill, L.; Stadelmann, P. A.; Peng, J.; Prawer, S. Surface plasmon observed for carbon nanotubes. *Physical Review B* **1994**, *49*, 2882.
- (231) Pichler, T.; Knupfer, M.; Golden, M.; Fink, J.; Rinzler, A.; Smalley, R. Localized and delocalized electronic states in single-wall carbon nanotubes. *Physical Review Letters* **1998**, *80*, 4729.
- (232) Kociak, M.; Henrard, L.; Stéphan, O.; Suenaga, K.; Colliex, C. Plasmons in layered nanospheres and nanotubes investigated by spatially resolved electron energy-loss spectroscopy. *Physical Review B* **2000**, *61*, 13936.
- (233) Reed, B.; Sarikaya, M. Electronic properties of carbon nanotubes by transmission electron energy-loss spectroscopy. *Physical Review B* **2001**, *64*, 195404.
- (234) Burghard, M.; Klauk, H.; Kern, K. Carbon-Based Field-Effect Transistors for Nanoelectronics. *Advanced materials* **2009**, *21*, 2586–2600.
- (235) Tans, S. J.; Verschueren, A. R.; Dekker, C. Room-temperature transistor based on a single carbon nanotube. *Nature* **1998**, *393*, 49–52.
- (236) Martel, R.; Schmidt, T.; Shea, H.; Hertel, T.; Avouris, P. Single- and multi-wall carbon nanotube field-effect transistors. *Applied Physics Letters* **1998**, *73*, 2447–2449.
- (237) Shlafman, M.; Tabachnik, T.; Shtempluk, O.; Razin, A.; Kochetkov, V.; Yaish, Y. Self

- aligned hysteresis free carbon nanotube field-effect transistors. *Applied Physics Letters* **2016**, *108*, 163104.
- (238) Myodo, M.; Inaba, M.; ; Ohara, K.; Kato, R.; Kobayashi, M.; Hirano, Y.; Suzuki, K.; Kawarada, H. Large-current-controllable carbon nanotube field-effect transistor in electrolyte solution. *Applied Physics Letters* **2015**, *106*, 213503.
- (239) Miyake, T.; Saito, S. Quasiparticle band structure of carbon nanotubes. *Physical Review B* **2003**, *68*, 155424.
- (240) Ajiki, H.; Ando, T. Magnetic properties of carbon nanotubes. *Journal of the Physical Society of Japan* **1993**, *62*, 2470–2480.
- (241) Ajiki, H.; Ando, T. Energy bands of carbon nanotubes in magnetic fields. *Journal of the Physical Society of Japan* **1996**, *65*, 505–514.
- (242) Chang, S.-L.; Wu, B.-R.; Yang, P.-H.; Lin, M.-F. Curvature effects on electronic properties of armchair graphene nanoribbons without passivation. *Physical Chemistry Chemical Physics* **2012**, *14*, 16409–16414.
- (243) Robertson, D.; Brenner, D.; Mintmire, J. Energetics of nanoscale graphitic tubules. *Physical Review B* **1992**, *45*, 12592.
- (244) Saito, R.; Fujita, M.; Dresselhaus, G.; Dresselhaus, u. M. Electronic structure of chiral graphene tubules. *Applied physics letters* **1992**, *60*, 2204–2206.
- (245) Saito, R.; Fujita, M.; Dresselhaus, G.; Dresselhaus, M. S. Electronic structure of graphene tubules based on C 60. *Physical Review B* **1992**, *46*, 1804.
- (246) Neto, A. C.; Guinea, F.; Peres, N. M.; Novoselov, K. S.; Geim, A. K. The electronic properties of graphene. *Reviews of modern physics* **2009**, *81*, 109.
- (247) others,, et al. Observation of graphene bubbles and effective mass transport under graphene films. *Nano letters* **2008**, *9*, 332–337.

- (248) Mintmire, J.; Dunlap, B.; White, C. Are fullerene tubules metallic? *Physical Review Letters* **1992**, *68*, 631.
- (249) Hamada, N.; Sawada, S.-i.; Oshiyama, A. New one-dimensional conductors: graphitic microtubules. *Physical Review Letters* **1992**, *68*, 1579.
- (250) Blase, X.; Benedict, L. X.; Shirley, E. L.; Louie, S. G. Hybridization effects and metallicity in small radius carbon nanotubes. *Physical review letters* **1994**, *72*, 1878.
- (251) Gülseren, O.; Yildirim, T.; Ciraci, S. Systematic ab initio study of curvature effects in carbon nanotubes. *Physical Review B* **2002**, *65*, 153405.
- (252) Wallace, P. R. The band theory of graphite. *Physical Review* **1947**, *71*, 622.
- (253) Lin, M. F.; Chuu, D.-S. Persistent currents in toroidal carbon nanotubes. *Physical Review B* **1998**, *57*, 6731.
- (254) Ajiki, H.; Ando, T. Magnetic properties of ensembles of carbon nanotubes. *Journal of the Physical Society of Japan* **1995**, *64*, 4382–4391.
- (255) Lu, J. P. Novel magnetic properties of carbon nanotubes. *Physical review letters* **1995**, *74*, 1123.
- (256) Lin, M. F.; Shung, K. W.-K. Magnetoconductance of carbon nanotubes. *Physical Review B* **1995**, *51*, 7592.
- (257) Lin, M. F.; Shung, K. W.-K. Magnetization of graphene tubules. *Physical Review B* **1995**, *52*, 8423.
- (258) Zaric, S.; Ostojic, G. N.; Kono, J.; Shaver, J.; Moore, V. C.; Strano, M. S.; Hauge, R. H.; Smalley, R. E.; Wei, X. Optical signatures of the Aharonov-Bohm phase in single-walled carbon nanotubes. *Science* **2004**, *304*, 1129–1131.

- (259) Akima, N.; Iwasa, Y.; Brown, S.; Barbour, A. M.; Cao, J.; Musfeldt, J. L.; Matsui, H.; Toyota, N.; Shiraishi, M.; Shimoda, H. Strong Anisotropy in the Far-Infrared Absorption Spectra of Stretch-Aligned Single-Walled Carbon Nanotubes. *Advanced Materials* **2006**, *18*, 1166–1169.
- (260) Cao, J.; Wang, Q.; Dai, H. Electron transport in very clean, as-grown suspended carbon nanotubes. *Nature materials* **2005**, *4*, 745–749.
- (261) Cao, J.; Wang, Q.; Rolandi, M.; Dai, H. Aharonov-Bohm interference and beating in single-walled carbon-nanotube interferometers. *Physical review letters* **2004**, *93*, 216803.
- (262) Bachtold, A.; Strunk, C.; Salvetat, J.-P.; Bonard, J.-M.; Forró, L.; Nussbaumer, T.; Schönenberger, C. Aharonov–Bohm oscillations in carbon nanotubes. *Nature* **1999**, *397*, 673–675.
- (263) Smith, B. W.; Monthieux, M.; Luzzi, D. E. Encapsulated C60 in carbon nanotubes. *Nature* **1998**, *396*, 323.
- (264) Zhao, X.; Ando, Y.; Liu, Y.; Jinno, M.; Suzuki, T. Carbon nanowire made of a long linear carbon chain inserted inside a multiwalled carbon nanotube. *Physical review letters* **2003**, *90*, 187401.
- (265) Yen, M.-Y.; Hsiao, M.-C.; Liao, S.-H.; Liu, P.-I.; Tsai, H.-M.; Ma, C.-C. M.; Pu, N.-W.; Ger, M.-D. Preparation of graphene/multi-walled carbon nanotube hybrid and its use as photoanodes of dye-sensitized solar cells. *Carbon* **2011**, *49*, 3597–3606.
- (266) Vinayan, B.; Nagar, R.; Raman, V.; Rajalakshmi, N.; Dhathathreyan, K.; Ramaprabhu, S. Synthesis of graphene-multiwalled carbon nanotubes hybrid nanostructure by strengthened electrostatic interaction and its lithium ion battery application. *Journal of Materials Chemistry* **2012**, *22*, 9949–9956.

- (267) Yu, D.; Dai, L. Self-assembled graphene/carbon nanotube hybrid films for supercapacitors. *The Journal of Physical Chemistry Letters* **2009**, *1*, 467–470.
- (268) Nasibulin, A. G.; Pikhitsa, P. V.; Jiang, H.; Brown, D. P.; Krasheninnikov, A. V.; Anisimov, A. S.; Queipo, P.; Moisala, A.; Gonzalez, D.; Lientschnig, G. A novel hybrid carbon material. *Nature Nanotechnology* **2007**, *2*, 156–161.
- (269) Lee, C.-H.; Yang, C.-K.; Lin, M. F.; Chang, C.-P.; Su, W.-S. Structural and electronic properties of graphene nanotube–nanoribbon hybrids. *Physical Chemistry Chemical Physics* **2011**, *13*, 3925–3931.
- (270) Lee, C.; Chen, S.; Yang, C.; Su, W.; Lin, M. Low-energy electronic structures of nanotube–nanoribbon hybrid systems. *Computer Physics Communications* **2011**, *182*, 68–70.
- (271) Pennington, G.; Goldsman, N. Semiclassical transport and phonon scattering of electrons in semiconducting carbon nanotubes. *Physical Review B* **2003**, *68*, 045426.
- (272) Dürkop, T.; Getty, S.; Cobas, E.; Fuhrer, M. Extraordinary mobility in semiconducting carbon nanotubes. *Nano letters* **2004**, *4*, 35–39.
- (273) Niimi, Y.; Matsui, T.; Kambara, H.; Tagami, K.; Tsukada, M.; Fukuyama, H. Scanning tunneling microscopy and spectroscopy of the electronic local density of states of graphite surfaces near monoatomic step edges. *Physical Review B* **2006**, *73*, 085421.
- (274) Misewich, J.; Martel, R.; Avouris, P.; Tsang, J.; Heinze, S.; Tersoff, J. Electrically induced optical emission from a carbon nanotube FET. *Science* **2003**, *300*, 783–786.
- (275) Yuksel, R.; Sarioba, Z.; Cirpan, A.; Hiralal, P.; Unalan, H. E. Transparent and flexible supercapacitors with single walled carbon nanotube thin film electrodes. *ACS applied materials & interfaces* **2014**, *6*, 15434–15439.

- (276) Liang, S.; Ma, Z.; Wu, G.; Wei, N.; Huang, L.; Huang, H.; Liu, H.; Wang, S.; Peng, L.-M. Microcavity-Integrated Carbon Nanotube Photodetectors. *ACS nano* **2016**, *10*, 6963–6971.
- (277) Zhang, T.-F.; Li, Z.-P.; Wang, J.-Z.; Kong, W.-Y.; Wu, G.-A.; Zheng, Y.-Z.; Zhao, Y.-W.; Yao, E.-X.; Zhuang, N.-X.; Luo, L.-B. Broadband photodetector based on carbon nanotube thin film/single layer graphene Schottky junction. *Scientific Reports* **2016**, *6*, 38569.
- (278) He, X.; Léonard, F.; Kono, J. Uncooled carbon nanotube photodetectors. *Advanced Optical Materials* **2015**, *3*, 989–1011.
- (279) Mueller, T.; Kinoshita, M.; Steiner, M.; Perebeinos, V.; Bol, A. A.; Farmer, D. B.; Avouris, P. Efficient narrow-band light emission from a single carbon nanotube p–n diode. *Nature nanotechnology* **2010**, *5*, 27–31.
- (280) Pyatkov, F.; Fütterling, V.; Khasminskaya, S.; Flavel, B. S.; Hennrich, F.; Kappes, M. M.; Krupke, R.; Pernice, W. H. Cavity-enhanced light emission from electrically driven carbon nanotubes. *Nature Photonics* **2016**, *10*, 420–427.
- (281) Wang, S.; Zeng, Q.; Yang, L.; Zhang, Z.; Wang, Z.; Pei, T.; Ding, L.; Liang, X.; Gao, M.; Li, Y. High-performance carbon nanotube light-emitting diodes with asymmetric contacts. *Nano letters* **2010**, *11*, 23–29.
- (282) Mittal, J.; Lin, K. Carbon nanotube-based interconnections. *Journal of Materials Science* **2017**, *52*, 643–662.
- (283) Singh, K.; Raj, B. Temperature-dependent modeling and performance evaluation of multi-walled CNT and single-walled CNT as global interconnects. *Journal of Electronic Materials* **2015**, *44*, 4825.

- (284) Xie, Y. E.; Chen, Y. P.; Zhong, J. Electron transport of folded graphene nanoribbons. *Journal of Applied Physics* **2009**, *106*, 103714.
- (285) Le, N. B.; Woods, L. M. Folded graphene nanoribbons with single and double closed edges. *Physical Review B* **2012**, *85*, 035403.
- (286) Yin, W.-J.; Xie, Y.-E.; Liu, L.-M.; Chen, Y.-P.; Wang, R.-Z.; Wei, X.-L.; Zhong, J.-X.; Lau, L. Atomic structure and electronic properties of folded graphene nanoribbons: A first-principles study. *Journal of Applied Physics* **2013**, *113*, 173506.
- (287) Zheng, X.; Song, L.; Wang, R.; Hao, H.; Guo, L.; Zeng, Z. Electronic structures and transverse electrical field effects in folded zigzag-edged graphene nanoribbons. *Applied Physics Letters* **2010**, *97*, 153129.
- (288) Li, C.; Chou, T.-W. A structural mechanics approach for the analysis of carbon nanotubes. *International Journal of Solids and Structures* **2003**, *40*, 2487–2499.
- (289) Birowska, M.; Milowska, K.; Majewski, J. Van der Waals density functionals for graphene layers and graphite. *Acta Phys Pol A* **2011**, *120*, 845–848.
- (290) Tran, N. T. T.; Lin, S.-Y.; Glukhova, O. E.; Lin, M. F. Configuration-induced rich electronic properties of bilayer graphene. *The Journal of Physical Chemistry C* **2015**, *119*, 10623–10630.
- (291) Bhattacharyya, S.; Singh, A. K. Lifshitz transition and modulation of electronic and transport properties of bilayer graphene by sliding and applied normal compressive strain. *Carbon* **2016**, *99*, 432–438.
- (292) Ho, J.-H.; Lu, C.; Hwang, C.; Chang, C.; Lin, M. F. Coulomb excitations in AA-and AB-stacked bilayer graphites. *Physical Review B* **2006**, *74*, 085406.
- (293) Wu, B.-R. Field modulation of the electronic structure of trilayer graphene. *Applied Physics Letters* **2011**, *98*, 263107.

- (294) Lammert, P. E.; Zhang, P.; Crespi, V. H. Gapping by squashing: Metal-insulator and insulator-metal transitions in collapsed carbon nanotubes. *Physical review letters* **2000**, *84*, 2453.
- (295) Yan, J.; Li, C.; Zhan, D.; Liu, L.; Shen, D.; Kuo, J.-L.; Chen, S.; Shen, Z. Graphene homojunction: closed-edge bilayer graphene by pseudospin interaction. *Nanoscale* **2016**, *8*, 9102–9106.
- (296) Tomanek, D.; Zhong, W.; Krastev, E. Stability of multishell fullerenes. *Physical Review B* **1993**, *48*, 15461.
- (297) Lavin, J. G.; Subramoney, S.; Ruoff, R. S.; Berber, S.; Tomanek, D. Scrolls and nested tubes in multiwall carbon nanotubes. *Carbon* **2002**, *40*, 1123–1130.
- (298) Huang, Y.-K.; Chen, S.-C.; Ho, Y.-H.; Lin, C.-Y.; Lin, M. F. Feature-rich magnetic quantization in sliding bilayer graphenes. *Scientific reports* **2014**, *4*, 7509.
- (299) Lu, C.; Chang, C.-P.; Huang, Y.-C.; Chen, R.-B.; Lin, M. Influence of an electric field on the optical properties of few-layer graphene with AB stacking. *Physical Review B* **2006**, *73*, 144427.
- (300) Jackson, J. D. *Classical Electrodynamics*, 3rd Ed. Wiley, London. 1998.
- (301) Zhang, Z.; Guo, W. Tunable ferromagnetic spin ordering in boron nitride nanotubes with topological fluorine adsorption. *Journal of the American Chemical Society* **2009**, *131*, 6874–6879.
- (302) Charlier, J.-C.; Amara, H.; Lambin, P. Catalytically assisted tip growth mechanism for single-wall carbon nanotubes. *Acs Nano* **2007**, *1*, 202–207.
- (303) Kim, Y.-H.; Sim, H.-S.; Chang, K. Electronic structure of collapsed C, BN, and BC 3 nanotubes. *Current Applied Physics* **2001**, *1*, 39–44.

- (304) Ahmadi Peyghan, A.; Hadipour, N. L.; Bagheri, Z. Effects of Al doping and double-antisite defect on the adsorption of HCN on a BC₂N nanotube: density functional theory studies. *The Journal of Physical Chemistry C* **2013**, *117*, 2427–2432.
- (305) Lu, W.; Ruan, G.; Genorio, B.; Zhu, Y.; Novosel, B.; Peng, Z.; Tour, J. M. Functionalized graphene nanoribbons via anionic polymerization initiated by alkali metal-intercalated carbon nanotubes. *ACS nano* **2013**, *7*, 2669–2675.
- (306) Haddon, R. Electronic structure, conductivity and superconductivity of alkali metal doped (C₆₀). *Accounts of chemical research* **1992**, *25*, 127–133.
- (307) Benedict, L. X.; Crespi, V. H.; Louie, S. G.; Cohen, M. L. Static conductivity and superconductivity of carbon nanotubes: Relations between tubes and sheets. *Physical Review B* **1995**, *52*, 14935.
- (308) Virojanadara, C.; Watcharinyanon, S.; Zakharov, A.; Johansson, L. I. Epitaxial graphene on 6 H-SiC and Li intercalation. *Physical Review B* **2010**, *82*, 205402.
- (309) Dresselhaus, M.; Dresselhaus, G. Intercalation compounds of graphite. *Advances in Physics* **1981**, *30*, 139–326.
- (310) Caragiu, M.; Finberg, S. Alkali metal adsorption on graphite: a review. *Journal of Physics: Condensed Matter* **2005**, *17*, R995.
- (311) Sohmen, E.; Fink, J.; Krätschmer, W. Electronic structure studies of undoped and n-type doped fullerene C₆₀. *EPL (Europhysics Letters)* **1992**, *17*, 51.
- (312) Lee, R.; Kim, H.; Fischer, J.; Thess, A.; Smalley, R. E. Conductivity enhancement in single-walled carbon nanotube bundles doped with K and Br. *Nature* **1997**, *388*, 255.
- (313) Rao, A. M.; Eklund, P.; Bandow, S.; Thess, A.; Smalley, R. E. Evidence for charge transfer in doped carbon nanotube bundles from Raman scattering. *Nature* **1997**, *388*, 257.

- (314) Chen, J. H.; Jang, C.; Adam, S.; Fuhrer, M.; Williams, E.; Ishigami, M. Charged impurity scattering in graphene. *Nature physics* **2008**, *4*, 377381.
- (315) Ellis, C. T.; Stier, A. V.; Kim, M.-H.; Tischler, J. G.; Glaser, E. R.; Myers-Ward, R. L.; Tedesco, J. L.; Eddy, C. R.; Gaskill, D. K.; Cerne, J. Magneto-optical fingerprints of distinct graphene multilayers using the giant infrared Kerr effect. *Scientific reports* **2013**, *3*.
- (316) Chen, J.-Y.; Zhu, J.; Zhang, D.; Lattery, D. M.; Li, M.; Wang, J.-P.; Wang, X. Time-Resolved Magneto-Optical Kerr Effect of Magnetic Thin Films for Ultrafast Thermal Characterization. *The journal of physical chemistry letters* **2016**, *7*, 2328–2332.
- (317) Han, W.; Kawakami, R. K.; Gmitra, M.; Fabian, J. Graphene spintronics. *Nature nanotechnology* **2014**, *9*, 794–807.
- (318) Friedman, A. L.; vant Erve, O. M.; Robinson, J. T.; Whitener Jr, K. E.; Jonker, B. T. Hydrogenated graphene as a homoepitaxial tunnel barrier for spin and charge transport in graphene. *ACS nano* **2015**, *9*, 6747–6755.
- (319) Ngoc Thanh Thuy, T.; Duy Khanh, N.; Olga E, G.; Ming-Fa, L. Coverage-dependent essential properties of halogenated graphene: A DFT study. *Scientific Reports* **2017**, *7*, 1–13.
- (320) Sun, C.; Feng, Y.; Li, Y.; Qin, C.; Zhang, Q.; Feng, W. Solvothermally exfoliated fluorographene for high-performance lithium primary batteries. *Nanoscale* **2014**, *6*, 2634–2641.
- (321) Zhao, F.-G.; Zhao, G.; Liu, X.-H.; Ge, C.-W.; Wang, J.-T.; Li, B.-L.; Wang, Q.-G.; Li, W.-S.; Chen, Q.-Y. Fluorinated graphene: facile solution preparation and tailorable properties by fluorine-content tuning. *J. Mater. Chem. A* **2014**, *2*, 8782–8789.

- (322) Katkov, M.; Sysoev, V.; Gusel’Nikov, A.; Asanov, I.; Bulusheva, L.; Okotrub, A. A backside fluorine-functionalized graphene layer for ammonia detection. *Phys. Chem. Chem. Phys.* **2015**, *17*, 444–450.
- (323) others,, et al. Fluorinated graphenes as advanced biosensors—effect of fluorine coverage on electron transfer properties and adsorption of biomolecules. *Nanoscale* **2016**, *8*, 12134–12142.
- (324) De Padova, P.; Perfetti, P.; Olivieri, B.; Quaresima, C.; Ottaviani, C.; Le Lay, G. 1D graphene-like silicon systems: silicene nano-ribbons. *Journal of Physics: Condensed Matter* **2012**, *24*, 223001.
- (325) Dávila, M.; Xian, L.; Cahangirov, S.; Rubio, A.; Le Lay, G. Germanene: a novel two-dimensional germanium allotrope akin to graphene and silicene. *New Journal of Physics* **2014**, *16*, 095002.
- (326) Zhu, F.-f.; Chen, W.-j.; Xu, Y.; Gao, C.-l.; Guan, D.-d.; Liu, C.-h.; Qian, D.; Zhang, S.-C.; Jia, J.-f. Epitaxial growth of two-dimensional stanene. *Nature materials* **2015**, *14*, 1020–1025.
- (327) Liang, L.; Wang, J.; Lin, W.; Sumpter, B. G.; Meunier, V.; Pan, M. Electronic bandgap and edge reconstruction in phosphorene materials. *Nano letters* **2014**, *14*, 6400–6406.
- (328) Li, Y.; Zhou, Z.; Zhang, S.; Chen, Z. MoS₂ nanoribbons: high stability and unusual electronic and magnetic properties. *Journal of the American Chemical Society* **2008**, *130*, 16739–16744.
- (329) Li, X.; Mullen, J. T.; Jin, Z.; Borysenko, K. M.; Nardelli, M. B.; Kim, K. W. Intrinsic electrical transport properties of monolayer silicene and MoS₂ from first principles. *Physical Review B* **2013**, *87*, 115418.

- (330) Lin, S.-Y.; Chang, S.-L.; Tran, N. T. T.; Yang, P.-H.; Lin, M.-F. H-Si bonding-induced unusual electronic properties of silicene: a method to identify hydrogen concentration. *Physical Chemistry Chemical Physics* **2015**, *17*, 26443–26450.
- (331) Lian, C.; Ni, J. Strain induced phase transitions in silicene bilayers: a first principles and tight-binding study. *Aip Advances* **2013**, *3*, 052102.
- (332) Berdiyrov, G.; Neek-Amal, M.; Peeters, F.; van Duin, A. C. Stabilized silicene within bilayer graphene: A proposal based on molecular dynamics and density-functional tight-binding calculations. *Physical Review B* **2014**, *89*, 024107.
- (333) Ritter, K. A.; Lyding, J. W. The influence of edge structure on the electronic properties of graphene quantum dots and nanoribbons. *Nature materials* **2009**, *8*, 235–242.
- (334) others,, et al. Experimentally engineering the edge termination of graphene nanoribbons. *ACS nano* **2012**, *7*, 198–202.
- (335) Xing, Y.; Sun, Q.-f.; Wang, J. Nernst and Seebeck effects in a graphene nanoribbon. *Physical Review B* **2009**, *80*, 235411.
- (336) Liu, Y.; Dong, X.; Chen, P. Biological and chemical sensors based on graphene materials. *Chemical Society Reviews* **2012**, *41*, 2283–2307.
- (337) Lin, J.; Peng, Z.; Xiang, C.; Ruan, G.; Yan, Z.; Natelson, D.; Tour, J. M. Graphene nanoribbon and nanostructured SnO₂ composite anodes for lithium ion batteries. *ACS nano* **2013**, *7*, 6001–6006.
- (338) others,, et al. Edge-Fluorinated Graphene Nanoplatelets as High Performance Electrodes for Dye-Sensitized Solar Cells and Lithium Ion Batteries. *Advanced Functional Materials* **2015**, *25*, 1170–1179.
- (339) An, H.; Li, Y.; Long, P.; Gao, Y.; Qin, C.; Cao, C.; Feng, Y.; Feng, W. Hydrothermal

- preparation of fluorinated graphene hydrogel for high-performance supercapacitors. *Journal of Power Sources* **2016**, *312*, 146–155.
- (340) Schrier, J. Fluorinated and nanoporous graphene materials as sorbents for gas separations. *ACS applied materials & interfaces* **2011**, *3*, 4451–4458.
- (341) Candini, A.; Klyatskaya, S.; Ruben, M.; Wernsdorfer, W.; Affronte, M. Graphene spintronic devices with molecular nanomagnets. *Nano letters* **2011**, *11*, 2634–2639.
- (342) Lin, J.; Raji, A.-R. O.; Nan, K.; Peng, Z.; Yan, Z.; Samuel, E. L.; Natelson, D.; Tour, J. M. Iron Oxide Nanoparticle and Graphene Nanoribbon Composite as an Anode Material for High-Performance Li-Ion Batteries. *Advanced Functional Materials* **2014**, *24*, 2044–2048.
- (343) Pumera, M. Graphene-based nanomaterials for energy storage. *Energy & Environmental Science* **2011**, *4*, 668–674.

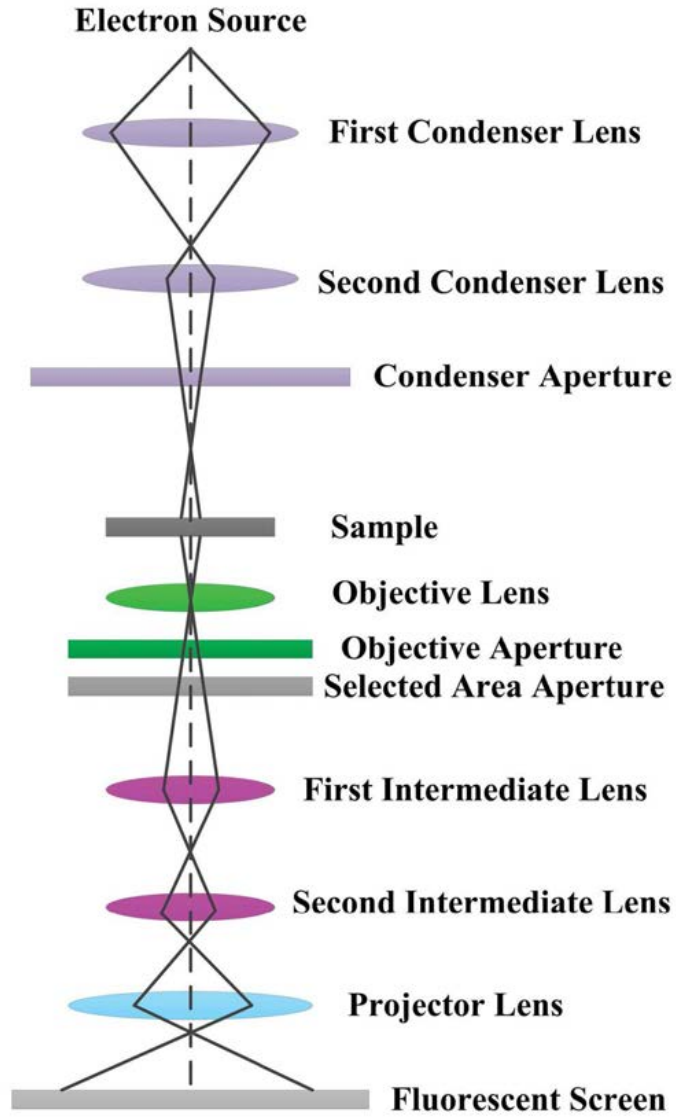


Figure 1: The TEM instrument in measuring electron diffraction pattern.

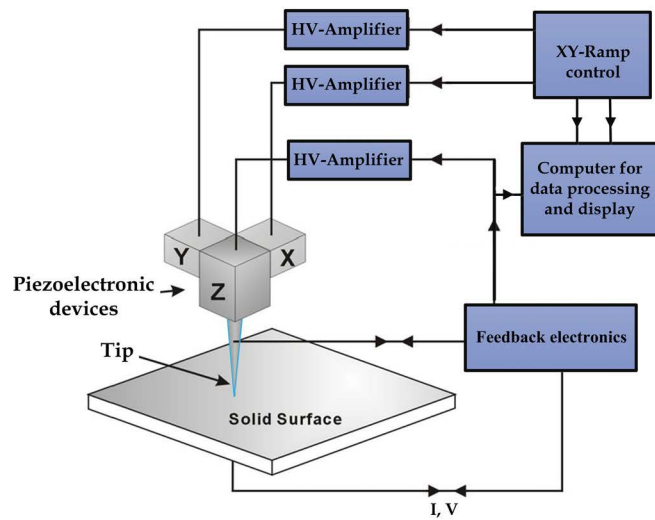


Figure 2: The schematic illustration of STM in observing surface configuration by controlling the tip height under a specific tunneling current.

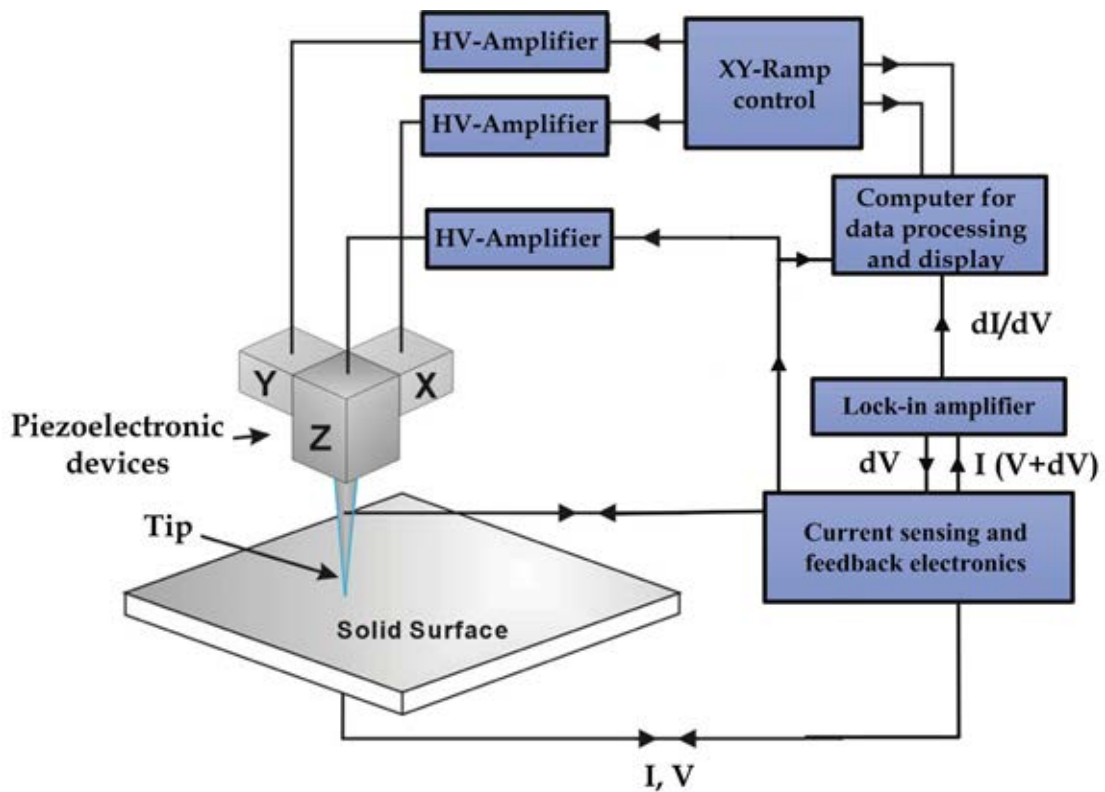


Figure 3: The schematic diagram of taking the current-dependent normalized conductance spectrum by using STS.

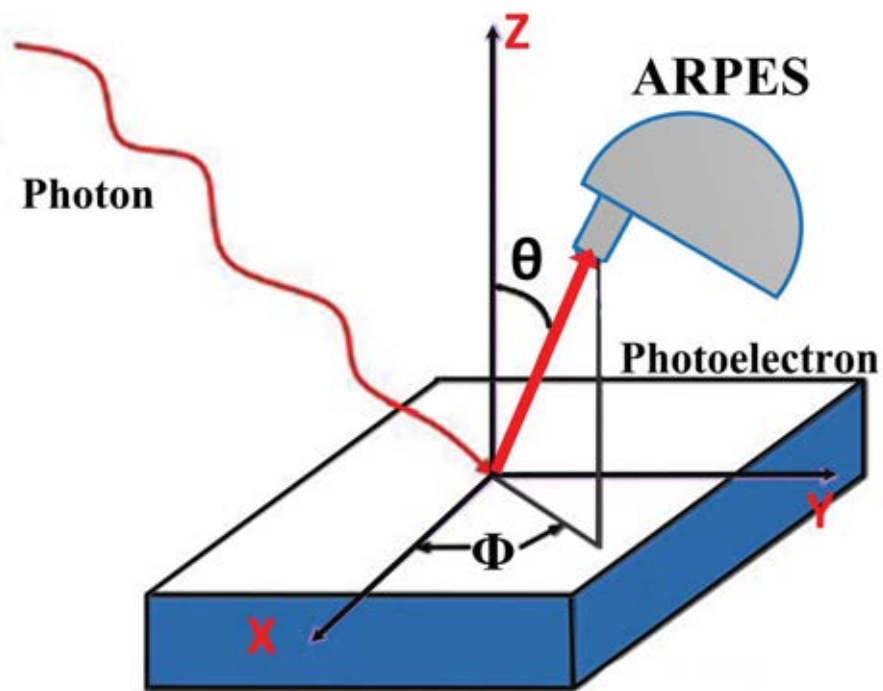


Figure 4: The photo-electronic spectrum of ARPES in determining the momentum-dependent valence state energies.

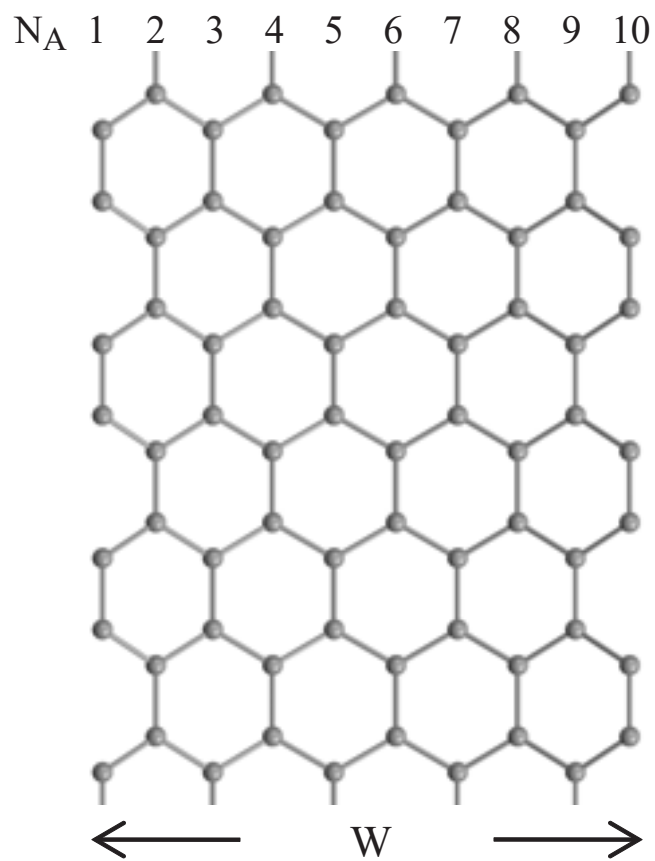


Figure 5: Geometric structures of $N_A = 10$ armchair nanoribbon.

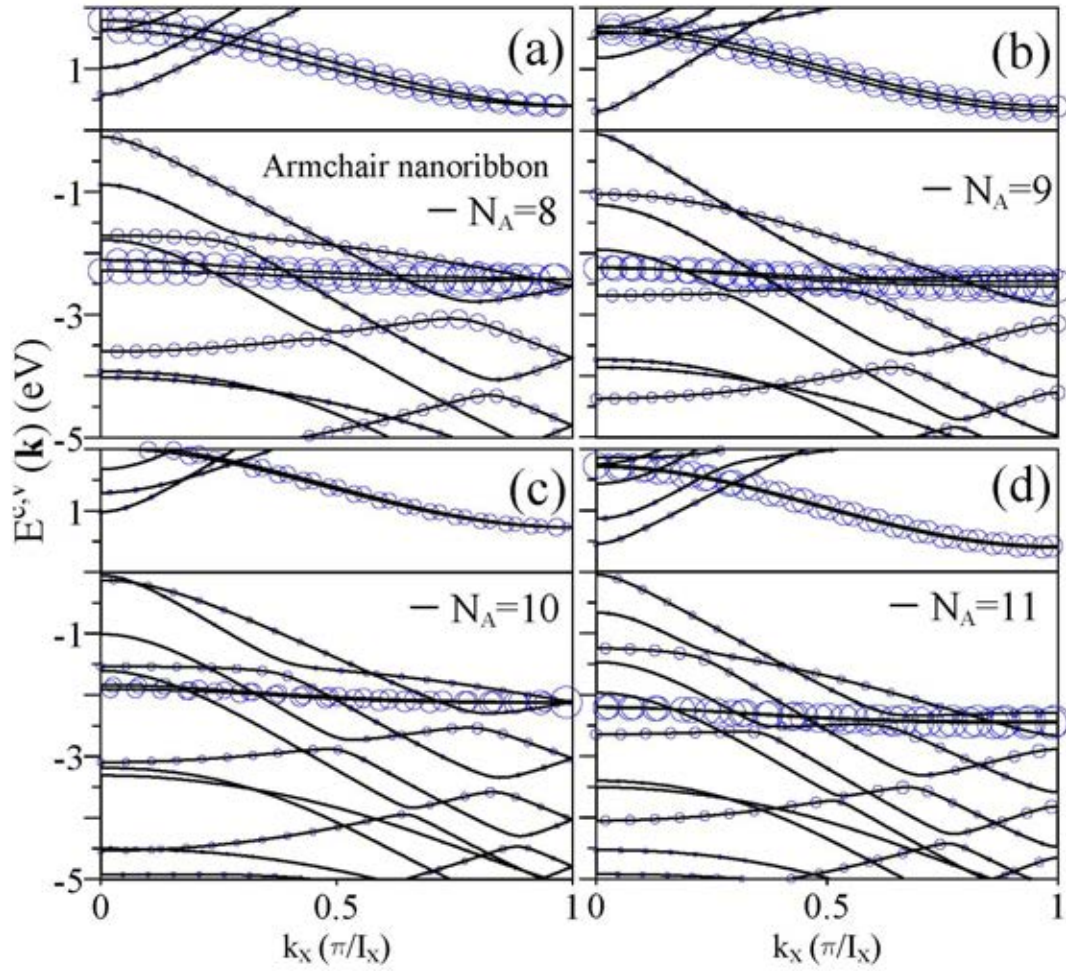


Figure 6: Energy bands of pristine (a) $N_A = 8$, (b) $N_A = 9$, (c) $N_A = 10$, and (d) $N_A = 11$ armchair nanoribbons, in which the contributions from the edge carbon atoms are denoted by the blue circles.

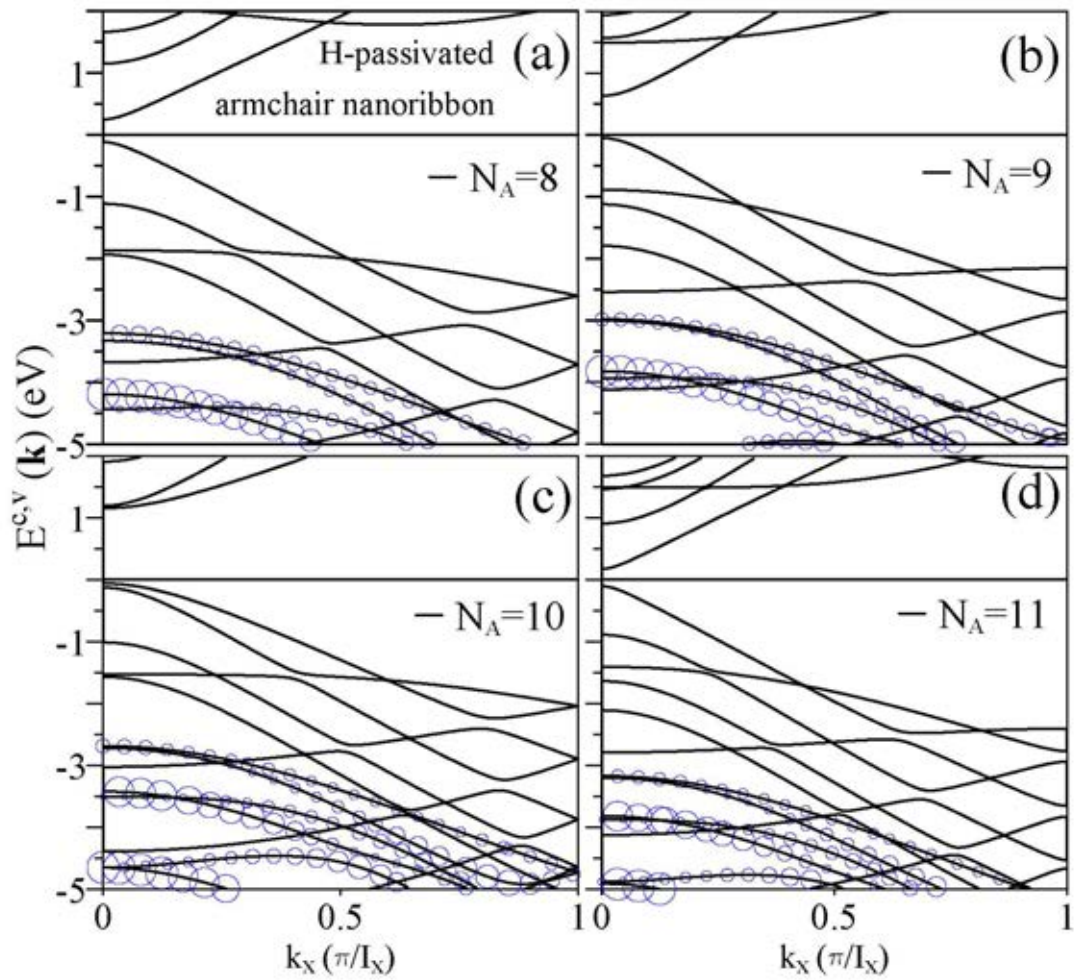


Figure 7: Energy bands of H-passivated (a) $N_A = 8$, (b) $N_A = 9$, (c) $N_A = 10$, and (d) $N_A = 11$ armchair nanoribbons, in which the contributions from the edge hydrogen atoms are denoted by the blue circles.

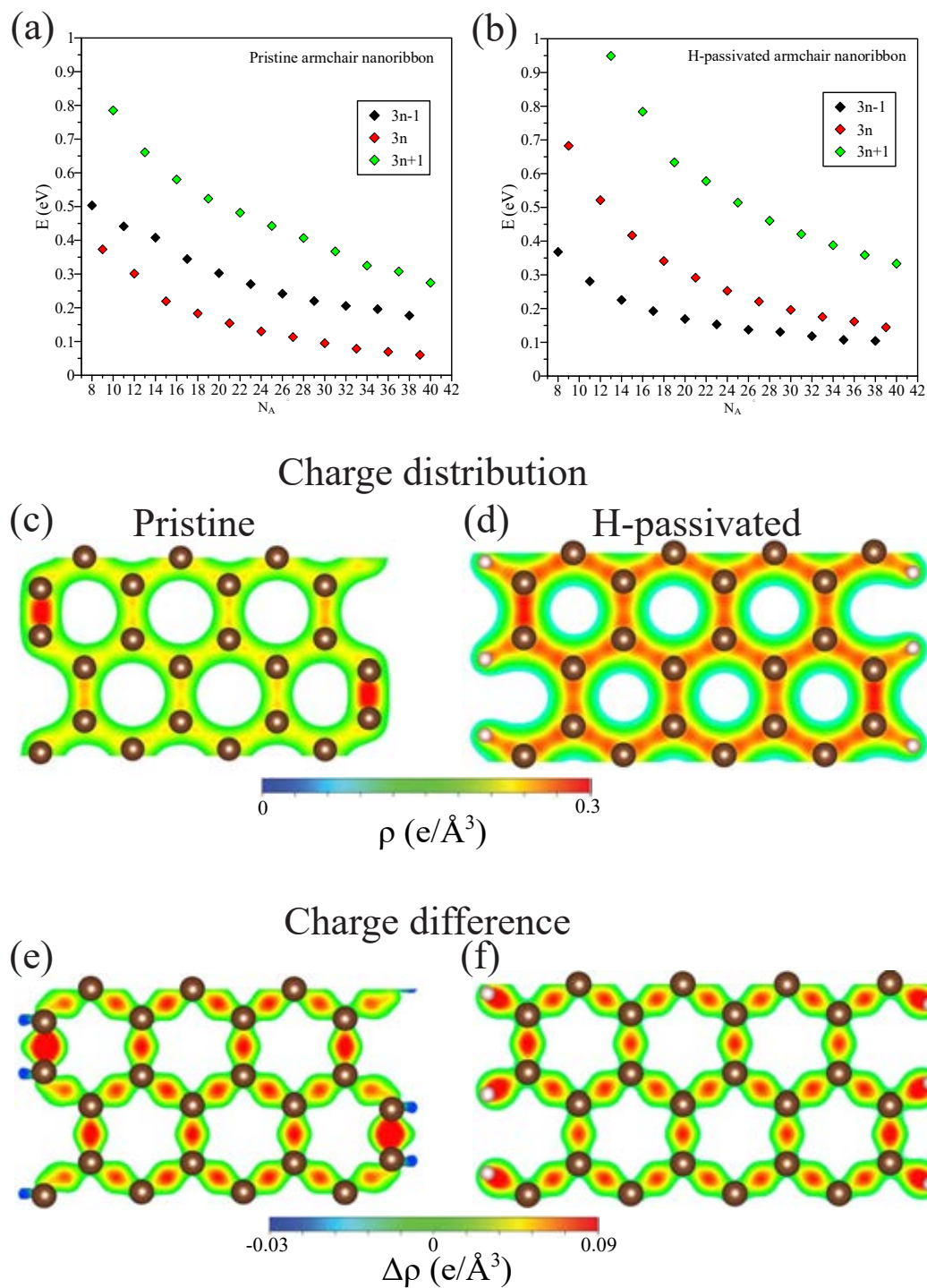


Figure 8: Width dependent energy gaps for (a) pristine and (b) H-passivated armchair graphene nanoribbon. The spatial charge distributions for (c) pristine and (d) H-passivated armchair nanoribbon. (e) and (f) are the charge differences for pristine and H-passivated armchair nanoribbon, respectively.

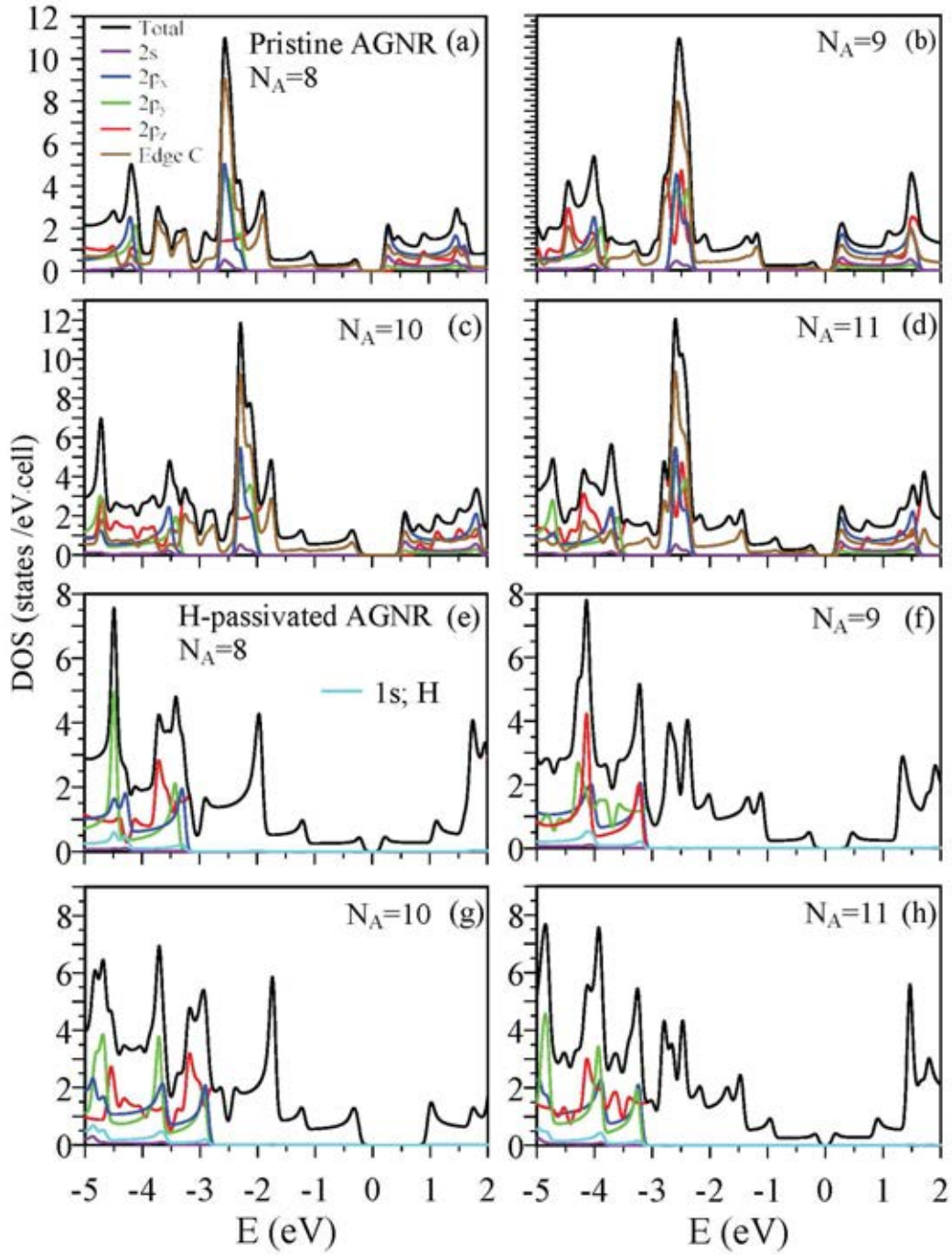


Figure 9: The total and orbital-projected DOSs for pristine (a) $N_A = 8$, (b) $N_A = 9$, (c) $N_A = 10$, and (d) $N_A = 11$ armchair nanoribbons and H-passivated (e) $N_A = 8$, (f) $N_A = 9$, (g) $N_A = 10$, and (h) $N_A = 11$ armchair nanoribbons.

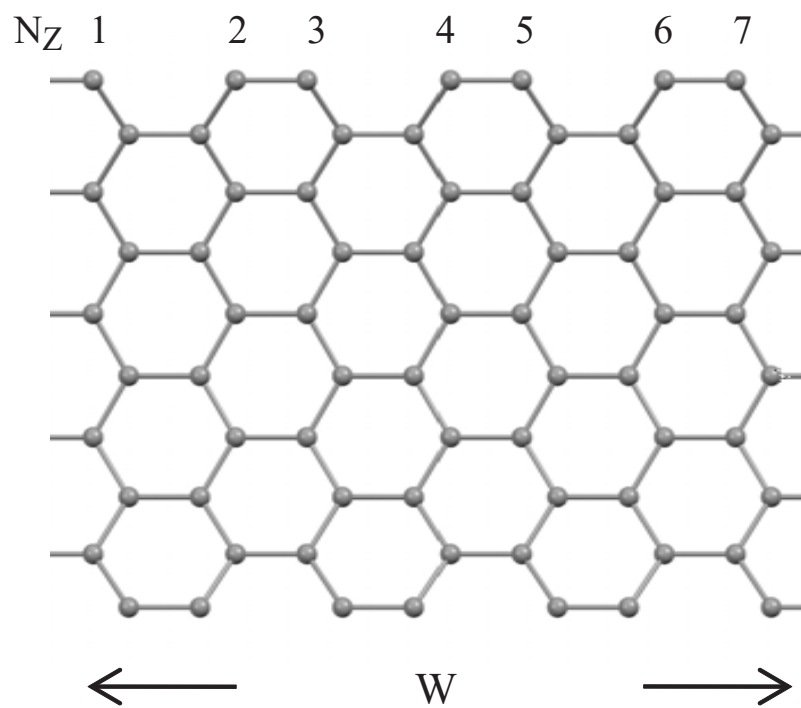


Figure 10: Geometric structures of zigzag nanoribbon.

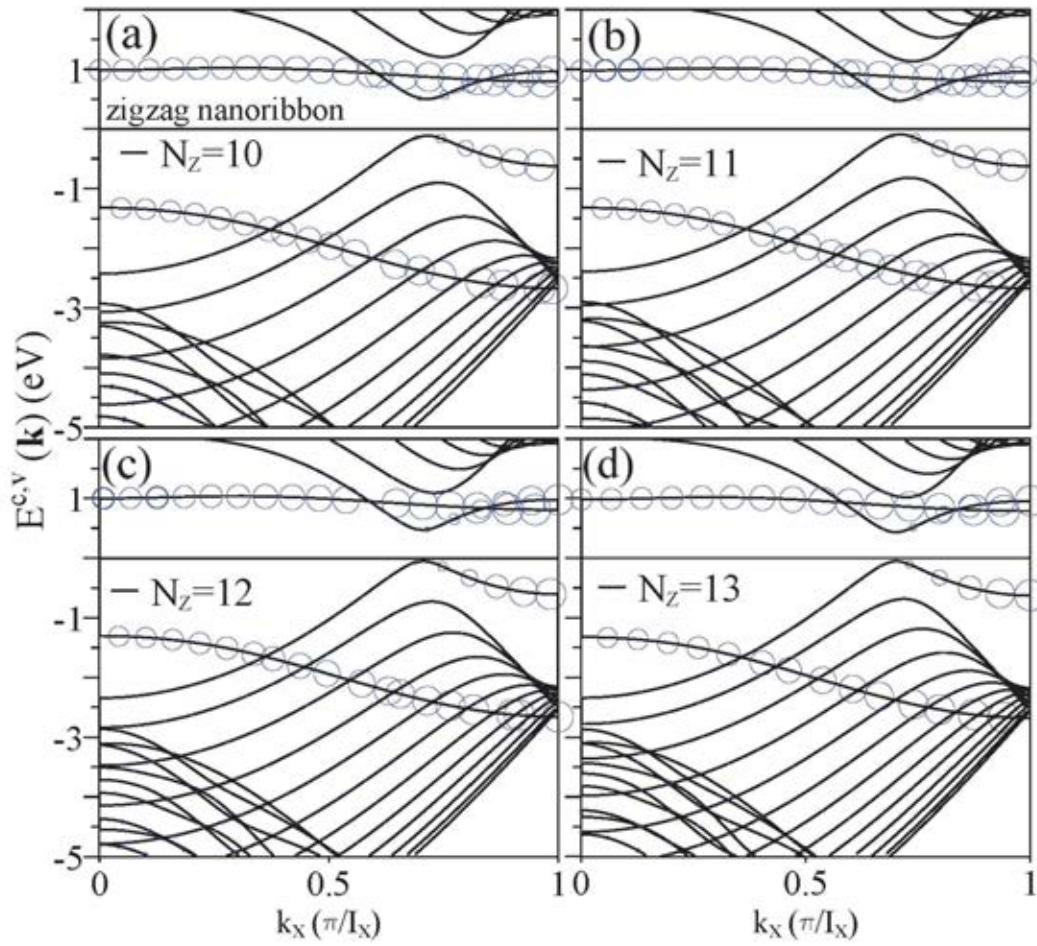


Figure 11: Energy bands of pristine (a) $N_Z = 10$, (b) $N_Z = 11$, (c) $N_Z = 12$, and (d) $N_Z = 13$ zigzag nanoribbons, in which the contributions from the edge carbon atoms are denoted by the blue circles.

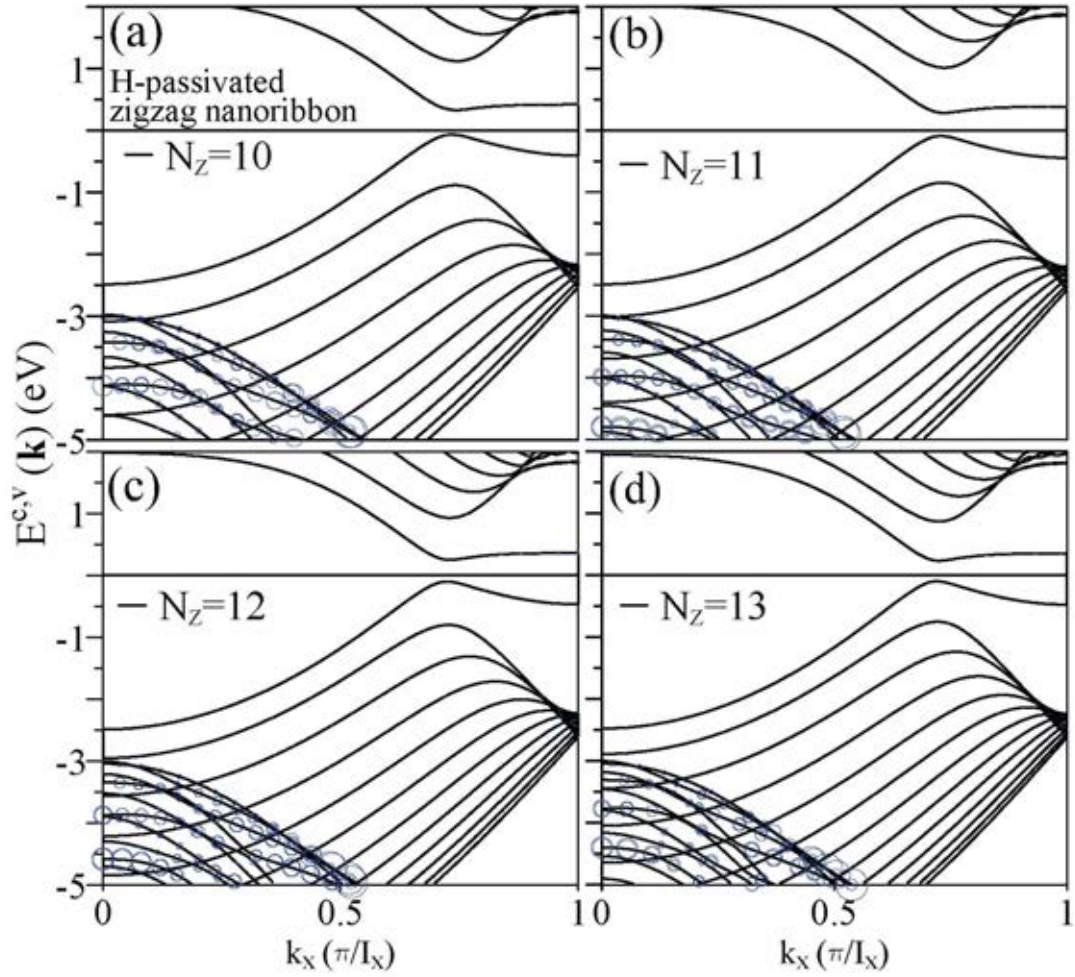


Figure 12: Energy bands of H-passivated (a) $N_Z = 10$, (b) $N_Z = 11$, (c) $N_Z = 12$, and (d) $N_Z = 13$ zigzag nanoribbons, in which the contributions from the edge hydrogen atoms are denoted by the blue circles.

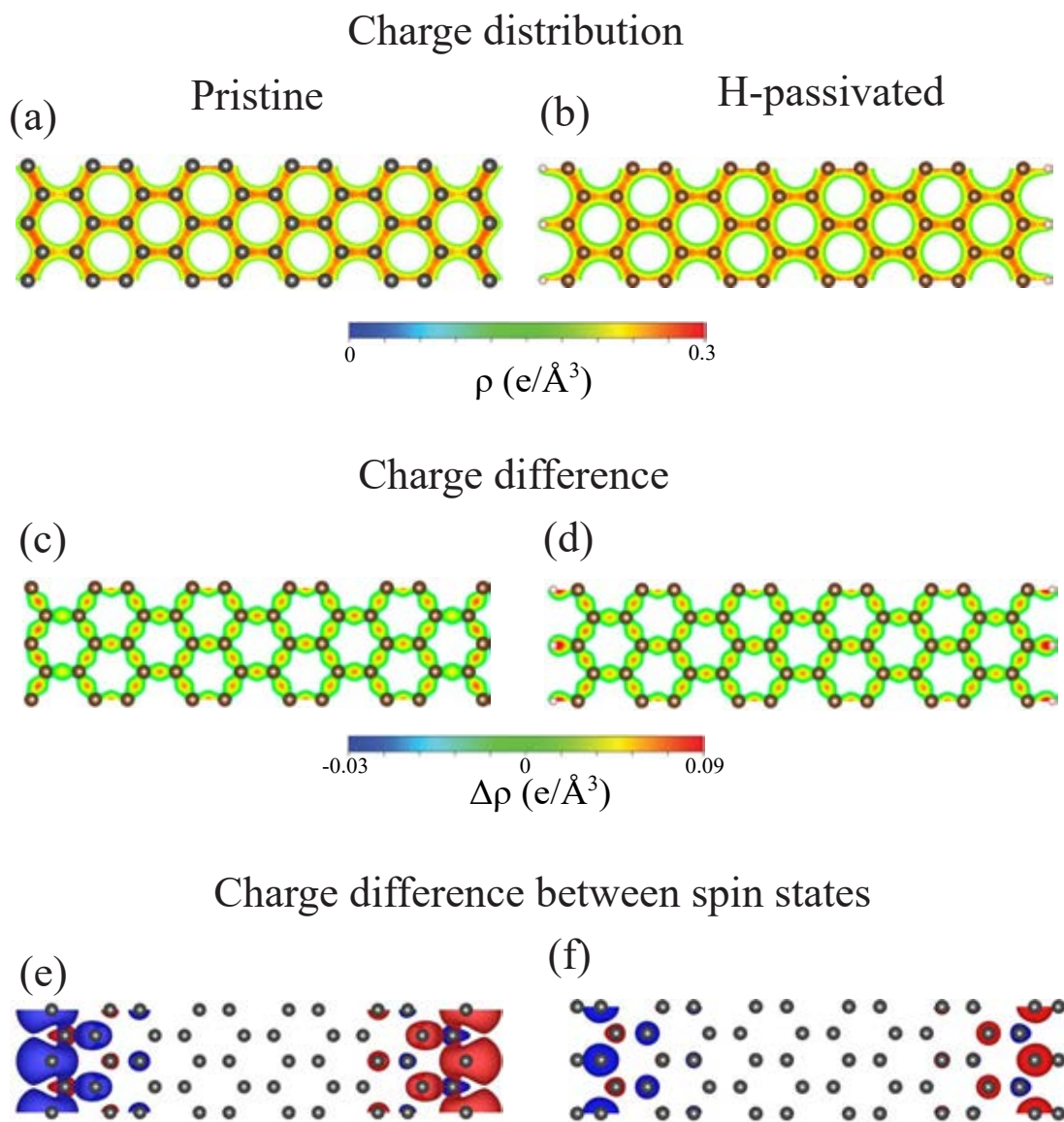


Figure 13: The spatial charge distributions for $N_Z = 10$ (a) pristine and (b) H-passivated zigzag nanoribbon. (c) and (d) are the charge differences for pristine and H-passivated zigzag nanoribbon, respectively. The difference between two spin states for (e) pristine and (f) H-passivated zigzag nanoribbon.

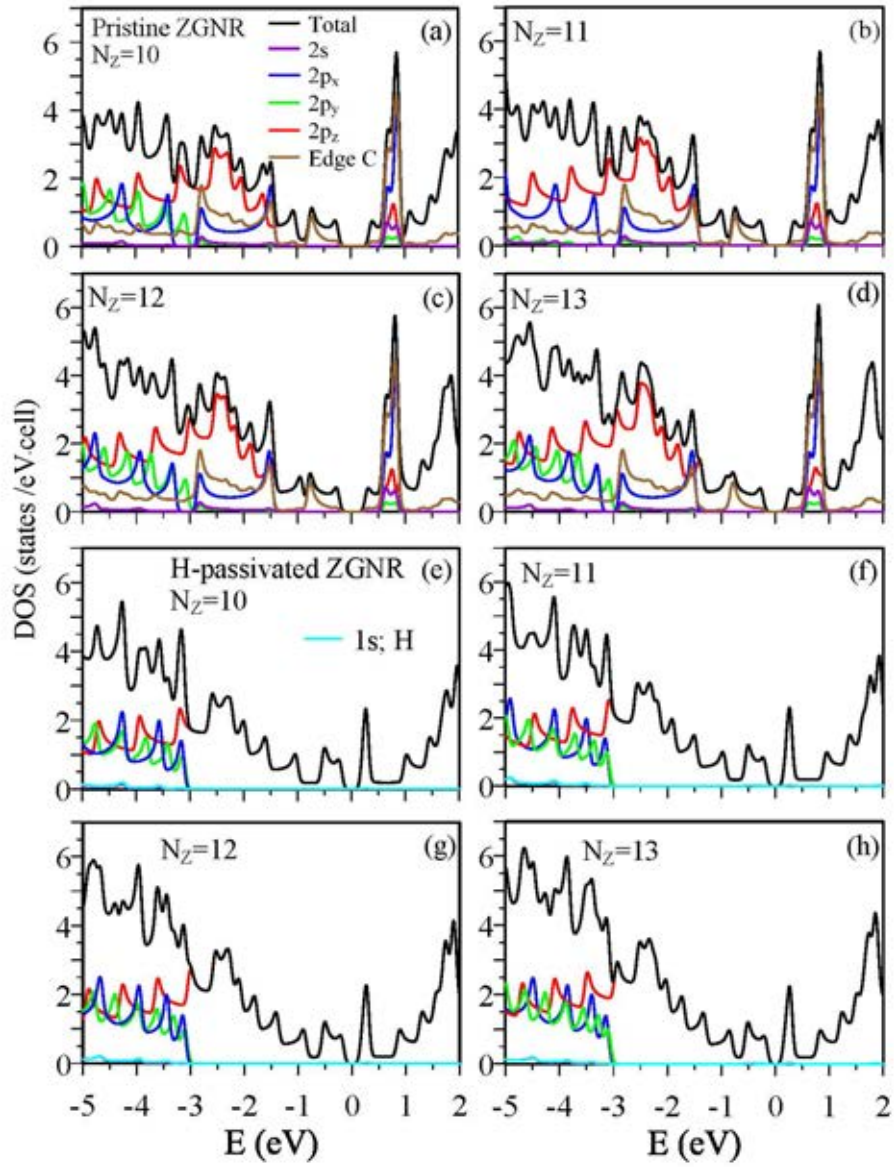


Figure 14: The total and orbital-projected DOSs for pristine (a) $N_Z = 10$, (b) $N_Z = 11$, (c) $N_Z = 12$, and (d) $N_Z = 13$ zigzag nanoribbons and H-passivated (e) $N_Z = 10$, (f) $N_Z = 11$, (g) $N_Z = 12$, and (h) $N_Z = 13$ zigzag nanoribbons.

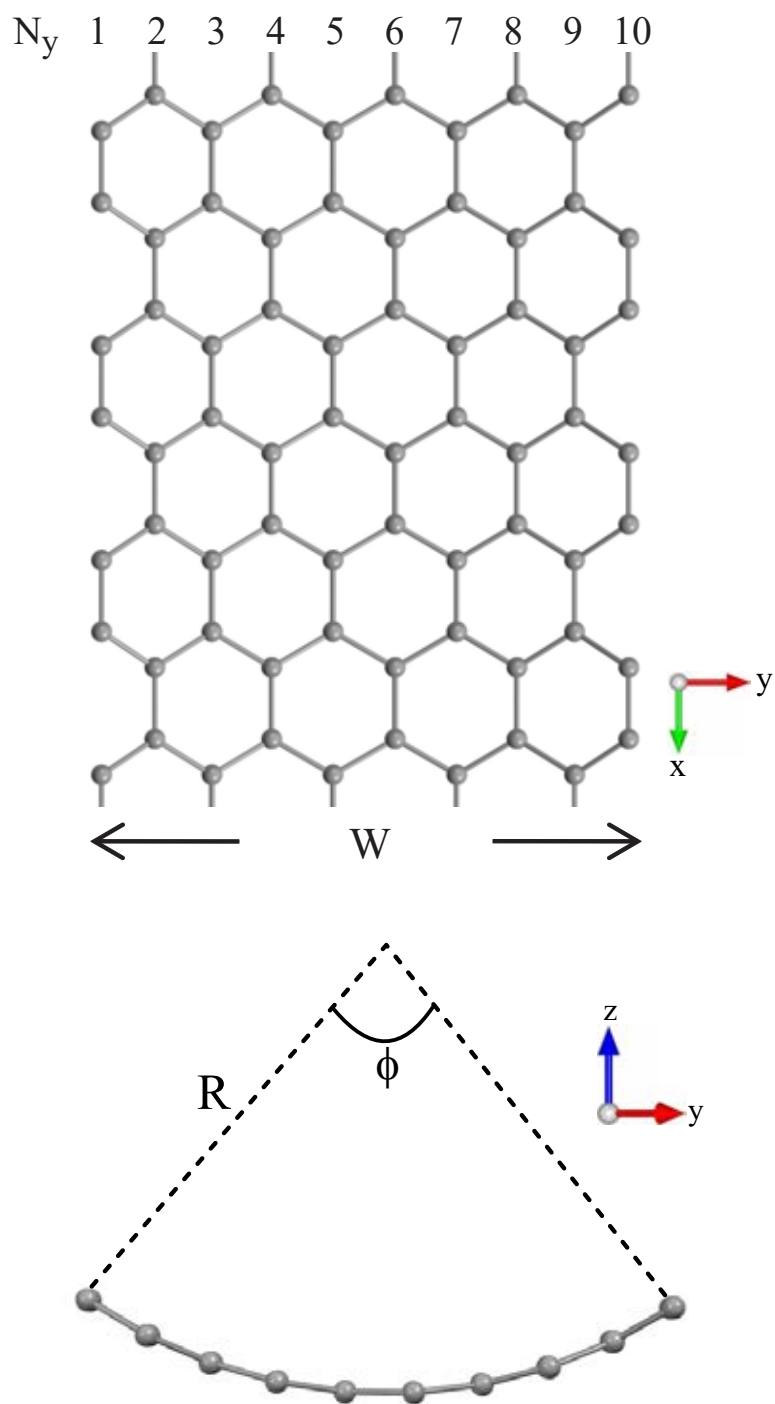


Figure 15: (a) Geometric structure of an $N_A=10$ curved armchair graphene nanoribbon with radius and arc angle, and (b) the dependence of the edge-C-C bond length on ϕ .

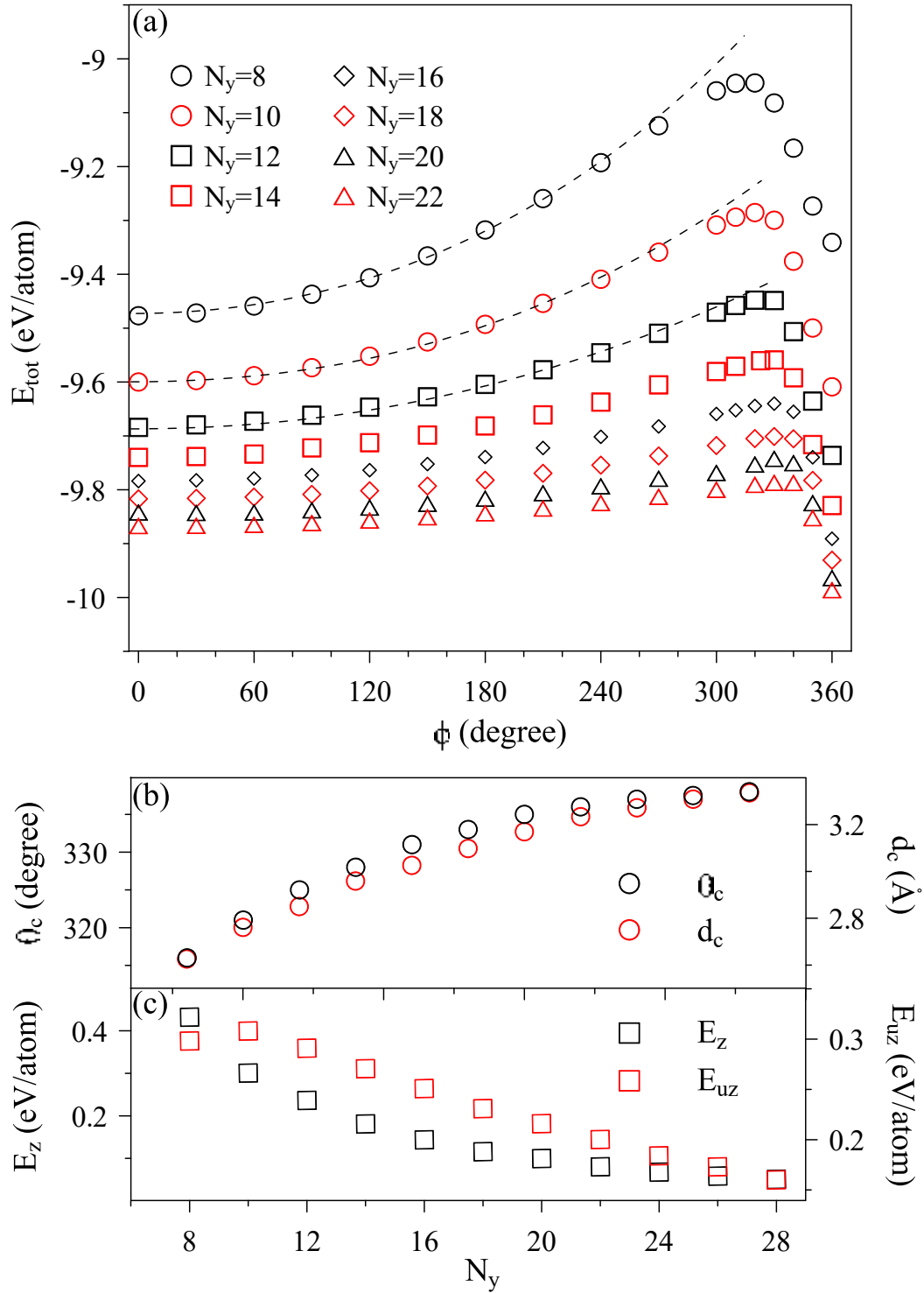


Figure 16: (a) The ϕ -dependent ground state energy per atom for armchair nanoribbons with distinct widths, (b) the critical arc angles and interaction distances; (c) the zipping and unzipping energies. Also shown in (a) are the strain energies fitted by the dashed curves.

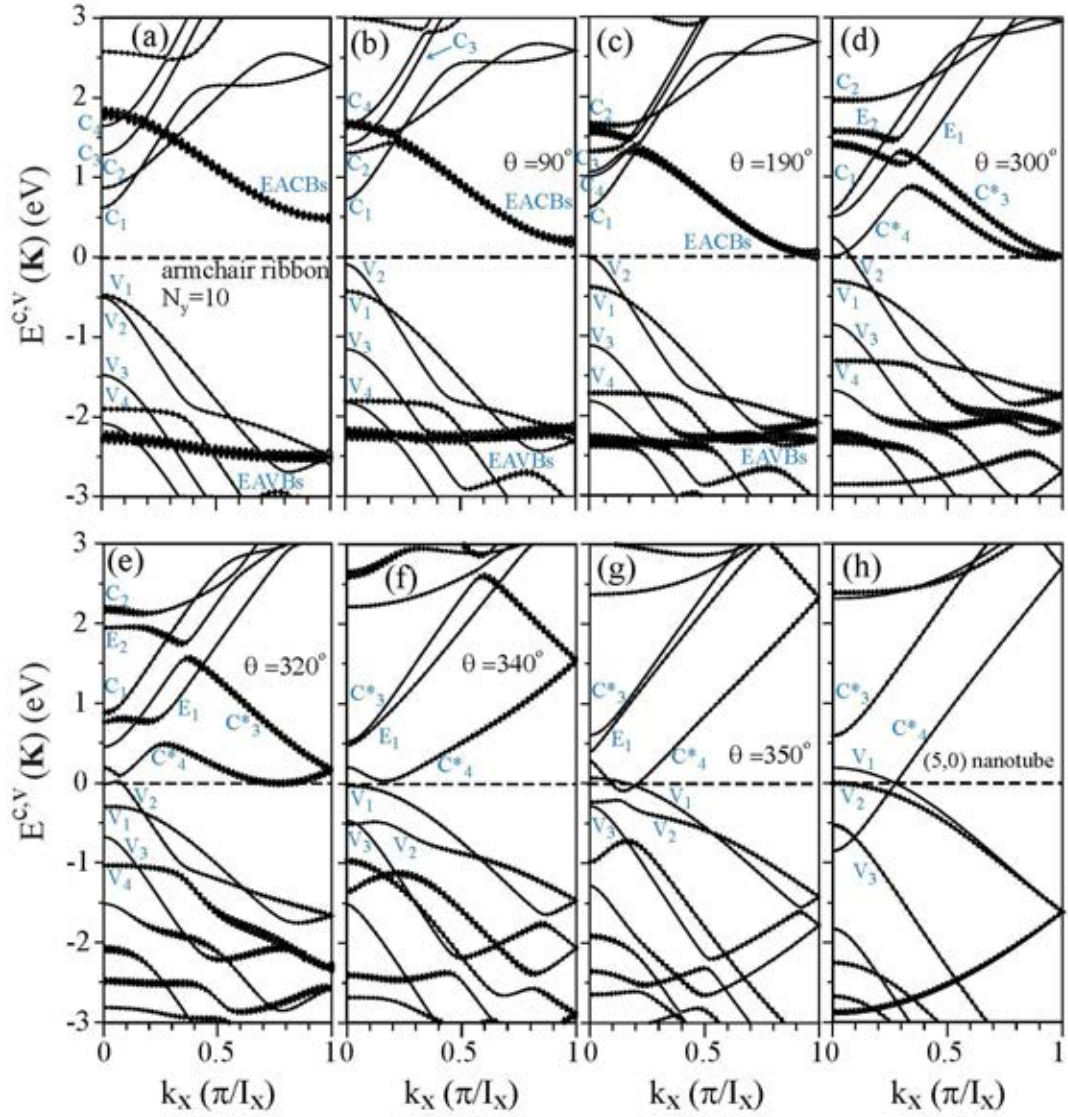


Figure 17: Band structures of the $N_A = 10$ curved armchair nanoribbon under (a) $\phi = 0^\circ$, (b) 90° , (c) 190° , (d) 300° , (e) 320° , (f) 340° , (g) 350° and (h) 360° . The radii of open circles represent the contributions due to edge atoms.

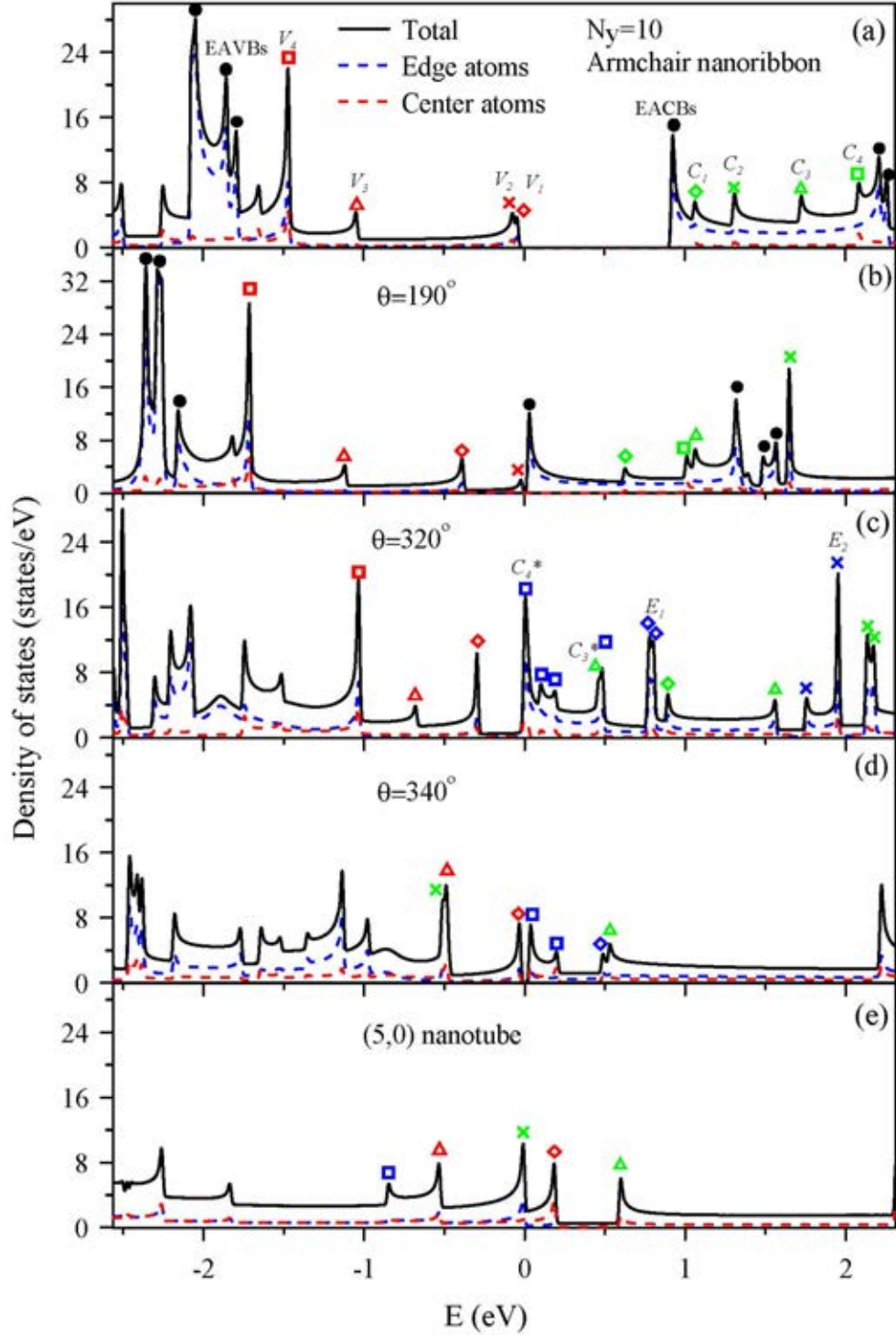


Figure 18: DOSs arising from the total atoms, edge atoms and center atoms for the $N_A = 10$ curved armchair nanoribbon under (a) $\phi = 0^\circ$, (b) 190° , (c) 320° , (d) 340° , and (e) 360° .

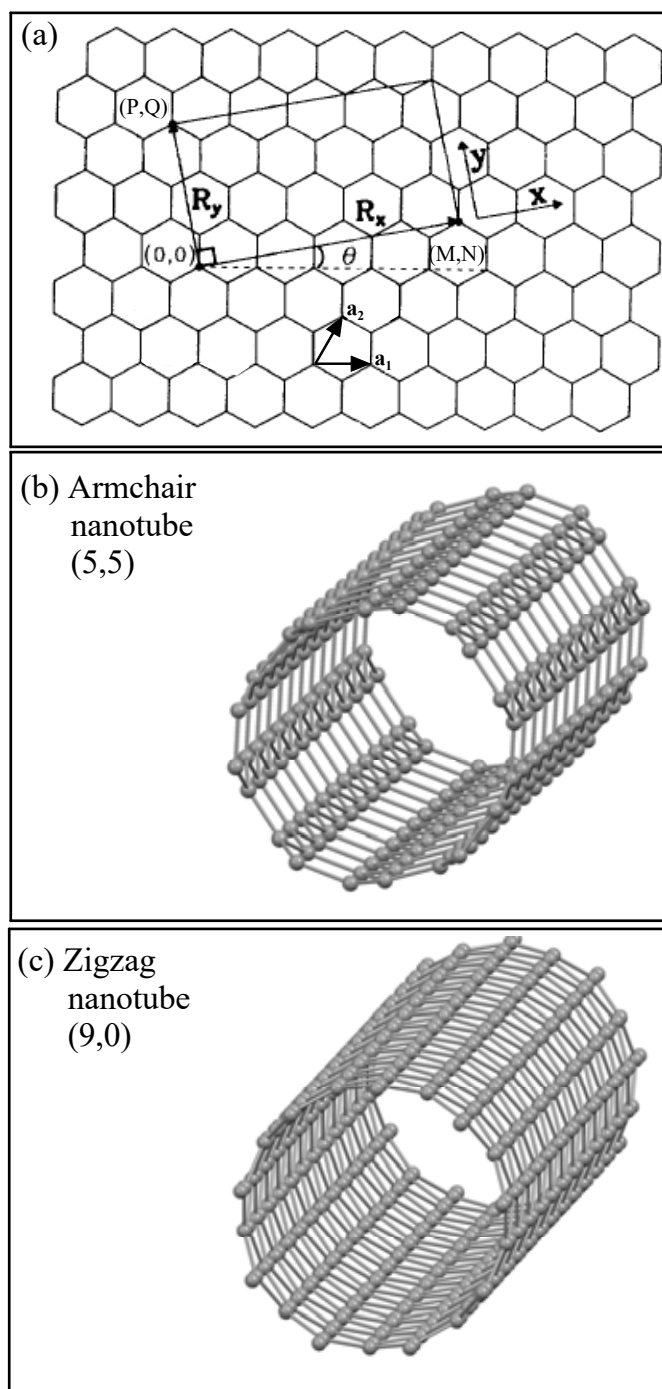


Figure 19: (a) A carbon nanotube, a rolled-up graphene sheet in the cylindrical structure from the origin to the vector $\mathbf{R}_x = m\mathbf{a}_1 + n\mathbf{a}_2$, (b) a (5,5) armchair nanotube and (c) a (9,0) zigzag nanotube.

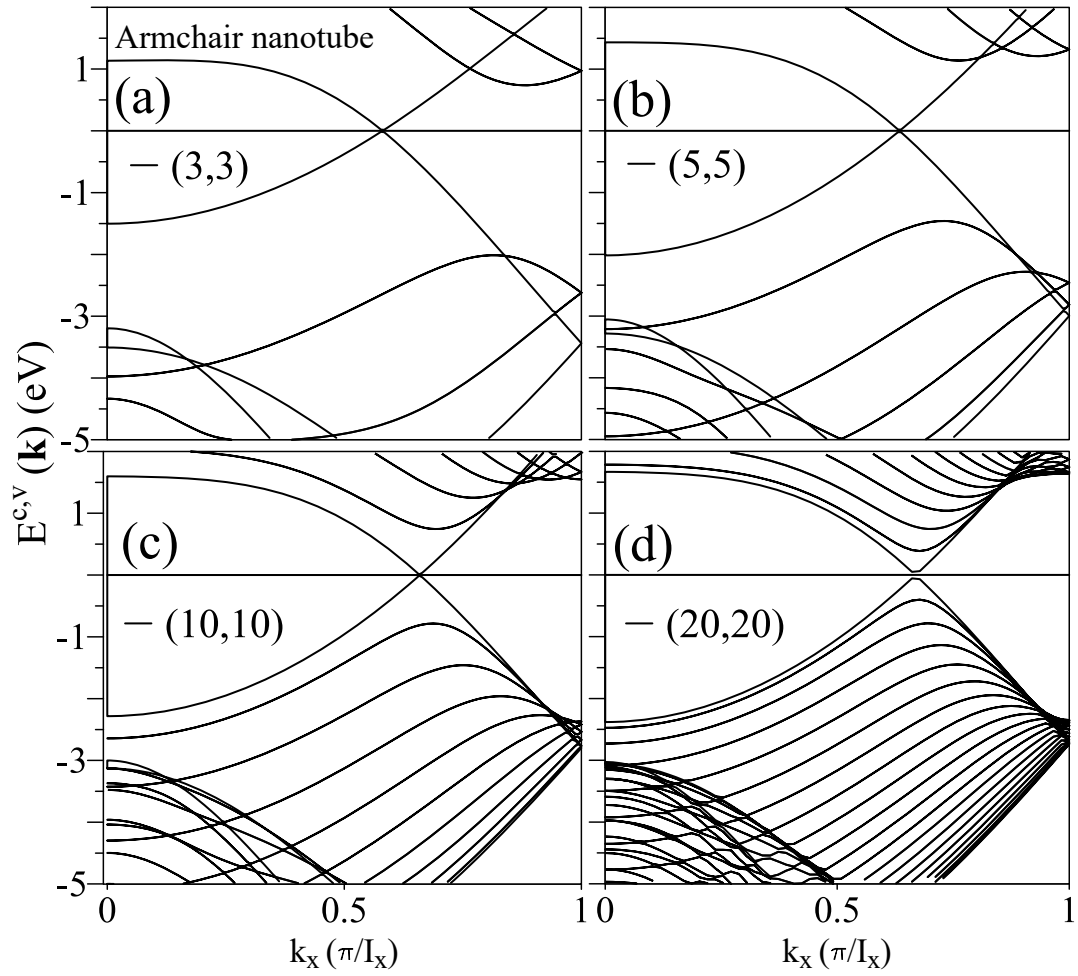


Figure 20: Energy bands of armchair nanotubes: (a) (3,3), (b) (5,5), (c) (10,10) and (d) (20,20).

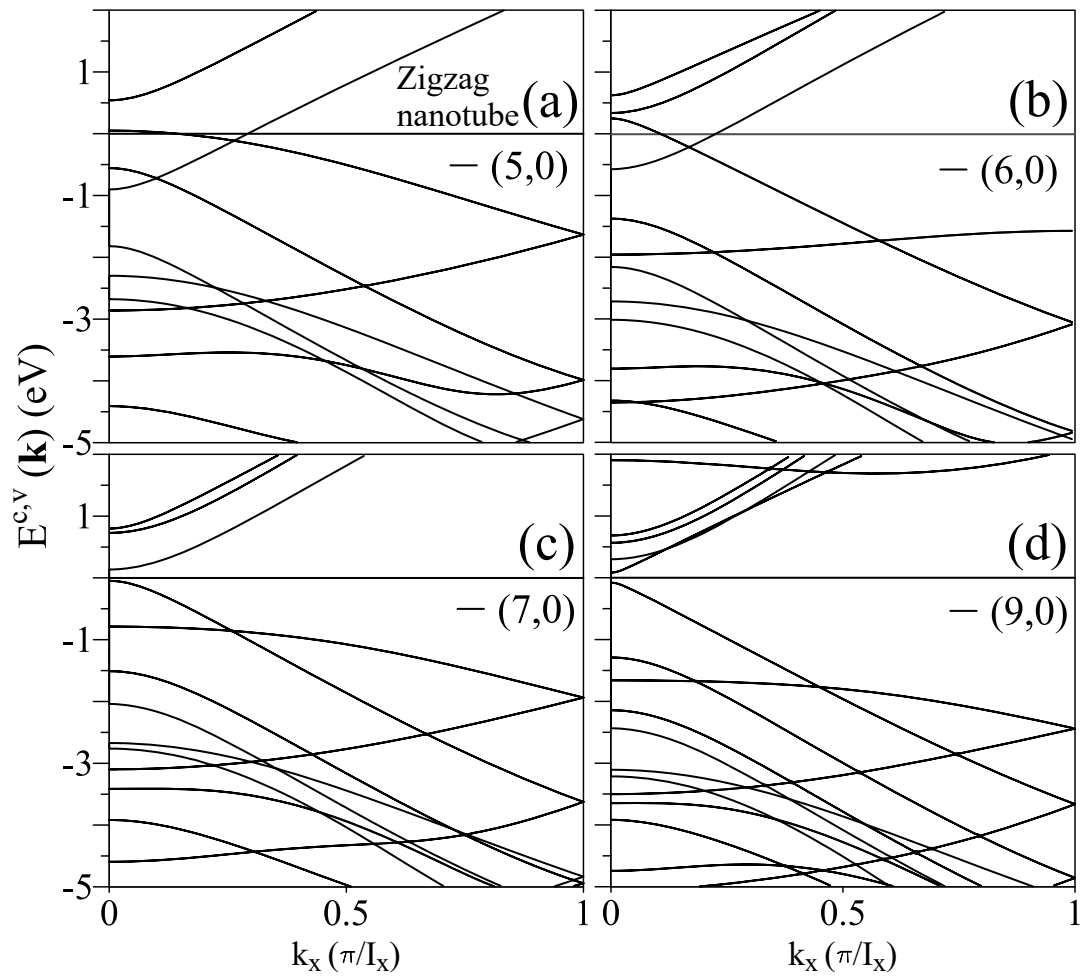


Figure 21: Electronic structures for zigzag nanotubes: (a) (5,0), (b) (6,0), (c) (7,0) and (d) (9,0).

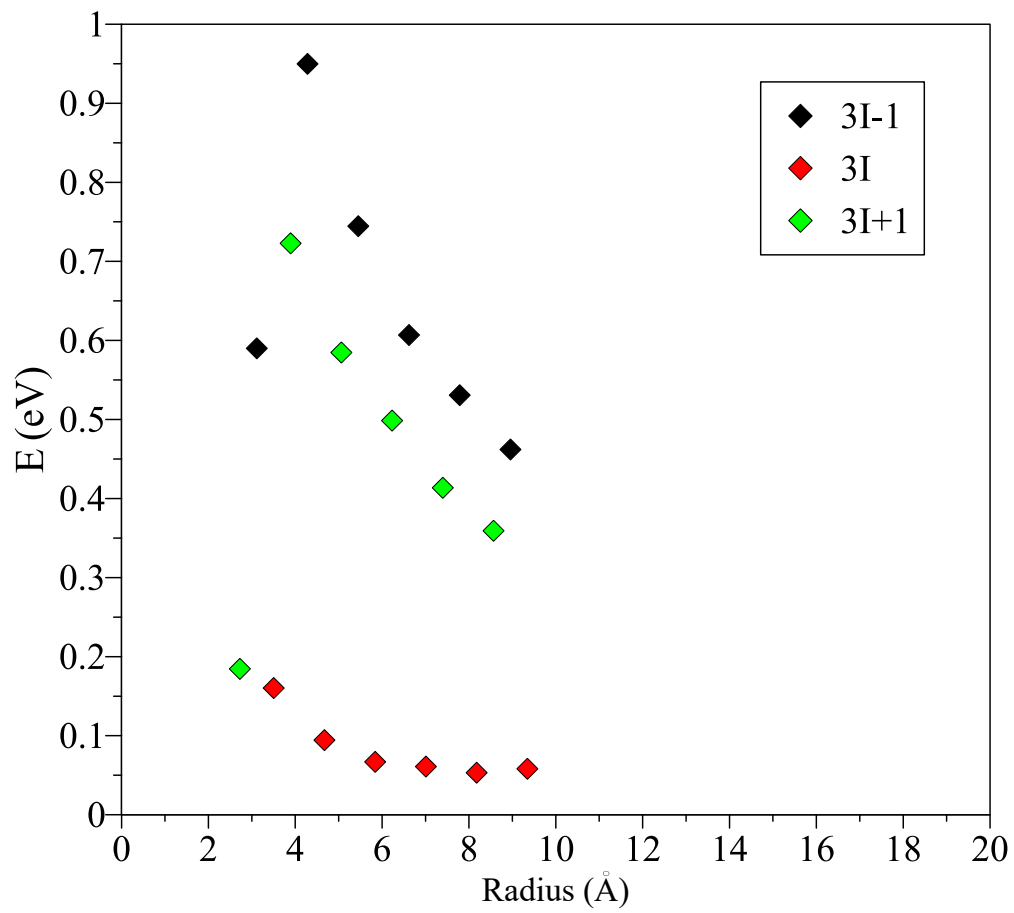


Figure 22: Energy gaps of zigzag carbon nanotubes including $(3I,0)$, $(3I + 1,0)$ and $(3I + 2,0)$.

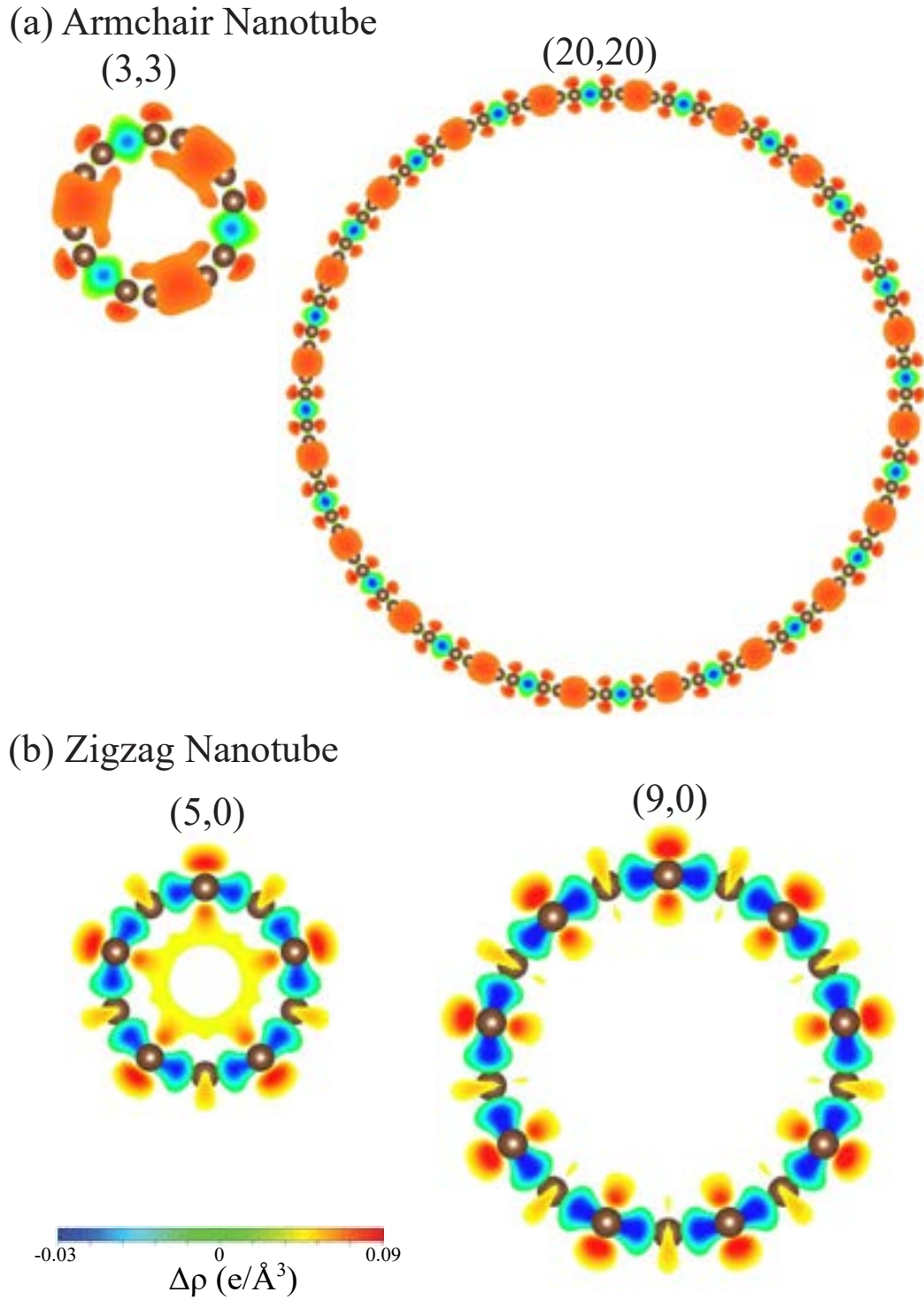


Figure 23: The spatial charge distributions for (a) (3,3) & (20,20) armchair nanotubes, and (b) (5,0) & (9,0) zigzag systems.

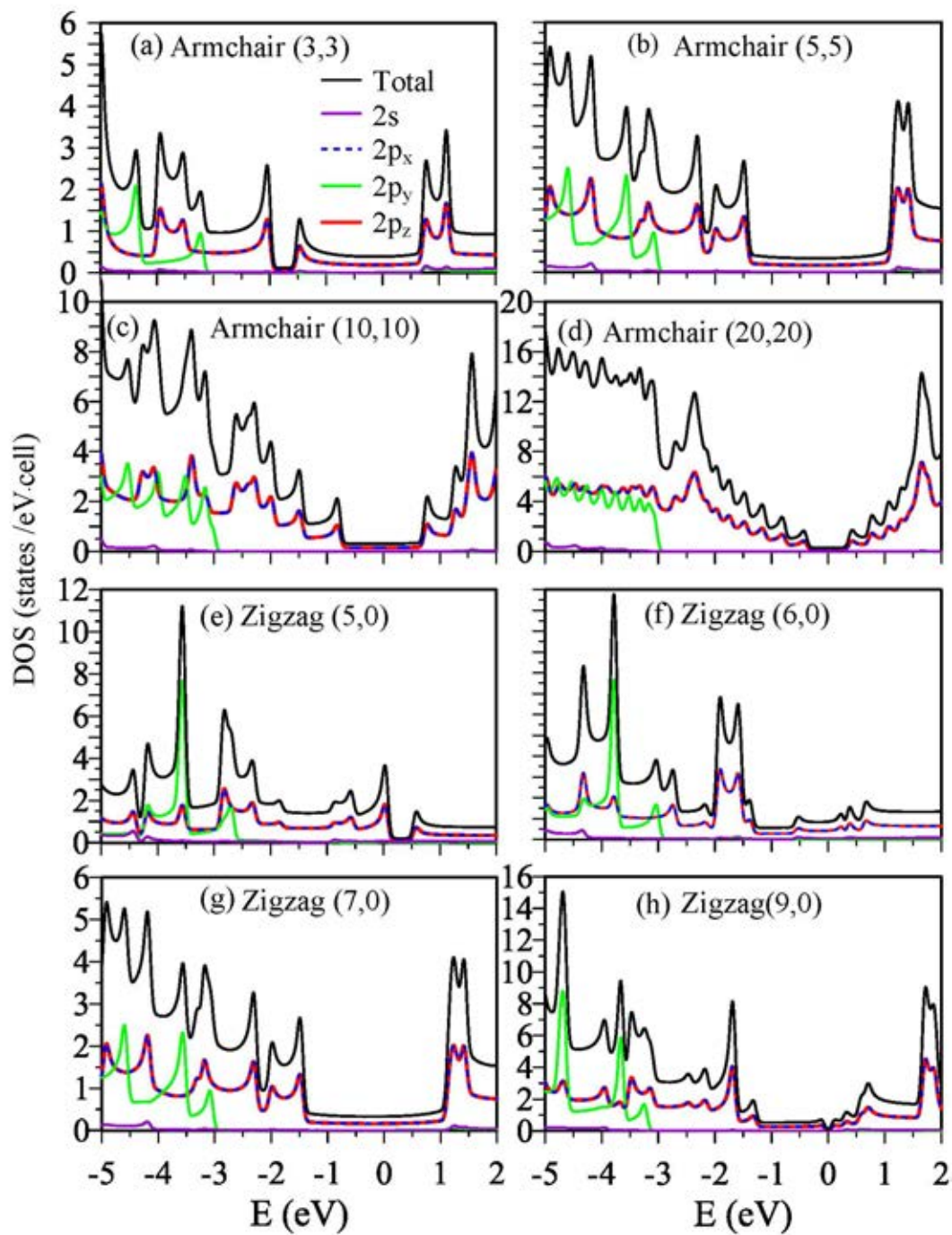


Figure 24: The total and orbital-projected DOSs for (a) (3,3), (b) (5,5), (c) (10,10), (d) (20,20). (e) (5,0), (f) (6,0), (g) (7,0) and (h) (9,0) nanotubes.

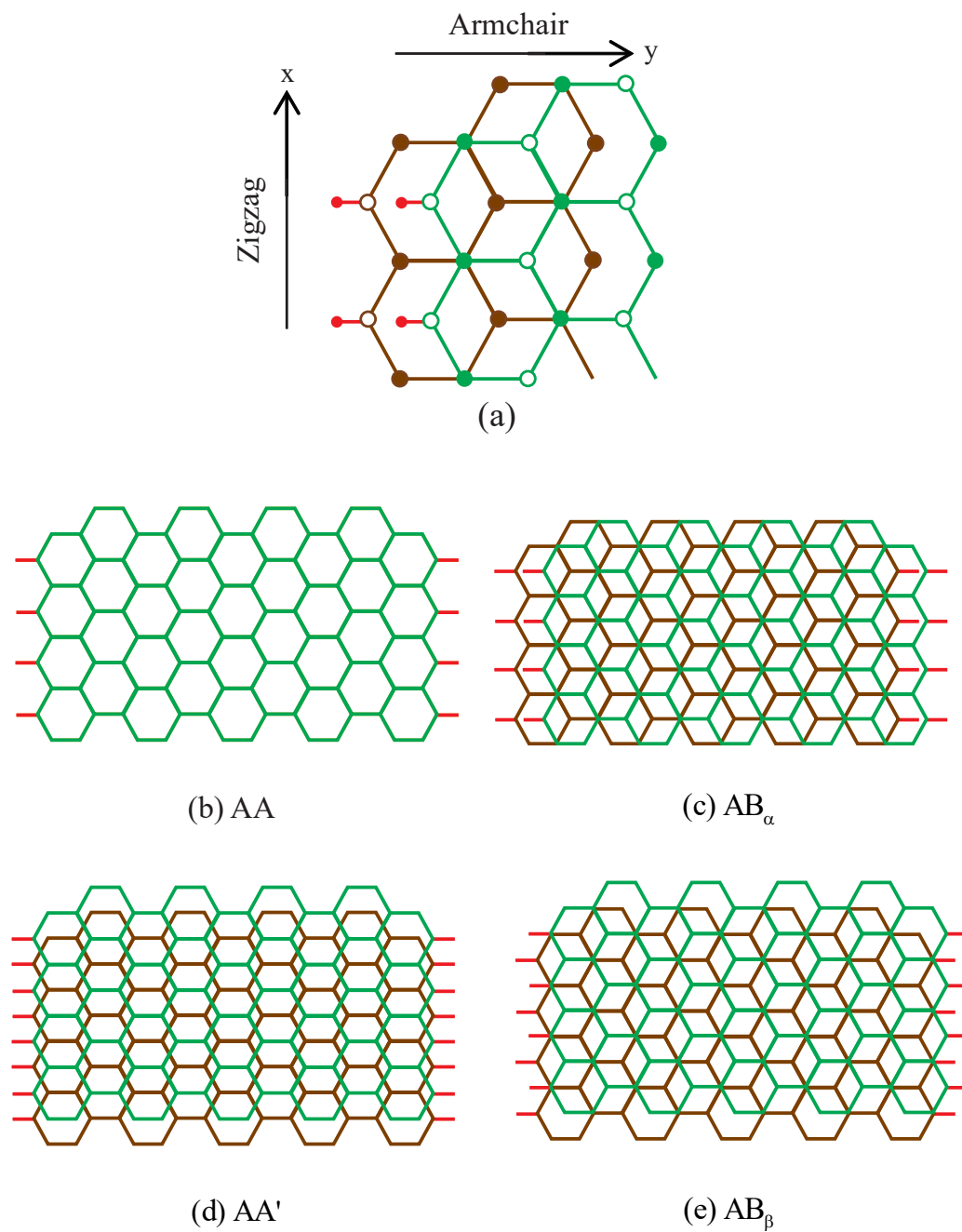


Figure 25: Geometric structures of bilayer zigzag graphene nanoribbons: (a) the relative displacement between the upper and lower layers along the armchair direction, (b) AA, (c) AB_α , (d) AA' and (e) AB_β stackings.

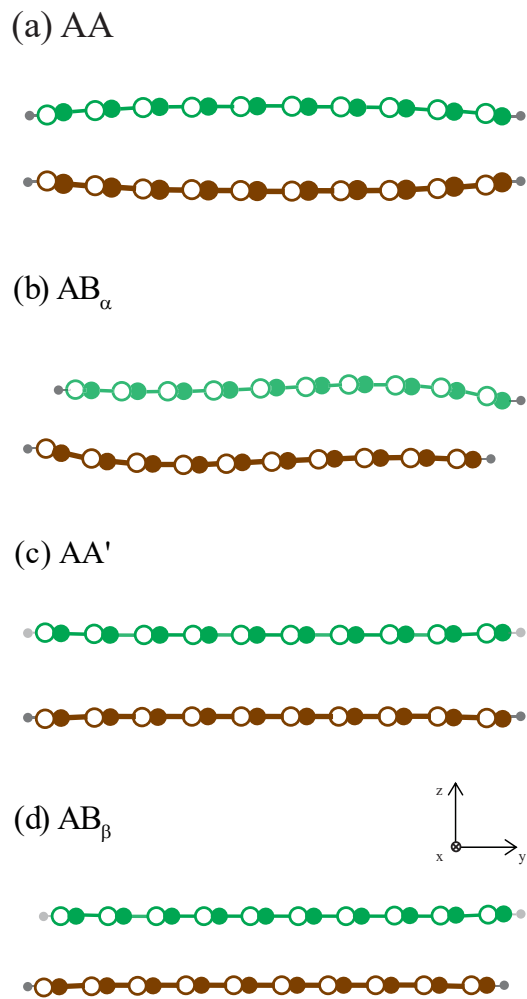


Figure 26: Optimal structures of bilayer zigzag graphene nanoribbons in the side view for (a) AA, (b) AB_α , (c) AA' and (d) AB_β stackings with width of $N_Z = 10$.

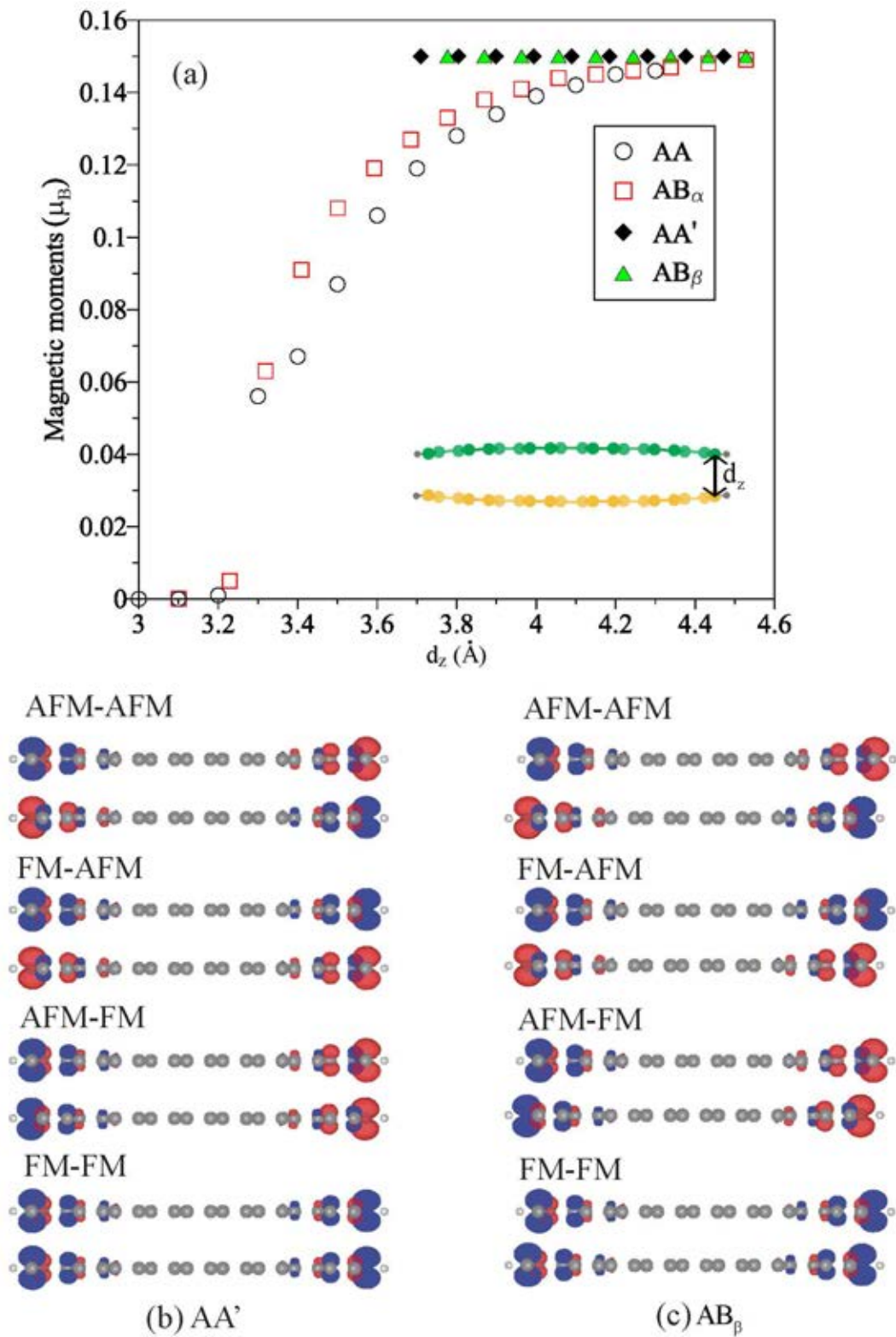


Figure 27: Dependence of the magnetic moment on the inter-edge distance for AA, AB_α , AA' and AB_β stackings with width of $N_Z = 10$.

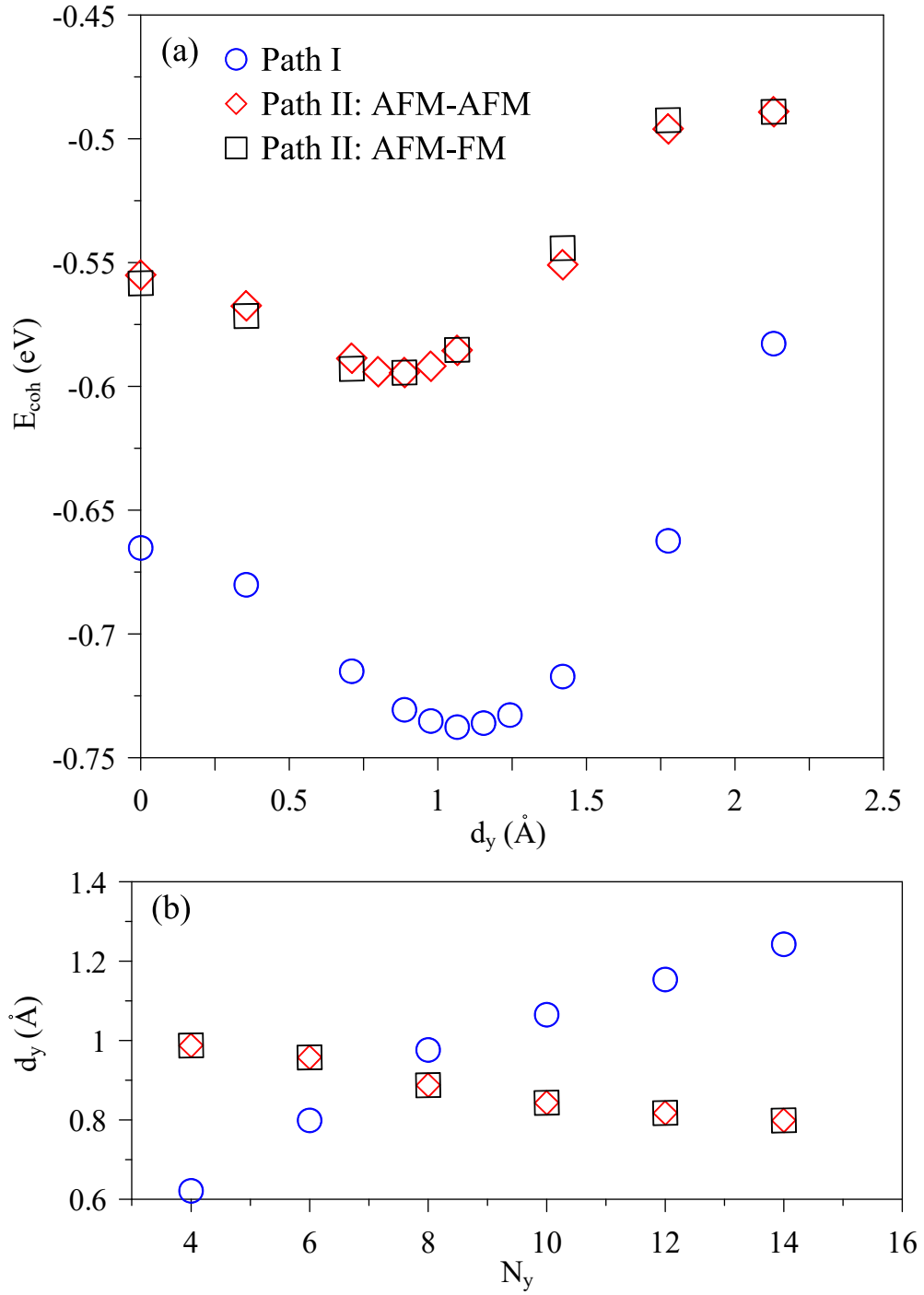


Figure 28: (a) The shift-dependent cohesive energy for the $N_Z = 10$ bilayer zigzag system along $AA \rightarrow AB_\alpha$ and $AA' \rightarrow AB_\beta$, and (b) the dependence of the critical shift on the nanoribbon width.

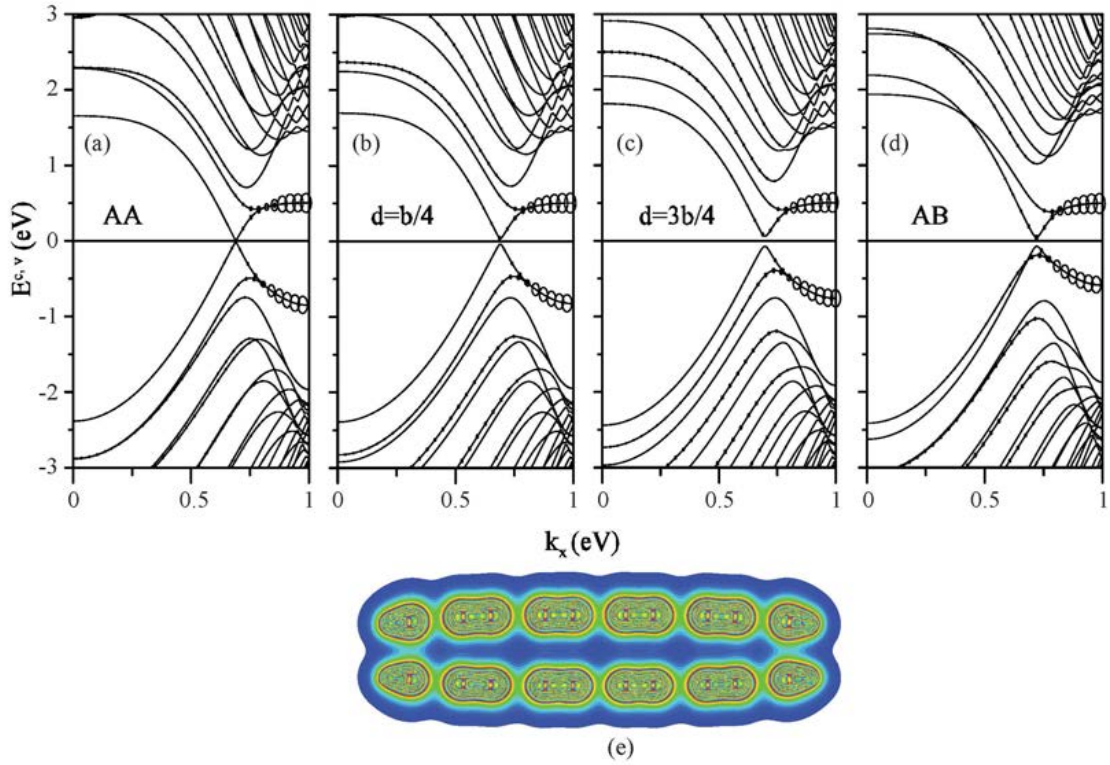


Figure 29: Band structures of $N_Z = 10$ bilayer zigzag nanoribbons under the shifts along Path I: (a) $d_y = 0$, (b) $b/4$, (c) $b/2$ and (d) b . Also shown are the spatial charge densities for (e) $d_y = 0$ and (f) b (?). Band structures of $N_y = 10$ for (a) AA: AFM-AFM, (b)

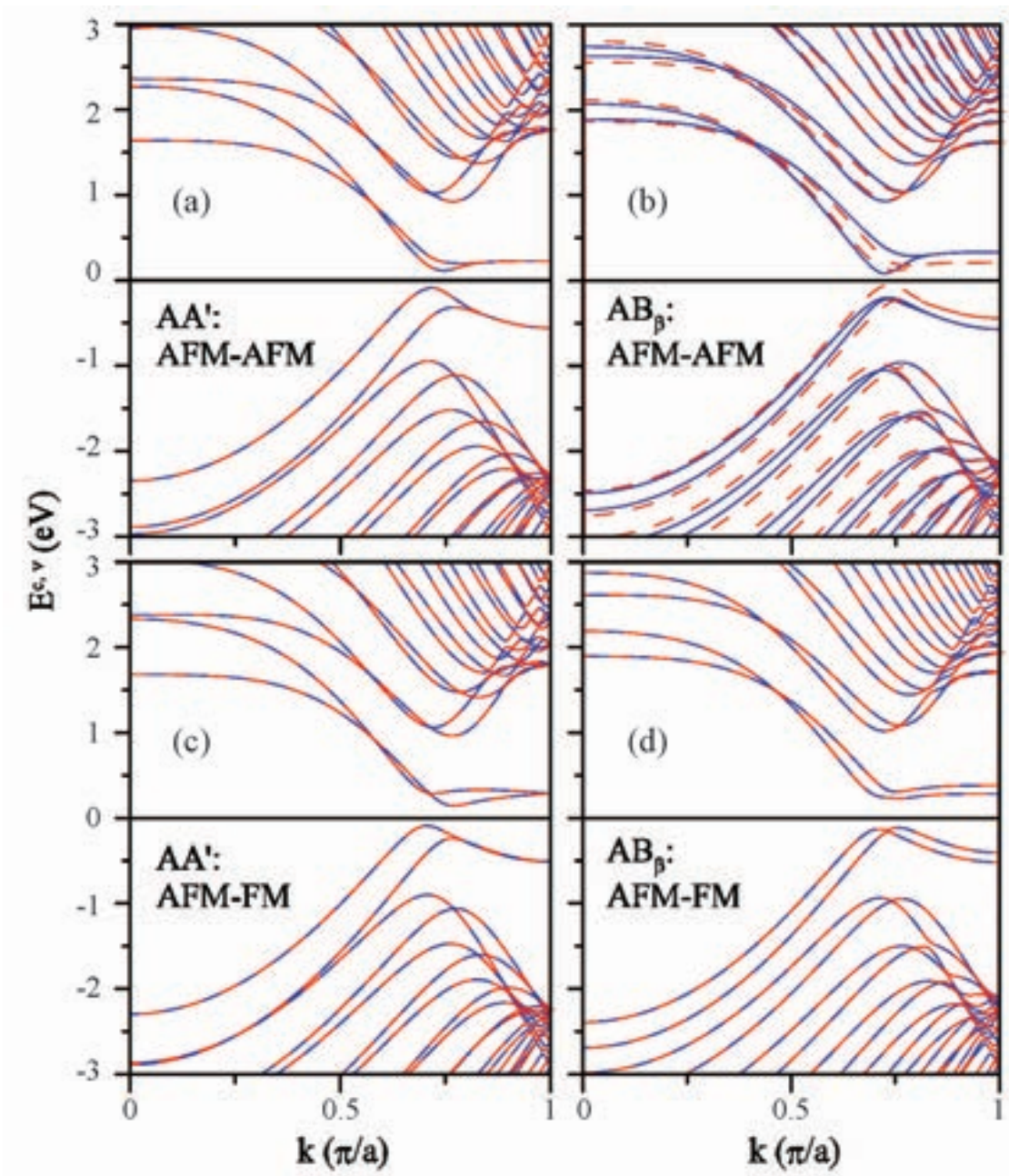


Figure 30: Same plot as Fig. 5, but shown for (a) AA' stacking with AFM-AFM, (b) AB_β stacking with AFM-AFM, (c) AA' stacking with AFM-FM; (d) AB_β stacking with AFM-FM. The spin-up and spin-down states are indicated by the red dashed and blue solid curves, respectively.

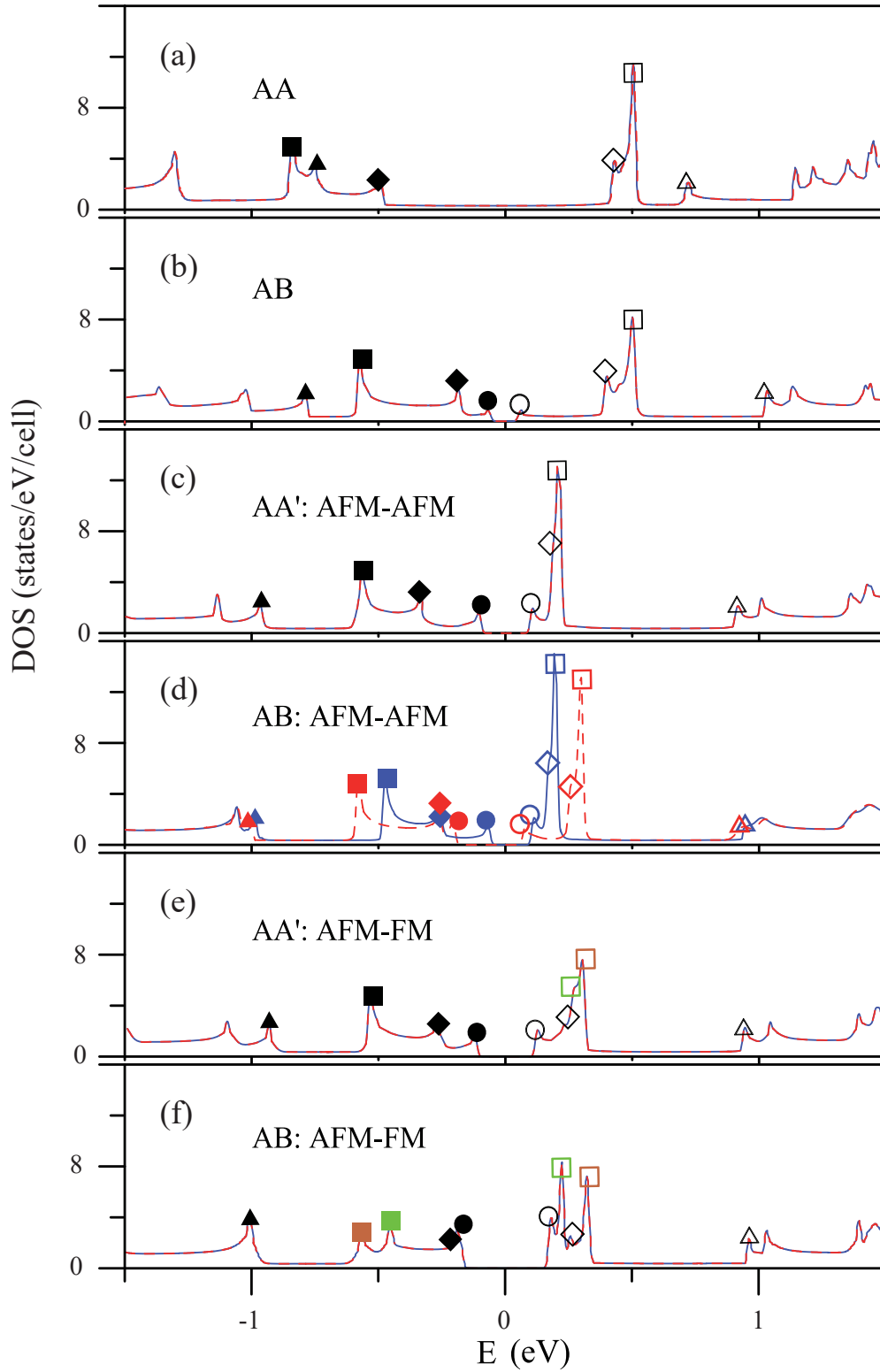


Figure 31: The stacking-dependent DOSs of the $N_Z = 10$ bilayer zigzag nanoribbons for (a) AA, (b) AB_α , (c) AA' with AFM-AFM, (d) AB with AFM-AFM, (e) AA' with AFM-FM; (f) AB_β with AFM-FM (colors of squares should be black in Carbon).

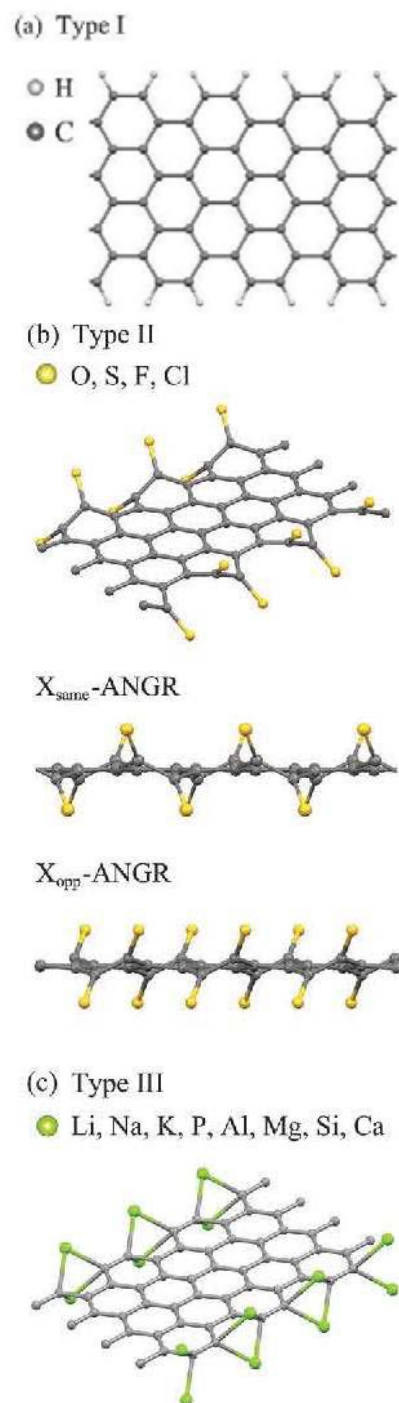


Figure 32: Geometric structures of (a) type-I, (b) type-II and (c) type-III edge-decorated graphene nanoribbons.

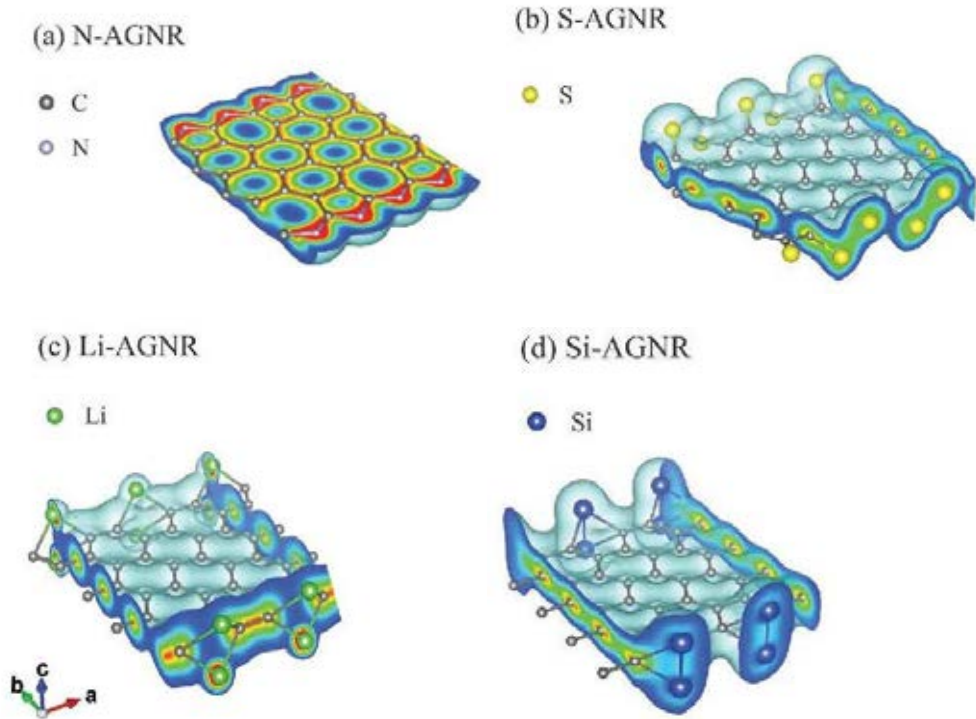


Figure 33: The spatial charge densities for (a) N-, (b) S-, (c) Li- and P-decorated $N_A = 8$ armchair nanoribbons.

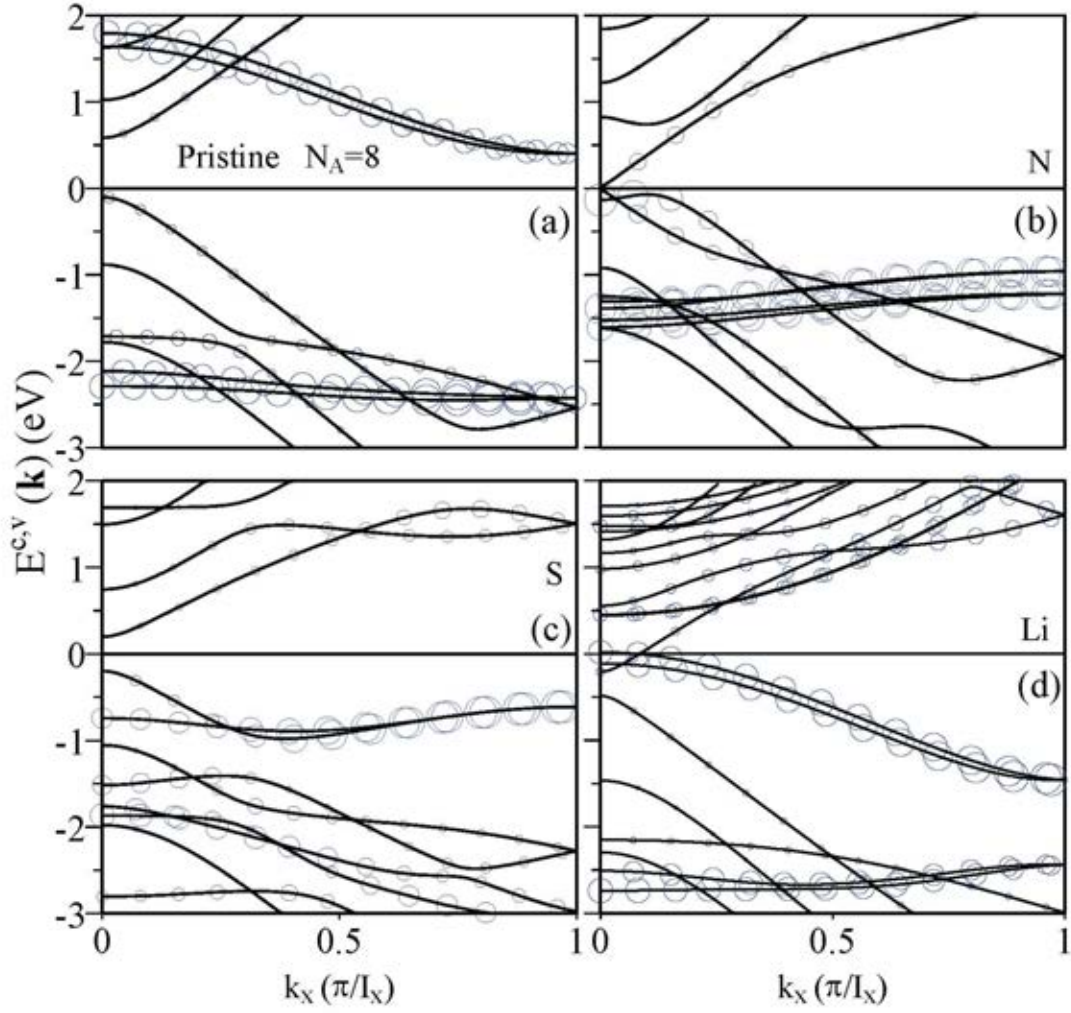


Figure 34: Energy bands of (a) pristine, (b) N-, (c) S-, and (d) Li-decorated $N_A = 8$ armchair nanoribbons, in which the contributions from the nonpassivated edge carbon atoms or the adatoms are denoted by the open circles.

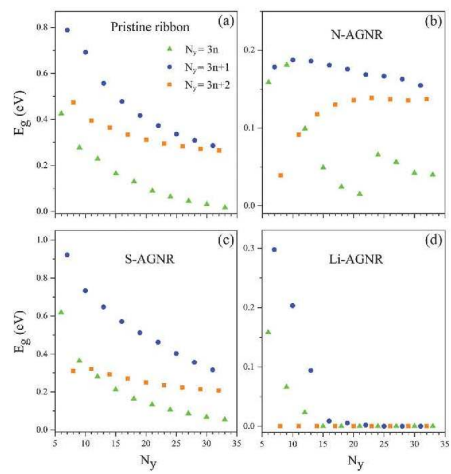


Figure 35: The width-dependent energy gaps for the (a) pristine, (b) N-, (c) S- and (d) Li-decorated armchair nanoribbons.

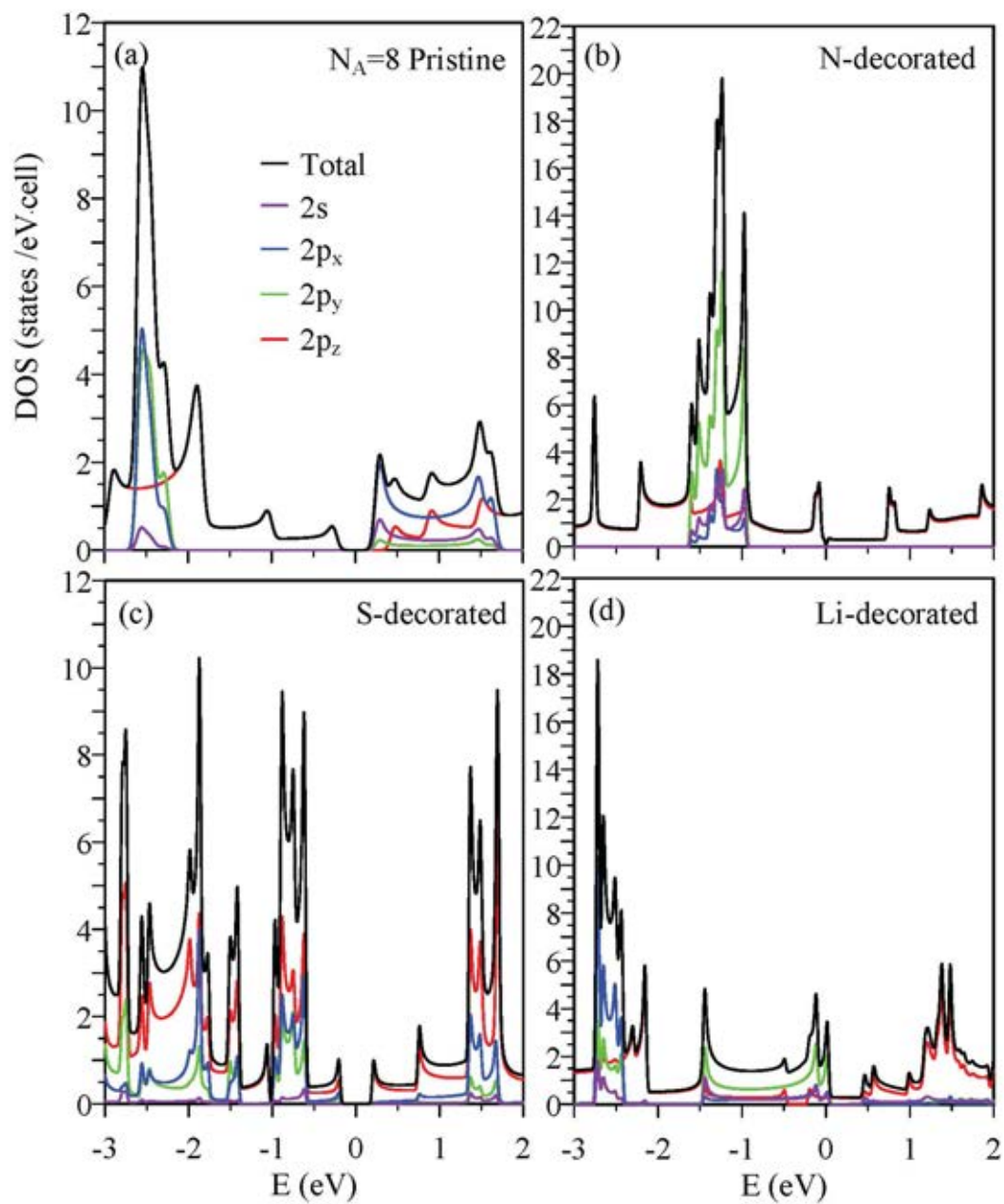


Figure 36: DOSs of the (a) pristine, (b) N-, (c) S- and Li-decorated $N_A = 8$ armchair nanoribbons. Also shown are the orbital-projected components due to the carbon atoms. The symmetric peaks are denoted by the red circles.

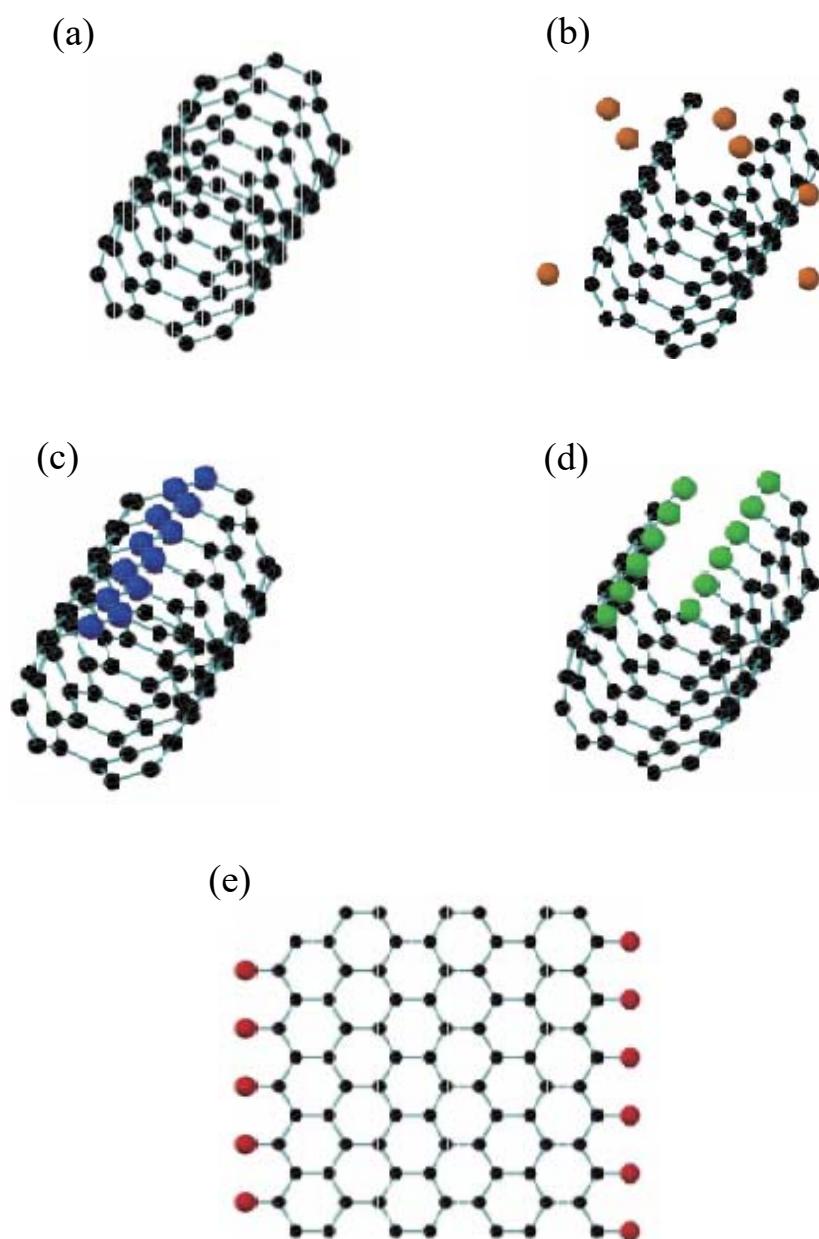


Figure 37: Geometric structures: (a) A single-walled armchair carbon nanotube as a starting material, (b) an unzipped nanotube in an environment of decorating adatoms, (c) type-I, (d) type-II, and (e) type-III adatom-decorated nanotube/nanoribbon-related systems.

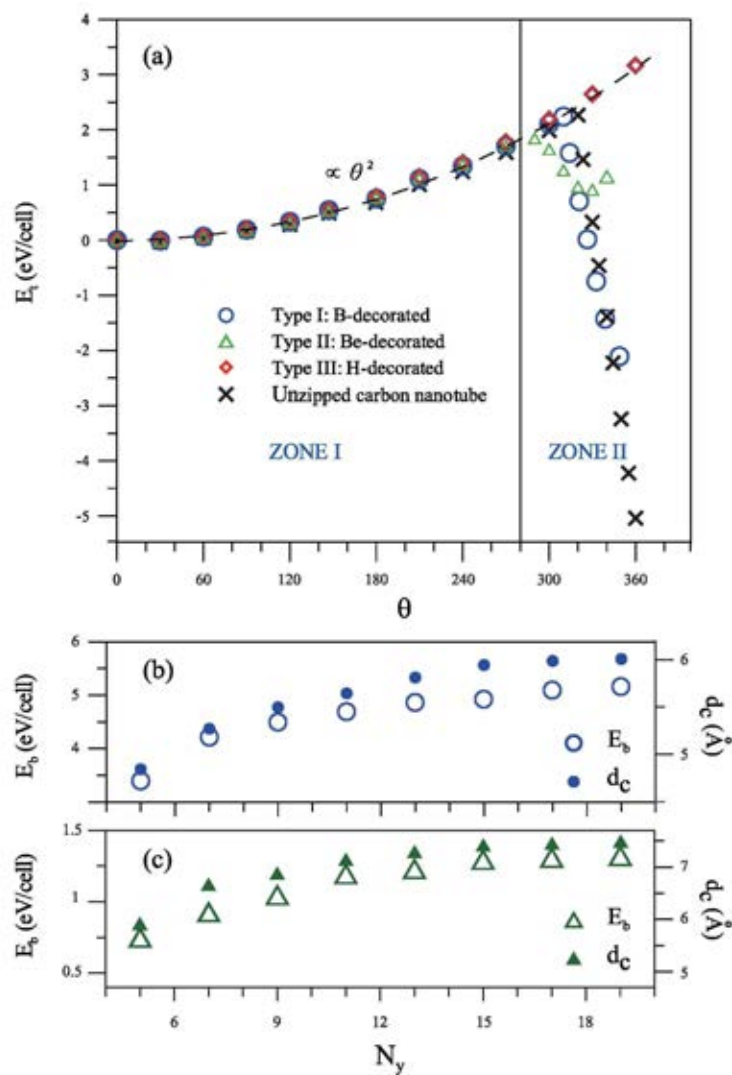


Figure 38: (a) The arc-angle-dependent total energies, measured from those at $\phi = 0^\circ$, for the B-, Be- and H-decorated $N_Z = 7$ armchair nanoribbons, as well as an unzipped carbon nanotube. The width dependence of the critical interaction distance and the energy barrier in (b) type-I and (c) type-II adatom-decorated systems.

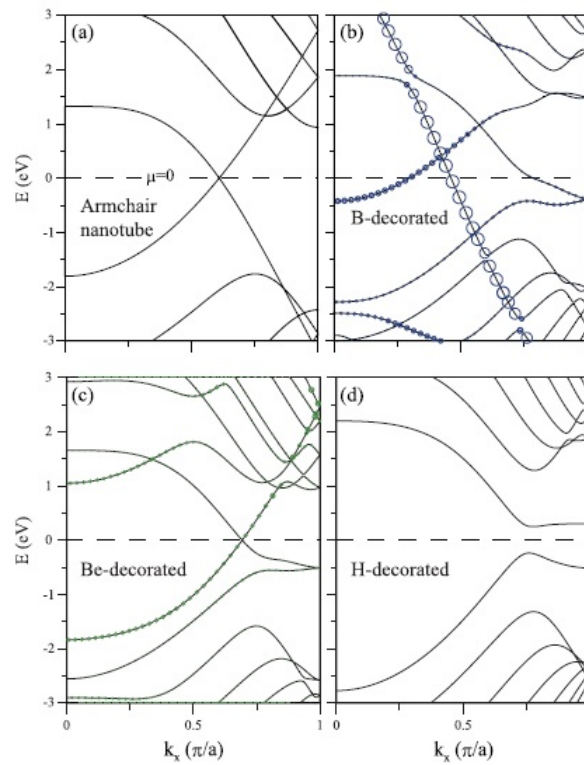


Figure 39: Band structures for (a) (4,4) armchair nanotube, (b) B-, (c) Be- and H-decorated $N_Z = 7$ systems, in which the adatom contributions are represented by the circle radii.

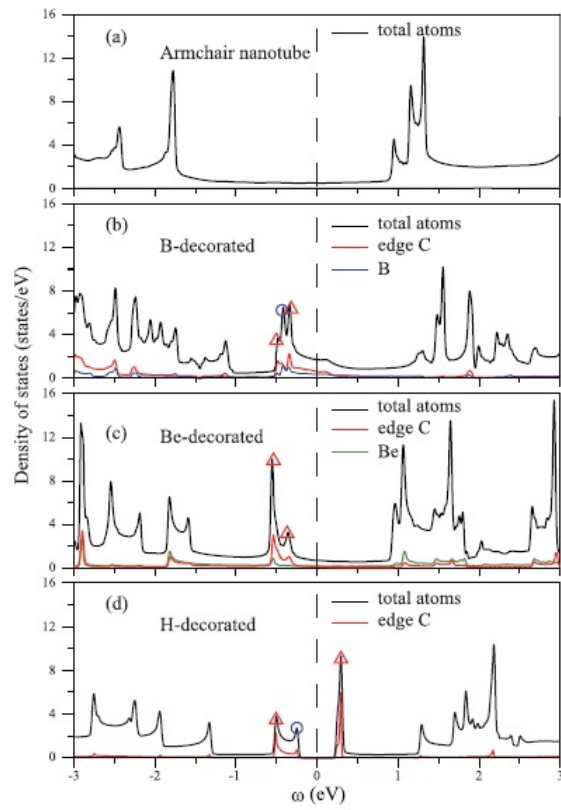
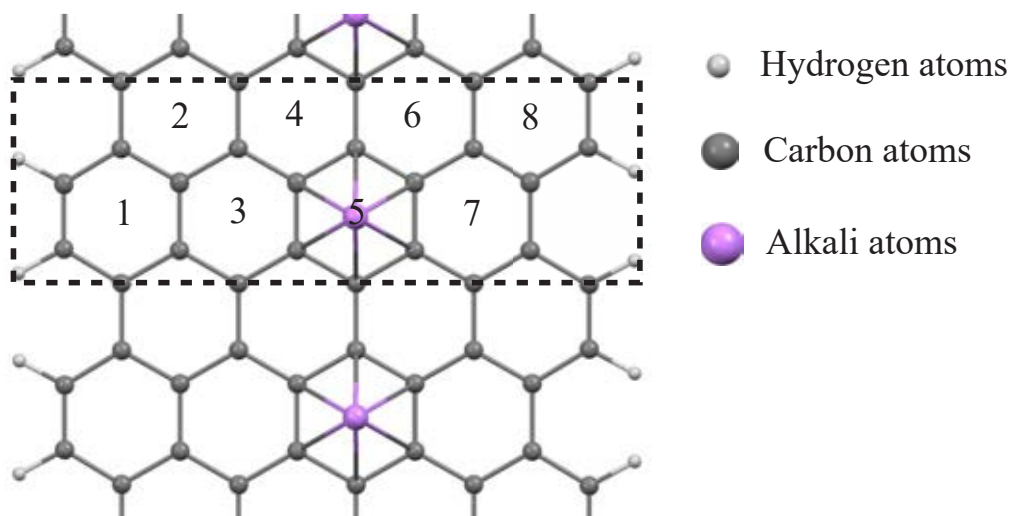


Figure 40: DOSs and local DOSs due to adatoms and edge carbons for (a) (4,4) armchair carbon nanotube, (b) B-, (c) Be- and (d) H-decorated $N_Z = 7$ zigzag nanoribbons.

(a) Armchair GNR $N_A=10$



(b) Zigzag GNR $N_Z=10$

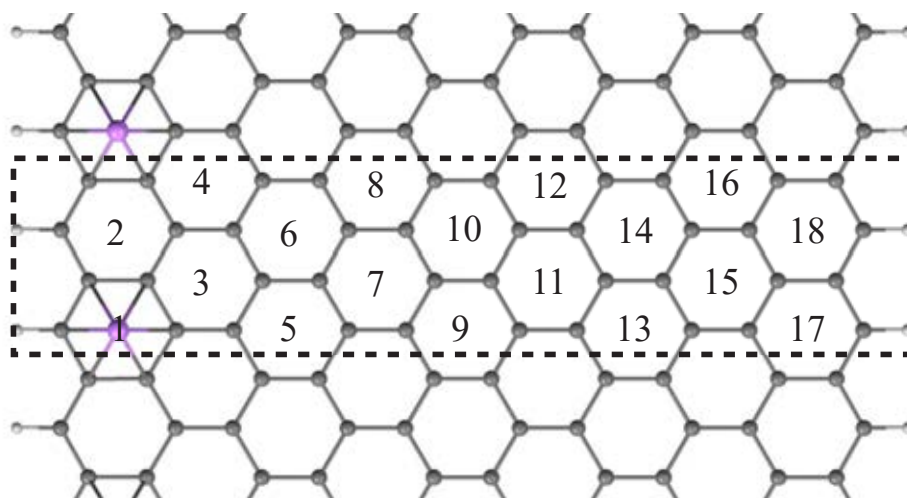


Figure 41: Geometric structures of alkali-adsorbed graphene nanoribbons: (a) $N_A = 10$ armchair and (b) $N_Z = 10$ zigzag systems with unit cells enclosed by the dashed rectangles. The grey, white and purple balls, respectively, represent carbon, hydrogen and alkali atoms.

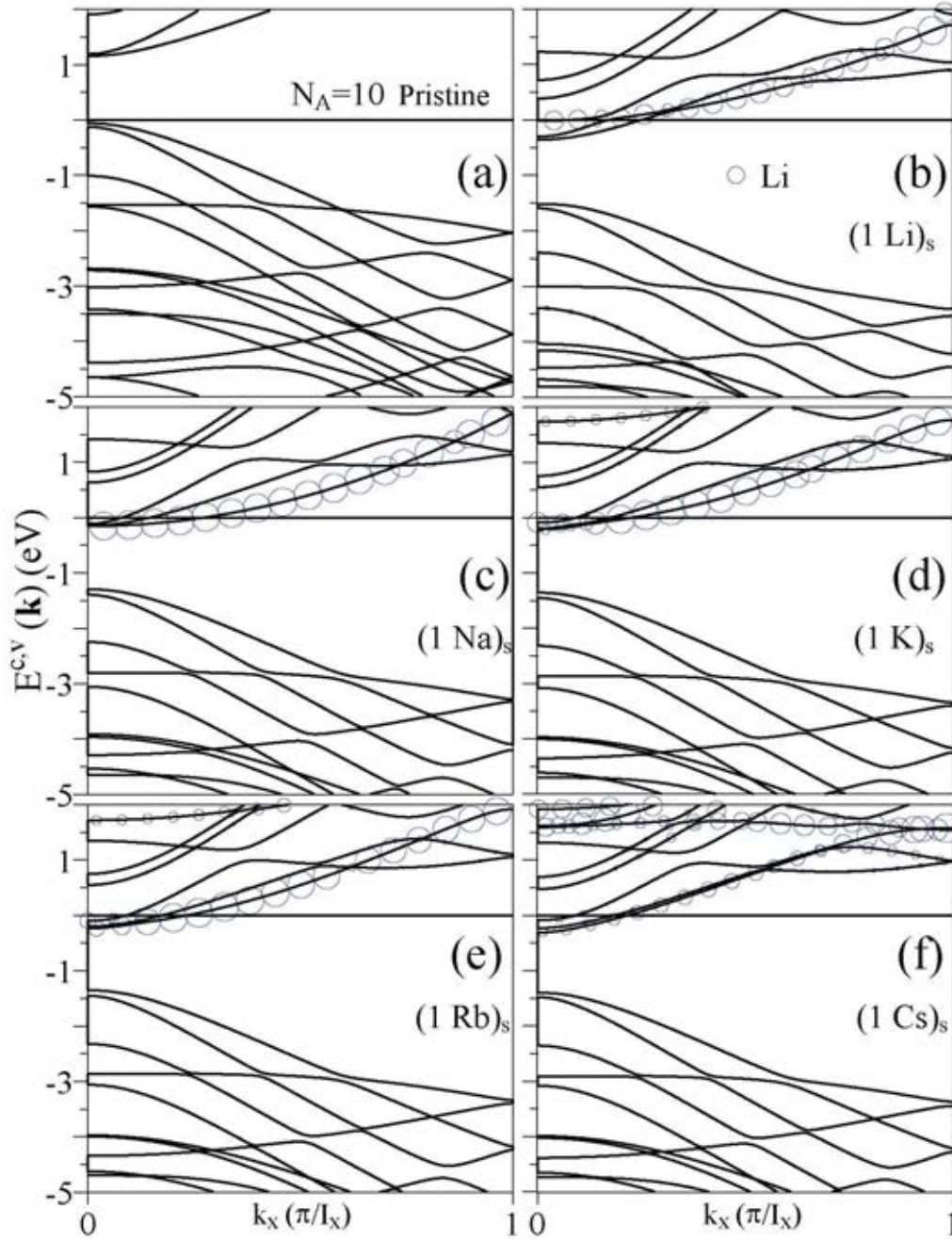


Figure 42: Band structures of $N_A = 10$ armchair graphene nanoribbons with hydrogen passivation for (a) pristine system and (b) Li-, (c) Na-, (d) K-, (e) Rb- and (f) Cs-adsorbed ones. Only one adatom is situated at $(1)_s$.

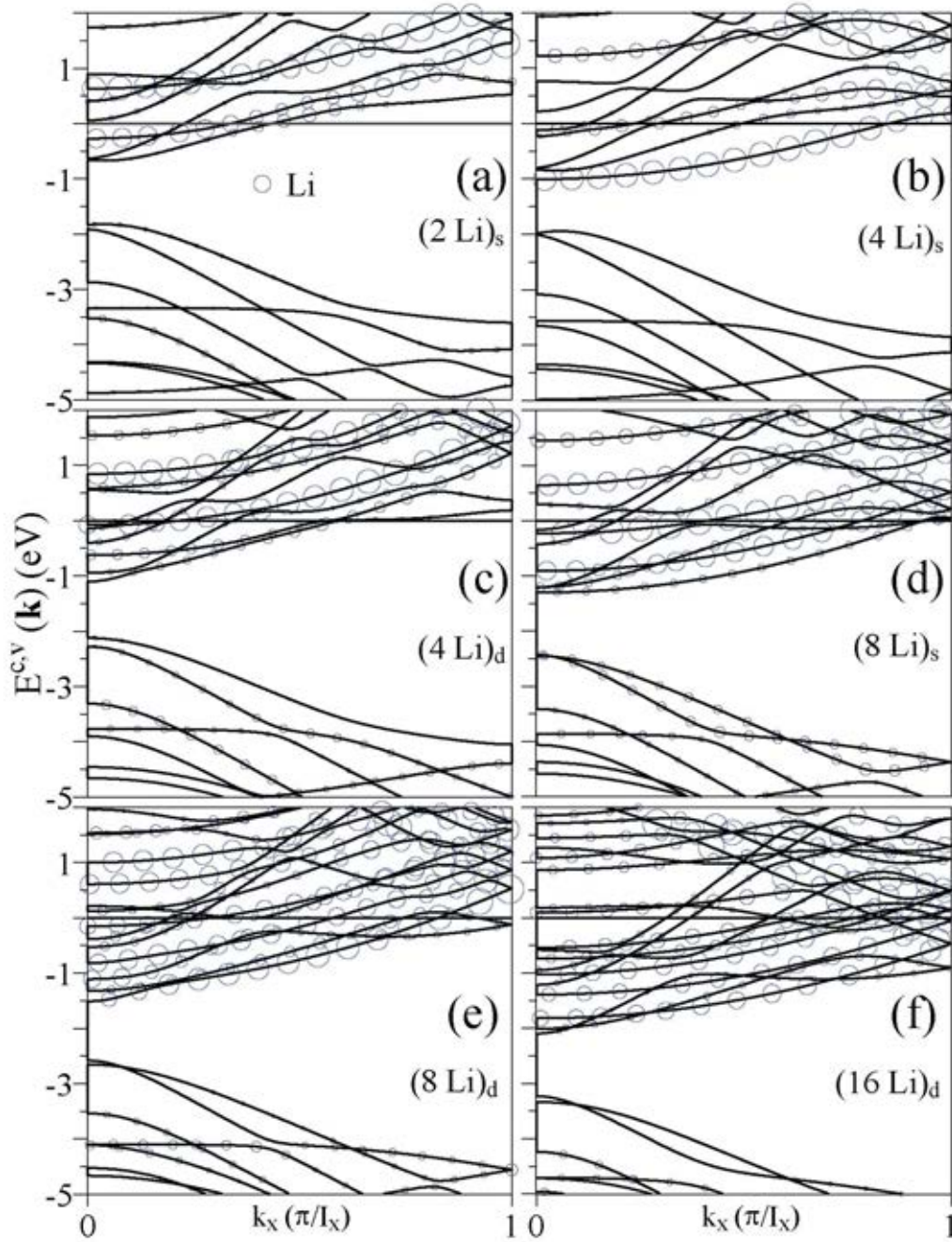


Figure 43: Energy bands of Li-adsorbed $N_A = 10$ armchair graphene nanoribbons under various distributions and concentrations: (a) $(2 \text{ Li})_s$, (b) $(4 \text{ Li})_s$, (c) $(4 \text{ Li})_d$, (d) $(8 \text{ Li})_s$, (e) $(8 \text{ Li})_d$, and (f) $(16 \text{ Li})_d$.

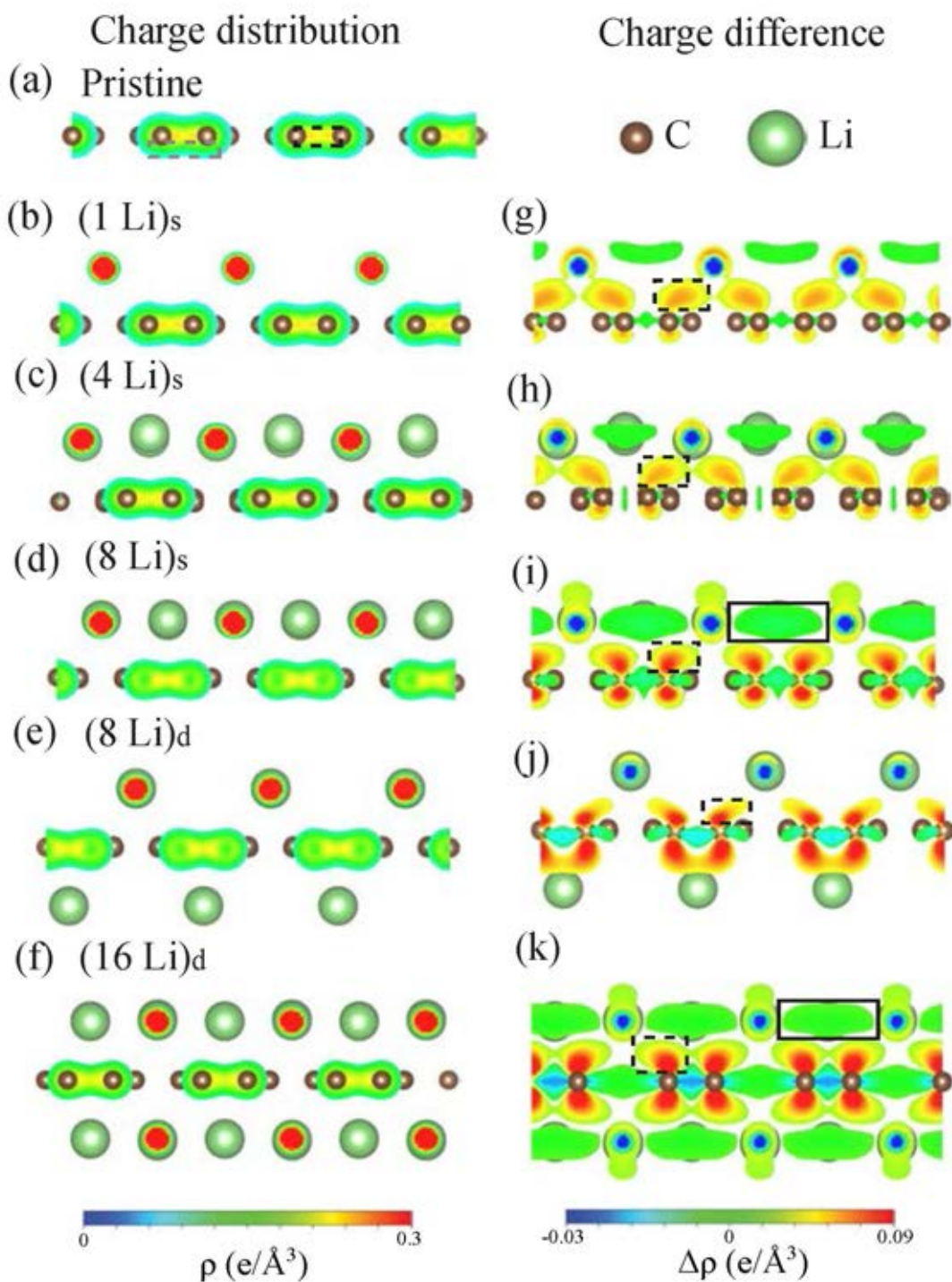


Figure 44: The spatial charge densities of Li-adsorbed $N_A = 10$ armchair nanoribbons under various adatom configurations: (a) pristine, (b) $(1, \text{Li})_s$, (c) $(4, \text{Li})_s$, (d) $(8, \text{Li})_s$; (e) $(8, \text{Li})_d$. The charge density differences, corresponding to (b)-(e), are shown in (g)-(j), respectively. (f) and (k) are those of $N_z = 10$ zigzag system under single adatom adsorption.

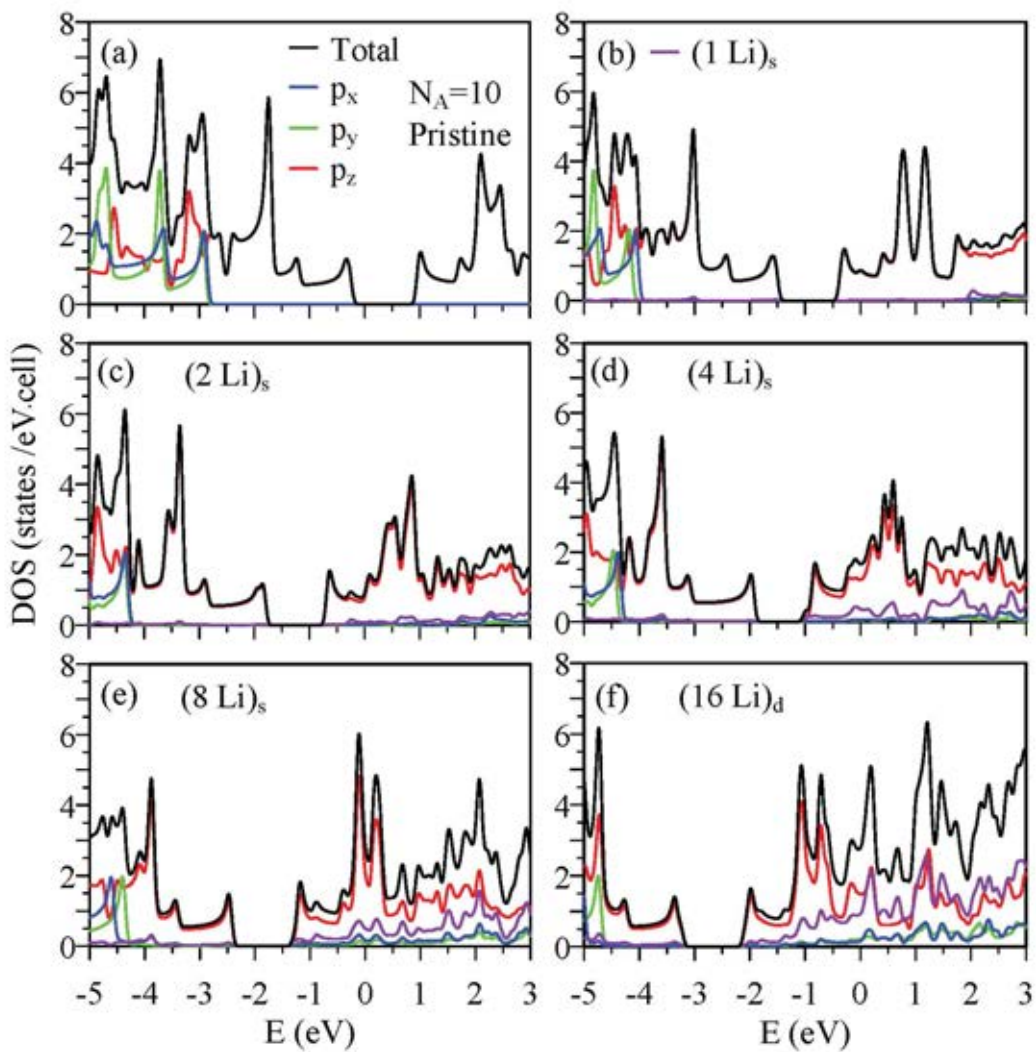


Figure 45: The atom- and orbital-projected DOSs of Li-adsorbed $N_A = 10$ armchair systems under various adatom configurations: (a) pristine, (b) $(1 \text{ Li})_s$, (c) $(2 \text{ Li})_s$, (d) $(4 \text{ Li})_s$, (e) $(8 \text{ Li})_s$; (f) $(16 \text{ Li})_d$.

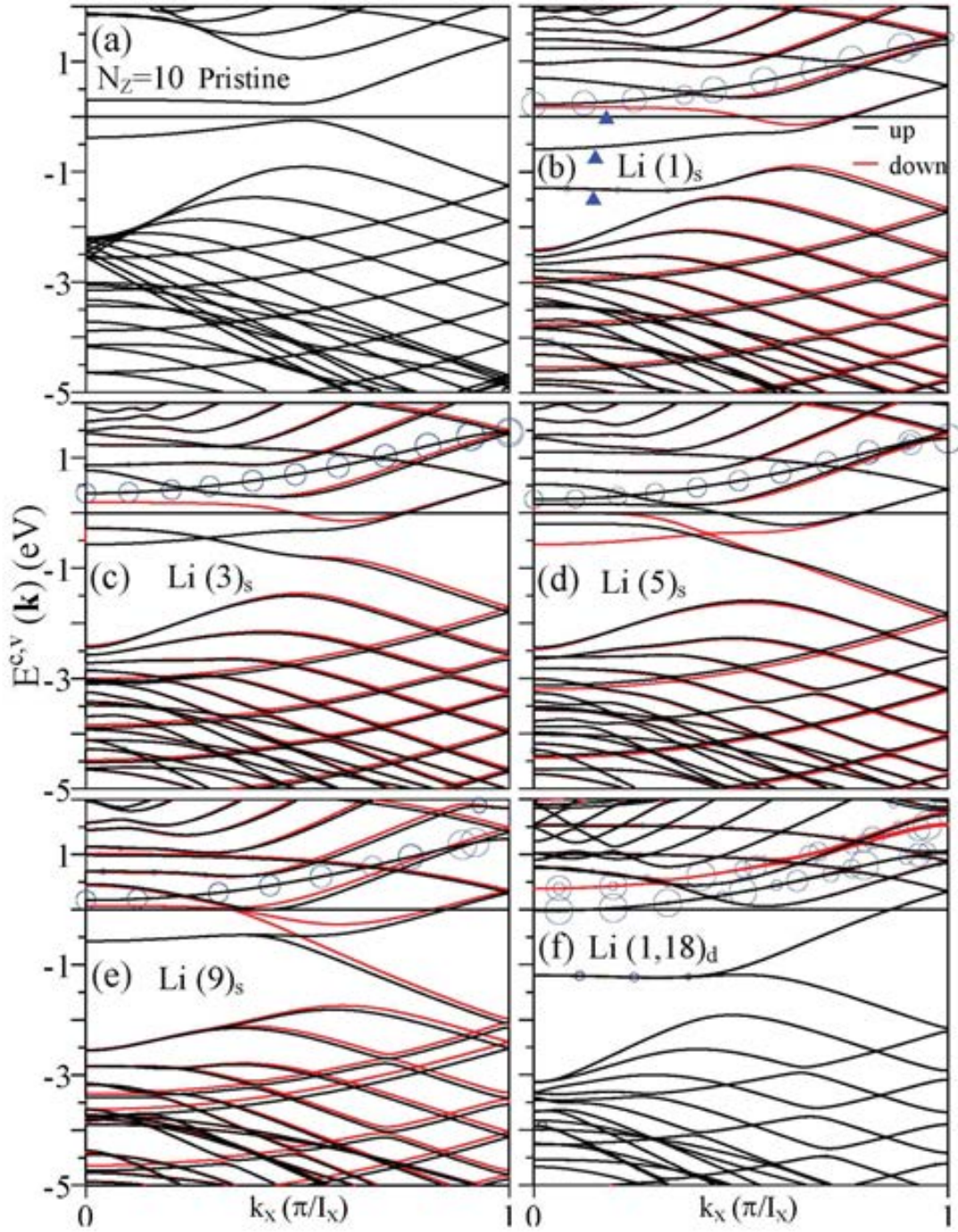


Figure 46: Band structures of $N_z = 10$ Li-adsorbed zigzag graphene nanoribbons for various adatom configurations: (a) pristine, (b) $(1)_s$, (c) $(3)_s$, (d) $(5)_s$, (e) $(9)_s$, and (f) $(1,18)_s$.

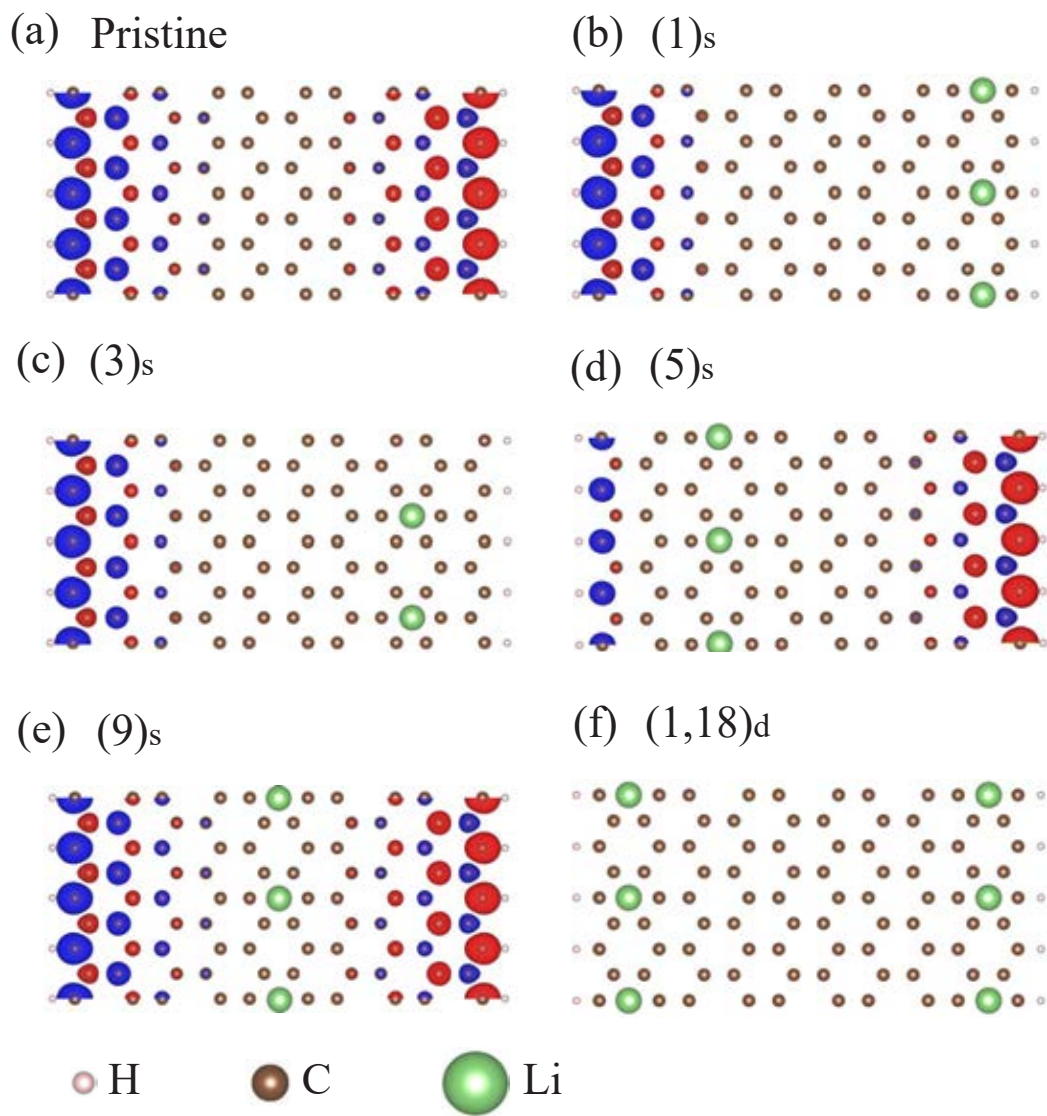


Figure 47: The spatial spin distributions for $N_z = 10$ Li-adsorbed zigzag graphene nanoribbons under various adatom configurations: (a) pristine, (b) $(1)_s$, (c) $(3)_s$, (d) $(5)_s$, (e) $(9)_s$, and (f) $(1,18)_d$.

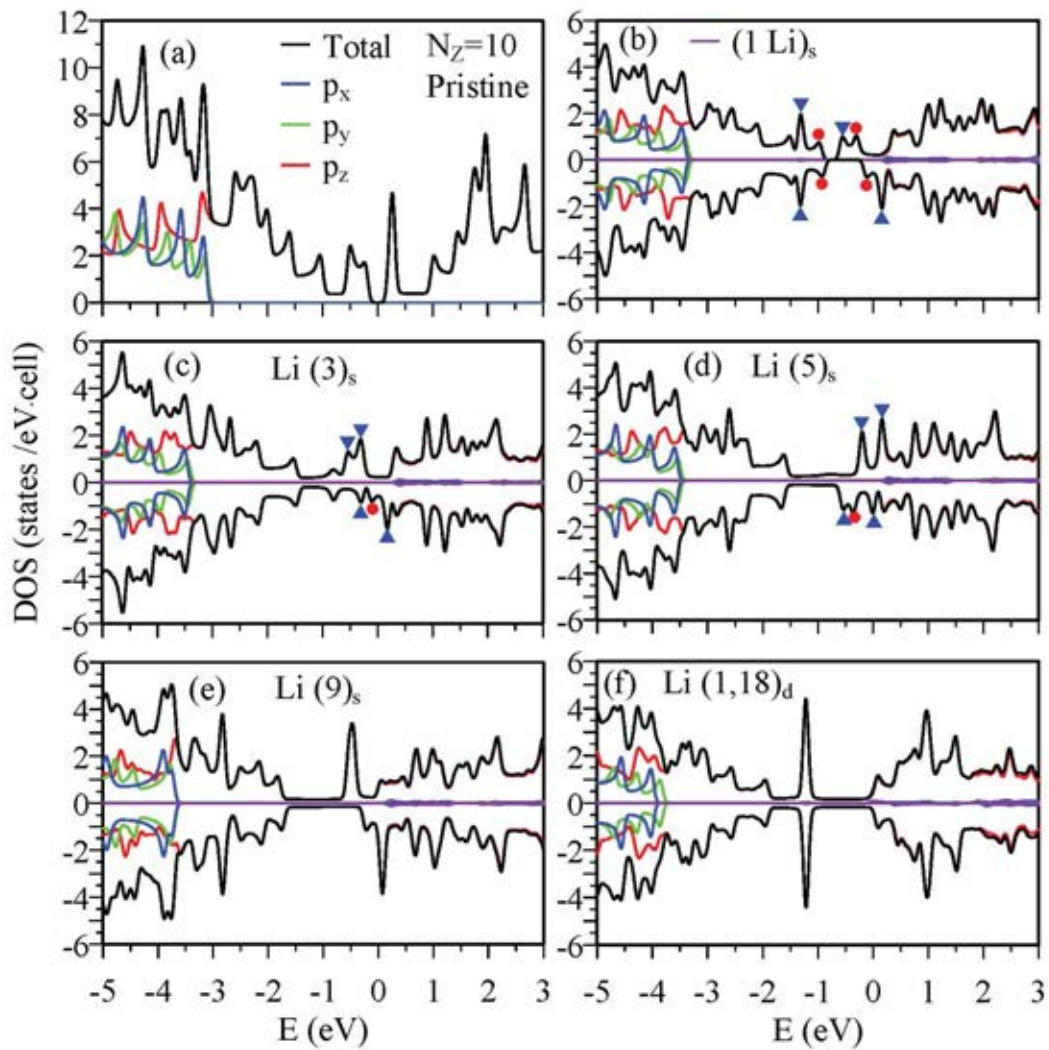
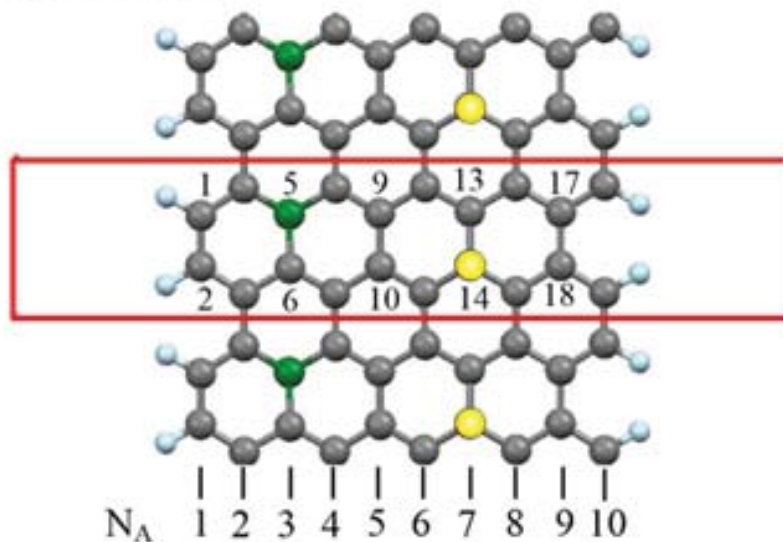


Figure 48: The atom- and orbital-projected DOSs of Li-adsorbed $N_z = 10$ zigzag systems for various adatom configurations: (a) pristine, (b) $(1)_s$, (c) $(3)_s$, (d) $(5)_s$, (e) $(9)_s$, and $(1,18)_s$.

(a) AGNR



(b) ZGNR

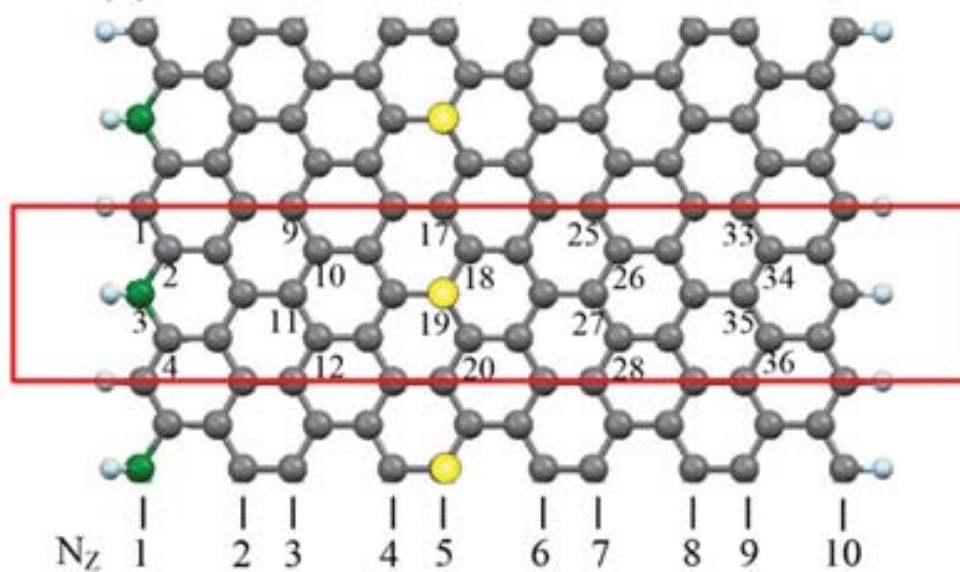


Figure 49: Geometric structures of F-adsorbed GNRs for (a) $N_A = 10$ armchair structure and (b) $N_Z = 10$ zigzag one. The red rectangles represent unit cells. The yellow color represents the F atoms adsorbed on the top side of GNR, whereas the green one means the bottom-side adsorption.

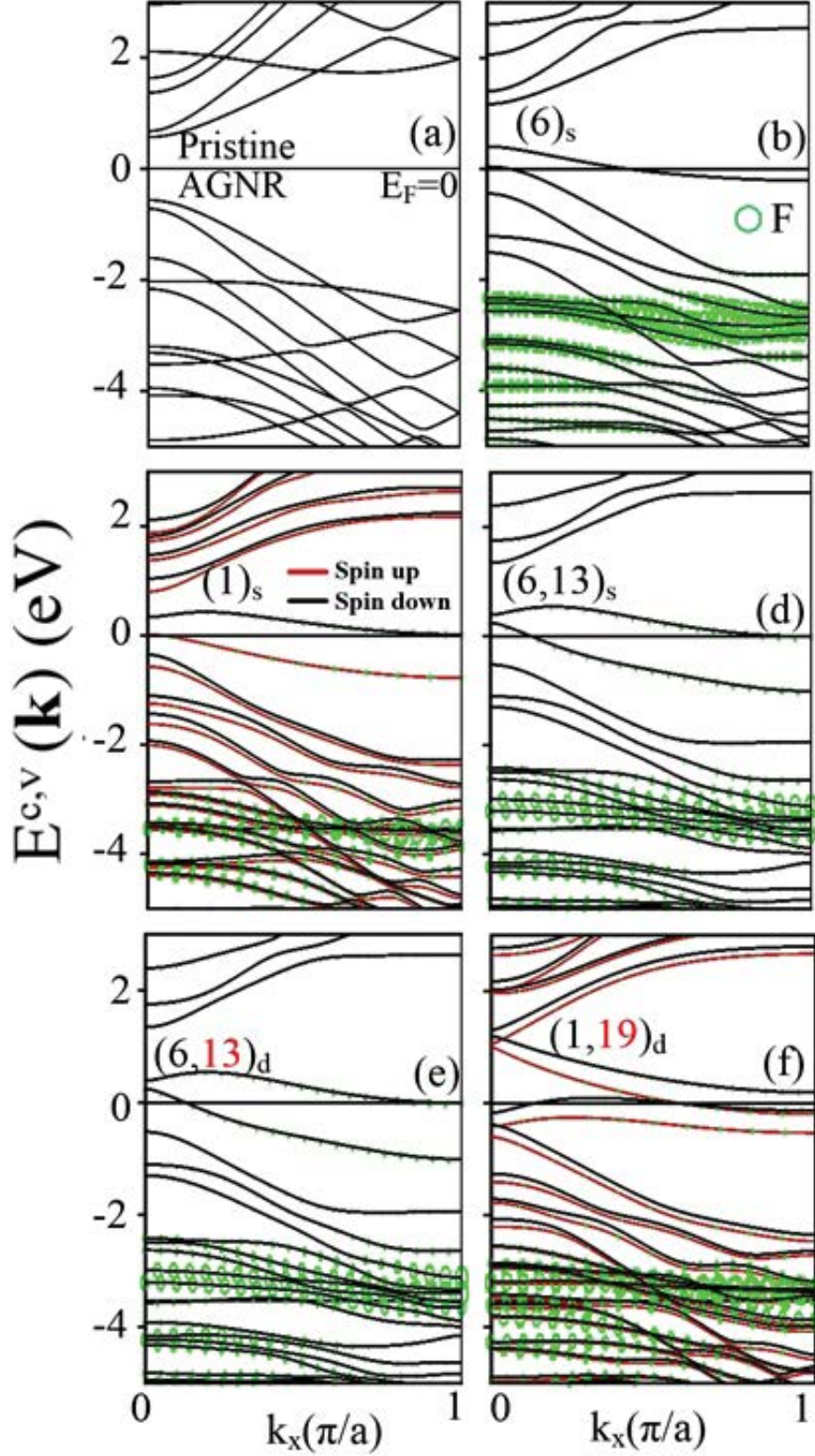


Figure 50: Band structures of $N_A = 10$ AGNR for (a) pristine, (b) $(6)_s$ -, (c) $(1)_s$ -, (d) $(6,13)_s$ -, (e) $(6,13)_d$ -, (f) $(1,20)_d$ -, (g) $(1,6)_d$ -, (h) $(1,6,13,20)_d$ -, (i) $(1,2,5,6)_d$ -, (j) $(8F)_d$ -, (k) $(10F)_d$ -, and (l) $(20F)_d$ -adatom adsorptions. The green circles represent the contribution of F adatoms. The black and red curves denote the spin-split energy bands. The subscripts s and d, respectively, correspond to the single- and double-side adsorptions, while the black and red numbers imply the top and bottom

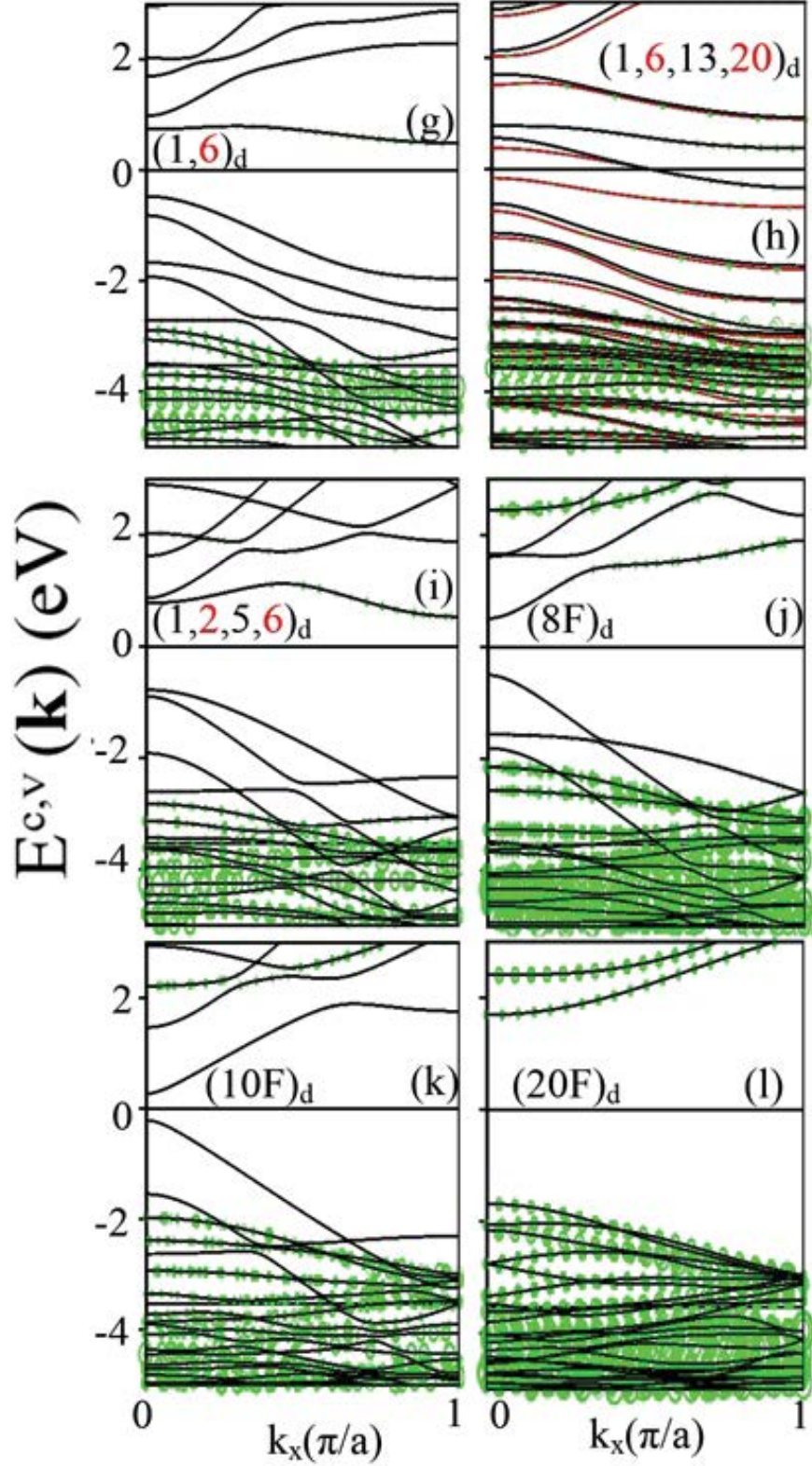


Figure 51: Band structures of $N_A = 10$ AGNR for (a) pristine, (b) $(6)_{s^-}$, (c) $(1)_{s^-}$, (d) $(6,13)_{s^-}$, (e) $(6,13)_{d^-}$, (f) $(1,20)_{d^-}$, (g) $(1,6)_{d^-}$, (h) $(1,6,13,20)_{d^-}$, (i) $(1,2,5,6)_{d^-}$, (j) $(8F)_{d^-}$, (k) $(10F)_{d^-}$, and (l) $(20F)_{d^-}$ -adatom adsorptions. Green circles represent the contribution of F adatoms. The red and black curves denote the spin-split energy bands. The subscripts s and d, respectively, correspond to the single- and double-side adsorptions, while the black and red numbers imply the top and bottom adsorption positions.

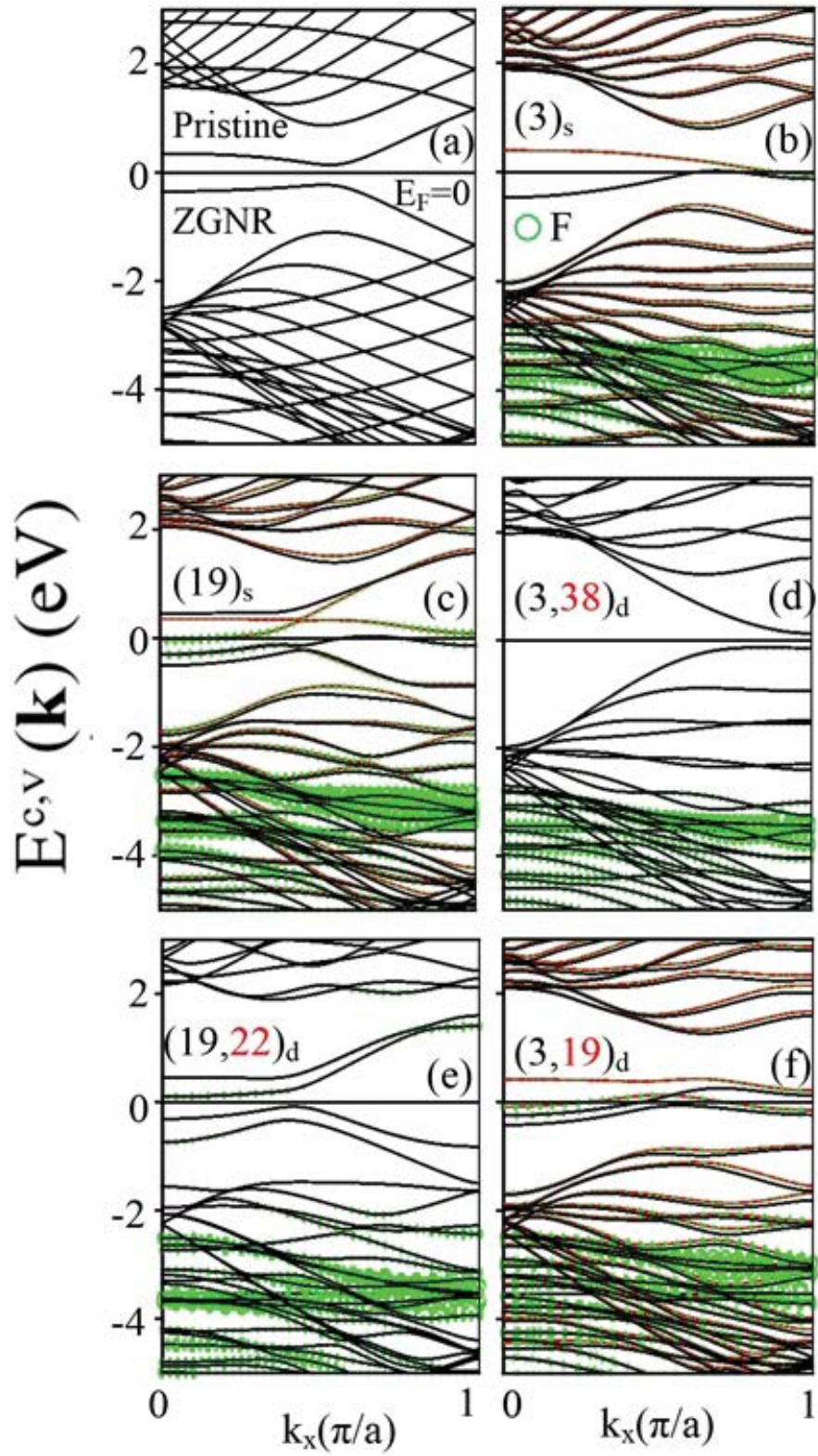


Figure 52: Band structures of $N_Z = 10$ ZGNR for (a) pristine, (b) $(3)_s$, (c) $(19)_s$, (d) $(3,38)_s$, (e) $(19,22)_d$, and (f) $(3,19)_d$ cases.

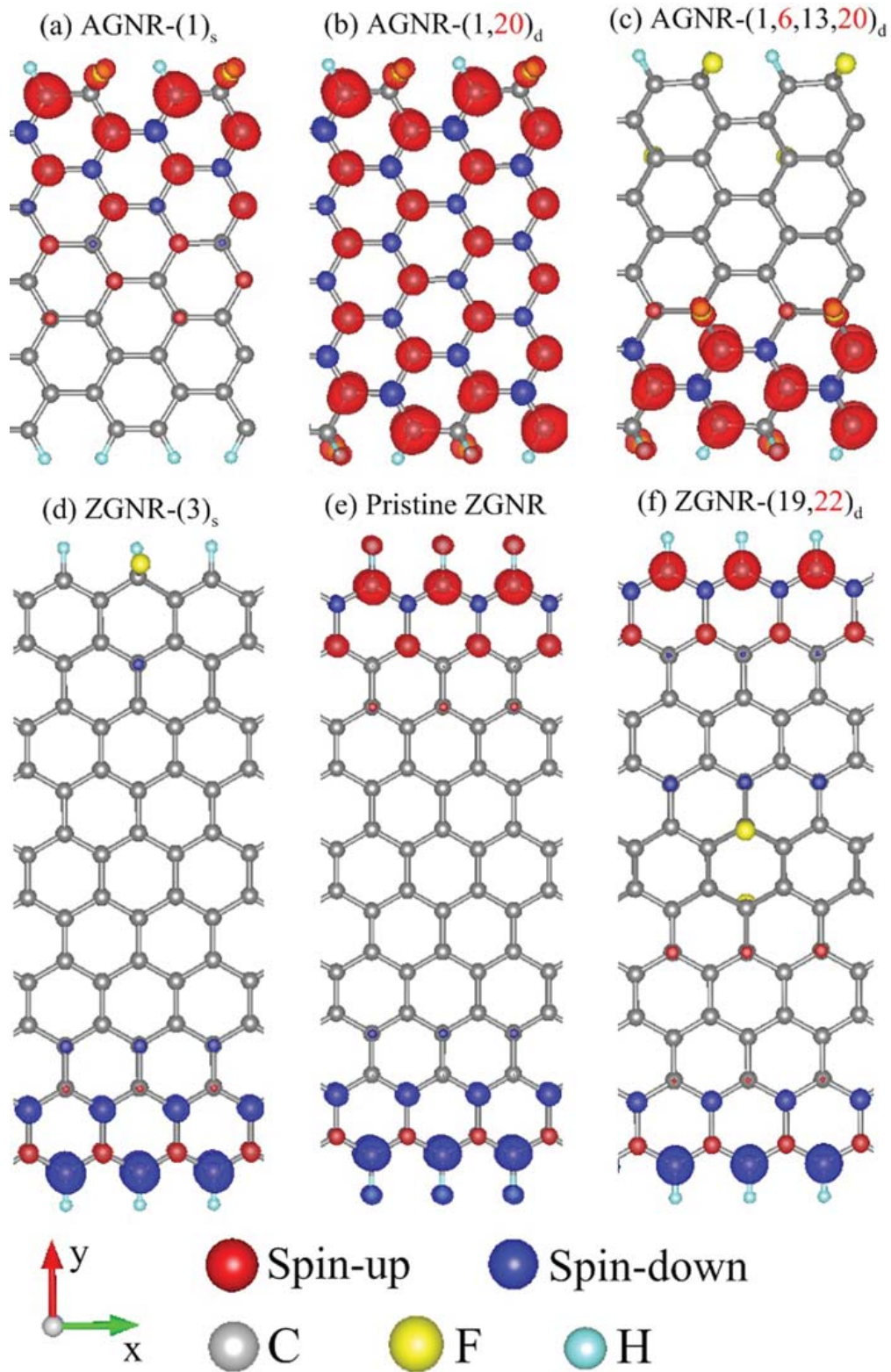


Figure 53: Spin density distributions of $N_A = 10$ fluorinated AGNR under (a) $(1)_s$, (b) $(1,20)_d$, (c) $(1,6,13,20)_d$ cases, and $N_Z = 10$ ZGNR for (d) $(3)_s$, (e) pristine, and (f) $(19,22)_d$ cases.

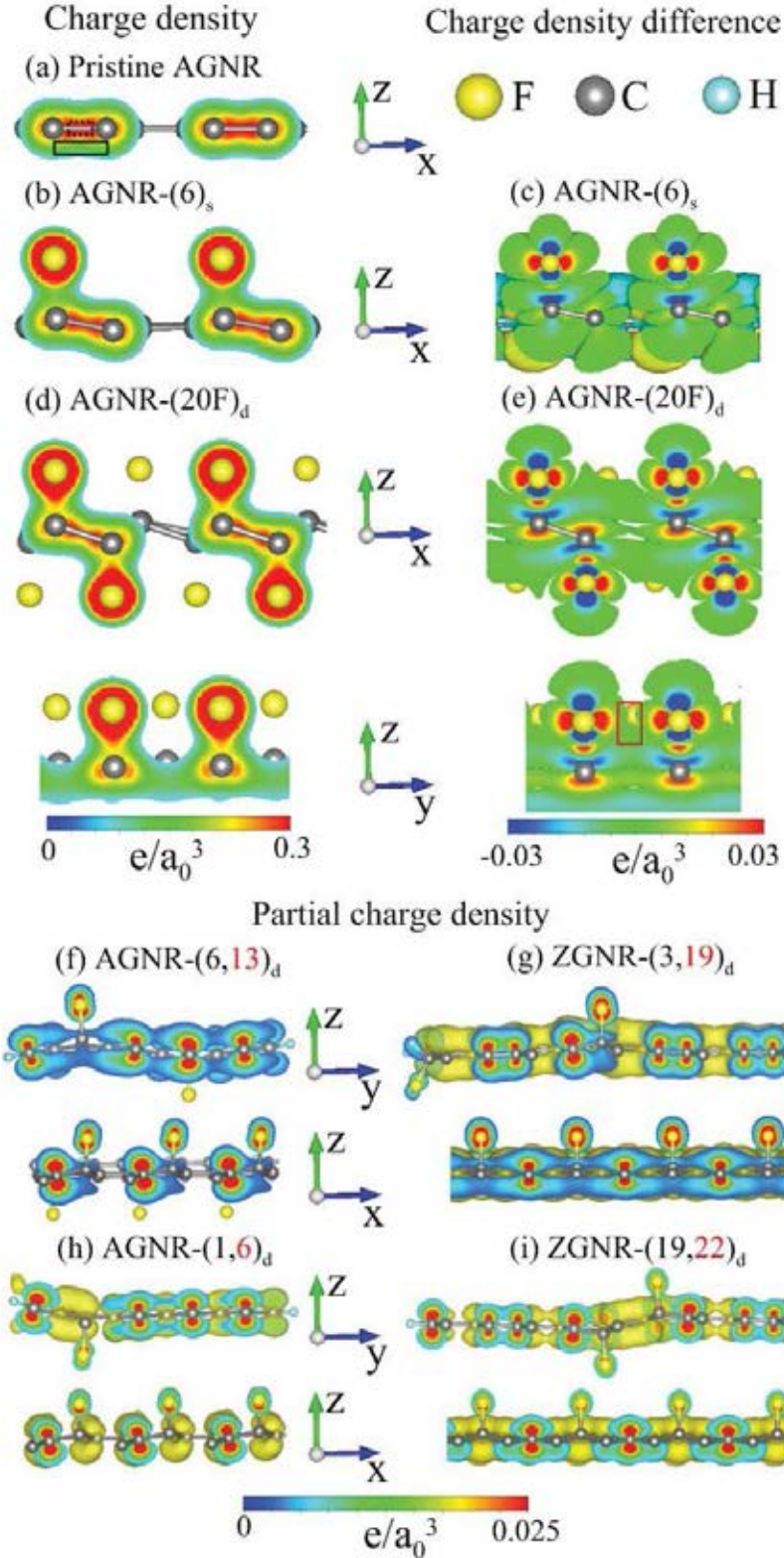


Figure 54: The spatial charge density of $N_A = 10$ armchair graphene nanoribbon for (a) Pristine, (b) $(6)_s$, & (d) $(20F)_d$ cases; the charge density difference for (c) $(6)_s$, & (e) $(20F)_d$ cases. The partial charge density is shown for (f) armchair- $(6,13)_d$, (g) zigzag- $(3,19)_d$, (h) armchair- $(1,6)_d$, and (i) zigzag- $(19,22)_d$.

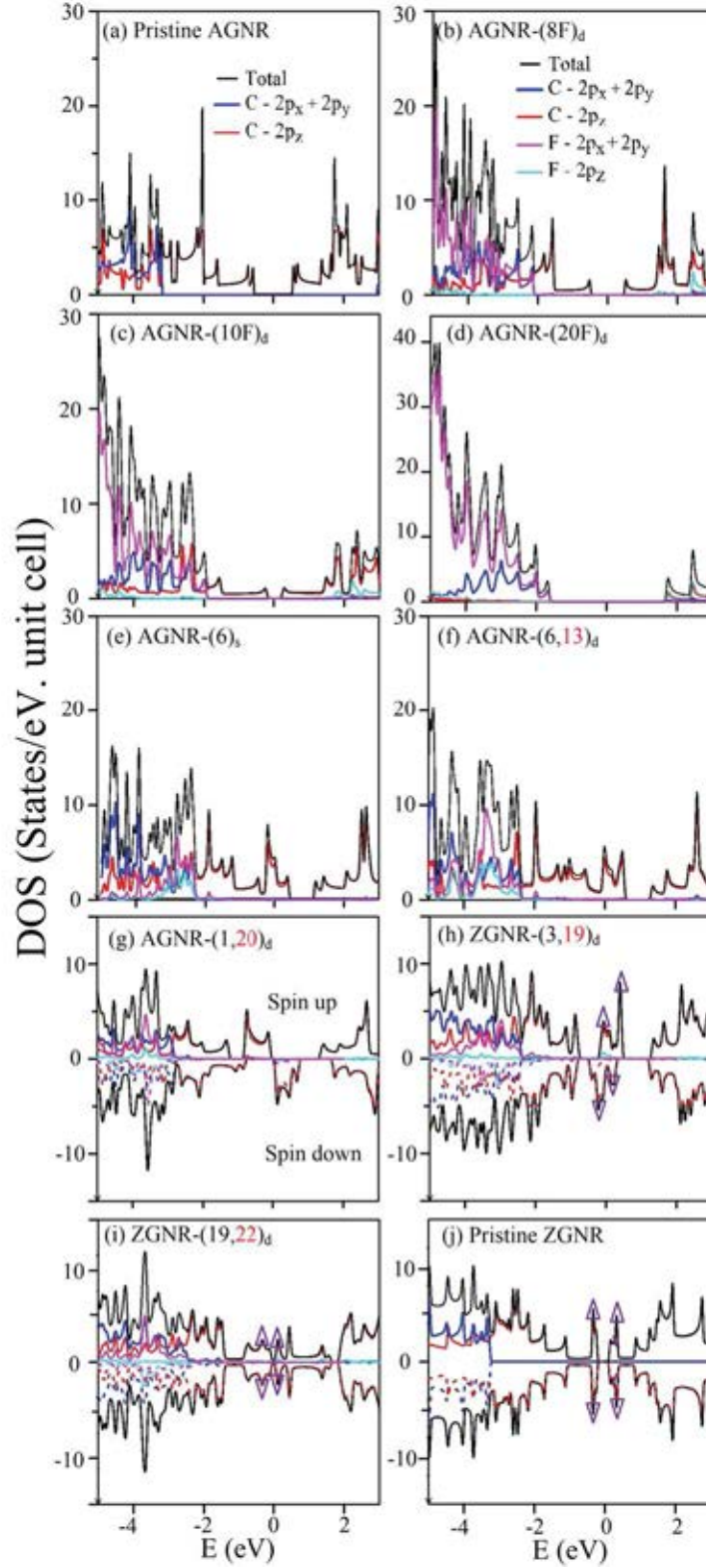


Figure 55: Orbital- and spin-projected DOSs for (a) pristine, (b) $(8F)_d$, (c) $(10F)_d$, (d) $(20F)_d$, (e) $(6)_s$, (f) $(6,13)_d$, (g) $(1,20)_d$ -adsorbed $N_A = 10$ armchair systems; (h) $(3,19)_d$ -& (i) $(19,22)_d$ -adsorbed and (j) pristine $N_Z = 10$ zigzag systems. Purple triangles arise from the partially at bands.